REPORT DOCUMENTATION PAGE

Form Approved OMB NO. 0704-0188

1. AGENCY USE ONLY (Leave Blank)	2. REPORT DATE:	3. REPORT TYPE AND DATES COVERED Final Report 1-Oct-2002 - 30-Jun-2006

4. TITLE AND SUBTITLE

Multi-Scale Dynamic Computational Models for Damage and Failure of Heterogeneous Materials

5. FUNDING NUMBERS

DAAD190210428

6. AUTHORS

Somnath Ghosh

8. PERFORMING ORGANIZATION REPORT NUMBER

7. PERFORMING ORGANIZATION NAMES AND ADDRESSES

Ohio State University Research Foundation
Office of Sponsored Programs
Ohio State University Research Foundation
Columbus, OH 43210 -1063

9. SPONSORING/MONITORING AGENCY NAME(S) AND ADDRESS(ES)

U.S. Army Research Office
P.O. Box 12211
Research Triangle Park, NC 27709-2211

10. SPONSORING / MONITORING AGENCY REPORT NUMBER

44363-EG.1

11. SUPPLEMENTARY NOTES

The views, opinions and/or findings contained in this report are those of the author(s) and should not contrued as an official Department of the Army position, policy or decision, unless so designated by other documentation.

12. DISTRIBUTION AVAILIBILITY STATEMENT

Approved for Public Release; Distribution Unlimited

12b. DISTRIBUTION CODE

13. ABSTRACT (Maximum 200 words)

The abstract is below since many authors do not follow the 200 word limit

14. SUBJECT TERMS

Multi-scale model, Extended Voronoi cell FEM, Crack propagation, Wave propagation

15. NUMBER OF PAGES

Unknown due to possible attachments

16. PRICE CODE

17. SECURITY CLASSIFICATION OF REPORT	18. SECURITY CLASSIFICATION ON THIS PAGE	19. SECURITY CLASSIFICATION OF ABSTRACT	20. LIMITATION OF ABSTRACT
UNCLASSIFIED	UNCLASSIFIED	UNCLASSIFIED	UL

Report Title

Multi-Scale Dynamic Computational Models for Damage and Failure of Heterogeneous Materials

ABSTRACT

This work develops an adaptive concurrent multi-level computational model for multi-scale analysis of composite structures undergoing damage initiation and growth due to microstructural damage induced by debonding at the fiber-matrix interface. The model combines macroscopic computations using a continuum damage model with explicit micromechanical computations, including explicit debonding at the fiber-matrix interface. Macroscopic computations are done by conventional FEM models while the Voronoi cell FEM is used for micromechanical analysis. Three hierarchical levels of different resolution adaptively evolve to improve the accuracy of solutions.

For micromechanical analysis, an eXtended Voronoi cell finite element model (X-VCFEM) is developed for modeling multiple cohesive crack propagation in brittle materials. The incremental crack directions and growth lengths are determined in terms of the cohesive energy near the crack tip. In addition to polynomial terms, stress functions include branch functions in conjunction with level set methods and multi-resolution wavelet functions. Next the X-VCFEM is used to model interfacial debonding with arbitrary matrix cohesive cracking in fiber-reinforced composites. Initiation and propagation of debonding depends not only on the total cohesive energy, but also on the traction-displacement curve. Finally, a VCFEM is also developed for transient elastodynamic analysis in time domain is developed.

List of papers submitted or published that acknowledge ARO support during this reporting period. List the papers, including journal references, in the following categories:

(a) Papers published in peer-reviewed journals (N/A for none)

1. S. Ghosh, J. Bai and P. Raghavan, “Concurrent multi-level model for damage evolution in microstructurally debonding composites”, Mechanics of Materials, (in press).

2. S. Li and S. Ghosh, “Multiple cohesive crack growth in brittle materials by the extended Voronoi cell finite element model”, International Journal of Fracture, (in press), Published online 2006: DOI: 10:1007/s10704-006-9000-2.

3. S. Li and S. Ghosh, “Extended Voronoi cell finite element model for multiple cohesive crack propagation in brittle materials”, International Journal for Numerical Methods in Engineering Vol. 65, pp. 1028-1067, 2006.

4. P. Raghavan and S. Ghosh, “A continuum damage mechanics model for unidirectional composites undergoing interfacial debonding”, Mechanics of Materials, Vol. 37, No. 9, pp. 955-979, 2005.

5. S. Swaminathan, S. Ghosh and N.J. Pagano, Statistically equivalent representative volume elements for composite microstructures, Part I: Without damage, Journal of Composite Materials Vol. 40, No. 7, pp. 583-604, 2006.

6. S. Swaminathan, S. Ghosh and N.J. Pagano, Statistically equivalent representative volume elements for composite microstructures, Part II: With evolving damage, Journal of Composite Materials, Vol. 40, No. 7, pp. 605-621, 2006.

7. S. Ghosh and P. Raghavan, “Multi-scale model for damage analysis in fiber reinforced composites with interfacial debonding materials”, International. Journal of Multiscale Computational Engineering, Vol.2, No. 4, pp. 621-645, 2004.

8. S. Ghosh and S. Moorthy, “Three dimensional Voronoi cell finite element model for microstructures with ellipsoidal heterogeneities", Vol. 34, pp. 510-531, 2004.

Number of Papers published in peer-reviewed journals: 8.00

(b) Papers published in non-peer-reviewed journals or in conference proceedings (N/A for none)

Number of Papers published in non peer-reviewed journals: 0.00

(c) Presentations

Keynote Lectures

1. S. Ghosh, “Computational multi-scale models for structure-material interaction,’’ AFOSR Workshop on Multiscale Modeling of Carbon Fiber Reinforced Composites, Long Beach, CA, May, 2006.

2. S. Ghosh, “Computational multi-scale models for structure-material interaction,’’ Mechanics of Materials Workshop, Mathematisches Forschungsinstitut, Oberwolfach, Germany, January, 2006.

3. S. Ghosh, “Concurrent multi-scale computational models for structure-material interaction,’’ Ohio Supercomputer Center on Materials for National Security, Santa FE, New Mexico, May, 2005

4. S. Ghosh “Multiple Scale Modeling for Deformation and Failure of Heterogeneous Materials’’, International Congress on Computational Mechanics and Simulation, Indian Institute of Technology, Kanpur, December 2004.

5. S. Ghosh, P. Raghavan and S. Li, “Multi-Level Computational Models For Multiple Scale Analysis of Composite Materials’’ International Workshops on Advances in Computational Mechanics: IWACOM, Hosei University, Tokyo, Japan, November 2004.

6. S. Ghosh and P. Raghavan, ` Multi-Level Models For Damage Analysis In Composite Materials’, 7th US National Congress of Computational Mechanics, Albuquerque, NM, July 2003.

7. S. Ghosh and P. Raghavan, `Adaptive Multi-Level Models For Damage Analysis In Composite Materials’, International Conference on Computational Engineering Science ICES 2003, Corfu, Greece, July 2003.

8. S. Ghosh, ` Multilevel Models for Multiple Scale Analysis of Composite Materials', Annual Symposium in the Computational Science and Engineering Program, The University of Illinois, Urbana-Champaign, April 2003

Invited Lectures at Conferences

9. S. Ghosh, J. Bai and P. Raghavan, “Concurrent multi-level model for damage evolution in microstructurally debonding composites,’’ 7th World Congress of Computational Mechanics, Los Angeles, CA, July, 2006.

10. S. Li and S. Ghosh, “Extended Voronoi cell finite element model for damage evolution in composite materials,’’ 7th World Congress of Computational Mechanics, Los Angeles, CA, July, 2006.

11. S. Li and S. Ghosh, “Extended Voronoi cell finite element model (X-VCFEM) for multiple cohesive crack propagation in brittle materials ,”8th US National Congress on Computational Mechanics, Austin, TX, July, 2005.

12. S. Ghosh and S. Li, “An Extended Voronoi cell FEM (X-VCFEM) for multiple cohesive crack evolution in composite materials,’’ 11th International Congress on Fracture, Turin, Italy, March, 2005.

13. S. Ghosh, P. Raghavan, J. Bai and S. Li, “Multi-Level computational models for multiple scale analysis of composite materials ’’, International Mechanical Engineering Conference and Exposition, IMECE 2004, Anaheim, California, November 2004.

14. S. Ghosh, “Multi-Scale model for damage analysis in fiber reinforced composites with debonding’’ Multiscale Modeling Conference: MMM-2, University of California, Los Angeles, October 2004.

15. S. Li and S. Ghosh, “A wavelet based Voronoi Cell FEM for crack evolution in composite materials’’ 6th World Congress of Computational Mechanics: WCCM, Beijing, China, September 2004.

16. P. Raghavan, J. Bai and S. Ghosh, “Multi-scale model for damage analysis in fiber-reinforced composites with debonding’’, NUMIFORM 2004: 8th International Conference on Numerical Methods in Industrial Forming Processes, The Ohio State University, Columbus Ohio, June 2004.

17. S. Ghosh and P. Raghavan, ` Multilevel models for multiscale damage analysis in composite materials ', 2nd MIT Conference, Cambridge MA, June 2003.
\end{enumerate}

Number of Presentations: 17.00

Non Peer-Reviewed Conference Proceeding publications (other than abstracts):

1. S. Ghosh and S. Li, "A wavelet based Voronoi cell FEM for crack evolution in composite materials,'' Proceedings of the 11th International Congress on Fracture, A. Carpinteri (eds.), Turin, Italy, pp. 4905-5001, 2005.

2. S. Ghosh, "Multiple scale modeling for deformation and failure of heterogeneous materials,'' Proceedings of the International Congress on Computational Mechanics and Simulation, NGR Iyengar and A. Kumar (eds.), IIT Kanpur Press, pp. 43-56, 2004.

3. S. Ghosh "Modeling at the interface of mechanics and materials for composite and polycrystalline materials'' Proceedings ICTACEM 2004; Third International Congress on Theoretical, Applied, Computational and Experimental Mechanics, S. Bhattacharyya and S. Ghosh (eds.), IIT Kharagpur Press, pp. 10-11, 2004.

4. P. Raghavan, J. Bai and S. Ghosh, "Multi-scale model for damage analysis in fiber-reinforced composites with debonding'', Materials Processing and Design: Modeling, Simulation and Application Proceedings of NUMIFORM, S. Ghosh, J. Castro and J.K. Lee (eds.), AIP Publishers, pp. 1911-1917, 2004.

Number of Non Peer-Reviewed Conference Proceeding publications (other than abstracts): 4

Peer-Reviewed Conference Proceeding publications (other than abstracts):

Number of Peer-Reviewed Conference Proceeding publications (other than abstracts): 0

(d) Manuscripts

1. J. R. Jain and S. Ghosh, A 3D continuum damage mechanics model for fiber reinforced composites with interfacial damage, submitted for publication.

2. J. R. Jain and S. Ghosh, Multi-resolution wavelet enriched Voronoi cell finite element model for elastic wave propagation in heterogeneous solids, in preparation.

3. S. Li and S. Ghosh, Modeling interfacial debonding and matrix cracking in fiber reinforced composites by the extended Voronoi cell FEM, submitted for publication.

Number of Manuscripts: 3.00

Number of Inventions:

Graduate Students

NAME	PERCENT_SUPPORTED	
Shriram Swaminathan	0.20	No
Jayesh Jain	1.00	No
Shanhu Li	0.25	No
FTE Equivalent:	**1.45**	
Total Number:	**3**	

Names of Post Doctorates

NAME	PERCENT_SUPPORTED
FTE Equivalent:	
Total Number:	

Names of Faculty Supported

NAME	PERCENT_SUPPORTED	National Academy Member
Somnath Ghosh	0.09	No
FTE Equivalent:	**0.09**	
Total Number:	**1**	

Names of Under Graduate students supported

NAME	PERCENT_SUPPORTED
FTE Equivalent:	
Total Number:	

Names of Personnel receiving masters degrees

NAME	
S. Swaminathan	No
Total Number:	**1**

Names of personnel receiving PHDs

NAME	
Shanhu Li	No
Total Number:	**1**

Names of other research staff

NAME	PERCENT_SUPPORTED
FTE Equivalent:	
Total Number:	

Sub Contractors (DD882)

Inventions (DD882)

Multi-Scale Dynamic Computational Models for Damage and Failure of Heterogeneous Materials

Sponsor: Army Research Office, Solid Mechanics

Grant No. DAAD190210428

Period of Performance: 2002-2006

Program Manager: Dr. Bruce Lamattina

By

Somnath Ghosh

Professor, Department of Mechanical Engineering

The Ohio State University, Columbus, Ohio

October 27, 2006

Acknowledgement

The author would like thank the Army Research Office, Solid Mechanics Program, for supporting this work through grant No. DAAD-190210428. He would like to express his sincere gratitude to Dr. Bruce Lamattina for his encouragement of the work and support. Extensive computer support by the Ohio Supercomputer Center through grant PAS813-2 is also gratefully acknowledged.

Contents

1 Relevant Information **1**

1.1 Personnel Supported 1

1.2 Completed Ph.D. Dissertations & M.S. Thesis 1

1.3 Refereed Journal Publications 2

1.4 Proceeding Publications 3

1.5 Keynote Lectures 4

1.6 Invited Lectures at Conferences 5

1.7 Honors and Awards 6

1.8 Collaborations with Army Research Laboratory 6

1.9 Technology Transfer to Army Research Laboratory 7

2 Introduction **9**

2.1 Organization of this Report 13

3 Multi-resolution Wavelet Enriched Hybrid Finite Element Method for One Dimensional Elastic Wave Propagation in Heterogeneous Solids **15**

3.1 Introduction 15

3.2 Assumed Stress Hybrid Formulation 17

3.3 Hybrid Element Assumptions and Weak Form 19

3.3.1 Element Assumptions 19

3.3.2 Weak Form . . . 20
3.4 Construction of Wavelet Based Stress Functions . . . 21
3.4.1 Principles of Wavelets and Multi-resolution Analysis . . . 21
3.4.2 Selection of the Wavelet Function . . . 23
3.4.3 Multi-resolution Wavelet Based Stress Functions . . . 25
3.4.4 Error Criteria for Time Dependent Adaptive Enrichment . . . 25
3.5 Solution Method and Numerical Aspects . . . 26
3.5.1 Solution for the Field Variables . . . 26
3.5.2 Stability Conditions . . . 27
3.6 Numerical Examples . . . 28
3.6.1 Wave Propagation through Layered Media . . . 28
3.6.2 Effect of Assumption of Periodicity . . . 29
3.7 Conclusions . . . 29

4 The Extended Voronoi Cell Finite Element Model For Multiple Cohesive Cracks Propagation 34

4.1 Introduction . . . 34
4.2 Voronoi Cell Fem Formulation for Multiple Propagating Cracks . . . 35
4.2.1 Cohesive zone models for crack propagation . . . 38
4.2.2 General element assumptions and weak form . . . 40
4.2.3 Stability conditions . . . 42
4.3 Creation of Enriched Stress Functions in X-VCFEM . . . 43
4.3.1 Pure Polynomial Forms of Stress Function: . . . 43
4.3.2 Branch Stress Functions Using Level Set Methods . . . 44
4.3.3 Multi-resolution Wavelet Functions for Modeling Cohesive Cracks . . . 47
4.3.4 Error measure for adaptive wavelet enrichment . . . 53
4.4 Solution Method . . . 54

4.5 Aspects of Numerical Implementation 56
4.5.1 Adaptive criteria for cohesive crack growth 56
4.5.2 Evaluation of stress intensity factors 61
4.5.3 Numerical integration schemes for [**H**] and [**G**] matrices 62
4.5.4 Invertibility of the [**H**] matrix 64
4.5.5 Elimination of element rigid body modes 64
4.6 Numerical Examples 65
4.6.1 Convergence tests for X-VCFEM for static cracks 65
4.6.2 Efficiency and Accuracy of X-VCFEM 68
4.6.3 Mesh independence of crack propagation with X-VCFEM 71
4.6.4 Effect of cohesive parameters on crack evolution 72
4.6.5 Propagation of multiple pre-existing cracks 73
4.7 Concluding Remarks 76

5 Extended Voronoi Cell Finite Element for Modeling Interfacial Debonding with Matrix Cohesive Cracking in Fiber Reinforced Composites 103

5.1 Introduction 103
5.2 Extended Voronoi cell FEM formulation for composites with interfacial debonding and matrix cracking 104
5.2.1 General element assumptions and weak form 106
5.2.2 Solution Method 108
5.2.3 Stability conditions 111
5.3 Aspects of Numerical Implementation 111
5.3.1 Adaptive criteria for cohesive crack growth 111
5.3.2 Generation of [$\mathbf{G}^c$] 113
5.4 Numerical Example 114
5.5 Concluding Remarks 115

6 Concurrent Multi-level Model for Damage Evolution in Microstructurally Debonding Composites **121**

6.1 Introduction 121

6.2 Levels in the Multi-scale Computational Model 123

6.2.1 Computational Subdomain Level-0 (Ω_{l0}) 124

6.2.2 Computational Subdomain Level-1 (Ω_{l1}) 127

6.2.3 Computational Subdomain Level-2 (Ω_{l2}) 128

6.2.4 Scale Transition Subdomain (Ω_{tr}) 131

6.3 Coupling Different Levels in the Concurrent Multi-Scale Algorithm 131

6.3.1 Modified Voronoi Cell FEM Formulation for a RVE in Level-1 Elements 135

6.4 Criteria for Adaptive Mesh Refinement and Level Transitions 137

6.4.1 Refinement of Level-0 and Level-1 Meshes by h-Adaptation 137

6.4.2 Criteria for Switching from Level-0 to Level-1 Elements 138

6.4.3 Criteria for Switching from Level-1 to Level-2 Elements 139

6.5 Numerical Examples with the Adaptive Multilevel Model 141

6.5.1 Multi-level Model vs. Micromechanical Analysis 141

6.5.2 A Composite Double Lap Joint with Microstructural Debonding 147

6.6 Conclusions 150

6.7 APPENDIX 151

6.7.1 Microscopic and Macroscopic Equations in Computational Subdomain Level-1 (Ω_{l1}) . 151

6.7.2 The Voronoi Cell Finite Element Model 152

List of Figures

3.1 Wave propagation through layered media: (a) Unit cell, (b) Impact load as a function of time, (c) Composite bar 31

3.2 Effect of assumption of periodicity: (a) Periodic model, (b) Full model 31

3.3 Displacement response at the center of a layered bar: Comparison with Abaqus 32

3.4 Displacement response at the center of a layered bar: Comparison with Abaqus 32

3.5 Stress response near the boundary 33

3.6 Stress response away from the boundary 33

4.1 (a) A mesh of Voronoi cell elements, each containing a single pre-existing crack, (b) a typical Voronoi cell element showing different topological features and loads. 78

4.2 Normal and tangential traction-separation behavior for the linear cohesive zone model. 78

4.3 (a) A schematic diagram of a crack surface showing parameters related to the distance functions; (b) depiction of the branched stress function Φ^{branch} near a crack for $s = 0,\ t = 0$. . . 79

4.4 Distribution of multi-resolution wavelet bases around a crack tip: (a) Crosses ($\times$) refer to the location of the origin of the basis vectors at a lower level corresponding to dilation parameters (tr_a and tr_c) and (b) adaptively upgraded to higher level wavelet bases with the addition of the next level of bases at locations indicated by the ($\square$). 80

4.5 Load-deflection behavior in a 3-point bend test with a crack, showing the softening snap back phenomenon. 81

4.6 A flowchart of the solution method. 82

4.7 The stress σ_{xx} at $x = -0.3$ for a double cantilever beam to demonstrate the effect of the branched stress function. 83

4.8 Algorithms for incremental propagation of cohesive cracks: (a) for direction and incremental length, (b) a cohesive crack going through the inter-element boundary, (c) for merger with other cracks and (d) for evaluation of $J-$ integral. 84

4.9 Subdivision of the Voronoi cell element for Gaussian quadrature, with a higher density of integration points near the crack tip. 85

4.10 (a) A center cracked plate loaded in tension, (b) a single X-VCFEM element with prescribed boundary conditions 86

4.11 X-VCFEM generated stress σ_{yy} at $y = 0$ for the cracked plate, to examine the effect of parameters in the wavelet basis: (a) dilation parameters and (b) translation parameters. . . . 87

4.12 X-VCFEM generated stress σ_{yy} at $y = 0$ for different enrichment orders of the wavelet basis functions. 88

4.13 Stress intensity factors for various values of $\mathbf{a/w}$. 89

4.14 (a) A plate with an edge crack under remote tension load, (b) comparison of load-deformation curves by X-VCFEM and ABAQUS. 90

4.15 (a) Prediction of the crack path by X-VCFEM for the Kalthoff experiment, (b) the macroscopic stress-strain response. 91

4.16 (a) Optical micrograph showing the path of cracking in a plate with a central crack subjected to far-field shear [28], (b) corresponding crack crack path generated by X-VCFEM, (c) crack opening displacement at the tip A. 92

4.17 A three-point symmetric bending specimen. 93

4.18 Comparison of normalized load-deflection curves for the three-point bending beam: (a) $\delta_e = 3.134796 \times 10^{-5}\ m$ and (b) $\delta_e = 6.26959 \times 10^{-6}\ m$. 94

4.19 (a) A three-point bending specimen with an unsymmetric initial crack, (b) comparison of load-deflection curves from X-VCFEM and literature [56] , (c) and (d) comparison of the crack paths by X-VCFEM with that in [56] for $\alpha = 0.25$ and $\alpha = 0.5$, respectively. 95

4.20 A plate with two cracks in arbitrary locations modeled by X-VCFEM using elements of different topologies located cracks, (b,c and d) show crack path at the end of the loading for the different elements and also a comparison with [87]. 96

4.21 (a) Optical micrograph showing the path of cracking in a plate with a central crack subjected to far-field shear [28], (b) 5 different sets of cohesive parameters for X-VCFEM simulations, (c) corresponding crack path generated by X-VCFEM, (d) comparison of the growth of cracks for different cases. 97

4.22 (a) X-VCFEM mesh for a plate with five randomly located cracks, (b) crack paths at the end of loading 98

4.23 Crack propagation in two square regions containing 28 cracks by X-VCFEM: (a) domain with horizontal cracks of equal length and random distribution, (b) domain with random orientation, length and distribution of cracks but containing a cluster. 99

4.24 Crack propagation in two square regions containing 28 cracks by X-VCFEM: (a,b) contour plots of σ_{yy} (MPa) with cohesive parameters *CP-1* for the domains in figure 23 (a) and (b), (c,d) contour plots of σ_{yy} (MPa) with cohesive parameters *CP-2* for the domains in figure 23 (a) and (b) 100

4.25 Comparison of the growth of crack **A** in *microstructure 1* with different cohesive parameters. 101

4.26 Macroscopic stress-strain response for different microstructural morphologies and cohesive parameters. 102

5.1 (a) Voronoi mesh for composite microstructure with interface debonding and matrix cracking, (b) a typical Voronoi cell element with interface and crack. 117

5.2 Cohesive zone models for calculating energy release rates: (a) the bilinear law for interface debonding and (b) the linear law for matrix cracking. 118

5.3 Node pairs (n_1, m_1) and (n_2, m_2) for describing damage advancing into matrix. 119

5.4 (a) A square microstructure containing a single circular fiber, (b) contour plot for σ_{yy} (GPa) with four cohesive cracks propagated from the interface. 120

6.1 Schematic of the two-way coupled concurrent multi-level model: (a) a representative volume element (RVE) for a non-uniformly distributed composite microstructure generated by tessellating the local microstructure, (b) the top-down multi-level model showing components of concurrent coupling, viz. continuum *level-0*, *level-1* of asymptotic homogenization and *level-2* of micromechanical analysis. 124

6.2 (a) Process of carving out *level-2* element microstructure (b) Interface constraints between *level-0/level-1* and *tr* elements 129

6.3 A typical *level-2* element containing an aggregate of microstructural Voronoi cell elements with relevant notations. 130

6.4 (a) Optical micrograph of a steel fiber-epoxy matrix composite with 264 fibers (b) the simulated computational model with a Voronoi cell mesh 142

6.5 The degrading dissipation energy W_d as a function of strain, evaluated for different cohesive zone parameters in the bilinear cohesive law 144

6.6 Contour plot of σ_{11} showing interfacial debonding at the end of the simulation, for: (a) pure micromechanical analysis, (b) analysis by multi-scale model with a smaller *level-2* region ($\frac{L_{tr/l2}}{L} = 0.35$), and (c) analysis by multi-scale model with a larger *level-2* region ($\frac{L_{tr/l2}}{L} = 0.45$).157

6.7 Computational mesh for the computational domain: (a) Macroscopic mesh with different RVE in every element, (b) Multi-level model with the interface between macroscopic and microscopic VCFE elements. 158

6.8 (a) A periodic microstructure containing the tessellated RVE (fibers in black), (b) placement of the RVE in the *level-1* element showing periodic nodes on the boundary. 158

6.9 Comparison of microscopic stress σ_{11} by different methods, plotted along a line through the middle of microstructure 159

6.10 Comparison of macroscopic (volume averaged) $\Sigma_{11} - e_{11}$ curves by different methods of analysis at (a) macroscopic element 1, and (b) macroscopic element 9. 160

6.11 (a) Schematic diagram of a composite double lap joint showing dimensions and boundary conditions, (b) the *level-0* computational mesh. 161

6.12 Contour plot of (a) degrading dissipation energy W_d and (b) its gradient $\sqrt{(\frac{\partial W_d}{\partial x_1})^2 + (\frac{\partial W_d}{\partial x_2})^2}$ at the final loading stage. 162

6.13 Evolution of the multi-level computational model with level transition (a) at 87 % loading, and (b) at the final loading stage. 163

6.14 *Level 2* microscopic VCFEM elements near the corner A showing microscopic stress distribution (GPa) and interfacial debonding at the end of the analysis by: (a) pure micromechanical analysis (b) multi-scale analysis. 164

6.15 (a) Evolved multi-level model and mesh at the final load step, (b) Microscopic stress distribution and interfacial debonding at the end of analysis for location near corner A, for $V_f = 40\%$ and case *C1*. 165

6.16 Macroscopic averaged stress-strain ($\Sigma_{11} - e_{11}$) plot at two locations in the double lap joint: (a) critical region A and (b) non-critical region B. 166

6.17 Degrading dissipation energy evolution near the corner A of the double lap joint for $V_f = 20\%$ and $V_f = 40\%$, and case *C1*. 167

6.18 Distribution of W_d with $V_f = 40\%$ and different cohesive parameters: (a) case *C1*, (b) case *C2*, and (c) case *C3*, at the end of loading. 168

List of Tables

4.1 Normalized stress intensity factors (K_I/K_{ref}) for different values of tr_a and b_1 in the multi-resolution wavelet representation. 77

4.2 Errors with varying enrichment order of multi-resolution wavelet functions for the different cases. 77

6.1 CPU time on a IA32 cluster to solve the double lap joint model by various methods. 149

Abstract

This work develops an adaptive concurrent multi-level computational model for multi-scale analysis of composite structures undergoing damage initiation and growth due to microstructural damage induced by debonding at the fiber-matrix interface. The model combines macroscopic computations using a continuum damage model developed in a preceding paper [75] with explicit micromechanical computations of stresses and strain, including explicit debonding at the fiber-matrix interface. The macroscopic computations are done by conventional FEM models while the Voronoi cell FEM is used for micromechanical analysis. Three hierarchical levels of different resolution adaptively evolve in this to improve the accuracy of solutions by reducing modeling and discretization errors. They levels include: (a) level-0 of pure macroscopic analysis using a continuum damage mechanics (CDM) model; (b) level-1 of asymptotic homogenization based macroscopic-microscopic RVE modeling to monitor the breakdown of continuum laws and signal the need for microscopic analyses; and (c) level-2 regions of pure micromechanical modeling with explicit depiction of the local microstructure. Two numerical examples are solved to demonstrate the effectiveness and accuracy of the multi-scale model. A double lap bonded composite joint is modeled for demonstrating the model's capability in handling large structural problems.

For micromechanical analysis, an eXtended Voronoi cell finite element model (X-VCFEM) is developed for modeling multiple cohesive crack propagation in brittle materials. The cracks are modeled by a cohesive zone model and their incremental directions and growth lengths are determined in terms of the cohesive energy near the crack tip. Extension to VCFEM is achieved through enhancements in stress functions in the assumed stress hybrid formulation. In addition to polynomial terms, the stress functions include branch functions in conjunction with level set methods, and multi-resolution wavelet functions in the vicinity of crack tips. Comparison of X-VCFEM simulation results with results in literature for several fracture mechanics problems validates the effectiveness of X-VCFEM. Effect of stereographic features such as size and distribution of heterogeneities on damage evolution in random microstructures are also discussed. In order

to study the interaction between interface debonding and cohesive matrix cracking, a criterion based on cohesive models is proposed to assess the crack penetrating into matrix from the interface and is validated by numerical examples.

Next the eXtended Voronoi cell finite element model(X-VCFEM) has been developed for modeling interfacial debonding with arbitrary matrix cohesive cracking in fiber-reinforced composites. To describe the onset and growth of damage along the fiber-matrix interface, normal and tangential cohesive zone models are coupled into VCFEM. It is shown that the initiation and especially propagation of debonding depends not only on the total cohesive energy, but also on the shape of the traction-displacement curve. The model is also used to study the influence of various local morphological parameters on damage evolution by interfacial debonding. A special function of various geometric parameters is developed to predict the location of debonding in microstructures with varying morphology.

Finally, a Voronoi cell finite element model is also developed for transient elastodynamic analysis in time domain is developed. In the present formulation, the inertia field is approximated in terms of stresses so as to satisfy the equilibrium equation a-priori. The weak forms of kinematics and traction reciprocity are obtained by minimization of the complementary variational principle. Stress wave is a local disturbance that propagates through the material, resulting in high stress gradients near the wave front. Therefore, localization and multi-resolution properties of the wavelet functions are exploited to enhance the computational efficiency by enriching the stress functions only locally near the wave front. The enrichment is carried out adaptively by employing posteriori local error estimators that determine the required translation and dilation of the wavelet functions at each time step. The accuracy and computational efficiency of the proposed method is demonstrated through comparison with analytical solutions and conventional FEM packages.

Chapter 1

Relevant Information

1.1 Personnel Supported

1. Somnath Ghosh, PI

2. Jayesh Jain, Ph.D. Student, Graduate Research Associate, 100%

3. Shanhu Li, Ph.D. Student, Graduate Research Associate, (partial support)

   Now at ALGOR Corporation.

4. Shriram Swaminathan, M.S. Student, Graduate Research Associate, (partial support)

   Now at ABAQUS

1.2 Completed Ph.D. Dissertations & M.S. Thesis

1. J. Jain, Ph.D. candidate, Dissertation Topic: Multiple Scale Modeling of Damage in Composite Materials under Dynamic Conditions

2. S. Li, Ph.D. 2005, Dissertation Title: Extended Voronoi Cell Finite Element Model for Damage in Brittle Matrix Composites

3. S. Swaminathan M.S. 2005, Thesis Title: Statistically Equivalent Representative Volume Elements for Composite Microstructures

1.3 Refereed Journal Publications

1. J. R. Jain and S. Ghosh, A 3D continuum damage mechanics model for fiber reinforced composites with interfacial damage, submitted for publication.

2. J. R. Jain and S. Ghosh, Multi-resolution wavelet enriched Voronoi cell finite element model for elastic wave propagation in heterogeneous solids, in preparation.

3. S. Li and S. Ghosh, Modeling interfacial debonding and matrix cracking in fiber reinforced composites by the extended Voronoi cell FEM, submitted for publication.

4. S. Ghosh, J. Bai and P. Raghavan, Concurrent multi-level model for damage evolution in microstructurally debonding composites, Mechanics of Materials, (in press).

5. S. Li and S. Ghosh, Multiple cohesive crack growth in brittle materials by the extended Voronoi cell finite element model, International Journal of Fracture, (in press), Published online 2006: DOI: 10:1007/s10704-006-9000-2.

6. S. Li and S. Ghosh, Extended Voronoi cell finite element model for multiple cohesive crack propagation in brittle materials, International Journal for Numerical Methods in Engineering Vol. 65, pp. 1028-1067, 2006.

7. P. Raghavan and S. Ghosh, A continuum damage mechanics model for unidirectional composites undergoing interfacial debonding, Mechanics of Materials, Vol. 37, No. 9, pp. 955-979, 2005.

8. S. Swaminathan, S. Ghosh and N.J. Pagano, Statistically equivalent representative volume elements for composite microstructures, Part I: Without damage, Journal of Composite Materials Vol. 40, No. 7, pp. 583-604, 2006.

9. S. Swaminathan, S. Ghosh and N.J. Pagano, Statistically equivalent representative volume elements for composite microstructures, Part II: With evolving damage, Journal of Composite Materials, Vol. 40, No. 7, pp. 605-621, 2006.

10. S. Ghosh and P. Raghavan, Multi-scale model for damage analysis in fiber reinforced composites with interfacial debonding materials, International. Journal of Multiscale Computational Engineering, Vol.2, No. 4, pp. 621-645, 2004.

11. S. Ghosh and S. Moorthy, Three dimensional Voronoi cell finite element model for microstructures with ellipsoidal heterogeneities", Vol. 34, pp. 510-531, 2004.

1.4 Proceeding Publications

1. S. Ghosh and S. Li, A wavelet based Voronoi cell FEM for crack evolution in composite materials, Proceedings of the 11th International Congress on Fracture, A. Carpinteri (eds.), Turin, Italy, pp. 4905-5001, 2005.

2. S. Ghosh, Multiple scale modeling for deformation and failure of heterogeneous materials, Proceedings of the International Congress on Computational Mechanics and Simulation, NGR Iyengar and A. Kumar (eds.), IIT Kanpur Press, pp. 43-56, 2004.

3. S. Ghosh Modeling at the interface of mechanics and materials for composite and polycrystalline materials Proceedings ICTACEM 2004; Third International Congress on Theoretical, Applied, Computational and Experimental Mechanics, S. Bhattacharyya and S. Ghosh (eds.), IIT Kharagpur Press, pp. 10-11, 2004.

4. P. Raghavan, J. Bai and S. Ghosh, Multi-scale model for damage analysis in fiber-reinforced composites with debonding, Materials Processing and Design: Modeling, Simulation and Application Proceedings of NUMIFORM, S. Ghosh, J. Castro and J.K. Lee (eds.), AIP Publishers, pp. 1911-1917, 2004.

1.5 Keynote Lectures

1. S. Ghosh, Computational multi-scale models for structure-material interaction, AFOSR Workshop on Multiscale Modeling of Carbon Fiber Reinforced Composites, Long Beach, CA, May, 2006.

2. S. Ghosh, Computational multi-scale models for structure-material interaction, Mechanics of Materials Workshop, Mathematisches Forschungsinstitut, Oberwolfach, Germany, January, 2006.

3. S. Ghosh, Concurrent multi-scale computational models for structure-material interaction, Ohio Supercomputer Center on Materials for National Security, Santa FE, New Mexico, May, 2005

4. S. Ghosh Multiple Scale Modeling for Deformation and Failure of Heterogeneous Materials, International Congress on Computational Mechanics and Simulation, Indian Institute of Technology, Kanpur, December 2004.

5. S. Ghosh, P. Raghavan and S. Li, Multi-Level Computational Models For Multiple Scale Analysis of Composite Materials International Workshops on Advances in Computational Mechanics: IWACOM, Hosei University, Tokyo, Japan, November 2004.

6. S. Ghosh and P. Raghavan, ' Multi-Level Models For Damage Analysis In Composite Materials, 7th US National Congress of Computational Mechanics, Albuquerque, NM, July 2003.

7. S. Ghosh and P. Raghavan, 'Adaptive Multi-Level Models For Damage Analysis In Composite Materials, International Conference on Computational Engineering Science ICES 2003, Corfu, Greece, July 2003.

8. S. Ghosh, ' Multilevel Models for Multiple Scale Analysis of Composite Materials', Annual Symposium in the Computational Science and Engineering Program, The University of Illinois, Urbana-Champaign, April 2003

1.6 Invited Lectures at Conferences

1. S. Ghosh, J. Bai and P. Raghavan, Concurrent multi-level model for damage evolution in microstructurally debonding composites, 7th World Congress of Computational Mechanics, Los Angeles, CA, July, 2006.

2. S. Li and S. Ghosh, Extended Voronoi cell finite element model for damage evolution in composite materials, 7th World Congress of Computational Mechanics, Los Angeles, CA, July, 2006.

3. S. Li and S. Ghosh, Extended Voronoi cell finite element model (X-VCFEM) for multiple cohesive crack propagation in brittle materials ,8th US National Congress on Computational Mechanics, Austin, TX, July, 2005.

4. S. Ghosh and S. Li, An Extended Voronoi cell FEM (X-VCFEM) for multiple cohesive crack evolution in composite materials, 11th International Congress on Fracture, Turin, Italy, March, 2005.

5. S. Ghosh, P. Raghavan, J. Bai and S. Li, Multi-Level computational models for multiple scale analysis of composite materials , International Mechanical Engineering Conference and Exposition, IMECE 2004, Anaheim, California, November 2004.

6. S. Ghosh, Multi-Scale model for damage analysis in fiber reinforced composites with debonding Multiscale Modeling Conference: MMM-2, University of California, Los Angeles, October 2004.

7. S. Li and S. Ghosh, A wavelet based Voronoi Cell FEM for crack evolution in composite materials 6th World Congress of Computational Mechanics: WCCM, Beijing, China, September 2004.

8. P. Raghavan, J. Bai and S. Ghosh, Multi-scale model for damage analysis in fiber-reinforced composites with debonding, NUMIFORM 2004: 8th International Conference on Numerical Methods in Industrial Forming Processes, The Ohio State University, Columbus Ohio, June 2004.

9. S. Ghosh and P. Raghavan, ' Multilevel models for multiscale damage analysis in composite materials ', 2nd MIT Conference, Cambridge MA, June 2003.

1.7 Honors and Awards

1. S. Ghosh: Fellow, ASM International, The Materials Information Society, 2006
2. S. Li: (Ph.D. student and GRA): Robert J. Melosh Medal Competition Finalist, 2006
3. S. Manchiraju: (Ph.D. student and GRA): Winner of Materials Modeling Student Competition, at the 7th World Congress of Computational Mechanics at Los Angeles, in 2006
4. S. Ghosh: John B. Nordholt Professorship, College of Engineering, The Ohio State University, 2004
5. S. Ghosh: Lumley Interdisciplinary Research Award, College of Engineering, The Ohio State University, 2004
6. S. Ghosh: Chairman of NUMIFORM 2004: Numerical Methods in Industrial Forming Processes', June 2004.
7. S. Ghosh: Lumley Faculty Research Award, College of Engineering, The Ohio State University, 2003
8. P. Raghavan: Robert J. Melosh Medal Winner, for best student paper in Finite Element Analysis, 2003
9. Member of Executive Council, U.S. Association of Computational Mechanics, 2002-

1.8 Collaborations with Army Research Laboratory

We have collaborated with Dr. Peter Chung and Dr. Raju Namburu, at the Army Research Laboratory. The PI has visited ARL several times to present seminar and discuss progress with researchers in the Computational and Informational Sciences Directorate at ARL. Dr. Namburu and Chung have also visited OSU twice to monitor the breadth and depth of progress at the PIs laboratory.

1.9 Technology Transfer to Army Research Laboratory

Technology transfer of some of the codes developed in the PIs research laboratory to ARL platforms has taken place in consultation with Dr. Peter Chung and Dr. Raju Namburu in the Computational and Informational Sciences Directorate at ARL. The PI visited has ARL several times in the last few years and Dr. Namburu and Dr. Chung have also visited the Computational Mechanics Laboratory at OSU several times. The recent visit by the PI to ARL in 2006 was on July 14, 2006. Significant exchange of ideas and future plans took place during this visit.

The PI has transferred major codes to the ARL platforms for use by ARL researchers. A special person with security clearance and authorized to work on US government systems has been recruited from the Ohio Supercomputer Center to facilitate the technology transfer process. The first code that has been transferred is the crystal plasticity model. Initial efforts were identified to provide access to the crystal plasticity model through a user defined material model in LS-DYNA. This required the proper LSTC software, a special version of LS-DYNA that allows user subroutines to be compiled in, to be verified on the target ARL systems. These systems are identified to be the SGI Origin, the IBM P3 system and the Linux cluster. Only the Origin had the software installed, so requests were entered through the ARL support staff and the software is now installed on these systems. Next, the user subroutines were moved to the three ARL systems and compilation and numerical accuracy needed to be verified. Compilation scripts have been customized for each system and a validation model was run so that numerical results could be compared. Compilation was verified on all three machines and numerical results have been verified on the Origin and IBM systems. Documentation is also provided for users to be able to reference a README file on each.

The second code and model that has been ported to ARL systems is an earlier version of the CDM model. The Fortran 90 code has been ported to JVN Linux cluster at ARL. We have created Make files to build the model and have created batch scripts documenting example usage. The User Manual for this code documents important control variables, input file structure and provides an example case to document

analysis workflow.

Chapter 2

Introduction

Analysis of composite materials with microstructural heterogeneities is conventionally done with macroscopic properties obtained by homogenizing response functions in the representative volume element (RVE) from microscopic analyses at smaller length scales. While these "bottom-up" homogenization models are efficient and can reasonably predict macroscopic or averaged behavior, such as stiffness or strength, they have limited predictive capabilities with problems involving localization, failure or instability. Assumptions of macroscopic uniformity and RVE periodicity, the two basic requirements of homogenization, break down under these circumstances. The uniformity assumption ceases to hold in critical regions of high local solution gradients, such as near free edges, interfaces, material discontinuities or evolving damage. RVE periodicity, on the other hand, is unrealistic for non-uniform microstructures, e.g. in the presence of clustering of heterogeneities or microscopic damage. Even with a uniform phase distribution in the microstructure, the evolution of localized stresses, strains or damage path can violate the periodicity conditions. Problems like this have been effectively tackled by multi-scale modeling methods e.g. in [72, 29, 44, 67, 66, 82, 81, 74, 73, 94, 108, 92]. Multi-scale analyses methods can be broadly classified into two classes. The first is known as "hierarchical models" [29, 44, 94, 92] in which information is passed from lower to higher scales, usually in the form of material properties. The hierarchical homogenization models assume periodic representative volume elements (RVE) in the microstructure and uniformity of macroscopic field variables. The second class, known as "concurrent methods" [81, 67, 66, 82, 74, 73, 108], implement sub-structuring and simultaneously solve different models

at regions with different resolutions or scales.

Two-way coupling of scales enabled in the concurrent methods is suitable for problems involving localization, damage and failure. Macroscopic analysis, using bottom-up homogenization in regions of relatively benign deformation, enhances the efficiency of the computational analysis. As a matter of fact, it would be impossible to analyze large structural regions without the advantage of a continuum model based macroscopic analysis. On the other hand, the top-down localization process cascading down to the microstructure in critical regions of localized damage or instability for pure microscopic analysis, is necessary for accurately predicting the damage path. These microscopic computations, depicting the real microstructure are often complex and computationally prohibitive. Hence, a concurrent setting makes such analyses feasible, provided the "zoom-in" regions are kept to a minimum. The adaptive multi-level models, promoted in [67, 66, 82, 74, 73, 108], are attempts to achieve this objective, with the adaptivity motivated from physical and mathematical perspectives. However, there is a paucity of such studies in the literature involving material nonlinearity and evolving microstructural damage. In their previous studies, Ghosh and coworkers have proposed adaptive multi-level analysis using the microstructural Voronoi cell FEM model for modeling elastic-plastic composites with particle cracking and porosities in [81], and for elastic composites with free edges and stress singularities in [74, 73].

In this work, we have derived and computationally modeled an anisotropic continuum damage mechanics (CDM) model for unidirectional fiber-reinforced composites undergoing interfacial debonding from by using homogenization theory. The CDM model homogenizes the damage incurred through initiation and growth of interfacial debonding in a microstructural RVE with nonuniform distribution of fibers. Additionally, arbitrary loading conditions are also effectively handled by this model. The CDM model is then used in an adaptive concurrent multi-level computational model to analyze multi-scale evolution of damage. Damage by fiber-matrix interface debonding, is explicitly modeled over extended microstructural regions at critical locations [35, 53]. The adaptive model addresses issues of efficiency and accuracy through considerations of physically-based modeling errors.

The adaptive multi-level model consists of three levels of hierarchy viz. *level-0*, *level-1* and *level-2*), which evolve in sequence. The continuum damage model developed in [75] is used for *level-0* computations. The

level-1 domain is used as a 'swing region' to establish criteria for switching from macroscopic to microscopic calculations. Physical criteria involving variables at the macroscopic and microstructural RVE levels, trigger switching from pure macroscopic to pure microscopic calculations, i.e. the $level-0 \rightarrow level-1 \rightarrow level-2$. A transition layer is placed between the $level-1$ and microscopic $level-2$ domains for smooth transition from one scale to the next.

An important damage phenomenon in composite microstructures is crack propagation in brittle matrix. Numerical analysis and simulation of the growth of multiple cracks in materials is a challenging enterprise due to morphological and constitutive complexities that govern its growth. Even a very high density mesh cannot overcome pathological mesh dependence near the crack tips and avoid biasing the direction of crack propagation. The difficulties aggravate in the presence of multiple cracks, due to their interaction with each other. Various methods have been proposed for improving the effectiveness of computational methods in modeling cracks. While most of these analyses are limited to stationary cracks, it is only recently that effective methods of analysis of crack propagation are being proposed. With increasing power of computational modeling and hardware, the cohesive zone models [63, 64, 65, 97, 30, 33, 39, 68] have emerged as important tools for modeling crack propagation in homogeneous and heterogeneous materials. In these models, interfaces of similar and dissimilar materials are treated as zero thickness non-linear springs. Interfacial traction is specified as nonlinear functions of tangential and normal separations across the interface to manifest crack evolution. These models have been used to simulate crack growth between elements in [13, 103, 39], by lacing the interface between contiguous elements with cohesive springs. The use of a highly refined computational mesh, especially near the crack tip is still a requirement, even though the effect is mitigated due to the finite crack tip stress with this model. Alternatively, intra-element enrichment approaches, based on the incorporation of embedded discontinuities in displacement or strain fields have been proposed ([48]), which eliminates mesh dependent prediction of the evolving crack path, and hence the need for remeshing. The extended FEM or X-FEM [8, 7, 9, 10, 24, 59, 60] is a powerful recent addition to this family of intra-element enrichment. Cohesive crack propagation has been modeled in this work by using the partition of unity concept to incorporate local enrichment functions that allows the preservation of the general displacement

based FEM formalism.

Stress-based finite element methods have had considerable success when stress fields are of interest in the analysis [96, 95]. Within this general formalism, the Voronoi cell finite element method (VCFEM) has been developed in [35, 61, 80, 36, 79, 78, 53] for micromechanical analysis of arbitrary heterogeneous microstructures. The method can effectively overcome requirements of large degrees of freedom in conventional finite element models. Morphological arbitrariness in dispersions, shapes and sizes of heterogeneities, as seen in real micrographs are readily modeled by this method. The VCFE model naturally evolves by tessellation of the microstructure into a network of multi-sided Voronoi polygons. Each Voronoi cell with embedded heterogeneities (particle, fiber, void, crack etc.) represents the region of contiguity for the heterogeneity, and is treated as an element in VCFEM. VCFEM elements are considerably larger than conventional FEM elements and incorporate a special assumed stress hybrid FEM formulation. Incorporation of known functional forms from analytical micromechanics substantially enhances its convergence. A high level of accuracy with significantly reduced degrees of freedom has been achieved with VCFEM. Computational efficiency is therefore substantially enhanced compared to conventional displacement-based FE models. Successful applications of 2D-small deformation VCFEM have been made in thermo-elastic-plastic problems of composite and porous materials [61, 80]. An adaptive VCFEM has been developed in [80], where optimal improvement is achieved by h-p adaptation of the displacement field and p-enrichment of the stress field.

The cohesive crack propagation model has been incorporated in VCFEM in [35, 53] to model interface debonding in fiber reinforced composites. However, in these models, the debonding or crack evolution path is along the interface and hence the cohesive zone regions are known a-priori. In the event that the crack branches off into the matrix, the path is no longer pre-assessed and needs to be determined at each load increment, consistent with the local state of stresses, strains and morphology. This task is considerably more challenging since a slight deviation can lead to completely wrong prediction.

The motivation of this work is derived from the need to create a robust finite element method, eXtended

Voronoi cell finite element model (X-VCFEM), for modeling interface debonding with arbitrary crack propagation in heterogeneous materials. This is an essential step, prior to simulating the entire microstructural failure problem. X-VCFEM incorporates: (a) stress discontinuities across the cohesive crack through branch functions in conjunction with level set methods, (b) crack tip stress concentration through the introduction of multi-resolution wavelet functions [38, 47, 71] in the vicinity of the crack tip, and (c) incremental crack propagation using a cohesive energy based criterion for estimating the direction and length of the incremental crack advance.

Finally, a Voronoi cell finite element model is developed for transient elastodynamic analysis in time domain is developed. In the present formulation, the inertia field is approximated in terms of stresses so as to satisfy the equilibrium equation a-priori. The weak forms of kinematics and traction reciprocity are obtained by minimization of the complementary variational principle. Stress wave is a local disturbance that propagates through the material, resulting in high stress gradients near the wave front. Therefore, localization and multi-resolution properties of the wavelet functions are exploited to enhance the computational efficiency by enriching the stress functions only locally near the wave front. The enrichment is carried out adaptively by employing posteriori local error estimators that determine the required translation and dilation of the wavelet functions at each time step. At the outset, a stable, accurate and computationally efficient adaptive computational framework in 1D is developed for micro-mechanical response of composites under impact loading. The accuracy and computational efficiency of the proposed method is demonstrated through comparison with analytical solutions and conventional FEM packages.

2.1 Organization of this Report

The report is divided into five subsequent chapters. In chapter 3, variational formulation and various aspects of the computational scheme for stress wave propagation in composites are presented. Extensions of the VCFEM (X-VCFEM) for cohesive crack propagation are developed in Chapter 4. Numerical validation of X-VCFEM for matrix cracking is also presented. Based on the preparation of previous two chapters,

the X-VCFEM for modeling interface debonding with matrix cohesive cracking are developed in chapter 5. Finally, an account of multi-scale modeling is presented with critical examples.

Chapter 3

Multi-resolution Wavelet Enriched Hybrid Finite Element Method for One Dimensional Elastic Wave Propagation in Heterogeneous Solids

3.1 Introduction

Heterogeneous materials are being used increasingly in impact related applications because of their high strength to weight ratio and improved dynamic properties [32, 58]. As a consequence, analysis of wave propagation through heterogeneous media is being pursued consistently by researchers. However, most of the methods available in the literature aim at obtaining macroscopic response using effective properties of the composites. The major challenge in obtaining actual micro-scopic response of composites under dynamic loading is the computational size of the problem and the complex nature of the wave propagation phenomena. Stress waves experience multiple reflections, transmissions and interference in the presence of heterogeneities

in the microstructure and produce dynamic stress concentrations that are significantly greater than that in global average response [69]. This initiates and propagates the damage, leading to failure of the material. Recently, attempts have been made to account for the micro-structural effects in the macro response. Wang and Sun [101] developed a technique that includes the effect of micro-inertia in the continuum model of the heterogeneous materials. Using these macro-equations, harmonic and transient response of one-dimensional layered medium was obtained which was in close agreement with the analytical results for a range of wavelengths. Fish et al [46, 45] developed a dispersive model for wave propagation using higher order homogenization theory with multiple spatial and temporal scales. A goal-oriented adaptive modeling technique that solves the micro-mechanical problem using actual material properties was developed in frequency domain by Romkes and Oden [77]. The method used local error estimators to identify the regions where actual properties are to be used and the critical frequencies for which the solution is to be improved.

In the last decade, Voronoi Cell Finite Element Method (VCFEM) has emerged as a powerful technique for micro-mechanical modeling of arbitrary heterogeneous materials. VCFEM has been developed for elastic, elasto-plastic response of heterogeneous materials [61], damage initiation and propagation in ductile as well as brittle materials [35, 36]. VCFEM has been shown to be significantly more efficient than the conventional displacement based methods for 2D static problems. In this work, a hybrid formulation based on same principle is presented for one dimensional elastic wave propagation in heterogeneous materials. There have been a few hybrid/mixed formulations in the literature for elastodynamic analysis [3, 89, 31]. Inclusion of adaptive techniques in such formulations could reduce the size of the problem substantially. The formulation proposed in this work utilizes the multi-resolution properties of the wavelets for adaptive enrichment of stress function so that least number of stress parameters are required.

The proposed formulation makes two independent approximations: stress field and the boundary displacement field. The internal displacement field is approximated in terms of stresses so as to satisfy the equilibrium equation in strong sense. The kinematic equation in the element, traction reciprocity and the compatibility of the internal displacement field are satisfied in weak sense as Euler-Lagrange equations.

The chapter is organized as follows: The hybrid stress formulation for one dimensional wave propagation is introduced first. The weak form is derived by taking variations of the Hamiltonian expressed in terms of complimentary energy. The stress function is constructed adaptively using multi-resolution wavelets and posteriori error indicator. The developed adaptive algorithm is implemented for simulating wave propagation through layered media.

3.2 Assumed Stress Hybrid Formulation

A typical 2D Voronoi cell element is multi-phase domain consisting of inclusion/cavity surrounded by matrix phase [61]. However, the two-noded 1D element presented here consists of a single phase such that each layer of heterogeneous layered media becomes one element Ω_e without need of any further refinement. The element boundary $\partial\Omega_e$ with unit outward normal n^e is formed by two nodes and may consist of prescribed traction Γ_{te}, prescribed displacement Γ_{ue} and inter-element boundary Γ_{me}. For the hybrid element formulation, in the absence of body forces, the micro mechanics elastodynamic initial boundary value problem is described as:

$$
\begin{aligned}
&\text{Find } (\boldsymbol{\sigma}, \mathbf{u}, \mathbf{u}_\Gamma) \ \in \mathcal{T} \times \mathcal{V} \times \mathcal{V}_\Gamma \ \text{ satisfying} \\
&\nabla \cdot \boldsymbol{\sigma} = \rho \ddot{\mathbf{u}} \quad \text{and} \quad \frac{\partial B}{\partial \boldsymbol{\sigma}} = \boldsymbol{\epsilon} \in \Omega_e && (a) \\
&\mathbf{u}_\Gamma = \bar{\mathbf{u}} \text{ on } \Gamma_{ue} \quad , \quad \boldsymbol{\sigma} \cdot \mathbf{n}^e = \bar{\mathbf{t}} \text{ on } \Gamma_{te} && (b) \\
&\boldsymbol{\sigma} = \boldsymbol{\sigma}_0 \ , \quad \mathbf{u} = \mathbf{u}_0 \ \text{ and } \ \dot{\mathbf{u}} = \dot{\mathbf{u}}_0 \ \text{ at } \ t = 0 && (c)
\end{aligned}
\tag{3.1}
$$

where $\nabla \equiv \frac{\partial}{\partial x}$. The variables $\boldsymbol{\sigma}$, $\boldsymbol{\epsilon}$ and B are the equilibrated stress field, the corresponding strain field and the complimentary energy respectively in the element interior. $\mathcal{T}, \mathcal{V}$ and $\mathcal{V}_\Gamma$ correspond to Hilbert spaces containing the stress, internal displacement and boundary displacement solutions respectively. $\boldsymbol{u}_\Gamma(x,t)$ is kinematically admissible compatible displacement field at the element boundary (nodal displacement), while, $\boldsymbol{u}(x,t)$, $\dot{\boldsymbol{u}}(x,t)$ and $\ddot{\boldsymbol{u}}(x,t)$ represent kinematically admissible internal displacement, velocity and acceleration fields respectively. Furthermore, ρ denote the material density and $\bar{\mathbf{t}}(t)$ is the applied traction ($\mathbf{F}(t) = \bar{\mathbf{t}}(t)A$

is nodal force where A is cross-sectional area).

The Hamiltonian for one element is written as

$$H(t) = \int_{t_1}^{t_2} (T(t) - V(t))dt \tag{3.2}$$

where $T(t)$ is the Kinetic Energy and $V(t)$ is the Potential Energy. Since the internal displacement field $\boldsymbol{u}$ is not compatible, the incompatible displacement at the boundary can be made zero by including the condition $\boldsymbol{u} - \boldsymbol{u}_\Gamma = 0$ as a constraint to the Hamiltonian and applying the Lagrange Multiplier technique. Also, expressing the Potential Energy in terms of Complementary Energy density, and applying divergence theorem, the Hamiltonian can be rewritten as

$$\begin{aligned} H(t) \quad &= \int_{t_1}^{t_2} \left\{ \frac{1}{2} \int_\Omega \rho \dot{\boldsymbol{u}} \dot{\boldsymbol{u}} d\Omega + \int_\Omega \boldsymbol{B} d\Omega + \int_\Omega \nabla\sigma \boldsymbol{u} d\Omega \right\} dt \\ &+ \int_{t_1}^{t_2} \left\{ - \int_{\partial\Omega_e} \sigma \boldsymbol{n} u d\partial\Omega + \int_{\partial\Omega_e} \bar{\boldsymbol{t}} \boldsymbol{u}_\Gamma d\partial\Omega + \int_{\partial\Omega_e} \mathbf{t}(\boldsymbol{u} - \boldsymbol{u}_\Gamma) d\partial\Omega \right\} dt \end{aligned} \tag{3.3}$$

where, $\mathbf{t} = \sigma\boldsymbol{n}$ is boundary traction. In the hybrid formulation, the equilibrium and constitutive equations, and the displacement compatibility at the inter-element boundary (i.e. nodes) are satisfied a-priori in strong sense. The kinematic equation, traction boundary condition, traction reciprocity on the inter-element boundary and compatibility of internal displacement field are obtained as the Euler-Lagrange equations from the stationarity of the complimentary energy functional (3.3) as follows: Setting the first variation of energy functional (3.3) equal to zero

$$\begin{aligned} \delta H \quad &= \int_{t_1}^{t_2} \left\{ - \int_\Omega \rho \ddot{\boldsymbol{u}} \delta \boldsymbol{u} d\Omega + \int_\Omega \frac{\partial \boldsymbol{B}}{\partial \sigma} \delta\sigma d\Omega + \int_\Omega \nabla(\delta\sigma) \boldsymbol{u} d\Omega + \int_\Omega \nabla\sigma \delta\boldsymbol{u} d\Omega \right\} dt \\ &+ \int_{t_1}^{t_2} \left\{ - \int_{\partial\Omega_e} \delta\sigma \boldsymbol{n} u d\partial\Omega + \int_{\partial\Omega_e} \bar{\boldsymbol{t}} \delta\boldsymbol{u}_\Gamma d\partial\Omega + \int_{\partial\Omega_e} \delta\sigma \boldsymbol{n}(\boldsymbol{u} - \boldsymbol{u}_\Gamma) d\partial\Omega - \int_{\partial\Omega_e} \sigma \boldsymbol{n} \delta\boldsymbol{u}_\Gamma d\partial\Omega \right\} dt = 0 \end{aligned} \tag{3.4}$$

where

$$\delta \left\{ \int_{t_1}^{t_2} \left\{ \int_\Omega \rho \dot{\boldsymbol{u}} \dot{\boldsymbol{u}} d\Omega \right\} dt \right\} = \int_{t_1}^{t_2} \left\{ - \int_\Omega \rho \ddot{\boldsymbol{u}} \delta\boldsymbol{u} d\Omega \right\} dt$$

has been used [102]. Since equation (3.5) is valid for any arbitrary time interval $\{\boldsymbol{t}_1, \boldsymbol{t}_2\}$, the term inside the

time integral can be set to zero. Applying divergence theorem to the sixth term in equation (3.5), and noting that equilibrium and constitutive equations are satisfied a-priori, we arrive at the following weak form:

$$\int_{\Omega} (\epsilon - \nabla \boldsymbol{u})\, \delta\sigma d\Omega + \int_{\partial\Omega} (\bar{\boldsymbol{t}} - \sigma \boldsymbol{n})\, \delta \boldsymbol{u}_{\Gamma} d\partial\Omega + \int_{\partial\Omega} \delta\sigma \boldsymbol{n}\, (\boldsymbol{u} - \boldsymbol{u}_{\Gamma})\, d\partial\Omega = 0 \tag{3.5}$$

which results in weak satisfaction of following equations

$$\begin{aligned}
&\epsilon = \nabla \boldsymbol{u} \quad \text{in} \quad \Omega_e && \text{(Kinematics)} \\
&\sigma \boldsymbol{n} = \bar{\boldsymbol{t}} \quad \text{on} \quad \partial\Omega_t && \text{(Traction Boundary)} \\
&\sigma \boldsymbol{n}^{+} = \sigma \boldsymbol{n}^{-} \quad \text{on} \quad \partial\Omega_m && \text{(Traction Reciprocity)} \\
&\boldsymbol{u} = \boldsymbol{u}_{\Gamma} \quad \text{on} \quad \partial\Omega_e && \text{(Compatibility of internal displacements)}
\end{aligned} \tag{3.6}$$

3.3 Hybrid Element Assumptions and Weak Form

3.3.1 Element Assumptions

In the hybrid stress formulation, stress field in the domain is approximated as

$$\sigma(x,t) = [\mathbf{P}(x,t)]\, \{\beta(t)\} \tag{3.7}$$

where $[\mathbf{P}(x,t)]$ is the matrix containing stress interpolation functions that are functions of time, and $\{\beta(t)\}$ are the corresponding unknown coefficients. To minimize the computational cost, it is desirable to have least number of terms in the stress interpolation function. In the present formulation the inertia field in the domain is approximated in terms of stress approximation. The acceleration field is interpolated in such a way that the equilibrium equation is satisfied a-priori.

$$\ddot{\boldsymbol{u}}(x,t) = \frac{1}{\rho} [\mathbf{P}(x,t)]\, \{\beta(t)\} \tag{3.8}$$

The velocity and internal displacement fields in the domain are obtained by numerical integration of acceleration. According to Newmark method, which is an implicit scheme, velocity and displacement are given as

$$\dot{\boldsymbol{u}}^{t+\Delta t} = \dot{\boldsymbol{u}}^{t} + \alpha_1 \ddot{\boldsymbol{u}}^{t} + \alpha_2 \ddot{\boldsymbol{u}}^{t+\Delta t} \tag{3.9}$$

$$\boldsymbol{u}^{t+\Delta t} = \boldsymbol{u}^{t} + \alpha_3 \dot{\boldsymbol{u}}^{t} + \alpha_4 \ddot{\boldsymbol{u}}^{t} + \alpha_5 \ddot{\boldsymbol{u}}^{t+\Delta t} \tag{3.10}$$

where $\alpha_1 = (1-\delta)\Delta t$, $\alpha_2 = \delta\Delta t$, $\alpha_3 = \Delta t$, $\alpha_4 = (1/2-\alpha)\Delta t^2$ and $\alpha_5 = \alpha\Delta t^2$, where α and δ are the integration constants and superscript $()^t$ denotes quantities at previous time step. The boundary displacements are approximated independently as

$$\{\boldsymbol{u}_\Gamma(x,t)\} = [\mathbf{L}(x)]\,\{\boldsymbol{q}_\Gamma(t)\} \tag{3.11}$$

In this one dimensional formulation, the boundary displacements $\{\boldsymbol{u}_\Gamma\}$ are same as nodal displacements $\{\boldsymbol{q}_\Gamma\}$ and therefore $[\mathbf{L}]$ is an identity matrix.

3.3.2 Weak Form

Substituting equilibrium and constitutive equations in equation (3.5), the weak form of complimentary energy functional can be written as

$$\int_\Omega \delta\sigma \boldsymbol{S}\sigma d\Omega + \int_\Omega \nabla(\delta\sigma)\boldsymbol{u} d\Omega + \int_{\partial\Omega_e} \bar{\boldsymbol{t}}\delta\boldsymbol{u}_\Gamma d\partial\Omega + \int_{\partial\Omega_e} \delta\sigma \boldsymbol{n}\boldsymbol{u}_\Gamma d\partial\Omega - \int_{\partial\Omega_e} \sigma\boldsymbol{n}\delta\boldsymbol{u}_\Gamma d\partial\Omega = 0 \tag{3.12}$$

The matrix equation of the weak form (3.12) is obtained by substituting the approximations for stress, internal displacement and boundary displacement fields from equations (3.7), (3.10) and (3.11) into equation (3.12)

$$\begin{aligned} &\{\delta\beta\}^T[\mathbf{H}]\{\beta\} + \{\delta\beta\}^T\{\boldsymbol{R}_I\} + \alpha_5\{\delta\beta\}^T[\mathbf{M}]\{\beta\} \\ &+ \{\boldsymbol{R}_t\}^T\{\delta\boldsymbol{q}_\Gamma\} - \{\delta\beta\}^T[\mathbf{G}]\{\boldsymbol{q}_\Gamma\} - \{\beta\}^T[\mathbf{G}]\{\delta\boldsymbol{q}_\Gamma\} = 0 \end{aligned} \tag{3.13}$$

$$\text{where} \qquad [\mathbf{H}] = \int_{\Omega_e} [\mathbf{P}]^T [\mathbf{S}][\mathbf{P}] d\Omega \qquad [\mathbf{M}] = \frac{1}{\rho} \int_{\Omega_e} [\nabla \mathbf{P}]^T [\nabla \mathbf{P}] d\Omega$$

$$[\mathbf{G}] = \int_{\partial\Omega_e} [\mathbf{P}]^T [\mathbf{n}][\mathbf{L}] d\partial\Omega \qquad \{\mathbf{R}_t\} = \int_{\Gamma_{tm}} \{\bar{\mathbf{t}}\}^T [\mathbf{n}][\mathbf{L}] d\Gamma_{tm}$$

$$\{\mathbf{R}_I\} = \int_{\Omega_e} [\nabla \mathbf{P}]^T \left\{ \{\boldsymbol{u}\}^t + \alpha_3 \{\dot{\boldsymbol{u}}\}^t + \alpha_4 \{\ddot{\boldsymbol{u}}\}^t \right\} d\Omega \tag{3.14}$$

3.4 Construction of Wavelet Based Stress Functions

Choice of functions for stress interpolation is the most imperative task in the hybrid stress formulations as it determines the computational effort required and the level of accuracy that can be achieved. VCFEM formulations in the past [61, 54] have employed polynomial, reciprocal and some special functions like branch functions, wavelets etc for stress interpolation to enhance the accuracy and computational efficiency.

Transient wave propagation in elastic solids is essentially traverse of a local disturbance of high stress gradients through the material. The formulation was tested with stress interpolation based on polynomial functions. It is observed that polynomials of order as high as 15 are not able to capture the abrupt variations in the stress field at the moving wave front. Wavelets are the functions that have localization and multi-resolution properties which, when coupled, facilitate local enrichment of the stress function and therefore are the most suitable candidates for this purpose. A brief introduction to wavelets is provided in the following paragraphs, which is followed by details on construction and use of wavelet basis for stress wave propagation problems.

3.4.1 Principles of Wavelets and Multi-resolution Analysis

Scaling function $\phi(x)$ and wavelet function $\psi(x)$ are the basic building blocks of the multi-resolution analysis. Scaling function is defined as a recursive function that satisfies the two-scale relation

$$\phi(x) = \sum_k p(k) \phi(2x - k) \tag{3.15}$$

where $\{p(k)\}_{k \in \mathcal{Z}}$ are the filter coefficients. The scaling function has a compact support if only a finite number of coefficients $p(k)$ are non-zero. Translation of scaling function ϕ by a factor of 2^n and dilation by a factor

of $k \cdot 2^{-n}$ forms unconditional basis of subspace $V_n \subset L^2(\mathcal{R})$ as

$$\phi_{n,k}(x) = 2^{n/2}\phi(2^n x - k) \tag{3.16}$$

where n is resolution level. The scaling function ϕ is orthonormal if translations at the same resolution level satisfy the orthogonality condition

$$\int_{-\infty}^{\infty} \phi_{n,k}(x)\phi_{n,l}(x)dx = \delta_{k,l} \quad \forall \;\; n,k,l \in \mathcal{Z} \tag{3.17}$$

If the scaling function is orthonormal, the best approximation of a function $f(x)$ at resolution level n is expressed as the orthogonal projection of f on subspace V_n as:

$$\mathcal{A}_n f(x) = \sum_k a_{n,k}\phi_{n,k}(x), \qquad \text{where} \quad a_{n,k} = \int_{-\infty}^{\infty} f(x)\phi_{n,k}(x)dx \tag{3.18}$$

In general, approximation of $f(x)$, at resolution level n is contained in approximation at any resolution level higher than n i.e. $\{0\} = V_{-\infty} \subset \cdots \subset V_{-1} \subset V_0 \subset V_1 \subset \cdots \subset V_\infty = L^2(\mathcal{R})$. This means that function $f(x)$ is approximated better at higher resolutions and some information is lost in transition from higher level V_{n+1} to lower level V_n. This difference is characterized by an orthogonal complementary subspace W_n so that $V_{n+1} = V_n \oplus W_n \;\; \forall\, n$. A basis that spans the subspace W_n can be obtained in the same manner as for scaling function, i.e. by translation and dilation of the mother wavelet function

$$\psi(x) = \sum_k q(k)\psi(2x - k) \tag{3.19}$$

The wavelet basis is orthonormal if any two translated and/or dilated wavelets satisfy the orthogonality condition

$$\int_{-\infty}^{\infty} \psi_{n,k}(x)\psi_{m,l}(x)dx = \delta_{n,m}\delta_{k,l} \quad \forall \;\; n,m,k,l \in \mathcal{Z} \tag{3.20}$$

The wavelet basis is semi-orthogonal if any two translated wavelets at different resolution levels satisfy the semi-orthogonality condition

$$\int_{-\infty}^{\infty} \psi_{n,k}(x)\psi_{m,l}(x)dx = 0, \quad n = m \quad \forall \;\; n, m, k, l \in \mathcal{Z} \tag{3.21}$$

An approximation of the function $f(x)$ at the $n-th$ resolution level may be expressed as the orthogonal projection of f on W_n as

$$\mathcal{D}_n f(x) = \sum_k b_{n,k}\psi_{n,k}(x), \qquad \text{where} \quad b_{n,k} = \int_{-\infty}^{\infty} f(x)\psi_{n,k}(x)dx \tag{3.22}$$

Thus, approximation of function $f(x)$ at higher resolution can be obtained as

$$\mathcal{A}_{n+1} f(x) = \sum_k a_{n,k}\phi_{n,k}(x) + \sum_k b_{n,k}\psi_{n,k}(x) \tag{3.23}$$

These multi-resolution properties of wavelet functions provide the basis for adaptive enrichment in the regions where residual is higher at the lower resolution level.

3.4.2 Selection of the Wavelet Function

In the present formulation, approximation for acceleration field is constructed on derivative of the stress interpolation functions. Also, the calculation of error norm discussed in section (3.4.4) involves second derivatives of stress functions. Therefore, it is desirable that the stress functions be differentiable and have explicit analytical expressions. One of the most commonly used wavelet functions is Daubechies' compactly supported orthonormal wavelets [21, 23]. However, they are constructed through recursive algorithms and do not have explicit analytic expressions, therefore are not suitable for present formulation. On the other hand, Chui-Wang's B-spline wavelet bases [16, 62] have explicit analytic expressions for scaling and wavelet functions, and therefore are implemented in this formulation. Chui-Wang wavelets, which are semi-orthogonal

and compactly supported, are based on B-spline functions, which are defined by recursive convolution

$$\phi(x) = \int_{-\infty}^{\infty} \mathbf{N}_{m-1}(x-t)\mathbf{N}_1(t)dt = \int_{x-1}^{x} \mathbf{N}_{m-1}(t)dt \tag{3.24}$$

where $\mathbf{N}_1(x)$ is a box function. The two scale relation for this scaling function is given as

$$\phi(x) = \mathbf{N}_m(x) = \sum_{k=0}^{m} 2^{-m+1} \frac{m!}{k!(m-k)!} \phi(2x-k) \tag{3.25}$$

The corresponding wavelet basis, which satisfies the semi-orthogonality condition (3.21), is given by

$$\psi(x) = 2^{-m+1} \sum_{k=0}^{2m-2} (-1)^k \mathbf{N}_{2m}(k+1)\mathbf{N}_{2m}^{(m)}(2x-k) \tag{3.26}$$

where

$$\mathbf{N}_{2m}^{(m)} = \sum_{k=0}^{m} (-1)^k \frac{m!}{k!(m-k)!} \phi(2x-k) \tag{3.27}$$

For B-spline wavelet bases, the scaling function and the wavelet function are compactly supported i.e. they are defined on a finite closed interval. The support for scaling and wavelet functions are given by

$$\begin{aligned} \text{supp } \phi_{n,k} &= [2^{-n}k, 2^{-n}(k+m)] \\ \text{supp } \psi_{n,k} &= [2^{-n}k, 2^{-n}(k+2m-1)] \end{aligned} \tag{3.28}$$

The finite number of non-zero translations that form a basis for interpolation on an interval $[a, b]$ can be identified using the above expressions for the support as

$$(2^n a - m + 1) \leq k_\phi \leq (2^n b - 1) \tag{3.29}$$

$$(2^n a - m + 1) \leq k_\psi \leq (2^n b - 1) \tag{3.30}$$

The total non-zero translations over the interval $[a, b]$ for the scaling function and the wavelet function are $[2^n(b-a) + m - 1]$ and $[2^n(b-a) + m - 1]$ respectively.

3.4.3 Multi-resolution Wavelet Based Stress Functions

The wavelet based stress function is constructed by forming a basis by translating the scaling function at resolution n. The required translations to span the volume of the element are calculated using expression (3.29). The stress function is expressed as

$$\sigma = \sum \phi_{n,k}(x)\beta_k(t) \tag{3.31}$$

The stress function is enriched locally in the vicinity of wave front by using wavelet functions at resolution n to form a basis at increased resolution level $(n+1)$

$$\sigma = \sum_k \phi_{n,k}(x)\beta_k(t) + \sum_l \psi_{n,l}(x)\beta_l(t) \tag{3.32}$$

The local region can be enriched further to resolution level $(n+2)$ by using wavelet functions at resolution $(n+1)$ and so on until the desired accuracy is achieved. While forming the wavelet basis in the element, some translations of the scaling and wavelet functions fall partially outside the element. In such cases, the wavelets are truncated at the element boundary.

3.4.4 Error Criteria for Time Dependent Adaptive Enrichment

It is imperative to accurately determine the location of the wave front where the local enrichment of stress function is to be carried out, for, it governs the accuracy of the solution and also determines the computational cost. As seen in section (3.2), the kinematic equation (3.6) in the domain is satisfied in an average sense. Therefore, the residual in satisfying this equation is used as error indicator for adaptive enrichment. The error norm is defined as

$$|\epsilon| = \frac{1}{\Delta\Omega} \frac{\left|\int_{\Delta\Omega}(\epsilon - \nabla \boldsymbol{u})dx\right|}{|\epsilon|_{max}} \times 100 \tag{3.33}$$

where $\Delta\Omega$ and $|\epsilon|_{max}$ are volume of subdomain and maximum strain in the element respectively. The domain is discretized into 2^n number of subdomains and error norm (3.33) is calculated in each subdomain. The subdomains for which the norm exceeds a pre-defined tolerance, are the regions where enrichment is to be

carried out using the procedure outlined in previous section. This increases the resolution level to $(n+1)$. The posteriori error analysis and corresponding enrichment is repeated until the tolerance is met.

3.5 Solution Method and Numerical Aspects

3.5.1 Solution for the Field Variables

The matrix equation (3.13) of the weak form of complimentary energy principle can be rewritten as

$$\{\delta\beta\}^T \{[\mathbf{H}]\{\beta\} + \{\boldsymbol{R}_I\} + \alpha_5[\mathbf{M}]\{\beta\} - [\mathbf{G}]\{\boldsymbol{q}_\Gamma\}\} + \{\{\boldsymbol{R}_t\}^T - \{\beta\}^T[\mathbf{G}]\} \{\delta\boldsymbol{q}_\Gamma\} = 0 \tag{3.34}$$

Since $\{\delta\beta\}$ and $\{\delta\boldsymbol{q}_\Gamma\}$ are arbitrary and can be varied independently, and the corresponding bracketed terms are independent of these variations, the two bracketed terms should vanish individually. Setting the first bracketed term in equation (3.34) equal to zero gives the local equations for each element:

$$[\mathbf{H}_M]_e\{\beta\}_e = [\mathbf{G}]_e\{q_\Gamma\}_e - \{\mathbf{R}_I\}_e \tag{3.35}$$

where

$$[\mathbf{H}_M]_e = [\mathbf{H}]_e - \alpha_5[\mathbf{M}]_e \tag{3.36}$$

Adding energy of all elements, and setting the second bracketed terms equal to zero gives weak form of global traction reciprocity condition

$$\sum_{e=1}^{N}[\mathbf{G}]_e^T\{\beta\}_e = \sum_{e=1}^{N}\{\mathbf{R}_t\}_e \tag{3.37}$$

If the element $[\mathbf{H}_M]_e$ matrix is invertible, the stress coefficients can be expressed in terms of nodal displacements using equation (3.35). The static condensation of equations (3.35) and (3.37) gives linear system of simultaneous equations

$$\sum_{e=1}^{N}[\mathbf{G}]_e^T[\mathbf{H}_M]_e^{-1}[\mathbf{G}]_e\{q_\Gamma\}_e = \sum_{e=1}^{N}\{\mathbf{R}_t\}_e \tag{3.38}$$

$$\text{or} \quad [\mathbf{K}]\{q_\Gamma\} = \{\mathbf{F}\} \tag{3.39}$$

which can be solved for the nodal displacement vector $\{q_\Gamma\}$.

3.5.2 Stability Conditions

The stability conditions for multi-field mixed variational formulations are derived in [4, 12, 104]. Within this framework, the stability conditions for the stress-displacement field variational problem in the dynamic hybrid FEM can be stated as follows:

- The matrix $[\mathbf{H}_M]$ should be positive definite. This also ensures invertability of the $[\mathbf{H}_M]$ matrix. From the definition of $[\mathbf{H}_M]$ in equation (3.35), the necessary condition for it to be positive definite is

$$\{x\}^T[\mathbf{H}_M]\{x\} > 0 \quad \Longrightarrow \quad \{x\}^T[\mathbf{H}]\{x\} > 0 \quad \& \quad \{x\}^T[\mathbf{M}]\{x\} \geq 0$$

  i.e. the matrix $[\mathbf{H}]$ should be positive definite and matrix $[\mathbf{M}]$ should be positive semi-definite. For matrix $[\mathbf{H}]$ to be positive definite, firstly, $[\mathbf{S}]$ be positive definite, which is true for elastic problems. Secondly, the finite-dimensional stress subspace $\mathcal{T}$ should be spanned uniquely by the basis functions $[\mathbf{P}]$. This is satisfied by assuring linear independence of the columns of basis functions $[\mathbf{P}]$. As discussed in previous section, stress function contains a basis formed by low resolution scaling function everywhere in the domain, and is enriched locally using wavelet function. Though the wavelet functions are orthogonal to the scaling function, the orthogonality is destroyed near the element boundaries where scaling and wavelet functions are partially outside the element. In situations where only a small portion of the scaling and wavelet functions fall inside the element, these portions could become dependent or nearly dependent. To encounter this problem, the rank of the $[\mathbf{P}]$ matrix is first determined from the diagonal matrix resulting from a Cholesky factorization of the square matrix

$$[\mathbf{H}^*] = \int_{\Omega_e} [\mathbf{P}]^T[\mathbf{P}]d\Omega$$

  Nearly dependent columns of $[\mathbf{P}]$ will result in very small pivots during Cholesky factorization. The corresponding wavelet function terms are dropped from the stress function to prevent numerical inac-

curacies in inverting $[\mathbf{H}_M]$.

- To ensure non-zero stress field in the element for all non-rigid body displacement fields on the element boundary $\mathbf{u}_e^E$, the dimensions of the stress and displacement subspaces must satisfy stability condition $n_\beta > n_{q_\Gamma} - 1$, where n_β is the number of β parameters, and n_{q_Γ} is the number of displacement degrees of freedom on the element boundary. In this one dimensional formulation, this is always satisfied if $n_\beta > 1$.

Another important factor that determines the stability and accuracy of solution of dynamic problems is the stability of the time integration scheme. Newmark method, being used here, is unconditionally stable and most accurate when the integration constants in equations (3.10) and (3.9) take values $\delta = \frac{1}{2}$ $\alpha = \frac{1}{4}$, which is constant-average-acceleration method, also called trapezoidal rule [6]. Therefore, there is no minimum time step size requirement and it is the accuracy of the solution that decides the time step size. In wave propagation problems, the time step size is determined as [6]

$$\Delta t = \frac{L_w}{nc}$$

where L_w is the critical wavelength to be represented, n is the number of time steps necessary to represent the travel of the wave, and $c = \sqrt{\frac{E}{\rho}}$ is the wave speed.

3.6 Numerical Examples

3.6.1 Wave Propagation through Layered Media

The problem of wave dispersion in layered media presented in [46] is considered here. A layered bar composed of two materials with properties $E_1 = 200$ GPa, $E_2 = 5$ GPa and $\rho_1 = \rho_2 = 8000 kg/m^3$ is shown in figure 3.1. The lengths of the two layers in a unit cell are $l_1 = l_2 = 0.01$ m and there are 50 unit cells. One end of the bar is fixed while other end is subjected to impact load $F(t) = F_0 \frac{1}{(T/2)^8} t^4 (t-T)^4 [1 - h(t-T)]$, where $T = 15.71$ μs is the duration and $F_0 = 50$ KN is the amplitude of the impact load, and $h(t)$ is heaviside function. Response of ABAQUS model with 50 T2D2 elements per layer is taken as a reference

and the response of hybrid finite element model with one element per layer is compared. Figure 3.4 shows displacement at $x = 0.5$ m as a function of time. It can be observed that proposed formulation predicts the phenomenon of dispersion very accurately.

3.6.2 Effect of Assumption of Periodicity

The homogenization methods often make assumption of periodicity in order to include microstrucutral effects in the macro-response. In this example, the accuracy of such assumption is investigated. A composite bar with properties given in previous example and with length $l_1 = l_2 = 0.1$ m is considered. Figure 3.2 (a) and (b) show a unit cell with periodic boundary conditions and a full model of 50 layers with fixed end conditions respectively. In this case $T = 63\ \mu s$ is the duration and $F_0 = 100$ KN is the amplitude of the impact load. Figures 3.5 and 3.6 show stress response near the boundary and away from the boundary as a function of time respectively. It can be observed that interference of waves reflected from the boundary produce significantly different response near the boundary. The assumption of periodicity is reasonably accurate away from the boundary. However, response deviates as the reflected waves arrive and interfere with the incoming waves.

3.7 Conclusions

An assumed stress hybrid Voronoi cell finite element model for analysis of elastic wave propagation in heterogeneous materials is proposed in this work. Stress field in the domain and compatible displacement field at the boundary are interpolated independently. The nonconforming internal displacement field is approximated in terms of stresses such that equilibrium equation is satisfied pointwise. Stress functions are based on low resolution B-spline scaling functions which are adaptively enriched using wavelet functions in the local region of high stress gradients determined by residual based posteriori error indicator. Adaptive enrichment of the stress function exploiting multi-resolution properties of wavelet functions reduces the degrees of freedom of the problem and enhances the computational efficiency significantly. As demonstrated through comparison with standard FEM packages, the proposed formulation predicts the phenomenon of wave reflection, transmission, dispersion etc accurately.

This work advocates multi-resolution wavelet enriched hybrid FEM as a potential method for micro-mechanical response of composites under impact loading in one dimension. Wave propagation through heterogeneous solids in two dimensions is more involving due to complex interaction of dilatational and distortional waves at the boundaries of heterogeneities. In the subsequent work, this formulation will be extended in two dimensions to develop dynamic VCFEM for investigating propagation of elastic waves in heterogeneous microstructures.

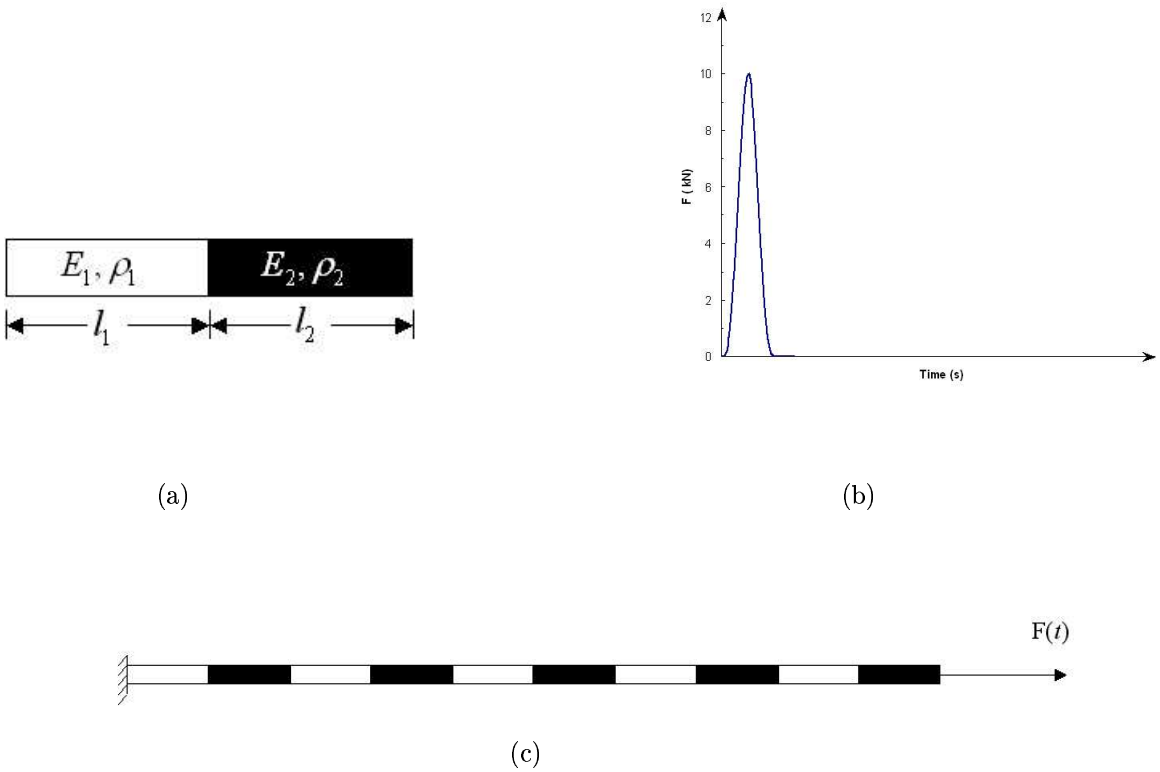

Figure 3.1: Wave propagation through layered media: (a) Unit cell, (b) Impact load as a function of time, (c) Composite bar

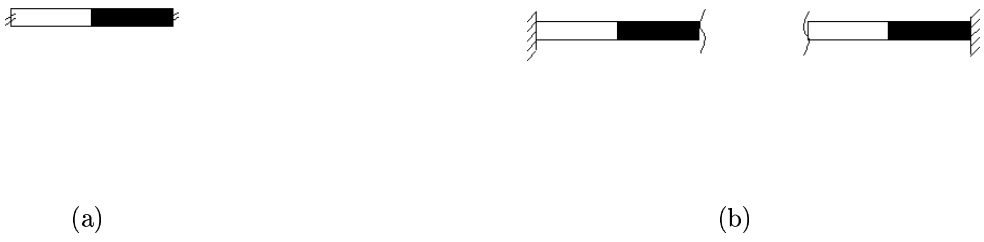

Figure 3.2: Effect of assumption of periodicity: (a) Periodic model, (b) Full model

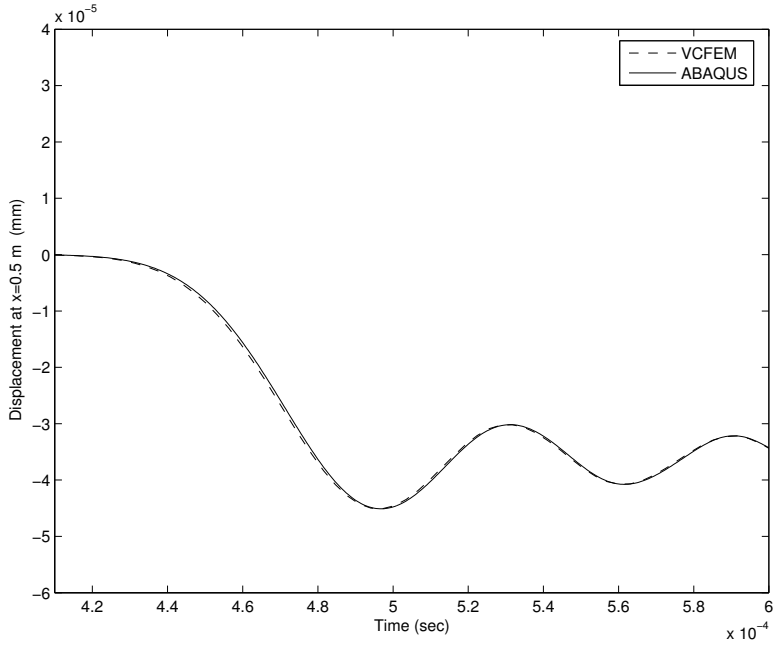

Figure 3.3: Displacement response at the center of a layered bar: Comparison with Abaqus

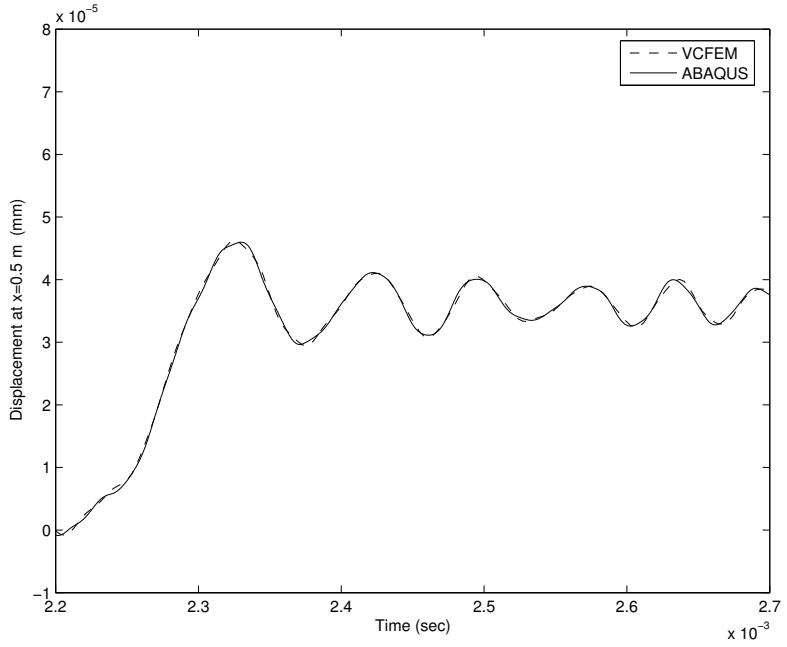

Figure 3.4: Displacement response at the center of a layered bar: Comparison with Abaqus

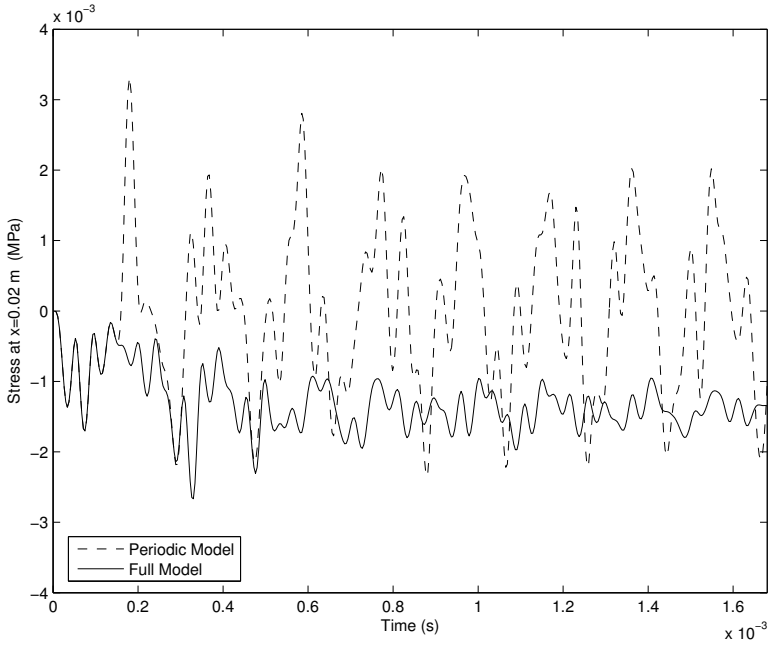

Figure 3.5: Stress response near the boundary

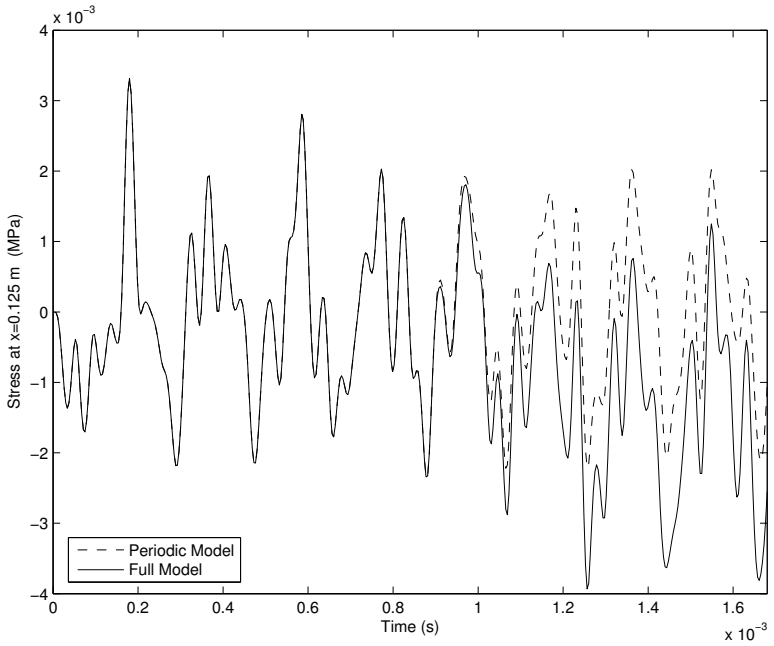

Figure 3.6: Stress response away from the boundary

Chapter 4

The Extended Voronoi Cell Finite Element Model For Multiple Cohesive Cracks Propagation

4.1 Introduction

Numerical analysis and simulation of the growth of multiple cracks in materials is a challenging enterprise due to morphological and constitutive complexities that govern its growth. The conventional finite element method suffers from very slow convergence since the element formulation does not account for high gradients and singularities. Even a very high density mesh cannot overcome pathological mesh dependence near the crack tips and avoid biasing the direction of crack propagation.

In this chapter, an extended VCFEM or X-VCFEM is developed for modeling the growth of multiple cohesive cracks in a brittle material. The model accounts for interaction between cracks and invokes an adaptive crack growth formulation to represent the continuously changing direction of evolving cracks. X-VCFEM augments the conventional VCFEM model by incorporating multi-resolution wavelet functions [38, 47, 71] in the vicinity of the crack tip, in addition to branch functions based on level set methods. The incremental

crack propagation direction and length are adaptively determined by a cohesive energy based criterion. No remeshing is needed in X-VCFEM for simulating crack growth, and this adds to its desirability and effectiveness. It begins with the X-VCFEM formulation, followed by numerical example showing the convergence of this model. Then, X-VCFEM is used to understand the influence of cohesive parameters, e.g. peak stress and critical separation on crack growth in a monolithic brittle material. Subsequently, the effect of morphological distributions including crack interaction, clustering, alignment, etc. on growth and merging are studied as important factors critical to the failure process.

4.2 Voronoi Cell Fem Formulation for Multiple Propagating Cracks

The Voronoi cell finite element mesh for a brittle matrix with a dispersion of pre-existing cracks is shown in figure 4.1(a). The typical Voronoi cell mesh corresponds to an unstructured mesh that is generated by Dirichlet or Voronoi tessellation of the domain, based on the position, shape and size of heterogeneities (inclusion, void, crack etc.). Various tessellation schemes have been discussed and developed in [35, 61]. While the name Voronoi cell has been historically used because of its association with point seeds in the generation process, the cells used in VCFEM may be variants of this construct. Essentially they represent neighborhood or regions of influence for each heterogeneity. Subsequently the Voronoi cell FE formulation considers each cell as a super-element consisting of a heterogeneity and its neighborhood surrounding matrix [61, 80] without any further subdivision. The interfacial debonding analyses in [35, 53] invoke the cohesive zone models to represent the growth of interfacial crack. However the main difference between that formulation and the present one is that, in the present case the path of the crack is arbitrary and is a-priori unknown. This poses significant challenges that have been overcome with the X-VCFEM formulation.

Consider a pre-cracked microstructural region Ω consisting of N cracks as shown in figure 4.1(a). The region is divided into an unstructured finite element mesh of arbitrary Voronoi cells. A typical VC element Ω_e containing a crack and its neighboring matrix is depicted in figure 4.1(b). The element boundary $\partial\Omega_e$ with outward normal $\mathbf{n}^E$ may consist of regions of prescribed traction Γ_{te}, prescribed displacement Γ_{ue} and inter-

element edges Γ_{me}, i.e. $\partial\Omega_e^E = \Gamma_{te} \bigcup \Gamma_{ue} \bigcup \Gamma_{me}$. Furthermore, each element consists of a crack containing a fracture process zone that is represented by a cohesive zone model. The incompatible displacement field across the crack Γ_{cr} is facilitated through a set of connected node-pairs along the crack length. The node-pair merges at the crack tip by enforcing the same displacement. The normal along the crack path is denoted by $\mathbf{n}^{cr}$. For the VCFEM element formulation, the micromechanics boundary value problem is described as:

$$
\begin{aligned}
&\text{Find } (\boldsymbol{\sigma}, \mathbf{u}^E, \mathbf{u}^{cr}) \ \in \mathcal{T} \times \mathcal{V}^E \times \mathcal{V}^{cr} \ \text{ satisfying} \\
&\nabla \cdot \boldsymbol{\sigma} + \bar{\mathbf{f}} = \mathbf{0} \quad \text{and} \quad \frac{\partial B}{\partial \boldsymbol{\sigma}} = \boldsymbol{\epsilon} \in \Omega_e \qquad (a) \\
&\mathbf{u}^E = \bar{\mathbf{u}} \text{ on } \Gamma_{ue} \quad , \quad \boldsymbol{\sigma} \cdot \mathbf{n}^E = \bar{\mathbf{t}} \text{ on } \Gamma_{te} \ \text{ and } \ \boldsymbol{\sigma} \cdot \mathbf{n}^{cr} = \mathbf{t}^{coh} \text{ on } \Gamma_{cr} \quad (b)
\end{aligned}
\tag{4.1}
$$

The variables $\boldsymbol{\sigma}$, $\boldsymbol{\epsilon}$, B and $\mathbf{f}$ are the equilibrated stress fields, the corresponding strain fields, the complimentary energy and body forces per unit volume respectively in the element interior. $\mathcal{T}, \mathcal{V}^E$ and $\mathcal{V}^{cr}$ correspond to Hilbert spaces containing the stress and displacement solutions respectively. $\mathbf{u}^E$ is the kinematically admissible displacement field on the element boundary $\partial\Omega_e^E$ and $\mathbf{u}^{cr}$ represents the displacements on the internal cohesive-crack surfaces Γ_{cr}. Variables with superscript E are on the element boundary while those with superscripts cr correspond to the crack surface. The traction $\mathbf{t}^{coh}$ between node-pairs on the crack surface are modeled by the cohesive zone traction-separation law. The VCFEM formulation is based on the assumed stress hybrid finite element method, in which stationarity conditions of the element energy functional in the variational principle yields weak forms of the kinematic equation and traction reciprocity conditions, as Euler equations. In the small deformation elasticity incremental formulation for evolving cracks, the element energy functional Π_e is defined in terms of increments of stresses and displacements as:

$$
\begin{aligned}
&\Pi_e(\sigma_{ij}, \Delta\sigma_{ij}, u_i^E, \Delta u_i^E, u_i^{cr}, \Delta u_i^{cr}) = -\int_{\Omega_e} \Delta B(\sigma_{ij}, \Delta\sigma_{ij}) d\Omega - \int_{\Omega_e} \epsilon_{ij} \Delta\sigma_{ij} d\Omega \\
+ \ &\int_{\partial\Omega_e} (\sigma_{ij} + \Delta\sigma_{ij}) n_j^E (u_i^E + \Delta u_i^E) d\partial\Omega - \int_{\Gamma_{tm}} (\bar{t_i} + \Delta\bar{t_i})(u^E{}_i + \Delta u^E{}_i) d\Gamma_{te} \\
+ \ &\int_{\Gamma_{cr}^1} (\sigma_{ij} + \Delta\sigma_{ij}) n_j^{cr} (u_i^{cr} + \Delta u_i^{cr}) d\Gamma_{cr} - \int_{\Gamma_{cr}^2} (\sigma_{ij} + \Delta\sigma_{ij}) n_j^{cr} (u_i^{cr} + \Delta u_i^{cr}) d\Gamma_{cr} \\
- \ &\int_{\Gamma_{cr}} \int_{u_i^{cr} - u_i^{cr}}^{u_i^{cr} + \Delta u_i^{cr} - u_i^{cr} - \Delta u_i^{cr}} t_i^{coh} d(u_i^{cr} - u_i^{cr}) d\Gamma_{cr}
\end{aligned}
\tag{4.2}
$$

where $B = \frac{1}{2}\boldsymbol{\sigma} : \mathbf{S} : \boldsymbol{\sigma}$ is the complimentary energy density and $\Delta B(\sigma_{ij}, \Delta\sigma_{ij})$ is its increment due to stress increase. $\mathbf{S}$ is the material compliance matrix. The notations $\overset{1}{(\bullet)}$ and $\overset{2}{(\bullet)}$ represent two sides of the internal cohesive crack surface. The last term provides the work done by the cohesive tractions t_i^{coh} due to crack surface separation. In VCFE formulation, the equilibrium conditions and constitutive relations in the matrix and the compatibility conditions on the element boundary and crack surface are satisfied a-priori in a strong sense. The element kinematic equation:

$$\nabla \mathbf{u}_e = \boldsymbol{\epsilon}_e \ \text{ in } \ \Omega_e \tag{4.3}$$

is however satisfied in a weak sense from the stationary condition of the element energy functional in equation(4.2). The weak form is obtained by setting the first variation of Π_e with respect to stress increments to zero, i.e.

$$\begin{aligned} &- \int_{\Omega_e} \left(\frac{\partial \Delta B}{\partial \Delta\sigma_{ij}} + \epsilon_{ij}\right) \delta\Delta\sigma_{ij} \, d\Omega + \int_{\partial\Omega_e} \delta\Delta\sigma_{ij} \, n_j^e \, (u_i^E + \Delta u_i^E) \, d\partial\Omega_e \\ &+ \int_{\overset{1}{\Gamma}_{cr}} \delta\Delta\sigma_{ij} \, n_j^{cr} \, (\overset{1}{u}_i^{cr} + \Delta \overset{1}{u}_i^{cr}) \, d\overset{1}{\Gamma}_{cr} - \int_{\overset{2}{\Gamma}_{cr}} \delta\Delta\sigma_{ij} \, n_j^{cr} \, (\overset{2}{u}_i^{cr} + \Delta \overset{2}{u}_i^{cr}) \, d\overset{2}{\Gamma}_{cr} \ = \ 0 \end{aligned} \tag{4.4}$$

Solution of equation (4.4) yields domain stresses. Furthermore, the VCFE formulation assumes weak satisfaction of the traction reciprocity conditions on (i) the inter-element boundary Γ_{me}, and (iii) the domain traction boundary Γ_{te} and (iii) the crack surfaces $\overset{1}{\Gamma}_{cr}$ and $\overset{2}{\Gamma}_{cr}$:

$$\begin{aligned} (\sigma_{ij} + \Delta\sigma_{ij}) n_j^{E+} &= -(\sigma_{ij} + \Delta\sigma_{ij}) n_j^{E-} \quad \text{on } \Gamma_{me} \quad \text{(inter-element boundary)} \\ (\sigma_{ij} + \Delta\sigma_{ij}) n_j^{E} &= \bar{t}_i + \Delta\bar{t}_i \qquad \text{on } \Gamma_{te} \quad \text{(traction boundary)} \\ (\sigma_{ij} + \Delta\sigma_{ij})^1 n_j^{cr} &= (\sigma_{ij} + \Delta\sigma_{ij})^2 n_j^{cr} \qquad \text{on } \Gamma_{cr} \end{aligned} \tag{4.5}$$

In the variational principle, the weak form is obtained by setting the first variation of the total energy functional $\Pi = \sum_{e=1}^{N} \Pi_e$ with respect to the displacements $\Delta\mathbf{u}^E$, $\Delta\overset{1}{\mathbf{u}}^{cr}$ and $\Delta\overset{2}{\mathbf{u}}^{cr}$ respectively, to zero, or

$$\sum_{e=1}^{N} \int_{\partial\Omega_e} [(\sigma_{ij} + \Delta\sigma_{ij}) n_j^e \delta u_i^E \; d\partial\Omega - \int_{\Gamma_{tm}} (\bar{t}_i + \Delta\bar{t}_i) \;] \; \delta u_i^E \; d\Gamma_{tm} = 0$$
$$\forall \; \delta \mathbf{u}_e^E \; \in \; \bar{\mathcal{V}}_e^E = \{\mathbf{v}_e^E \in \; \mathcal{H}^o(\partial\Omega_e^E) : \mathbf{v}_e^E = \mathbf{0} \; on \; \Gamma_{ue}\} \; \forall \; e \text{ on } \partial\Omega_e \tag{4.6}$$

and

$$\int_{\Gamma_{cr}^1} [(\sigma_{ij} + \Delta\sigma_{ij}) n_j^{cr} - \phi_i'] \; \delta u_i^{1cr} \; d\Gamma_{cr} = 0$$
$$\int_{\Gamma_{cr}^2} [(\sigma_{ij} + \Delta\sigma_{ij}) n_j^{cr} + \phi_i'] \delta u_i^{2cr} \; d\Gamma_{cr} = 0$$
$$\forall \; \delta \mathbf{u}_e^{cr} \; \in \; \mathcal{V}_e^{cr}, \; \forall \; e \text{ on } \Gamma_{cr} \tag{4.7}$$

where $\phi = \int_{u_i^{1cr} - u_i^{2cr}}^{u_i^{1cr} + \Delta u_i^{1cr} - u_i^{2cr} - \Delta u_i^{2cr}} t_i^{coh} d(u_i^{1cr} - u_i^{2cr})$ is the cohesive energy function and $\phi_i' = \frac{\partial \phi}{\partial u_i^{cr}}$.

4.2.1 Cohesive zone models for crack propagation

Cohesive zone models, introduced in [5, 25] and developed in [63, 64, 65, 97, 30, 33, 39, 68], are effective in depicting material failure as a separation process across an extended crack tip or fracture process zone. In these models, the tractions across the crack reach a maximum, subsequently decrease and eventually vanish with increasing separation across the crack. The cohesive model used in this chapter is a three parameter rate independent linear cohesive model, proposed in [39, 68]. This is an extrinsic (two stage) model which has an infinite stiffness or slope in the rising portion of the traction-separation law up to a peak traction value. This is followed by linear descending segment till a zero traction value is reached. The model assumes a free cohesive energy potential ϕ such that the traction across the cohesive surface is expressed as:

$$\mathbf{t}^{coh} = \frac{\partial \phi}{\partial \delta_n} \mathbf{n} + \frac{\partial \phi}{\partial \delta_t} \mathbf{t} \tag{4.8}$$

Here δ_n and δ_t correspond to the normal and tangential components of the opening displacements over the cohesive surface in the $\mathbf{n}$ and $\mathbf{t}$ directions respectively. An effective opening displacement is defined as

$$\delta = \sqrt{\delta_n^2 + \beta^2 \delta_t^2} \tag{4.9}$$

where β is a coupling coefficient to allow assignment of different weights to normal and tangential opening displacements. Consequently the cohesive surface traction reduces to

$$\mathbf{t}^{coh} = \frac{t}{\delta}(\beta^2 \delta_t \mathbf{t} + \delta_n \mathbf{n}), \quad \text{where} \quad t = \frac{\partial \phi}{\partial \delta} = \sqrt{t_n^{coh^2} + \beta^{-2} t_t^{coh^2}} \tag{4.10}$$

where t_n^{coh} and t_t^{coh} are the normal and tangential components of surface tractions. The effective cohesive force t in this model for increasing δ takes the form

$$t = \begin{cases} \frac{\sigma_{max}(\delta_e - \delta)}{\delta_e} & \forall \delta < \delta_e \\ 0 & \forall \delta \geq \delta_e \end{cases} \tag{4.11}$$

δ_e corresponds to the separation at which t goes to zero and σ_{max} is the peak value of t. The effective normal traction-separation response of this model is depicted in figure (4.2). In the softening region, Unloading from any point on the traction-separation curve, proceeds along a linear path from the current position to the origin as shown by the line BO in figure 4.2. The corresponding $t - \delta$ relation is

$$t = \frac{\sigma_{max}}{\delta_e} \frac{\delta_e - \delta_{max}}{\delta_{max}} \delta \qquad \forall \delta \leq \delta_{max} \leq \delta_e \tag{4.12}$$

Reloading follows the path OBC with a reduced stiffness in comparison with the original stiffness. Traction vanishes for $\delta \geq \delta_e$.

For negative normal displacement (compression), stiff penalty springs with high stiffness are introduced between the node-pairs on the crack face. To define the tangent stiffness matrix, it is necessary to distinguish between crack initiation ($\delta = 0$) and crack propagation from an initialized state ($\delta > 0$). In the former,

$t_n^{coh} = t$, and $t_t^{coh} = 0$ are assumed, which implies that the initiation is in pure mode I. The cohesive parameters in this study are calibrated from experiments done for epoxy-steel composites as discussed in [53, 35].

Recent experimental-computational studies on composites, conducted in [93] show that the three or four parameter cohesive models are more suitable for modeling interfacial debonding in comparison with the two parameter models based on Ferrante's law [63, 64, 65]. Similar conclusions have also been drawn in the work by Ghosh et. al. [35, 53], where bilinear cohesive models were chosen to study interfacial debonding in fiber reinforced composites.

4.2.2 General element assumptions and weak form

In the absence of body forces, two dimensional stress fields satisfying equilibrium relations can be generated from the Airy's stress function $\Phi(x, y)$. In the incremental formulation, stress increments are obtained from derivatives of the stress functions $\Delta\Phi(x, y)$ as:

$$\begin{pmatrix} \Delta\sigma_{xx} \\ \Delta\sigma_{yy} \\ \Delta\sigma_{xy} \end{pmatrix} = \begin{pmatrix} \frac{\partial^2 \Delta\Phi}{\partial y^2} \\ \frac{\partial^2 \Delta\Phi}{\partial x^2} \\ -\frac{\partial^2 \Delta\Phi}{\partial x \partial y} \end{pmatrix} = [\mathbf{P}(x, y)]\{\Delta\beta\} \tag{4.13}$$

where $\{\Delta\beta\}$ is the column of unknown stress increment coefficients, associated with the stress interpolation matrix $[\mathbf{P}(x, y)]$. Convergence properties and efficiency of VCFEM depend on the choice of Φ. These functions should adequately account for the geometry and location of the heterogeneity in the element. Polynomial functions alone do not contribute to this requirement and hence lead to poor convergence [61, 80]. Consequently, stress functions in X-VCFEM are constructed from different expansion functions that have complementary effects on the solution convergence for the propagating crack. Compatible displacement fields satisfying inter-element continuity on the element boundary $\partial\Omega_e^E$ and intra-element continuity on the crack

face Γ_{cr} are generated by interpolation of nodal displacements, [35, 61, 80] as:

$$\begin{aligned}
\{\Delta u^e\} &= [\mathbf{L}_e]\{\Delta q^e\} \quad on \ \ \partial\Omega_e \\
\{\Delta \overset{1}{u}{}^{cr}\} &= [\overset{1}{\mathbf{L}}_{cr}]\{\Delta \overset{1}{q}{}^{cr}\} \quad on \ \ \overset{1}{\Gamma}_{cr}, \\
\{\Delta \overset{2}{u}{}^{cr}\} &= [\overset{2}{\mathbf{L}}_{cr}]\{\Delta \overset{2}{q}{}^{cr}\} \quad on \ \ \overset{2}{\Gamma}_{cr}
\end{aligned} \tag{4.14}$$

The interpolation matrices $[\mathbf{L}_e], [\overset{1}{\mathbf{L}}_{cr}], [\overset{2}{\mathbf{L}}_{cr}]$ for the nodal displacements on the respective boundaries are constructed using standard linear or hierarchical shape functions.

Remark: It is desirable that the displacement interpolations on the crack surface in equation (4.14) have adequate resolution, consistent with the high resolution in the stress fields near the crack tip. To accommodate this, hierarchical shape functions are added to standard linear shape functions to describe displacements on the crack surface as:

$$\mathbf{u}^{cr} = \sum_{i=1}^{4} N_i(s) * \mathbf{q}_i^{cr} \tag{4.15}$$

where $N_1 = \frac{1}{2}(1-s),\ N_2 = \frac{1}{2}(1+s),\ N_3 = \frac{1}{2}(s^2-1),$ and $N_4 = \frac{1}{6}(s^3-s)$. The first two are the standard linear shape functions, while the last two are the hierarchical shape functions in natural coordinates s. The degrees of freedom corresponding to higher order shape functions (i.e. to quadratic, cubic, etc.) cannot be interpreted as nodal values of displacement. Instead, they are values of some higher order derivatives of the solution at the midpoints (or linear combination of these derivatives).

Substituting the interpolations of stress and displacement fields from equations (4.13) and (4.14) into

equation (4.2) results in the matrix form of the element complimentary energy

$$\begin{aligned}
\Pi_e &= -\frac{1}{2}\{\beta+\Delta\beta\}^T[\mathbf{H}]\{\beta+\Delta\beta\} + \{\beta+\Delta\beta\}^T[\mathbf{G}]^e\{\mathbf{q}^e+\Delta\mathbf{q}^e\} \\
&+ \{\beta+\Delta\beta\}^T[\mathbf{G}^{\overset{1}{cr}}]\{\mathbf{q}^{\overset{1}{cr}}+\Delta\mathbf{q}^{\overset{1}{cr}}\} - \{\hat{\mathbf{t}}\}^T\{\mathbf{q}^e+\Delta\mathbf{q}^e\} \\
&- \{\beta+\Delta\beta\}^T[\mathbf{G}^{\overset{2}{cr}}]\{\mathbf{q}^{\overset{2}{cr}}+\Delta\mathbf{q}^{\overset{2}{cr}}\} \\
&- \int_{\Gamma_{cr}}\int_{\mathbf{u}^{\overset{1}{cr}}-\mathbf{u}^{\overset{2}{cr}}}^{\mathbf{u}^{\overset{1}{cr}}+\Delta\mathbf{u}^{\overset{1}{cr}}-\mathbf{u}^{\overset{2}{cr}}-\Delta\mathbf{u}^{\overset{2}{cr}}} t_i^{coh}d(u_i^{\overset{1}{cr}}-u_i^{\overset{2}{cr}})d\Gamma_{cr}
\end{aligned} \tag{4.16}$$

where

$$\begin{aligned}
[\mathbf{H}] &= \int_{\Omega_e}[\mathbf{P}]^T[\mathbf{S}][\mathbf{P}]d\Omega \qquad [\mathbf{G}^e] = \int_{\partial\Omega_e}[\mathbf{P}]^T[\mathbf{n}^e][\mathbf{L}_e]d\partial\Omega \\
[\mathbf{G}^{\overset{1}{cr}}] &= \int_{\Gamma_{cr}^{\overset{1}{}}}[\mathbf{P}]^T[\mathbf{n}^{cr}][\mathbf{L}_{cr}^{\overset{1}{}}]d\Gamma_{cr} \; [\mathbf{G}^{\overset{2}{cr}}] = \int_{\Gamma_{cr}^{\overset{2}{}}}[\mathbf{P}]^T[\mathbf{n}^{cr}][\mathbf{L}_{cr}^{\overset{2}{}}]d\Gamma_{cr} \\
\{\hat{\mathbf{t}}\} &= \int_{\Gamma_{tm}}\{\bar{\mathbf{t}}+\Delta\bar{\mathbf{t}}\}^T[\mathbf{L}_e]d\Gamma_{tm}
\end{aligned} \tag{4.17}$$

Construction of appropriate stress functions with optimally high resolution is necessary for accurately depicting high stress gradients near the crack tip.

4.2.3 Stability conditions

Following the stability conditions derived for displacement-based and stress-based finite element approximations in [4, 12, 104], the stability conditions of the stress-displacement field variational problem in X-VCFEM depend on the following conditions.

- The matrix $[\mathbf{H}]$ should be positive definite. From the definition of $[\mathbf{H}]$ in equation (4.17), the necessary condition for it to be positive definite is that the compliance tensor $[\mathbf{S}]$ be positive definite, which is true for elastic problems.

- A second condition is that the finite-dimensional stress subspaces $\mathcal{T}$ be spanned uniquely by the basis functions $[\mathbf{P}]$. This is satisfied by assuring linear independence of the columns of basis functions $[\mathbf{P}]$, which also guarantees the invertibility of $[\mathbf{H}]$.

- Additional stability conditions should be satisfied to guarantee non-zero stress parameters β for all non-rigid body displacement fields on the element boundary $\mathbf{u}_e^E$ or on the crack face $\mathbf{u}_e^{cr}$. This is accomplished by careful choice of the dimensions of the stress and displacement subspaces, i.e. $n_\beta > n_q^E + n_q^{cr} * 2 - 3$, where n_β is the number of β parameters, and n_q^E and n_q^{cr} are the number of displacement degrees of freedom on the element boundary and crack face respectively.

4.3 Creation of Enriched Stress Functions in X-VCFEM

VCFEM formulations for micromechanical analysis of heterogeneous materials have incorporated polynomial and reciprocal stress functions based on analytical micromechanics results in [35, 61, 80, 36]. In the present work, the heterogeneity is in the form of an evolving cohesive crack. Two conditions need to be considered in the choice of stress functions. The first is that it should adequately represent crack tip high stress concentration as required by the cohesive zone models. Polynomial functions alone are unable to satisfy this requirement and hence suffers from poor convergence. The second condition is that the stress function should account for stress jump across the crack surface. The stress functions in X-VCFEM incorporate three different components, namely: (a) a purely polynomial function Φ^{poly} to yield the far field stress distributions away from the crack tip, (b) a branch function Φ^{branch} that is constructed from level set functions, and (c) a multi-resolution wavelet function Φ^{wvlt} to account for the moving crack tip stress concentration. Thus, $\Phi = \Phi^{poly} + \Phi^{branch} + \Phi^{wvlt}$.

4.3.1 Pure Polynomial Forms of Stress Function:

The pure polynomial component of the stress function Φ^{poly} is written in terms of scaled local coordinates ($\hat{\xi} = \frac{x-x_c}{L}$, $\hat{\eta} = \frac{y-y_c}{L}$) with origin at the element centroid (x_c, y_c), as:

$$\Phi^{poly}(\hat{\xi}, \hat{\eta}) = \sum_{p=0,q=0}^{p_n, q_n} \hat{\xi}^p \hat{\eta}^q \beta_{pq} \tag{4.18}$$

The scaling parameter in the coordinate representation is $L = \sqrt{\max(x - x_c) \times \max(y - y_c)}$

$\forall (x, y) \in \partial\Omega_e$. The use of the scaled local coordinates $(\hat{\xi}, \hat{\eta})$, as opposed to global coordinates (x, y) in the

construction of stress functions, prevents ill conditioning of the [**H**] matrix due to the high exponents of (x, y) in Φ^{poly}. As discussed in [88], invariance of stresses with respect to coordinate transformations can be ensured by a complete polynomial representation of Φ^{poly}, while stability of the algorithm requires linear independence of the columns of stresses derived from Φ^{poly}.

4.3.2 Branch Stress Functions Using Level Set Methods

The branch function Φ^{branch} facilitates jumps in stresses across the crack surfaces. These functions should not affect the solutions in the continuous region beyond the crack. This construction requires a functional representation of the surface or line of discontinuity. Level set methods, introduced by Sethian [1, 85] for following the evolution of interfaces, is ideal for representing arbitrary contours. The method has been used by Belytschko and coworkers in [10] for the construction of branch functions associated with the partition of unity in a displacement based FEM formulation. The standard level set methods invoke continuous evolution of the entire surface of discontinuity. However for problems involving cracks, the only evolution occurs at the crack tip and the crack surface needs to be frozen behind tip. A vector level set method has been developed in [100, 99] to freeze the crack surface in accordance with geometric updating. This method is used in this work.

An approximation to the crack surface Γ_{cr} in figure 4.1 is constructed to describe the discontinuous stress fields across crack paths. As shown in figure 4.3(a), the discontinuous surface is expressed by a signed distance function $f(\mathbf{x})$ defined as

$$f(\mathbf{x}) = \min_{\bar{\mathbf{x}} \in \Gamma} \parallel \mathbf{x} - \bar{\mathbf{x}} \parallel \text{sign}(\mathbf{n}^+ \cdot (\mathbf{x} - \bar{\mathbf{x}})) \tag{4.19}$$

where $\bar{\mathbf{x}}$ is a point on the surface of discontinuity and $\mathbf{n}^+$ is a unit normal pointing in the direction of the region of positive distance function.

Consequently, $\bar{\mathbf{x}}$ is the closest point projection of any point $\mathbf{x}$ on Γ_{cr}. In order to describe the crack path accurately, the signed function $f(\mathbf{x})$ is evaluated at every integration point in the Voronoi cell element directly. The process of constructing branch functions involves steps that are described below.

- Radial distance functions to the two crack tips $r_1(\mathbf{x})$ and $r_2(\mathbf{x})$ and the corresponding angular positions $\theta_1(\mathbf{x})$ and $\theta_2(\mathbf{x})$ are depicted in figure 4.3(a). These functions are expressed in terms of coordinates of local systems (ξ,η) with origins at the crack tips. For the local system at crack tip 1, the coordinates of $\mathbf{x}$ are (ξ_1,η_1). In accordance with the definition of the signed distance function, the radial distance and angle functions are expressed as

$$r_1(\mathbf{x}) = \sqrt{\xi_1^2 + \eta_1^2} \quad \text{and} \quad \theta_1(\mathbf{x}) = \begin{cases} \pi - sin^{-1}\frac{f}{r_1} & \xi_1 < 0, f \geq 0 \\ -sin^{-1}\frac{f}{r_1} - \pi & \xi_1 < 0, f < 0 \\ sin^{-1}\frac{f}{r_1} & \xi_1 \geq 0 \end{cases} \tag{4.20}$$

Similarly, the radial distance and angle functions for the coordinate system at crack tip 2 are defined as:

$$r_2(\mathbf{x}) = \sqrt{\xi_2^2 + \eta_2^2} \quad \text{and} \quad \theta_2(\mathbf{x}) = \begin{cases} \pi - sin^{-1}\frac{f}{r_2} & \xi_2 < 0, f \geq 0 \\ -sin^{-1}\frac{f}{r_2} - \pi & \xi_2 < 0, f < 0 \\ sin^{-1}\frac{f}{r_2} & \xi_2 \geq 0 \end{cases} \tag{4.21}$$

- The branched stress function is constructed in terms of the functions $f(\mathbf{x})$, θ_1, r_1, θ_2, and r_2, as:

$$\Phi^{branch} = \sum_{s=0,t=0}^{s_n,t_n} r_1^2 sin\frac{\theta_1}{2} r_2^2 cos\frac{\theta_2}{2} \xi_1^s \eta_1^t \beta_{st} \tag{4.22}$$

The terms r_1^2 and r_2^2 in Φ^{branch} are necessary for avoiding crack tip singularity in the stresses due to this function and for improving the accuracy. Along the tangential extension to the crack path at the tip 1, Φ^{branch} is zero since $\sin\frac{\theta_1}{2} = 0$. Hence Φ^{branch} does not contribute to the stresses ahead of the crack tip 1. In an analogous manner, Φ^{branch} goes to zero along the extension to the crack path at the tip 2, since $\cos\frac{\theta_2}{2} = 0$. Therefore Φ^{branch} does not contribute to the stresses in this region also. However, along the crack surface between the two crack tips, $\sin\frac{\theta_1}{2} = \pm 1$ on both sides of the crack, and $\cos\frac{\theta_2}{2} = 1$. This renders Φ^{branch} in equation (4.22) discontinuous across the crack path. In Φ^{branch}, θ_1 is used to create the discontinuity across the crack surface, while θ_2 eliminates the discontinuity ahead

of crack tip 2. In some special instances with only one crack tip such as a panel with an edge crack, equation (4.22) may be simplified by removing r_2 and θ_2 dependence to yield

$$\Phi^{branch} = \sum_{s,t} r_1^2 sin\frac{\theta_1}{2} \xi_1^s \eta_1^t \beta_{st} \tag{4.23}$$

A coordinate transformation is required to obtain stress components in the global coordinate system from $\Phi^{branch}(\xi, \eta)$ based on the local coordinate system.

$$\begin{bmatrix} \sigma_{xx} & \sigma_{xy} \\ \sigma_{xy} & \sigma_{yy} \end{bmatrix}^{branch} = [\mathbf{Q}_b]^T \begin{bmatrix} \frac{\partial^2 \Phi^{branch}}{\partial \eta_1^2} & -\frac{\partial^2 \Phi^{branch}}{\partial \xi_1 \partial \eta_1} & & \\ -\frac{\partial^2 \Phi^{branch}}{\partial \xi_1 \partial \eta_1} & \frac{\partial^2 \Phi^{branch}}{\partial \xi_1^2} & & \\ & & \frac{\partial^2 \Phi^{branch}}{\partial \eta_2^2} & -\frac{\partial^2 \Phi^{branch}}{\partial \xi_2 \partial \eta_2} \\ & & -\frac{\partial^2 \Phi^{branch}}{\partial \xi_2 \partial \eta_2} & \frac{\partial^2 \Phi^{branch}}{\partial \xi_2^2} \end{bmatrix} [\mathbf{Q}_b] \tag{4.24}$$

where $[\mathbf{Q}_b]$ is the transformation matrix from (ξ_1, η_1) and (ξ_2, η_2) systems to (x, y), and is expressed as

$$[\mathbf{Q}_b] = \begin{bmatrix} \frac{\partial \eta_1}{\partial y} & \frac{\partial \eta_1}{\partial x} \\ \frac{\partial \xi_1}{\partial y} & \frac{\partial \xi_1}{\partial x} \\ \frac{\partial \eta_2}{\partial y} & \frac{\partial \eta_2}{\partial x} \\ \frac{\partial \xi_2}{\partial y} & \frac{\partial \xi_2}{\partial x} \end{bmatrix} \tag{4.25}$$

The branch function is evaluated at every integration point in the element. A typical function Φ^{branch} for $s = 0$ and $t = 0$ is plotted in figure 4.3(b). The plot shows that the function is continuous everywhere in the domain except across the crack surface. The example of a double cantilever beam under a sliding load, as shown in figure 4.7, explains the effect of level-set method based branch functions. In figure 4.7(a), the dimension is $a = 1.5m$. Figure 4.7(b) shows the stress σ_{xx} plots as a function of y at $x = -0.3m$. The stress functions are constructed with and without branch functions in this example. σ_{xx} changes its sign with a jump in its magnitude on different sides of the crack and the jump at $y = 0$ is predicted well. However, the transition is gradual from negative to positive values for the curve without branch functions. Although the

transition takes place in a short interval, the method is not able to catch the discontinuity without branch functions. This also results in the matrices $[\overset{1}{G}^{cr}]$ and $[\overset{2}{G}^{cr}]$ in equation (4.16), on different sides of the crack to be linearly dependent on each other (one is the negative of the other).

4.3.3 Multi-resolution Wavelet Functions for Modeling Cohesive Cracks

Wavelet bases, discussed in [16, 62], are $L^2(\mathcal{R})$ and generally have compact support. Only the local coefficients in wavelet approximations are affected by abrupt changes in the solution, such as for shock waves. This localization property makes the wavelet basis a desirable tool for problems with a high solution gradients, concentrations or even singularity. A brief introduction to wavelet basis functions is provided next.

Principles of wavelets and multi-resolution analysis

The construction of wavelet functions starts from a scaling or dilatation function $\phi(x)$ and a set of related coefficients $\{p(k)\}_{k\in\mathcal{Z}}$ which satisfy the two-scale relation

$$\phi(x) = \sum_k p(k)\phi(2x-k) \tag{4.26}$$

The scaling function has a compact support only if many coefficients $p(k)$ are non-zero. Translations of the scaling function $\phi(x-k)$ form an unconditional basis of a subspace $V_0 \subset L^2(\mathcal{R})$. Through a translation of ϕ by a factor of 2^n and dilation by a factor of $k \cdot 2^{-n}$ the unconditional basis is obtained for the subspace $V_n \subset L^2(\mathcal{R})$ as

$$\phi_{n,k}(x) = 2^{n/2}\phi(2^n x - k) \tag{4.27}$$

for a resolution level n. The scaling function ϕ is defined as orthonormal if translations at the same level of resolution satisfies the condition

$$\int_{-\infty}^{\infty} \phi_{n,k}(x)\phi_{n,l}(x)dx = \delta_{k,l} \quad \forall \;\; n,k,l \in \mathcal{Z} \tag{4.28}$$

Consequently, the best approximation of a function $f(x)$ in the subspace V_n of $L^2(\mathcal{R})$ is expressed as the orthogonal projection of f on V_n as:

$$\mathcal{A}_n f(x) = \sum_k a_{n,k}\phi_{n,k}(x), \qquad \text{where} \quad a_{n,k} = \int_{-\infty}^{\infty} f(x)\phi_{n,k}(x)dx \tag{4.29}$$

Approximation of $f(x)$, can be made at different resolution levels, and these approximations in subspaces $\cdots$, V_{n-1}, V_n, V_{n+1}, $\cdots$, follow the relation

$$\begin{aligned} &\{0\} = V_{-\infty} \subset \cdots \subset V_{-1} \subset V_0 \subset V_1 \subset \cdots \subset V_\infty = L^2(\mathcal{R}), \quad \text{where} \\ &lim_{n\to\infty} V_n = \bigcup V_n \ \text{ is dense in } \ L^2(\mathcal{R}) \quad \text{and} \ \ lim_{n\to-\infty} \cap_n V_n = \{0\} \end{aligned} \tag{4.30}$$

In the multi-resolution level transition, the information lost in the transition from level V_{n+1} to level V_n is characterized by an orthogonal complementary subspace W_n. A basis for the subspace W_n can be obtained is in the same manner as for scaling function, i.e. by dilating and translating the mother wavelet function

$$\psi(x) = \sum_k q(k)\psi(2x-k) \tag{4.31}$$

The subspaces spanned by the wavelet functions have the following essential properties:

$$\begin{aligned} &(i) \quad V_{n+1} = V_n \oplus W_n \ \ \forall, \ \ i.e.\ W_n \text{ is the orthogonal complement of } V_n \text{ to} V_{n+1}; \\ &(ii) \quad \text{For orthonormal bases, } \ W_{n1} \ \text{ is orthogonal to } \ W_{n2}; \\ &(iii) \quad \text{For orthonormal bases, } \ \oplus_{n=-\infty}^{\infty} W_n = L^2(\mathcal{R}) \end{aligned} \tag{4.32}$$

An approximation of the function $f(x)$ at the $n-th$ resolution level may be expressed as the orthogonal projection of f on W_n as

$$f \to \mathcal{D}_n f(x) = \sum_k b_{n,k}\psi_{n,k}(x), \qquad \text{where} \quad b_{n,k} = \int_{-\infty}^{\infty} f(x)\psi_{n,k}(x)dx \tag{4.33}$$

Due to the orthonormality and multi-resolution properties of wavelet basis functions, higher level approximate solutions can be generated from results of lower level solutions (see [16, 62]) by selective superposition of complementary solutions. The use of adaptive enrichment is very attractive to those regions where a pre-determined 'error or residual' tolerance is not met at the lower level.

Selection of the wavelet function

Various wavelet functions have been proposed in the literature for numerical solutions of ODEs and PDEs. These functions have been incorporated in the method of weighted residuals like the Galerkin's method and collocation method to solve problems with multi-level features in [38, 47, 71]. Among the large number of wavelet functions proposed are the Haar function [40], the Meyer's wavelets [57], the Chui-Wang's B-spline wavelets [17], etc. One of the most commonly used wavelet functions is Daubechies' compactly supported orthonormal wavelets [21, 23, 38]. However, they are constructed through recursive algorithms and do not have an explicit analytic expressions. This makes it is difficult to obtain their first and second derivatives, which is a requirement in X-VCFEM for deriving stresses in terms of stress functions. Also the orthonormality of the Daubechies wavelet cannot be transferred to the orthonormality for stresses by differentiation, and hence they are not considered to be suitable for stress functions in X-VCFEM. Alternatively a family of Gaussian functions, for which the first and second order derivatives are popular wavelets bases [11, 27, 52], is implemented in the representation of X-VCFEM stress functions and stresses. The expressions for the Gaussian function and its $n-th$ order derivative are:

$$G(x) = e^{-(\frac{x-b}{a})^2/2} \quad \text{and} \quad \Psi_{a,b}^{G_n} = (-1)^n \frac{d^n}{dx^n}(e^{-(\frac{x-b}{a})^2/2}) \tag{4.34}$$

The dilation and translation parameters a and b respectively can assume arbitrary values and can be changed in a continuous fashion. The ability of wavelets to translate diminishes the need to re-define new elements or remesh in conventional FEM solution of problems with moving boundaries. By changing translation parameters, the multi-levels of wavelet bases can be made to closely follow a moving crack tip. Additionally the dilation parameter with compact adjustable window support can be used to provide high refinement

and resolution. Hence it is a convenient way of moving the stress concentrations using the multi-resolution properties.

Multiresolution wavelet based stress functions for crack problems

The wavelet based stress function is constructed in a local orthogonal coordinate system (ξ, η), centered at the crack tip. The ξ direction corresponds to the local tangent to the crack surface. The corresponding stress function $\Phi_{a,b,c,d}$ in the Gaussian wavelet basis is given as:

$$\Phi_{a,b,c,d}(\xi,\eta) = e^{-(\frac{\xi-b}{a})^2/2} e^{-(\frac{\eta-d}{c})^2/2} \beta_{a,b,c,d} \tag{4.35}$$

where a, b, c, d are parameters that can take arbitrary continuous values. For implementation in multi-resolution analysis involving discrete levels, the translation and dilation parameters should be expressed as discrete multiples of some starting values. Consequently, these discrete values a_m, b_n, c_k and d_l are expressed as:

$$\begin{cases} a_m = a_1 \cdot (tr_a)^{m-1} \\ b_n = n \cdot b_1 \cdot a_m \\ c_k = c_1 \cdot (tr_c)^{k-1} \\ d_l = l \cdot d_1 \cdot c_k \end{cases} \tag{4.36}$$

Here (m, k) correspond to the levels and (n, l) correspond to the discrete translation of the bases in the (ξ, η) directions respectively. The parameters (a_1, c_1) are the initial dilating values at the first level $m = 1$, while $tr_a(< 1)$, $tr_c(< 1)$ are the transfer rates from one level to the next higher one. The parameters b_1, d_1 represent the starting values of a step translation quantity at the $m - th$ dilation level. The narrow (higher level) wavelets are translated by small steps, whereas the wider (lower level) wavelets are translated by large steps. Parameters $tr_a = tr_c = 1$ and $b_1 = d_1 = 0$ imply no dilation and translation respectively. Parameters c_0, c_c, and d_0 are counterparts of a_0, a_c, and b_0 in η direction. With the specific relations between dilation

and translation parameters, the Gaussian wavelet enriched stress function in equation (4.35) becomes

$$\Phi_{m,n,k,l}(\xi,\eta) = e^{-(\frac{\xi-b_n}{a_m})^2/2} e^{-(\frac{\eta-d_l}{c_k})^2/2} \beta_{m,n,k,l} \tag{4.37}$$

The family of wavelet enriched stress functions in equation (4.37) are not orthonormal, but they construct a linearly independent basis [22]. This leads to robustness and high precision in the reconstruction of any function f even with low level coefficients. The wavelet enriched stress function in X-VCFEM is thus written as

$$\Phi^{wvlt}(\xi,\eta) = \sum_{m=1,n=-\frac{n_n}{2},k=1,l=0}^{m_n,\frac{n_n}{2},k_n,l_n} \Phi_{m,n,k,l}(\xi,\eta) \tag{4.38}$$

The corresponding stresses are:

$$\left\{ \begin{array}{c} \sigma_{\xi\xi} \\ \sigma_{\eta\eta} \\ \sigma_{\xi\eta} \end{array} \right\} = \left\{ \begin{array}{c} \frac{\partial^2 \Phi^{wvlt}}{\partial \eta^2} \\ \frac{\partial^2 \Phi^{wvlt}}{\partial \xi^2} \\ -\frac{\partial^2 \Phi^{wvlt}}{\partial \xi \partial \eta} \end{array} \right\} = \left\{ \begin{array}{l} \sum_{m=1,n=-\frac{n_n}{2},k=1,l=0}^{m_n,\frac{n_n}{2},k_n,l_n} \frac{\partial^2 \left(e^{-(\frac{\xi_1-b_n}{a_m})^2/2} e^{-(\frac{\eta_1-d_l}{c_k})^2/2} \right)}{\partial \eta^2} \beta_{m,n,k,l} \\ \sum_{m=1,n=-\frac{n_n}{2},k=1,l=0}^{m_n,\frac{n_n}{2},k_n,l_n} \frac{\partial^2 \left(e^{-(\frac{\xi_1-b_n}{a_m})^2/2} e^{-(\frac{\eta_1-d_l}{c_k})^2/2} \right)}{\partial \xi^2} \beta_{m,n,k,l} \\ -\sum_{m=1,n=-\frac{n_n}{2},k=1,l=0}^{m_n,\frac{n_n}{2},k_n,l_n} \frac{\partial^2 \left(e^{-(\frac{\xi_1-b_n}{a_m})^2/2} e^{-(\frac{\eta_1-d_l}{c_k})^2/2} \right)}{\partial \xi \partial \eta} \beta_{m,n,k,l} \end{array} \right\} \tag{4.39}$$

The stress components in the global coordinate system are obtained by the transformation from the local coordinate system as

$$\left[\begin{array}{cc} \sigma_{xx} & \sigma_{xy} \\ \sigma_{xy} & \sigma_{yy} \end{array} \right]^{wvlt} = [\mathbf{Q}_w]^T \left[\begin{array}{cc} \frac{\partial^2 \Phi^{wvlt}}{\partial \eta^2} & -\frac{\partial^2 \Phi^{wvlt}}{\partial \xi \partial \eta} \\ -\frac{\partial^2 \Phi^{wvlt}}{\partial \xi \partial \eta} & \frac{\partial^2 \Phi^{wvlt}}{\partial \xi^2} \end{array} \right] [\mathbf{Q}_w] \tag{4.40}$$

where $[\mathbf{Q}_w]$ is the transformation matrix from (ξ,η) to (x,y):

$$[\mathbf{Q}_w] = \left[\begin{array}{cc} \frac{\partial \eta}{\partial y} & \frac{\partial \eta}{\partial x} \\ \frac{\partial \xi}{\partial y} & \frac{\partial \xi}{\partial x} \end{array} \right] \tag{4.41}$$

Figure 4.4 shows the support region for the wavelets enriched $\Phi^{wvlt}(\xi,\eta)$ in a X-VC element. This region is positioned symmetrically in the vicinity of evolving crack tips. The crosses ($\times$) corresponds to the position of each wavelet basis function b_n, d_n at a lower level, and the squares ($\square$) correspond to additional locations at a higher level in the multi-resolution algorithm. Only the points at the top half are shown in the figure due to symmetry.

The method of implementation of the multi-resolution wavelet enriched stress functions in X-VCFEM is described below.

1. For the starting level $m = k = 1$, 20 points marked by crosses ($\times$) in figure 4.4 (a), are used to delineate the wavelet enriched function $\Phi^{wvlt}(\xi,\eta)$ in equation (4.38). This corresponds to $m = 1,\ n = 5,\ k = 1$ and $l = 4$.

2. With ensuing higher levels in the multi-resolution wavelet functions according to the equation (4.36), higher level wavelet bases are added to the stress function as marked by squares ($\square$) in figure 4.4 (b). The addition is done adaptively in accordance with error criteria discussed in section (4.3.4). A refinement in the starting region of wavelet enrichment occurs in each added level, i.e. the window size of additional wavelet basis functions is smaller than ones at a lower level. This allows a zoom in to catch higher gradients that are missed at the coarser scales.

3. The process of successive multi-level refinement can continue till a predetermined error tolerance is reached.

Remark: The line of the cohesive crack is likely to intersect the region of support of the wavelet bases functions. It is important for the numerical algorithms to assure that wavelet functions based on one side of the cohesive crack does not contribute to stresses on the other side. The influence of wavelet stress functions should be cut off across this line of discontinuity by establishing a truncated effective support domain for the wavelet function. This is accommodated by ignoring the contribution of quadrature points in the numerical integration on the other side of the crack as detailed in section 4.5.3.

In summary, the stresses in an element are computed by adding contributions from equations (4.20), (4.22) and (4.39), to yield

$$\left\{ \begin{array}{c} \sigma_{xx} \\ \sigma_{yy} \\ \sigma_{xy} \end{array} \right\}_e = \left\{ \begin{array}{c} \sigma_{xx} \\ \sigma_{yy} \\ \sigma_{xy} \end{array} \right\}_e^{poly} + \left\{ \begin{array}{c} \sigma_{xx} \\ \sigma_{yy} \\ \sigma_{xy} \end{array} \right\}_e^{branch} + \left\{ \begin{array}{c} \sigma_{xx} \\ \sigma_{yy} \\ \sigma_{xy} \end{array} \right\}_e^{wvlt} =$$

$$\left[[\mathbf{P}]^{poly} \quad [\mathbf{P}]^{branch} \quad [\mathbf{P}]^{wvlt} \right]_e \left\{ \begin{array}{c} \beta_{pq} \\ \beta_{st} \\ \beta_{m,n,k,l} \end{array} \right\}_e = [\mathbf{P}]_e \{\beta\}_e \tag{4.42}$$

4.3.4 Error measure for adaptive wavelet enrichment

The Euler equation (4.3) indicates that the error in the kinematic equation, which is satisfied in a weak sense, may be primarily attributed to the lack of adequate resolution in the equilibrated stress fields. A strain energy based element error measure, derived in [80], is extended to the present problem. Let a stress field be enriched from a level n to level $n+1$ by adding the wavelet-based enrichment stress $\boldsymbol{\sigma}^{enr}$, i.e.

$$\boldsymbol{\sigma}^{level(n+1)} = \boldsymbol{\sigma}^{level(n)} + \boldsymbol{\sigma}^{enr} \tag{4.43}$$

The corresponding percentage change in the strain energy ($SE = \int_{\Omega_{enr}} \sigma_{ij} S_{ijkl} \sigma_{kl} \, d\Omega$), may be expressed as

$$\Delta \; SE = \frac{SE(\boldsymbol{\sigma}^{level:n+1}) - SE(\boldsymbol{\sigma}^{level:n})}{SE(\boldsymbol{\sigma}^{level:n+1})} \text{x} 100\% \tag{4.44}$$

In view of the local properties of wavelets and stress concentration at crack tips, the strain energy in equation (4.44) is calculated only in a small region around crack tip Ω_{enr}. Adding levels is conditioned upon the requirement that ΔSE is less than a preset tolerance, which in this work is chosen to be $\approx 4\%$.

4.4 Solution Method

Crack growth in multiply cracked materials is solved using an incremental approach, where a set of elemental and global equations are solved in each increment for stresses and displacements.

1. Local equations for each element are obtained by substituting the stress interpolations of equation (4.42) and boundary/crack face displacement interpolations of equation (4.14) in the element energy functional equation (4.16) and setting its variation with respect to the stress coefficients $\Delta\boldsymbol{\beta}$ to zero. This results in the weak form of the element kinematic relations

$$[\mathbf{H}]_e\{\boldsymbol{\beta}+\Delta\boldsymbol{\beta}\}_e = \left[[\mathbf{G}^e] \quad [\overset{1}{\mathbf{G}}{}^{cr}] \quad -[\overset{2}{\mathbf{G}}{}^{cr}]\right]_e \left\{\begin{array}{l} \mathbf{q}^e+\Delta\mathbf{q}^e \\ \overset{1}{\mathbf{q}}{}^{cr}+\Delta\overset{1}{\mathbf{q}}{}^{cr} \\ \overset{2}{\mathbf{q}}{}^{cr}+\Delta\overset{2}{\mathbf{q}}{}^{cr} \end{array}\right\}_e \tag{4.45}$$

or in a condensed form

$$[\mathbf{H}]_e\{\boldsymbol{\beta}+\Delta\boldsymbol{\beta}\}_e = [\mathbf{G}]_e\{\mathbf{q}+\Delta\mathbf{q}\}_e \tag{4.46}$$

Since equation (4.46) is linear, the stress coefficients can be directly expressed in terms of the nodal displacements, provided the element $[\mathbf{H}]_e$ matrix is invertible.

2. Subsequently, the weak forms of the global traction continuity conditions are solved by setting the variation of the total domain energy functional with respect to the generalized displacement components to zero. This results in the weak form of the traction reciprocity conditions

$$\sum_{e=1}^{N}\left[[\mathbf{G}^e] \quad [\overset{1}{\mathbf{G}}{}^{cr}] \quad -[\overset{2}{\mathbf{G}}{}^{cr}]\right]_e^T \{\boldsymbol{\beta}+\Delta\boldsymbol{\beta}\}_e = \sum_{e=1}^{N}\left\{\begin{array}{l} \hat{\mathbf{t}} \\ \bar{\mathbf{f}}_{coh} \\ -\bar{\mathbf{f}}_{coh} \end{array}\right\}_e \tag{4.47}$$

or in a condensed form:

$$\sum_{e=1}^{N}[\mathbf{G}]_e^T\{\beta+\Delta\beta\}_e=\sum_{e=1}^{N}\{\bar{\mathbf{T}}_{ext}\}_e \tag{4.48}$$

The forces at the crack surface are expressed in terms of the cohesive energy as

$$\bar{\mathbf{f}}_{coh}=\int_{\Gamma_{cr}}\frac{\partial}{\partial\Delta\mathbf{q}^{\overset{1}{cr}}}\left[\int_{\mathbf{u}^{\overset{1}{cr}}-\mathbf{u}^{\overset{2}{cr}}}^{\mathbf{u}^{\overset{1}{cr}}+\Delta\mathbf{u}^{\overset{1}{cr}}-\mathbf{u}^{\overset{2}{cr}}-\Delta\mathbf{u}^{\overset{2}{cr}}}t_i^{coh}d(u_i^{\overset{1}{cr}}-u_i^{\overset{2}{cr}})\right]d\Gamma_{cr} \tag{4.49}$$

Combining equations (4.46) and (4.48) and eliminating the stress coefficients $\{\beta+\Delta\beta\}_e$, results in the equation for solving the generalized displacements

$$\sum_{e=1}^{N}\{[\mathbf{G}]_e^T[\mathbf{H}]_e^{-1}[\mathbf{G}]_e\}\{\mathbf{q}+\Delta\mathbf{q}\}=\sum_{e=1}^{N}\{\bar{\mathbf{T}}_{ext}\}_e \tag{4.50}$$

Equation (4.50) is a nonlinear matrix equation system due to the cohesive laws. Consequently, a Newton-Raphson iterative solver is invoked to solve for the increments of nodal displacements. The linearized form of equation (4.50) for the j-th iteration is

$$\begin{aligned}&\left\{\sum_{e=1}^{N}\frac{\partial\{\bar{\mathbf{T}}_{ext}\}_e}{\partial\{\mathbf{q}\}}-\sum_{e=1}^{N}\{[\mathbf{G}]^T[\mathbf{H}]^{-1}[\mathbf{G}]\}_e\right\}^j\{d\mathbf{q}\}^j=\\&\left\{\sum_{e=1}^{N}\{\bar{\mathbf{T}}_{ext}\}_e-\sum_{e=1}^{N}\{[\mathbf{G}]^T[\mathbf{H}]^{-1}[\mathbf{G}]\}_e\{\mathbf{q}+\Delta\mathbf{q}\}\right\}^j\end{aligned} \tag{4.51}$$

which, in a condensed form is

$$[\mathbf{K}^g]^j d\mathbf{q}^j=\{\mathbf{R}^g_{ext}\}-\{\mathbf{R}^g_{int}\}^j \tag{4.52}$$

A numerical problem associated with modeling cohesive crack growth is the occurrence of snap-back as is shown in the macroscopic load-deformation behavior plot of figure 4.5.

This has been discussed for a three point bending solution in [59]. For a deformation controlled process

with monotonically changing deformation, the solution ignores the reverse portion of the displacement BCD, occurring with snap-back. The Newton-Raphson solver, where the loading process is monotonically controlled by incremental deformation or load conditions, exhibits a discontinuous drop from point B to point D. It is obvious, that this solver needs to be augmented with the capability to account for the part BCD, i.e. to decrease both load and deformation with the growth and opening of the crack. The arc-length solver has been proposed in [19, 20, 84] as a method of overcoming this shortcoming by introducing an unknown loading parameter $(\lambda + d\lambda)$ to govern the load increments. Equation (4.52) is modified with this loading parameter as

$$[\mathbf{K}^g]^j d\mathbf{q}^j = (\lambda^j + d\lambda^j)\{\mathbf{R}^g_{ext}\} - \{\mathbf{R}^g_{int}\}^j \tag{4.53}$$

where both $d\lambda^j$ and $d\mathbf{q}^j$ are unknowns, and $d\lambda^j$ can be either positive or negative. The additional unknown $d\lambda^j$ requires the solution of a constraint equation, written in terms of the magnitude of the deformation of all the nodes on the crack surface as

$$\sum_{i \in Crk} ((\overset{1}{\Delta \mathbf{u}}{}^{cr}_i)^2 + (\overset{2}{\Delta \mathbf{u}}{}^{cr}_i)^2) = \Delta l^2 \tag{4.54}$$

where Crk represents the set of all nodes on crack surfaces. A summary of the solution process is explained in the flowchart of figure 4.6.

4.5 Aspects of Numerical Implementation

4.5.1 Adaptive criteria for cohesive crack growth

A. Direction of incremental cohesive crack advance: In linear elastic fracture mechanics, it is common to use the "maximum hoop stress criterion" to determine the direction of crack propagation [7, 10]. Cracks are assumed to propagate in a direction normal to the maximum hoop stress in this criterion. Since stresses at crack tip are singular in LEFM, stress intensity factors are usually used to determine the direction of crack propagation. This criterion is only suitable for K-dominated problems, where the size of the fracture process

zone is small compared to the size of the specimen. A different criterion, based on the cohesive energy at the crack tip is used in X-VCFEM. A relation between the cohesive energy ϕ for complete decohesion and the critical energy release rate G_c has been established in [68] from the definition of the $J-$integral as:

$$G_c = J = \int_0^R t \, \frac{\partial \delta}{\partial x_1} dx_1 = \int_0^{\delta_e} t d\delta = \phi \tag{4.55}$$

where R is the length of the cohesive zone. Consequently, the crack growth direction is estimated as that, along which G_c or equivalently the cohesive energy ϕ is maximized for a given crack tip state of stress. The cohesive energy ϕ_A at the crack tip A along any direction α can be expressed for an arbitrary separation $\delta(\alpha)$ as:

$$\phi_A(\alpha) = \left(\int_0^{\delta(\alpha)} t(\alpha) d\delta \right)_A = \left(\int_{\sigma_{max}}^{t(\alpha)} t(\alpha) \cdot \frac{\partial \delta}{\partial t} dt \right)_A \tag{4.56}$$

where $t(\alpha) = \sqrt{(t_n^{coh})^2 + \beta^{-2}(t_t^{coh})^2}$ is the magnitudes of the effective cohesive force. The corresponding unit normal $\mathbf{n}$ and tangential $\mathbf{t}$ vectors along the direction α are expressed as

$$\mathbf{n} = -\sin\alpha \mathbf{i} + \cos\alpha \mathbf{j} \quad , \quad \mathbf{t} = \cos\alpha \mathbf{i} + \sin\alpha \mathbf{j} \tag{4.57}$$

The normal and tangential components of the cohesive traction force at an angle α may then be deduced as:

$$\begin{Bmatrix} t_n^{coh} \\ t_t^{coh} \end{Bmatrix} = \begin{bmatrix} n_x & n_y \\ t_x & t_y \end{bmatrix} \begin{Bmatrix} \sigma_{xx} n_x + \sigma_{xy} n_y \\ \sigma_{xy} n_x + \sigma_{yy} n_y \end{Bmatrix} = \begin{Bmatrix} \sigma_{xx} \sin^2\alpha - \sigma_{xy} \sin 2\alpha + \sigma_{yy} \cos^2\alpha \\ -\frac{1}{2}\sigma_{xx} \sin 2\alpha + \sigma_{xy} \cos 2\alpha + \frac{1}{2}\sigma_{yy} \sin 2\alpha \end{Bmatrix} \tag{4.58}$$

and hence the effective cohesive traction for direction α is

$$t(\alpha) = \frac{\sigma_{max}}{\sqrt{(\sigma_{xx}\sin^2\alpha - \sigma_{xy}\sin 2\alpha + \sigma_{yy}\cos^2\alpha)^2 + \beta^{-2}(-\frac{1}{2}\sigma_{xx}\sin 2\alpha + \sigma_{xy}\cos 2\alpha + \frac{1}{2}\sigma_{yy}\sin 2\alpha)^2}} \tag{4.59}$$

The incremental direction of crack propagation is assumed as that which maximizes the cohesive energy at A, according to the criterion:

$$\frac{\partial \phi_A(\alpha)}{\partial \alpha} = 0 \quad \text{and} \quad \frac{\partial^2 \phi_A(\alpha)}{\partial \alpha^2} < 0 \tag{4.60}$$

A combination of equations (4.56), (4.59) and (4.60), yield

$$\phi_A(\alpha) = \frac{\delta_e}{2\sigma_{max}}(\sigma_{max}^2 - t(\alpha)^2) \tag{a}$$

$$\frac{\partial \phi_A}{\partial \alpha} = -\frac{\delta_e}{\sigma_{max}} t \frac{\partial t}{\partial \alpha} = 0 \Longrightarrow$$

$$\frac{\partial t}{\partial \alpha} = [(\sigma_{xx}\sin^2\alpha - \sigma_{xy}\sin 2\alpha + \sigma_{yy}\cos^2\alpha)(\sigma_{xx}\sin 2\alpha - 2\sigma_{xy}\cos 2\alpha - \sigma_{yy}\sin 2\alpha) +$$

$$\beta^{-2}(-\frac{1}{2}\sigma_{xx}\sin 2\alpha + \sigma_{xy}\cos 2\alpha + \frac{1}{2}\sigma_{xx}\sin 2\alpha)(-\sigma_{xx}\cos 2\alpha - 2\sigma_{xy}\sin 2\alpha + \sigma_{yy}\cos 2\alpha)]/$$

$$((\sigma_{xx}\sin^2\alpha - \sigma_{xy}\sin 2\alpha + \sigma_{yy}\cos^2\alpha)^2 + \beta^{-2}(-\frac{1}{2}\sigma_{xx}\sin 2\alpha + \sigma_{xy}\cos 2\alpha + \frac{1}{2}\sigma_{yy}\sin 2\alpha)^2)^{0.5}$$

$$= 0 \tag{b}$$

$$\frac{\partial^2 \phi_A}{\partial \alpha^2} = \frac{\delta_e}{\sigma_{max}}[(\sigma_{xy}\sin 2\alpha - \sigma_{xx}\sin^2\alpha - \sigma_{yy}\cos^2\alpha)(\sigma_{xx}\sin 2\alpha - 2\sigma_{xy}\cos 2\alpha - \sigma_{yy}\sin 2\alpha)$$

$$+\beta^{-2}(\frac{1}{2}\sigma_{xx}\sin 2\alpha - \sigma_{xy}\cos 2\alpha - \frac{1}{2}\sigma_{yy}\sin 2\alpha)^2(-\sigma_{xx}\cos 2\alpha - 2\sigma_{xy}\sin 2\alpha + \sigma_{yy}\cos 2\alpha)]$$

$$< 0 \tag{c}$$

(4.61)

Equation (4.61)b results from the fact that t cannot be equal to zero for decohesion to initiate and hence the necessary condition evolves from its derivative. The direction of crack propagation α_c is obtained as the solution of equation (4.61)b as

$$\alpha_c^{XVCFEM} = \begin{cases} \arctan\left(\frac{-\sigma_{xx}+\sigma_{yy}\pm\sqrt{(\sigma_{xx}-\sigma_{yy})^2+4\sigma_{xy}^2}}{2\sigma_{xy}}\right) \\ \arctan\left(\frac{2(\beta^2-1)\sigma_{xy}\pm\sqrt{(4\beta^4-8\beta^2+4)\sigma_{xy}^2-(4\beta^4-4\beta^2+2)\sigma_{xx}\sigma_{yy}-(2\beta^2-1)(\sigma_{xx}^2+\sigma_{yy}^2)}}{2\beta^2\sigma_{xx}-\sigma_{xx}+\sigma_{yy}}\right) \end{cases} \tag{4.62}$$

The optimal angle α_c^{XVCFEM} is chosen as the one that satisfies the condition in equation (4.61)c. The corresponding angle given by the maximum hoop stress criterion in LEFM is expressed in terms of the stress intensity factors $K_I,\ K_{II}$ as:

$$\alpha_c^{LEFM} = 2\ \arctan\frac{1}{4}\left(K_I/K_{II} \pm \sqrt{(K_I/K_{II})^2+8}\right) \tag{4.63}$$

where the sign is chosen to make the hoop stress positive. The first of equation (4.62), which is the only choice for $\beta = 1$, exactly matches the angle given by the maximum hoop stress criterion (4.63). For the pure sliding problem shown in figure 4.7, α_c predicted by the equation (4.63) is 70.5^o, while that by X-VCFEM for cohesive stresses is 68.2^o.

B. Length of the incremental cohesive crack advance: Upon establishing the direction of incremental cohesive crack growth α_c, the length of cohesive zone advance ($\Delta\bar{l}$) should be estimated in the crack evolution scheme. The criterion used is that the cohesive energy goes zero at the end of the new segment as shown in figure 4.8(a). To achieve this, the cohesive energy at two points A (present crack tip) and B (close to A in the direction of crack propagation) are evaluated by substituting the stresses in equation (4.61)a. The tip of the cohesive zone is obtained from the linear extrapolation of this line to yield zero cohesive energy. From figure 4.8 (a), the increment of cohesive crack length is defined as:

$$\Delta\bar{l} = \frac{\phi_A}{\phi_A - \phi_B}|AB| \tag{4.64}$$

C. Cracks crossing the interelement boundaries and merging with each other: Crack advance from one Voronoi cell element to the next is conducted in X-VCFEM using an algorithm depicted in figure 4.8(b). A continuous tracking method is implemented to monitor if a cohesive surface has reached or gone past an element boundary. In this method, the intersection of the crack surface and an element boundary is obtained by solving the equation system

$$\frac{x - x_i}{x_{i+1} - x_i} = \frac{y - y_i}{y_{i+1} - y_i}, \quad \frac{x - x_n}{x_{n+1} - x_n} = \frac{y - y_n}{y_{n+1} - y_n} \tag{4.65}$$

where (x_i, y_i) represents the tip of the cohesive crack line for the ith increment, and (x_n, y_n) is the position of the nth node on the element boundary. If the intersection point is outside of the cohesive line or the element boundary, no intersection is assumed. Once a cohesive crack has reached its intersection with the boundary, a new node pair $(n_1\ n_2)$ is introduced on the element boundary at this point. The node pair belongs to the intersection of the element boundary and the cohesive crack, i.e. $n_1 n_2 \in \partial\Omega_e^E \cap \Gamma_{cr}$. The crack is subsequently advanced to the next element following the usual procedure outlined before.

Another condition that is considered in this work is the merger of multiple cracks as shown in figure 4.8(c) for two cohesive cracks. The algorithm for crack merging is an extension of the intersection algorithm, discussed above. At the end of every increment, all the cracks that have propagated in that increment are recorded. Subsequently, the intersection of the last incremental segment of the cohesive crack with those of all neighboring cracks, that belong to either the same element or neighboring elements, is checked using equation (4.65). Once the intersection of two crack segments is ascertained, a three-node junction (m_1, m_2, m_3), as shown in figure 4.8(c), is inserted at the point of intersection. The contribution of the junctions nodes e.g. (m_1, m_2) to the load vector in the assembled matrix equation, requires special treatment. For each of these nodes, contributions of integrals from adjoining crack segments belonging to two different cohesive cracks, are summed.

4.5.2 Evaluation of stress intensity factors

The stress intensity factors and $J-$ integral are evaluated in the post-processing phase of the computations. From linear fracture mechanics, the relation between $J-$ integral, stresses and stress intensity factors are given as

$$J = \int_{\Gamma} (\frac{1}{2}\sigma_{ik}\epsilon_{ik}\delta_{1j} - \sigma_{ij}u_{i,1})n_j ds = \frac{K_I^2}{E^*} + \frac{K_{II}^2}{E^*} \tag{4.66}$$

where $E^* = E$ (Young's modulus) for plane stress, $E^* = \frac{E}{1-\nu^2}$ for plane strain, and ν is the Poisson's ratio. In displacement based FEM [59, 26], the contour integral is converted into a domain integral to improve the accuracy of the stress intensity factors, since the stresses are more accurate in the interior of an element. However in X-VCFEM, stresses on the contour and the interior are equally accurate due to stress interpolation and the contour integral can provide similar accuracy as the domain integral. A method to extract the stress intensity factors K_I and K_{II} from the J-integral, proposed in Yau [105], is implemented in X-VCFEM. Displacement fields are not interpolated in the interior of the Voronoi cell element, and hence the term $u_{2,1}$ in equation (4.66) requires a special evaluation method.

1. Compute ϵ_{11}, ϵ_{22}, and ϵ_{12} at a series of points $(x_i, y_i,\ i = 1...N)$, in a small shadowed region around the integration point (x_0, y_0) in figure 4.8(d). The displacement gradient $u_{1,1}$ is calculated from ϵ_{11}.

2. For evaluating $u_{2,1}$ displacements u_1 and u_2 at any point (x_i, y_i) are interpolated using polynomial functions,

$$\begin{aligned} u_1(x_i, y_i) &= a_0 + a_1 x_i + a_2 y_i + a_3 x_i^2 + \cdots, \\ u_2(x_i, y_i) &= b_0 + b_1 x_i + b_2 y_i + b_3 x_i^2 + \cdots \end{aligned} \tag{4.67}$$

   where $a_0, a_1, \cdots, a_M$ and $b_0, b_1, \cdots, b_M$ are unknown coefficients. To constrain the rigid body motion, coefficients are evaluated from displacement values at two points on boundaries.

3. Displacement gradient expressions, $u_{1,1}(x_i, y_i)$, $u_{2,2}(x_i, y_i)$, $u_{1,2}(x_i, y_i)$ and $u_{2,1}(x_i, y_i)$ are obtained by

taking derivatives of the expressions in equation (4.67). Strain expressions in terms of the unknown coefficients are computed from these derivatives. At each point (x_i, y_i), the strains can also be computed from the known stresses and the compliance tensor, i.e. $\{\boldsymbol{\epsilon}\} = [\mathbf{S}][\mathbf{P}]\{\beta\}$. The unknown coefficients a_0, $a_1, \cdots, a_M$ and $b_0, b_1, \cdots, b_M$ in equation (4.67) are estimated by solving a least square minimization problem for the strains. Subsequently the displacement gradient $u_{2,1}$ is determined at the integration point (x_0, y_0).

4.5.3 Numerical integration schemes for [H] and [G] matrices

Integration of [H] matrix:

Numerical integration over each element is conducted by the Gaussian quadrature method to form the matrix [**H**] in equation (4.17). In this method, each Voronoi cell element is recursively subdivided into triangular subdomains, on which, integration points are generated for the Gaussian quadrature. The steps involved are discussed below.

1. For each Voronoi cell element shown in figure 4.9, the centroid **O** is first generated. The first set of triangular subdomains is created by joining each of the vertices of the cell e.g. (**A**, **B**, **C**, **D**, **E**, **F**) with the centroid **O**.

2. Each triangle is further subdivided into two triangles if:

$$\frac{Area\ of\ triangle}{Area\ of\ Voronoi\ cell\ element} > TOL_{area} \tag{4.68}$$

   For the subdomain triangle **BCO** shown in figure 4.9, two triangles are created by bisecting the longest edge **BC** at **O'** and joining it with the opposite vertex **O**.These new smaller triangles are again checked against the tolerance condition and further dissection is executed if necessary. Numerical integration in each triangular subdomain is done using 13 Gauss points.

3. For the region containing the crack tip shown in figure 4.9, a smaller value of TOL_{area} is chosen in comparison with other regions. This facilitates a higher density of integration points in regions of high

stress gradients. The tolerance in an element is consequently adjusted according to the distance of the center of the triangular subdomain from the crack tip, i.e.

$$TOL_{area} = TOL^{min}_{area} + \frac{(TOL^{max}_{area} - TOL^{min}_{area}) * d_{tri}}{L} \tag{4.69}$$

where L is a scaling parameter defined in subsection (4.3.1), d_{tri} is the distance of the crack tip from the subdomain and $TOL^{max}_{area}, TOL^{min}_{area}$ are assumed tolerances. In this work the tolerances are chosen as $TOL^{max}_{area} = 10\%$ and $TOL^{min}_{area} = 1\%$.

4. The intersection of the support of wavelet functions with the cohesive crack line call for a truncated support. This is done by eliminating the contribution of quadrature points that lie on the other side of crack face from the wavelet center. A visibility criterion introduced in [8] provides an easy way to accommodate this discontinuity in the construction of truncated support. In this method, the cracks are considered to be opaque when generating valid numerical integration regions. A ray is emitted from the center $\mathbf{W}$ of a wavelet basis function in an arbitrary direction as shown in figure 4.4. If it encounters an internal crack, the ray is terminated. All quadrature points lying in the dark shadow region on the other side of the crack CC' are suppressed during numerical integration of this wavelet basis.

Integration of the [G] matrices:

In equation (4.17), the matrices $[\overset{1}{\mathbf{G}}^{cr}]$ and $[\overset{2}{\mathbf{G}}^{cr}]$ are numerically integrated over the crack surfaces and the matrix $[\mathbf{G}^e]$ over the element boundary. All numerical integrations on the element boundary and crack surfaces are executed using the Gaussian quadrature method. The number of integration points N_{int} on each boundary/crack-face segment depends on the distance d_{side} between its center and the crack tip, and is chosen from the condition

$$N_{int} = \begin{cases} 9 & d_{side} \geq 0.1L \\ 16 & d_{side} < 0.1L \end{cases} \tag{4.70}$$

where L is the scaling parameter.

4.5.4 Invertibility of the [H] matrix

A nonsingular or invertible [**H**] matrix necessitates the linear independence of the columns of the [**P**] matrix. For pure polynomial expansions of the stress functions, this condition is naturally attained. However when adding the other terms, some of the terms in the branch and wavelet functions may have linear dependence on the polynomial terms. In X-VCFEM, the rank of the [**P**] matrix is first determined from the diagonal matrix resulting from a Cholesky factorization of the square matrix

$$[\mathbf{H}^*] = \int_{\Omega_e} [\mathbf{P}]^T [\mathbf{P}] d\Omega \tag{4.71}$$

Nearly dependent columns of [**P**] will result in very small pivots during Cholesky factorization. The corresponding branch and wavelet function terms are dropped from the stress function to prevent numerical inaccuracies in inverting [**H**].

4.5.5 Elimination of element rigid body modes

X-VCFEM uses a stress-based formulation with independent representation of displacement fields on the element and crack boundaries. In general, the nodes of the crack face are not topologically connected to the element boundary nodes. However it is important that all nodes in the element possess the same rigid body modes. The rigid body modes of the element boundary displacements $\{\mathbf{q}^e\}$ are directly constrained in the solution process through prescribed displacement boundary conditions. However, it is necessary to connect these with rigid-body modes for the crack face displacement fields $\{\overset{1}{\mathbf{q}}^{cr}\}$ and $\{\overset{2}{\mathbf{q}}^{cr}\}$. Singular value decomposition or SVD has been discussed in [80] as an effective method for identifying and constraining

rigid body modes at interfaces inside the Voronoi cell elements. The matrix product may be expressed as

$$\left[\begin{matrix}[\mathbf{G}^{cr}_{1}] & -[\mathbf{G}^{cr}_{2}]\end{matrix}\right]\left\{\begin{matrix}\mathbf{q}^{cr}_{1}\\ \mathbf{q}^{cr}_{2}\end{matrix}\right\} = [\mathbf{U}][\boldsymbol{\lambda}][\mathbf{V}]\left\{\begin{matrix}\mathbf{q}^{cr}_{1}\\ \mathbf{q}^{cr}_{2}\end{matrix}\right\} = [\mathbf{U}][\boldsymbol{\lambda}]\left\{\begin{matrix}\hat{\mathbf{q}}^{cr}_{1}\\ \hat{\mathbf{q}}^{cr}_{2}\end{matrix}\right\}$$
$$= \left[\begin{matrix}[\hat{\mathbf{G}}^{cr}_{1}] & -[\hat{\mathbf{G}}^{cr}_{2}]\end{matrix}\right]\left\{\begin{matrix}\hat{\mathbf{q}}^{cr}_{1}\\ \hat{\mathbf{q}}^{cr}_{2}\end{matrix}\right\} \tag{4.72}$$

$[\mathbf{U}]$ and $[\mathbf{V}]$ are orthonormal matrices obtained by SVD of $\left[\begin{matrix}[\mathbf{G}^{cr}_{1}] & -[\mathbf{G}^{cr}_{2}]\end{matrix}\right]$. $[\boldsymbol{\lambda}]$ is a rectangular matrix with nonnegative values on the diagonal. The zero or singular (very small values in numerical computations) values in $[\boldsymbol{\lambda}]$ corresponds to either trivial solutions or rigid body modes of the displacement solution. For accurate displacements, elements in $\{\hat{\mathbf{q}}^{cr}\}$ corresponding to small or zero eigen-values in $[\boldsymbol{\lambda}]$ are eliminated.

4.6 Numerical Examples

The numerical examples solved, are divided into four categories. In the first set of examples, the convergence of X-VCFEM enriched by multi-resolution wavelet functions is demonstrated for static cracks by comparison with theoretical predictions and results available in the literature. The second set of examples show the effectiveness of X-VCFEM in modeling the propagation of multiple cohesive cracks. The third set of examples is intended to investigate the effect of cohesive parameters on crack growth. The final set of examples looks into the growth of multiple pre-existing cracks to comprehend the effect of morphology, e.g. distribution, orientation etc..

4.6.1 Convergence tests for X-VCFEM for static cracks

Effects of translation and dilation parameters

Figure 4.10(a) shows a center cracked plate of width $2\mathbf{w}$=$4cm$ and length $\mathbf{b}$=$12cm$ with a crack length of $2\mathbf{a}$=$1.6cm$. The plate is loaded in simple tension with a constant remote load of $\boldsymbol{\sigma} = 5\ MPa$. The material parameters are: Young's modulus $E = 1\ MPa$ and Poisson ratio $\nu = 0.3$. Due to problem symmetry, only the right half of the plate is modeled with one X-VCFEM element, as shown in figure

4.10(b). Symmetry conditions are imposed on the left edge. The crack face is modeled using 10 node-pairs and the element boundary consists of 22 segments. The stress function used in this example consists of the three parts discussed in section 4.3. For the polynomial function, the order of interpolation in equation (4.18) corresponds to $p_n = 13$ and $q_n = 13$ for a total of 102 terms. For the branch function in equation (4.22) consists of only 1 term with $s_n = 0$ and $t_n = 0$. The wavelet functions are changed from a lower level to a higher level using the adaptation criterion discussed in section 4.3.4. Similar parameters are assumed for the ξ_1 and η_1 directions, i.e., $a_1 = c_1$, $tr_a = tr_c$ and $b_1 = d_1$ in equation (4.36). The starting values of the parameters for the lower level ($m = k = 1$) are: $-2 \leq n \leq 3$, $0 \leq l \leq 1$, and $a_1 = c_1 = 0.1$. The result of X-VCFEM for this problem is plotted in terms of the stress σ_{yy} along the crack face ($y = 0$) as a function of the distance from the center of the crack in figure 4.11. The figure 4.11(a) corresponds to the stresses by varying the translation parameter b_1, while figure 4.11(b) is for the variation of the dilation parameter a_1. From figure 4.11(a) it is evident that a smaller b_1 make the stress concentration at the crack tip higher. However, very small $b_1 \leq 0.001$ (no translation) leads to linear dependence of the columns of the $[\mathbf{P}]$ matrix generated from the wavelet basis functions, and should be avoided. Figure 4.11(b) shows that smaller a_1 results in faster convergence to higher crack tip stress concentration. However, very small values of a_1 can also lead to oscillatory stresses. On the other hand, large a_1 values (≈ 0.15) shifts the stress peak. The optimal selection of these parameters is therefore very important. This is obtained through the multi-resolution construction of bases, discuss next. The multi-resolution wavelet bases are significantly more effective in simulating crack problems. Table 4.7 shows the effect of the dilation transfer rate $tr_a = tr_c$ on the stress intensity factors for variation in the translation parameters $b_1 = d_1$. Other parameters in the simulation are $a_1 = c_1 = 0.1$, $m_n = k_n = 3$, $n_n = 6$, and $l_n = 2$. The values $tr_a = tr_c = 1$ imply no dilation. As tr_a approaches 1, the different levels functions become more and more dependent on each other. From the table, the minimum error is achieved for $b_1 = 0.1$ and $tr_a = tr_c = 0.5$ or 0.6.

Convergence with multi-resolution wavelet bases

The example in section 4.6.1 is considered again for studying the solution convergence behavior with multi-resolution wavelet functions. The four sets of parameters represent four instances of multi-resolution stress

function enrichment. The first case consists of only polynomial and branch functions for the stress interpolation, for which the details are provided in section 4.6.1. Cases 2, 3, 4, and 5, introduce different levels of the wavelet basis functions. The wavelet parameters common to these four cases are: $n_n = 6$, $l_n = 2$, $a_1 = c_1 = b_1 = d_1 = 0.1$, and $tr_a = tr_c = 0.5$. The parameters corresponding to the levels of the multi-resolution enrichment ($m_n = k_n$) are listed in table 4.7.

The mode I stress intensity factor is calculated for all the five cases and is normalized with respect to the analytical prediction K_{ref} by linear elastic fracture mechanics (LEFM), reported in [91]. The second row of table 4.7 compares this value for the different cases. Without the wavelet bases (case 1), the solution is 16% higher than the theoretical value. Cases 2-5 results demonstrate that the wavelet basis effectively reduces the error with increasing resolution level (m_n). The X-VCFEM generated stress σ_{yy} at $y = 0$ is plotted in figure 4.12 for cases 1-4. Without the wavelet enrichment, the stress concentration at the crack tip ($x = 0.8$) is completely misrepresented. The stress peaks are represented with increasing accuracy with additional levels of multi-resolution wavelet functions. The strain energy error in equation (4.44) is also calculated for the cases 2-5 and tabulated in table 4.7. The error rapidly decreases with increasing wavelet enrichment, confirming the fast convergence rate of the multi-resolution algorithm. However, the stress intensity factor K_I is calculated from a contour that is away from the crack tip. The stresses on this contour are much more stabilized and additional wavelet bases do not affect these stresses considerably. Hence, the error in K_I is not significantly affected by their addition. From the above convergence tests, the optimal parameters for stress function representations in X-VCFEM are chosen to be $p_n = q_n = 13$, $s_n = t_n = 0$, $n_n = 6$, $l_n = 1$, $m_n = k_n = 4$, $a_1 = c_1 = b_1 = d_1 = 0.1$ and $tr_a = tr_c = 0.5$. These are retained for all subsequent simulations. X-VCFEM simulations of the cracked plate are further conducted for different crack lengths, to study the effect of this length on the solution convergence. The specific dimensions in figure 4.10(a) are $2\mathbf{w}$=2 cm, $\mathbf{b}$=6 cm, while the crack length $2\mathbf{a}$ is varied. The plate is loaded under remote tension of $\boldsymbol{\sigma} = 40Pa$. X-VCFEM solution of K_I for various values of $\mathbf{a/w}$ are plotted in figure 4.13 and compared with the theoretical predictions of [91]. X-VCFEM predictions match the theoretical results extremely well.

4.6.2 Efficiency and Accuracy of X-VCFEM

Prior to studying the effect of cohesive parameters and multi-crack distributions, the accuracy and efficiency of X-VCFE model are validated by several numerical examples.

Comparing efficiency with ABAQUS for a simple crack propagation problem

A plate with a pre-existing edge crack under remote tension load is solved for plane strain by X-VCFEM and ABAQUS as shown in figure 4.14(a). The material Young's modulus $E = 70,000MPa$, and Poisson ratio $\nu = 0.33$. A bilinear cohesive zone model discussed in [53] is used to describe the crack growth and the cohesive model parameters are $\sigma_{max} = 5\ MPa$, $\delta_c = 1 \times 10^{-6}\ mm$, $\delta_e = 5 \times 10^{-3}\ mm$ and $\beta = 0.707$. The entire domain is represented by a single element in X-VCFEM, consisting of 142 nodes for displacement interpolation. The adaptive enrichment of wavelet bases is determined by the strain energy error in equation (4.44). As shown in previous section, the optimal parameters for stress function representations in X-VCFEM are chosen to be $p_n = q_n = 13$, $s_n = t_n = 0$, $n_n = 8$, $l_n = 1$, $m_n = k_n = 4$, $a_1 = c_1 = b_1 = d_1 = 0.1$ and $tr_a = tr_c = 0.5$, which means that stress function interpolations consist of 102 terms of polynomial functions, 1 term in the branch function, and 128 terms in the wavelet function representation. These are retained for all subsequent simulations. It is assumed that the crack propagates horizontally due to symmetry, and hence the modules for determining incremental crack direction in section 4.5 is switched off for this problem. A special UEL subroutine is developed in ABAQUS for incorporating the cohesive model at a given interfaces. A total of 12840 4-node 2D element and 77 cohesive elements are used in ABAQUS. Figure 4.14(b) shows the load σ-vertical displacement u_y plot at point **A**. The two codes yield very similar results, an attestation of X-VCFEM accuracy. However, the X-VCFEM simulation takes only 1.6 minutes on a single CPU in the Pentium 4 cluster with 2.4Ghz Intel P4 Xeon processors, as opposed to 13.9 minutes by the ABAQUS run on the same machine. Thus, even for this simple example, a tenfold advantage in computing speed is achieved by X-VCFEM. It is expected that this factor will increase considerably with increasing complexity, such as more cracks.

A classical problem on dynamic crack propagation

This numerical example is based on Kalthoff's well known experiment on dynamic crack propagation in a impact loaded prenotched plate, that has been the subject of many studies [50, 51, 76]. These studies suggest that a crack, subjected to a tension-compression load as shown in figure 4.15(a), propagates at an angle of approximately $60^o - 70^o$ with respect to the initial notch in the plate. The present X-VCFEM does not explicitly incorporate inertia terms, and hence a quasi-static crack propagation problem is simulated instead of the dynamic test. The configuration in figure 4.15(a), shows that the experimental projectile motion is replaced by the traction boundary conditions in the simulation under plane strain conditions. A small initial crack length of a=0.02m is chosen to mitigate the effect of the constrained right hand boundary on crack propagation. Material properties for this problem are: Young's modulus $E = 207\ GPa$ and Poisson ratio $\nu = 0.3$ and cohesive zone model parameters in equation (4.11) are: $\sigma_{max} = 0.1\ MPa$, $\delta_e = 1 \times 10^{-6} m$, and $\beta = 0$. The entire domain is represented by a single element in X-VCFEM, consisting of 132 nodal degrees of freedom. The results of the X-VCFEM simulation is shown in figure 4.15. From figure 4.15(a) the initial crack growth angle is around 70^o, which is corroborated by brittle failure experiments at very low velocities [28]. Subsequently, the crack propagation takes place within the envelope of $60^o - 70^o$, which is in agreement with studies in [50, 51, 76]. The dynamic conditions, as well as boundary constraints are responsible for the small difference between X-VCFEM results and those in [76]. Volume-averaged or macroscopic shear stress-shear strain behavior for this problem is plotted in figure 4.15(b). The volume averaging of the local stress and strain fields over the entire microscopic domain Ω is performed as

$$\begin{aligned} \bar{\sigma}_{ij}(t) &= \frac{1}{\Omega}\int_{\Omega} \sigma_{ij}(x_k, t) dV \\ \bar{\epsilon}_{ij}(t) &= \frac{1}{\Omega}\int_{\Omega} \epsilon_{ij}(x_k, t) dV - \alpha_{ij}(t). \end{aligned} \tag{4.73}$$

where x_k and t are the spatial coordinates and time (cumulative increments in these problems) respectively, and

$$\alpha_{ij}(t) = \frac{1}{2\Omega}\int_{\Gamma_{cr}} ([u_i(t)]n_j + [u_j(t)]n_i) d\partial\Omega \tag{4.74}$$

$\alpha_{ij}(t)$ represents the effective strain field caused by the possible displacement jump at the crack. It is calculated along the crack path Γ_{cr} with $[u_i(t)]$ denoting the displacement jump.

Crack propagation in sheared plate with a central crack

This example is based on a classical problem of a single crack propagation in a large plate with a central crack. The plate is subjected to a far field shear load. The problem was experimentally studied by Erdogan and Sih [28] and an optical micrograph of their cracked specimen is shown in figure 4.16(a). The specimen material in their experiment were assumed to be homogeneous, isotropic and linearly elastic and the crack was assumed to be brittle. A single element of dimension 10 $m \times 8$ m in X-VCFEM is used to simulate this experiment as shown in figure 4.16(b). The initial crack length is **a**=1.6 m. The material parameters are: Young's modulus $E = 100$ GPa, Poisson ratio $\nu = 0.3$ and the cohesive law parameters are: $\sigma_{max} = 0.1$ MPa, $\beta = 1$, and $\delta_e = 1 \times 10^{-7} m$. The shear stress applied on the top and bottom surfaces, is varied from 0 to 0.041 GPa with plane stress assumptions. As shown in figure 4.16(b), the crack path predicted by X-VCFEM compares well with the observations in [28]. Figure 4.16(c) shows the growth of the crack opening displacement components at the right tip A. The entire computational process took 20 minutes on a single CPU in the Pentium 4 cluster with 2.4Ghz intel P4 Xeon processors.

Crack propagation in three-point bending specimen

Two numerical examples are considered for this specimen. In the first example, symmetric mode I crack propagation in a three-point bending test, as shown in figure 4.17, is modeled. Plane stress conditions are assumed in the simulation. This problem of cohesive crack propagation has been studied by Carpinteri [14] using node release technique and by Moës and Belytschko [59] using the extended FEM or XFEM. The geometrical dimensions for the specimen in figure 4.17 are **b**= 0.15 m,**l**=4**b**, **t**(specimen thickness)= **b**,**a**=0, and **d**=0.001 m. The material properties are: Young's modulus $E = 36,500$ MPa, Poisson ratio $\nu = 0.1$, and the cohesive parameters are $\sigma_{max} = 3.19$ MPa, and $\beta = 0$. The X-VCFEM solution is compared with that in [59] through the load-deflection curve of figure 4.18. The cohesive displacement parameters are $\delta_e = 3.134796 \times 10^{-5}$ m and $\delta_e = 6.26959 \times 10^{-6} m$ for figures 4.18(a) and 4.18(b) respectively. A sharper

snap-back is seen for the latter case. Excellent match is observed between the X-VCFEM and XFEM results The second example shows a mixed-mode cohesive crack propagation in a three-point bend test due to an unsymmetrically positioned initial crack. The problem, shown in figure 4.19(a), has been studied by Mariani and Perego[56] using XFEM under plane stress conditions. The initial crack position is determined by the offset ratio α, defined as the ratio of the distance of the initial crack from the mid-span cross-section to half of the beam span. The material Young's modulus $E = 31370\ MPa$, and Poisson ratio $\nu = 0.2$. The cohesive model parameters are $\sigma_{max} = 4.4\ MPa$, $\delta_e = 0.07719298\ mm$ and $\beta = 1.0$. Once again, the entire domain is represented by a *single element* in X-VCEFM with 154 nodal degrees of freedom. Figure 4.19(b) shows the load-deflection curve for two values of the offset parameter, i.e. $\alpha = 0.5$ and $\alpha = 0.25$. The initial elastic response in the load **P**-displacement **u** curve is stiffer and also the peak load is higher for higher values of α. The load-displacement response exhibits softening in the later stages of crack propagation due to the significantly evolved crack. The path of crack propagation for the two cases are shown in figures 4.19(c) and (d). The cracks move towards the point of applied load and align themselves perpendicular to the edge of the specimen.Excellent agreement is obtained between the results by X-VCFEM and in [56].

4.6.3 Mesh independence of crack propagation with X-VCFEM

A panel with domain 5 $cm \times 3\ cm$ containing two initial cracks is remotely loaded in tension as shown in figure 4.20(a). The problem has been solved by Sharma et. al. [87] using the element free Galerkin meshless method. For X-VCFEM solution, the domain is meshed into two elements with three different topologies shown in figure 4.20. Plane stress conditions are again assumed. A total of 11 increments is used to model the entire crack propagation process. The material parameters are: Young's modulus $E = 207\ GPa$ and Poisson ratio $\nu = 0.3$ and cohesive zone parameters are: $\sigma_{max} = 0.1\ MPa$, $\delta_e = 1 \times 10^{-6} cm$, and $\beta = 1$. The three figures 4.20(b,c,d) show no mesh dependence of the X-VCFEM predictions and the comparison with results in [87] is excellent.

4.6.4 Effect of cohesive parameters on crack evolution

This example is intended to investigate the effect of cohesive parameters on crack growth. Cohesive zone model parameters, e.g. σ_{max} and δ_e in equation (4.11), can significantly affect the propagation and overall behavior of a cracking material. The effects of these cohesive parameters are studied for crack propagation in a sheared plate with a central crack subjected to a far field shear load. This classical problem was experimentally studied by Erdogan and Sih [28] and an optical micrograph of their cracked specimen is shown in figure 4.21(a). The specimen material in their experiment was assumed to be homogeneous, isotropic and linearly elastic and the crack was assumed to be brittle. A single element of dimension 10 $m \times 8$ m in X-VCFEM is used to simulate this experiment as shown in figure 4.21(b). The initial crack length is $\mathbf{l_0}$=1.6 m. The material parameters are: Young's modulus $E = 100$ GPa, Poisson ratio $\nu = 0.3$. Five different sets of cohesive parameters, illustrated in figure 4.21(b) are considered for this example. These are

- **A:** σ_{max}=3.0 MPa, δ_e=3.0 e-4m, $\beta = 1.0$
- **B:** σ_{max}=6.0 MPa, δ_e=1.5 e-4m, $\beta = 1.0$
- **C:** σ_{max}=3.0 MPa, δ_e=6.0 e-4m, $\beta = 1.0$
- **D:** σ_{max}=6.0 MPa, δ_e=3.0 e-4m, $\beta = 1.0$
- **E:** σ_{max}=1.5 MPa, δ_e=6.0 e-4m, $\beta = 1.0$

As shown in figure 4.21(b), all the cases correspond to the same cohesive energy. The load is applied by controlling the opening of crack propagation through fixed values of the increment Δl in equation (4.54). Further a uniform shear load per unit length τ_0 is applied on the top and bottom surfaces as shown in figure 4.21(c). In each increment, the applied load is scaled by the arc-length parameter λ of equation (4.53), to yield an equilibriated applied load corresponding to a prescribed crack propagation length. The crack path for all the different cohesive parameters predicted by X-VCFEM are very similar and compare well with experimental observations in [28]. However a considerable dependence on cohesive parameters is seen in the

shear-crack length response, demonstrated in figure 4.21(d), where the normalized crack length is defined as

$$l_r = \frac{\text{The current crack length}}{\text{The initial crack length}} \tag{4.75}$$

This points to the fact that the rate of propagation, and not the direction, is dependent on the parameters for this problem. For the cases with larger peak traction cases: **B** and **D**, higher applied loads are needed for causing similar crack growths as for cases with lower peak traction: **A** and **C**. Comparison of the results for cases **B** and **D**, show that a smaller δ_e (case **B**) results in quicker reduction of the local cohesive traction. This makes the overall load for the case B to increase slower than that for case **D** with a higher δ_e. The case **E** consistent with the trends exhibited by the other load cases. Although, the simulation results show that both σ_{max} and δ_e affect the crack growth, comparison of cases **A, B, C** with **D** shows that the crack growth is more sensitive to σ_{max} than to δ_e. The results also imply that the cohesive energy, or effectively the energy release rate G_c does not alone determine the properties of crack propagation. The individual parameters, affecting the shape of the cohesive law, play an important role in predicting the growth characteristics. These effects are also tested for multiple crack growth in the next set of examples.

4.6.5 Propagation of multiple pre-existing cracks

The final set of examples looks into the growth of multiple pre-existing cracks to comprehend the effect of morphology, e.g. distribution, orientation etc..

Firstly, a plate with five randomly located cracks is simulated under a tensile loading as shown in figure 4.22(a). The plate has dimensions 0.6 $m \times 0.4$ m; material parameters: Young's modulus $E = 10^5$ MPa and Poisson ratio $\nu = 0.3$; and cohesive parameters: $\sigma_{max} = 0.1$ MPa, $\beta = 1$, and $\delta_e = 1 \times 10^{-5} cm$. Figure 4.22(b) shows the final positions of the cracks that have grown with the loading. The cracks propagate across element boundaries and are attracted to each other in certain regions till they nearly merge.

A plate with 28 randomly located and oriented cracks is simulated under a tensile loading. Figures 4.23(a) and (b) show the two microstructures with different crack distributions. For the *microstructure 1*, all the cracks of equal length are oriented horizontally and their distribution is random. The *microstructure 2* has

cracks of random length and orientation. In addition, it contains a cluster of 8 cracks in a otherwise random distribution as shown in figure 4.23(b). The plate is of dimension 0.1 $m \times 0.1$ m, and the material parameters are: Young's modulus $E = 10^4$ MPa and Poisson ratio $\nu = 0.3$. To understand the effect of cohesive parameters on crack propagation, two different sets of cohesive parameters are considered. They are:

CP-1: σ_{max}=1.0 MPa, δ_e=1.0 e-5m, $\beta = 0.707$

CP-2: σ_{max}=2.0 MPa, δ_e=0.5 e-5m, $\beta = 0.707$

A uniform tension load per unit length σ is applied on the top and bottom surfaces as shown in figure 4.23(a,b). In each increment, the applied load is scaled by the arc-length parameter λ of equation (4.53), to yield an equilibriated applied load corresponding to a prescribed crack opening deformation.

Figures 4.24(a,b) and (c,d) show the contour plots of the microstructural stress σ_{yy} together with evolved position of the cracks at the final stage of loading, for the two sets of microstructures and cohesive parameter respectively. The growth pattern of each crack can be observed by comparing with its initial configuration in figures 4.23(a) and (b). The cracks propagate across element boundaries, interact with each other and in some cases, they merge. The relation of the propagation of multiple cracks to the morphology and cohesive parameters is in general complicated. However, several observations can be made based on the results of the simulation by this model.

- Larger stress concentrations develop at tips of cracks that are nearly perpendicular to the direction of loading. Consequently, this subset of cracks grow more easily than others that are more aligned with the loading direction. From figure 4.24(b) and (d), it can be seen that some cracks that are nearly parallel to the load direction never propagate.

- Stress concentrations are higher at tips of longer cracks. The reason is stress concentrations at crack tips come from the external load, which cannot be handled by the weak crack. Longer cracks lead to more external load concentrating to tips. This is verified by results shown in figure 4.24(b) and (d), where longer cracks are easier to propagate than shorter ones.

- Irrespective of the initial orientation, the evolved crack path tends to align in a direction perpendicular to the applied load direction. This correspond to an optimal direction for releasing the cohesive energy.

This observation is dominant, when the influence of nearby cracks on the local stress field is small. The local stress field for this phenomenon is mainly governed by the influence of applied load on this single crack.

- Cracks are attracted towards weak surfaces, such as other cracks or voids and prefer to propagate in those directions. This may be attributed to the fact that the cohesive energy in the direction of these weaker surfaces with lower (or zero) tractions is naturally lower in comparison with other directions.

- Figures 4.24(b) and (d) show that the longest crack does not necessarily evolve from a cluster. Not all cracks in a cluster grow considerably. This is somewhat in contrast to observations made with particle reinforced composites, where almost always clusters cause a local stress concentration. The interaction between neighboring cracks contributes to the enhancement or mitigation of stresses, depending on their orientations and length. This dictates their propagation, and just being in a cluster does not guarantee significant growth.

- The different cohesive parameters show very little difference in the final configuration and hence the propagation direction. However, the rate of crack growth varies considerably with these parameters as seen in the crack length-macroscopic strain plot of figure 4.25

Figure 4.26 shows the macroscopic stress-strain response for the two microstructures and cohesive parameters. Even before the cracks propagate (corresponding to the change in slope), the stiffness of the *microstructure 2* is higher than that of *microstructure 1* due to a higher level of effective damage caused by crack lengths and more importantly orientations. Orientations perpendicular to the load direction causes a larger reduction in stiffness in comparison with other directions. With additional loading, the overall damage caused by the growth of cracks is also higher for the *microstructure 1.* This is seen by the lower values of the macroscopic stress for this case. The effect of the cohesive parameters on the stress-strain response is quite pronounced. The maximum macroscopic stress for both microstructures increases significantly for higher values of σ_{max}, even though the cohesive energy is the same for the two cohesive models. This is caused by a slowdown in the growth rate of the cracks with overall deformation.

4.7 Concluding Remarks

The extended Voronoi cell finite element model is developed in this chapter to predict initiation and growth of damage by crack propagation in brittle matrix. The cracks are modeled by a linear cohesive zone model and their incremental directions and growth lengths are determined in terms of the cohesive energy near the crack tip. Important enhancements are made to the element to allow stress discontinuities across the cohesive crack and to accurately depict the crack tip stress concentrations. These features are accommodated through the incorporation of (a) branch functions in conjunction with level set methods across crack contours, and (b) adaptive multi-resolution wavelet functions in the vicinity of the crack tip. Several problems are solved and compared with existing solutions in the literature for validation of the X-VCFEM algorithms, both with respect to macroscopic (load-deformation behavior) and microscopic (crack path). The X-VCFEM results show excellent accuracy in their comparison with analytical and other numerical solutions. Also comparison with ABAQUS shows the efficiency of X-VCFEM. Numerical simulations are conducted with different σ_{max} and δ_e to understand the effect of cohesive parameters on the crack propagation. It's observed that in addition to the total cohesive energy, the individual parameters have effects on crack growth. The effect of geometrical information of multiple pre-existing cracks, including the lengths, positions and orientations of cracks, on their propagation is studied by simulating a plate with 28 randomly located and oriented cracks. Simulation results show that the crack with a longer length and nearly perpendicular to load direction is easier to propagation than other cracks. Cracks propagation direction is dependent on the local stress field, which is managed by both the external load and nearby material phases, such as other cracks in a cluster. This research reveals the significance of analyzing large regions of the microstructure and proves the effectiveness of the X-VCFEM. The simulation results based on X-VCFEM could also provide positive feedback for design modification.

Based on the study on interfacial debonding and cohesive matrix cracking in composites, the interaction of the two damage phenomena is studied in the next chapter, where the X-VCFEM is improved and a criterion for assessing the direction of damage development is proposed.

tr_a	0.6	0.6	0.6	0.5	0.5	0.5	0.4	0.4	0.4
b_1	0.05	0.1	0.2	0.05	0.1	0.2	0.05	0.1	0.2
K_I/K_{ref}	1.019	**1.014**	1.040	1.017	**1.014**	1.027	1.020	1.020	1.035

Table 4.1: Normalized stress intensity factors (K_I/K_{ref}) for different values of tr_a and b_1 in the multi-resolution wavelet representation.

	Case 1	Case 2	Case 3	Case 4	Case 5
$m_n = k_n$	0	1	2	3	4
K_I/K_{ref}	1.1642	1.0361	1.0208	1.0062	1.0020
ΔSE		96.45%	45.91%	7.06%	3.01%

Table 4.2: Errors with varying enrichment order of multi-resolution wavelet functions for the different cases.

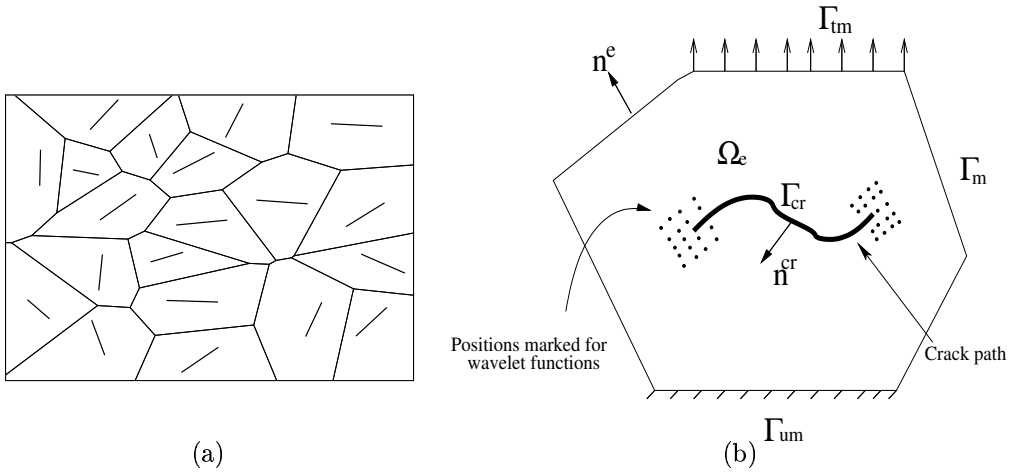

Figure 4.1: (a) A mesh of Voronoi cell elements, each containing a single pre-existing crack, (b) a typical Voronoi cell element showing different topological features and loads.

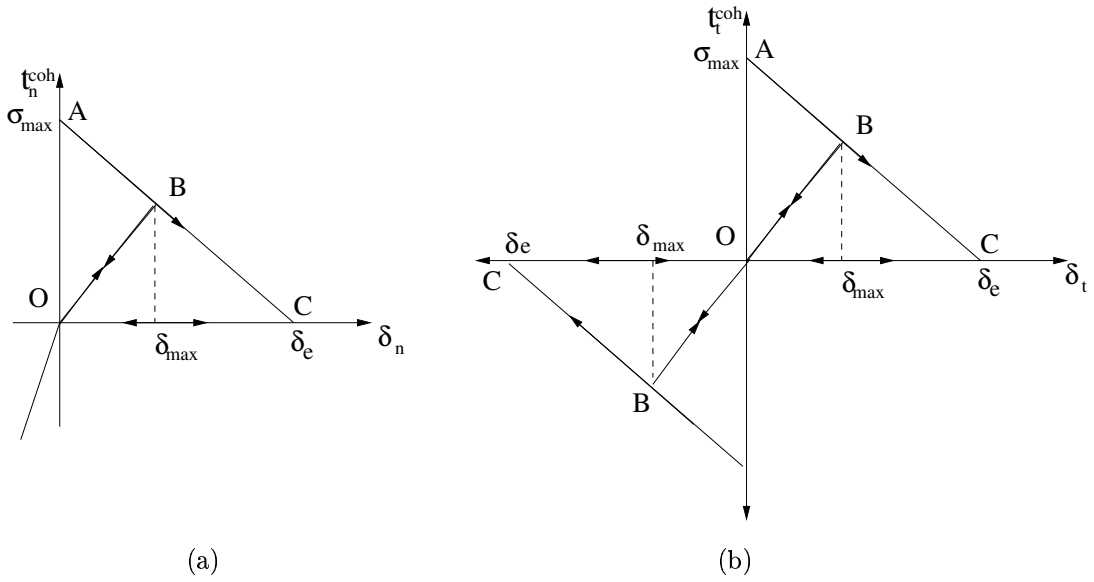

Figure 4.2: Normal and tangential traction-separation behavior for the linear cohesive zone model.

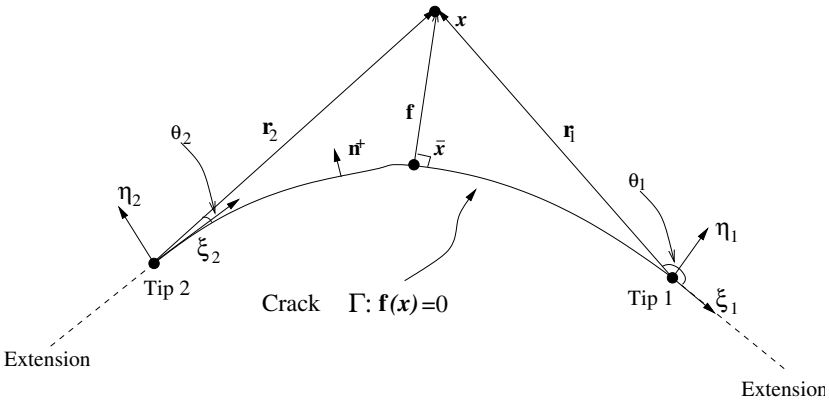

(a)

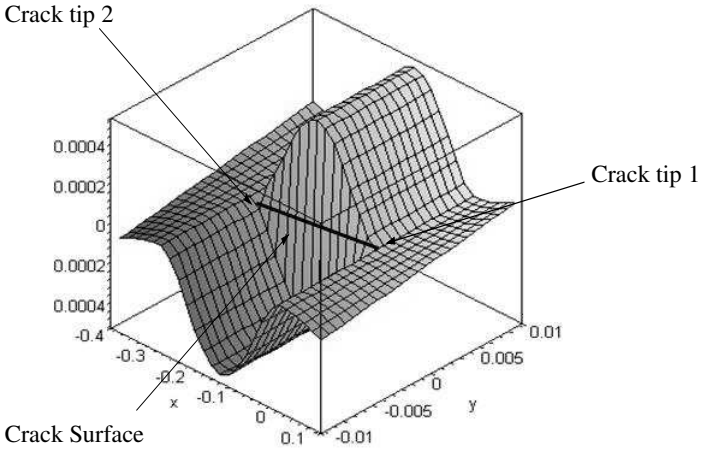

(b)

Figure 4.3: (a) A schematic diagram of a crack surface showing parameters related to the distance functions; (b) depiction of the branched stress function Φ^{branch} near a crack for $s = 0,\ t = 0$.

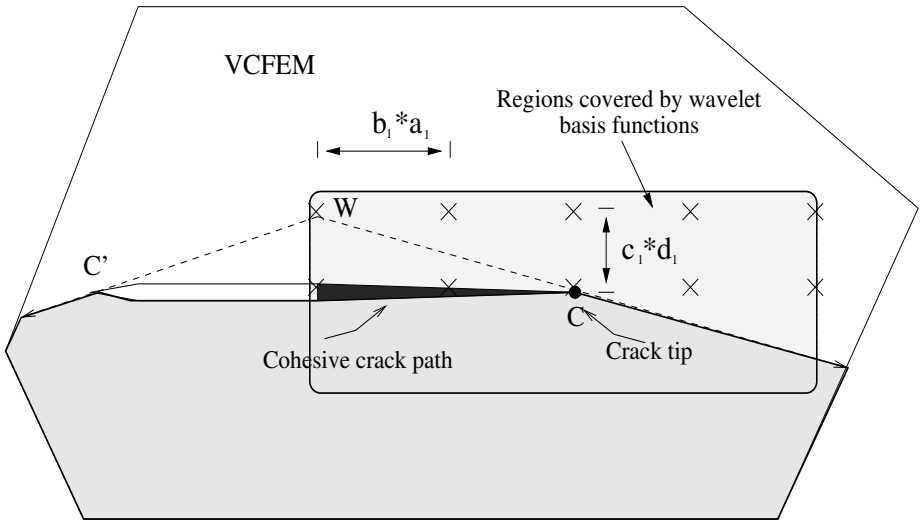

(a)

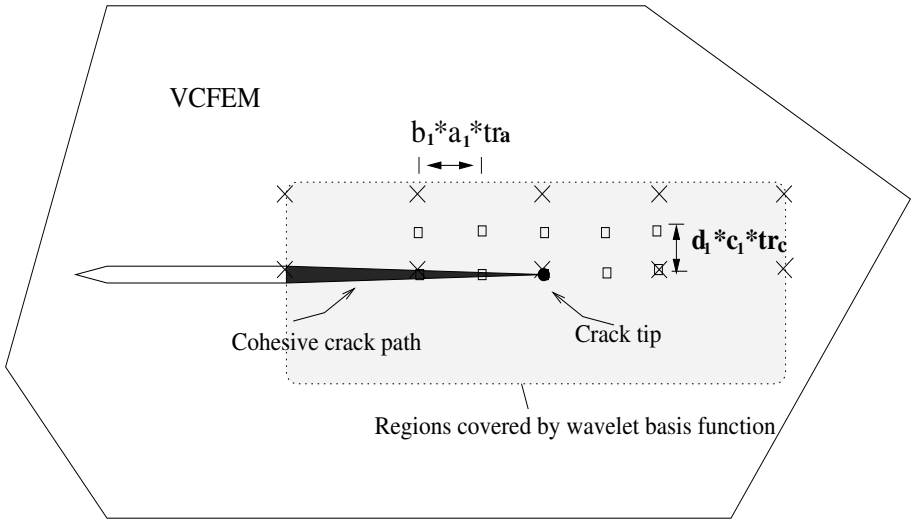

(b)

Figure 4.4: Distribution of multi-resolution wavelet bases around a crack tip: (a) Crosses (×) refer to the location of the origin of the basis vectors at a lower level corresponding to dilation parameters (tr_a and tr_c) and (b) adaptively upgraded to higher level wavelet bases with the addition of the next level of bases at locations indicated by the (□).

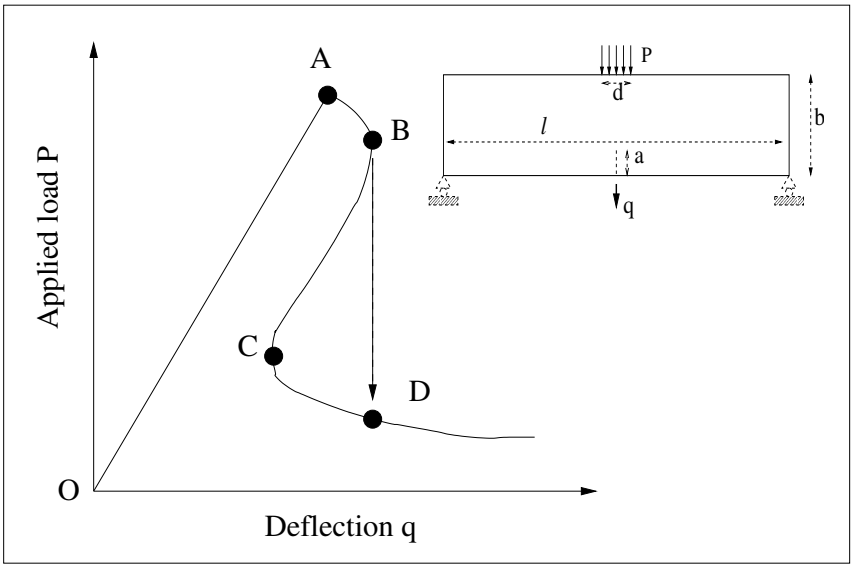

Figure 4.5: Load-deflection behavior in a 3-point bend test with a crack, showing the softening snap back phenomenon.

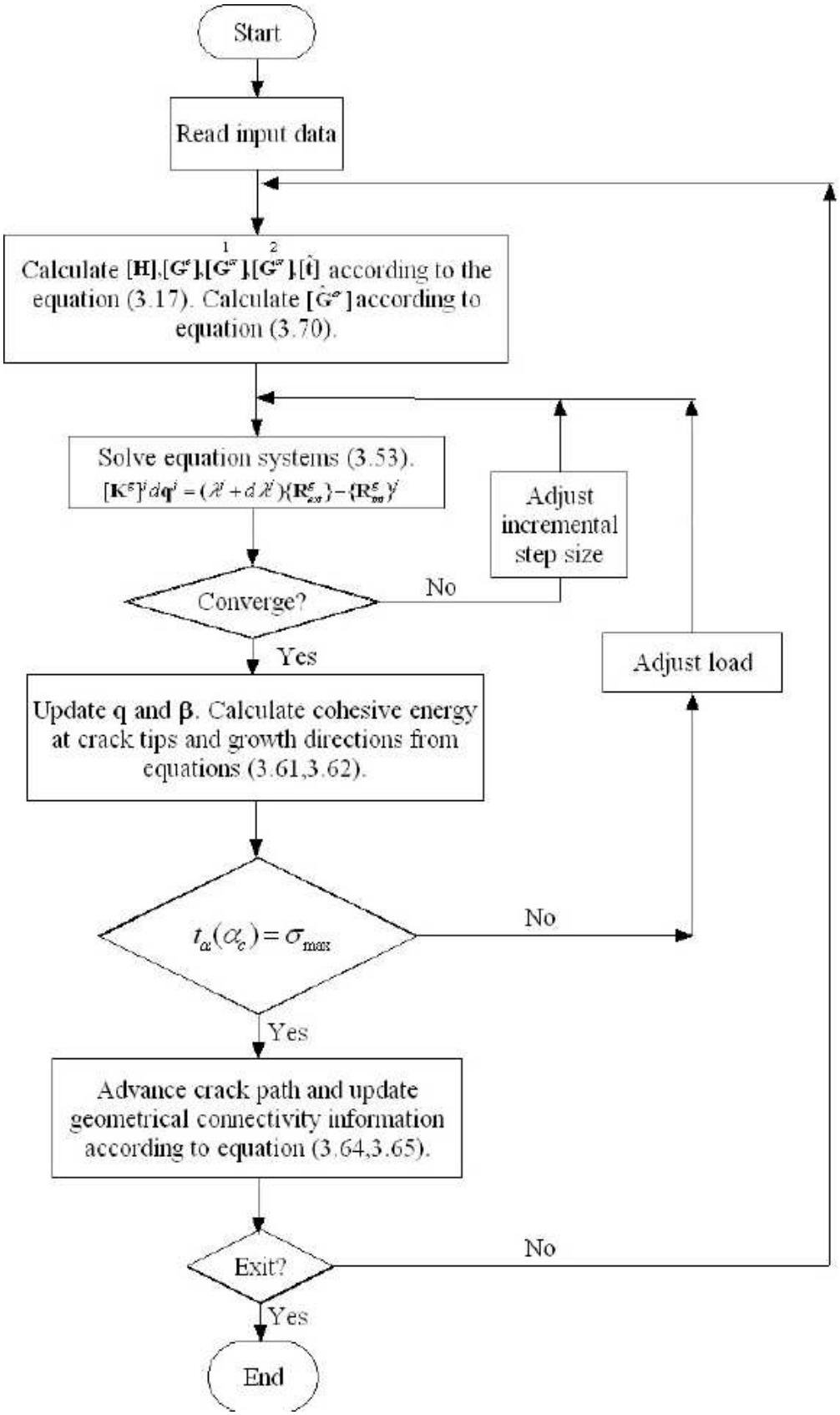

Figure 4.6: A flowchart of the solution method.

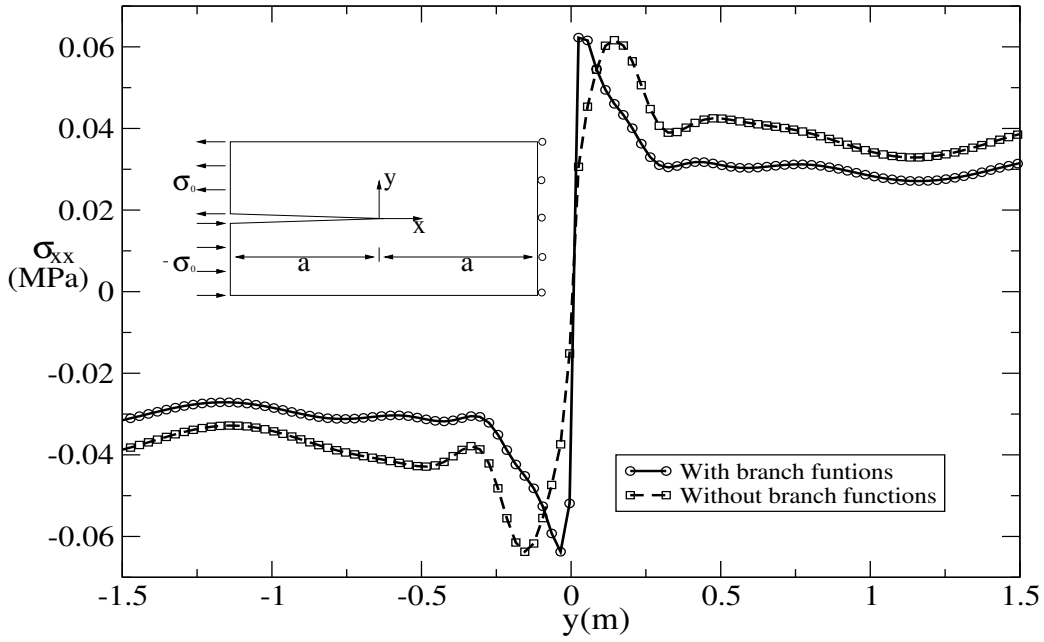

Figure 4.7: The stress σ_{xx} at $x = -0.3$ for a double cantilever beam to demonstrate the effect of the branched stress function.

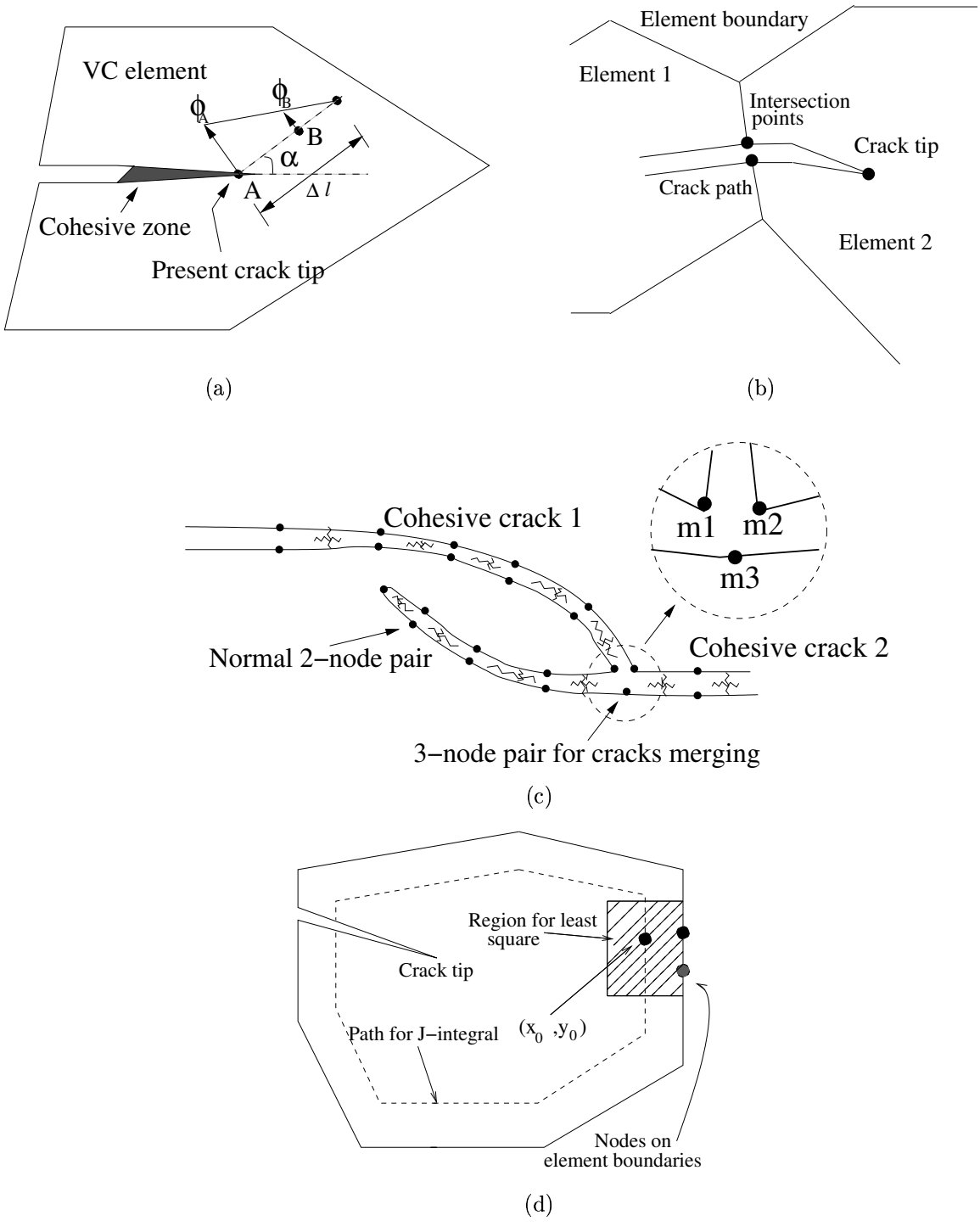

Figure 4.8: Algorithms for incremental propagation of cohesive cracks: (a) for direction and incremental length, (b) a cohesive crack going through the inter-element boundary, (c) for merger with other cracks and (d) for evaluation of $J-$ integral.

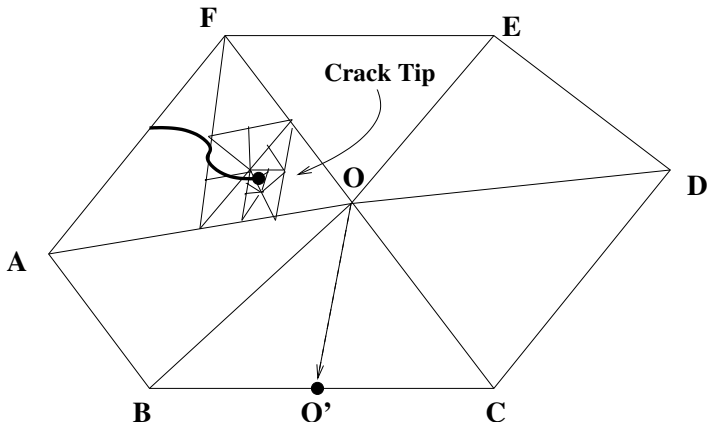

Figure 4.9: Subdivision of the Voronoi cell element for Gaussian quadrature, with a higher density of integration points near the crack tip.

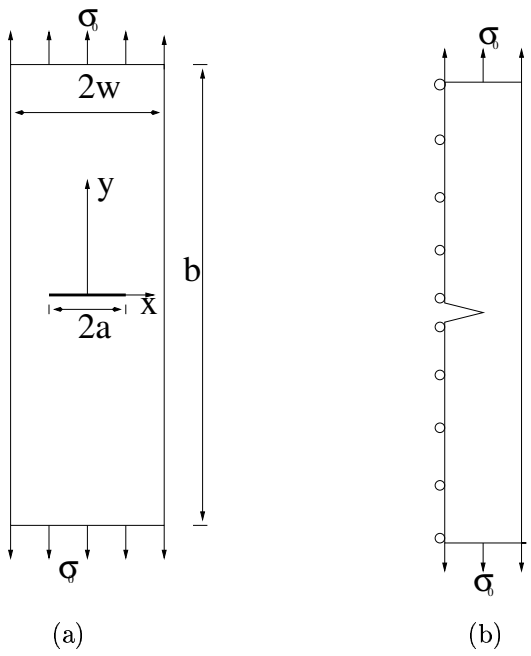

(a) (b)

Figure 4.10: (a) A center cracked plate loaded in tension, (b) a single X-VCFEM element with prescribed boundary conditions

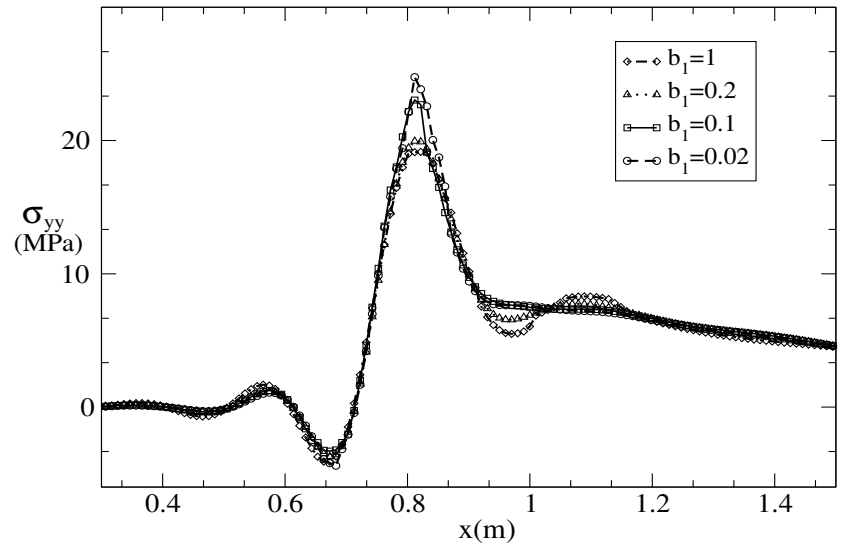

(a)

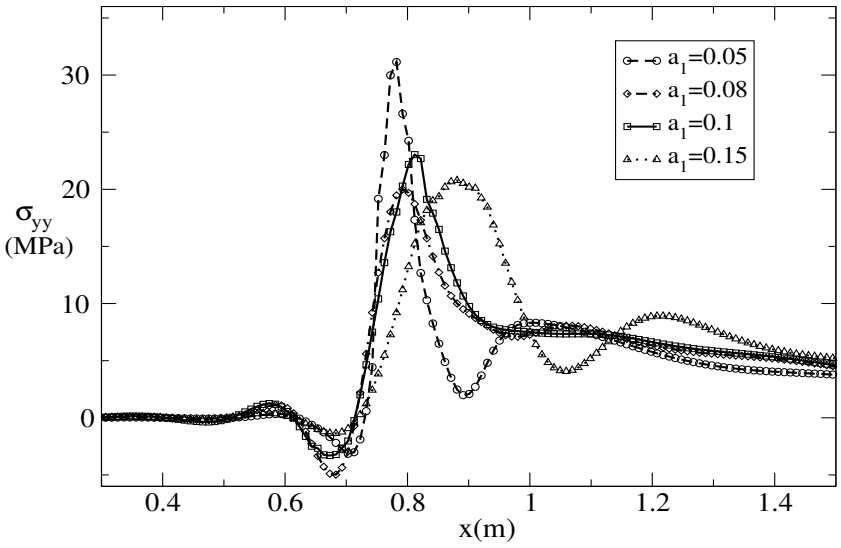

(b)

Figure 4.11: X-VCFEM generated stress σ_{yy} at $y = 0$ for the cracked plate, to examine the effect of parameters in the wavelet basis: (a) dilation parameters and (b) translation parameters.

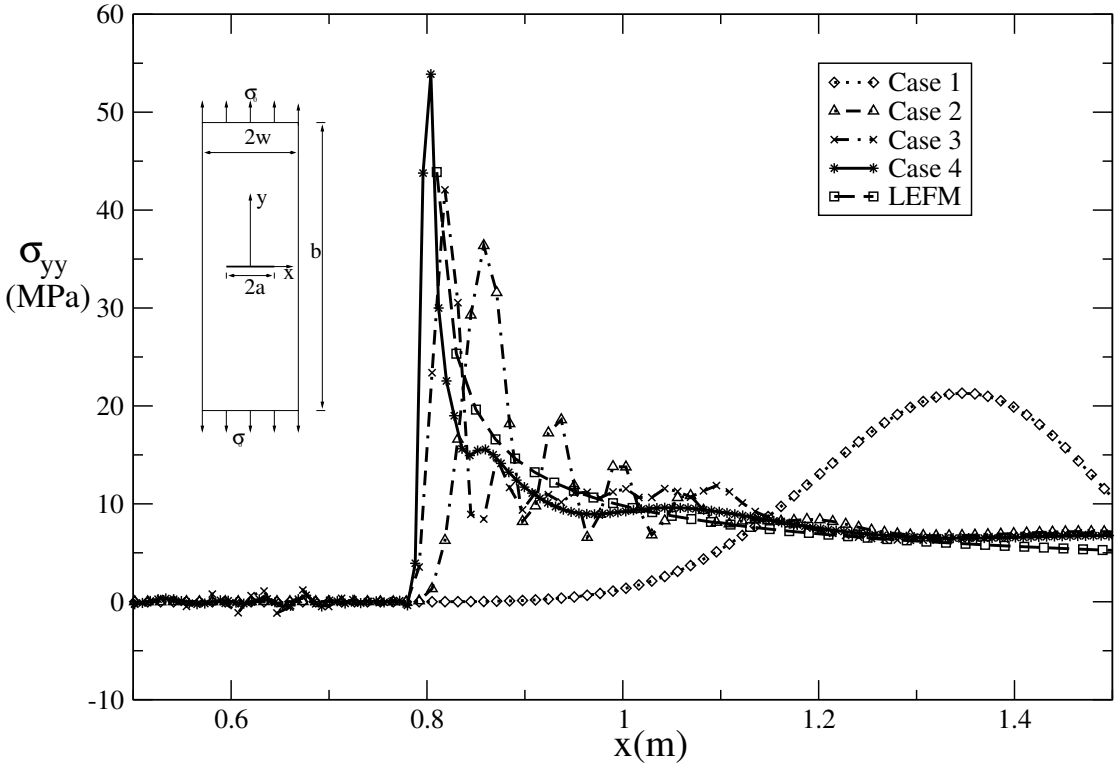

Figure 4.12: X-VCFEM generated stress σ_{yy} at $y = 0$ for different enrichment orders of the wavelet basis functions.

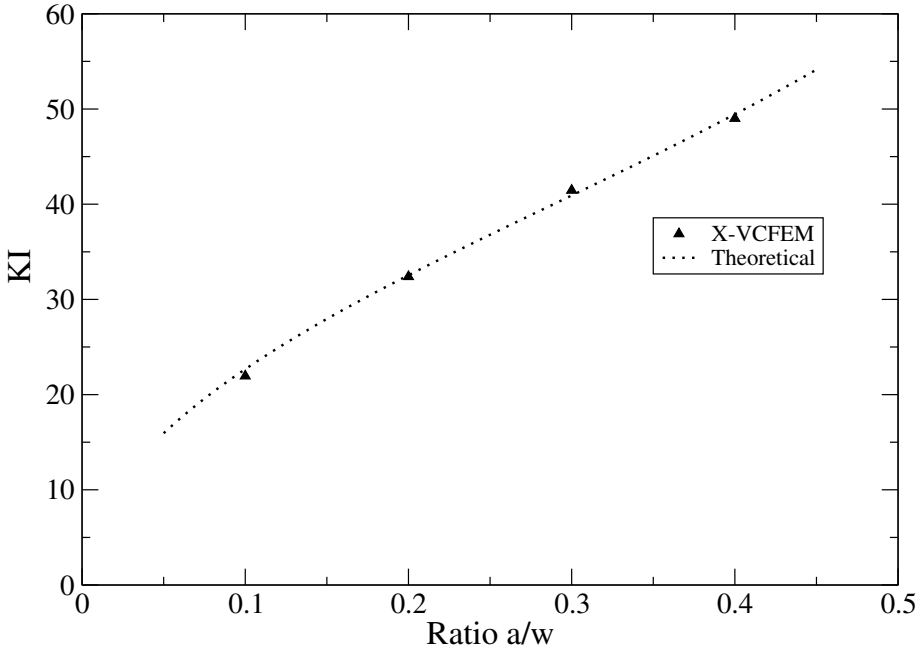

Figure 4.13: Stress intensity factors for various values of **a/w**.

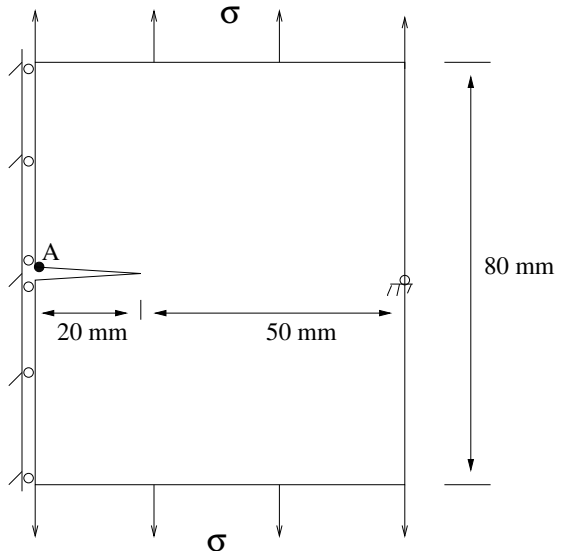

(a)

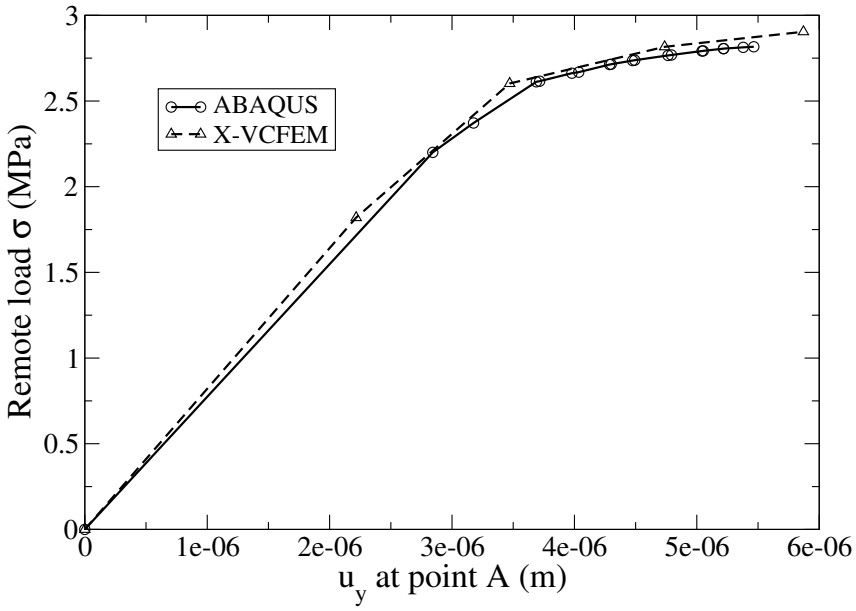

(b)

Figure 4.14: (a) A plate with an edge crack under remote tension load, (b) comparison of load-deformation curves by X-VCFEM and ABAQUS.

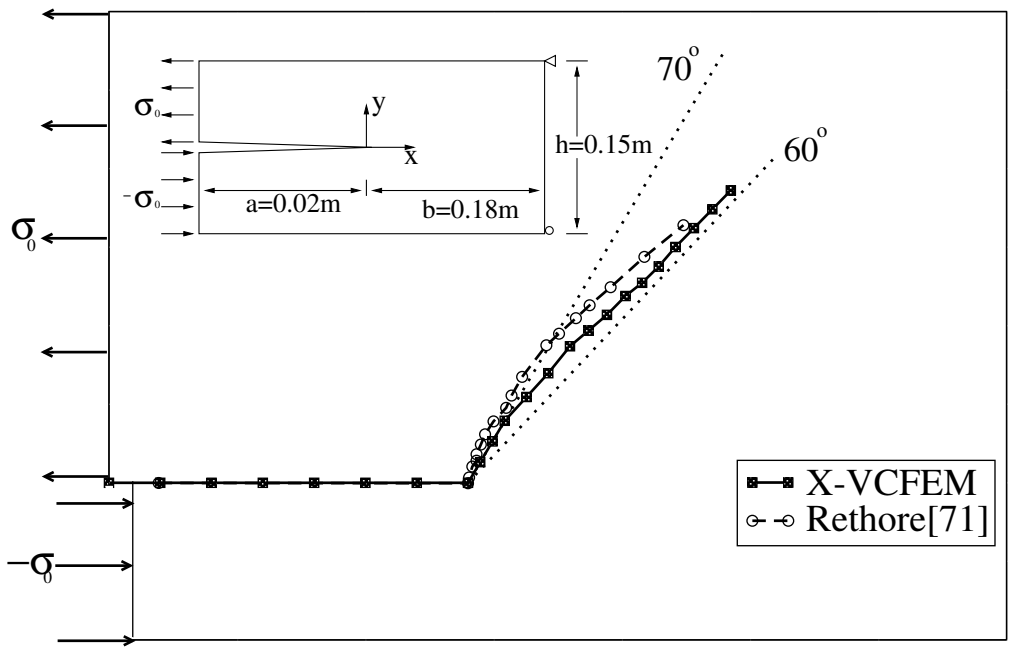

(a)

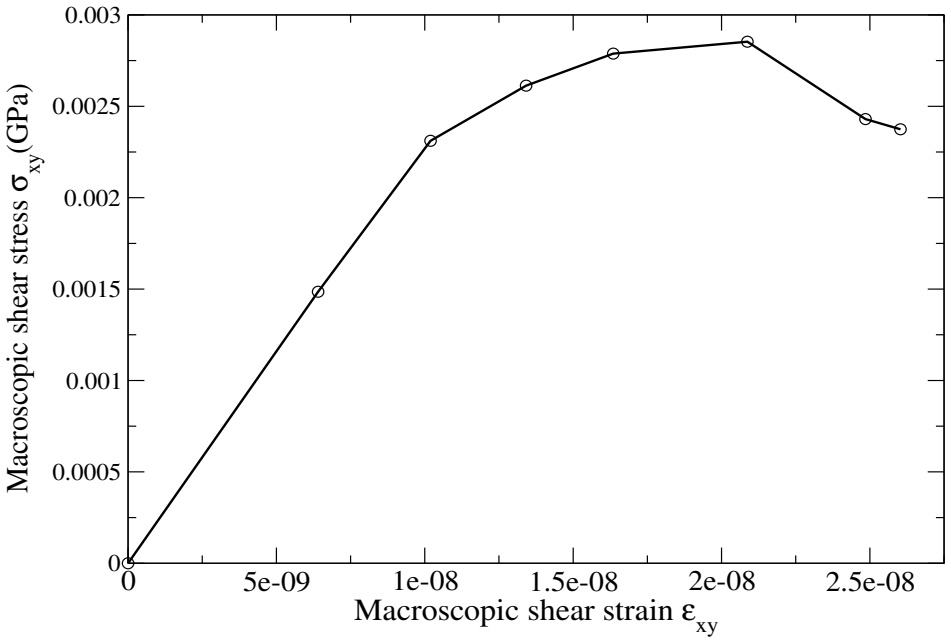

(b)

Figure 4.15: (a) Prediction of the crack path by X-VCFEM for the Kalthoff experiment, (b) the macroscopic stress-strain response.

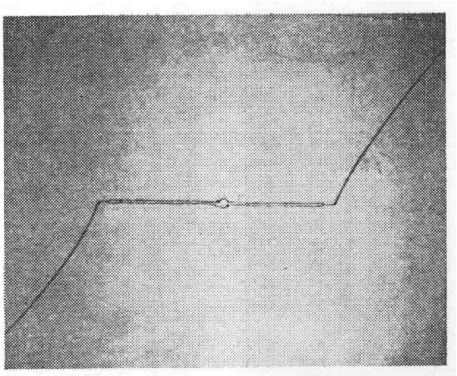

(a)

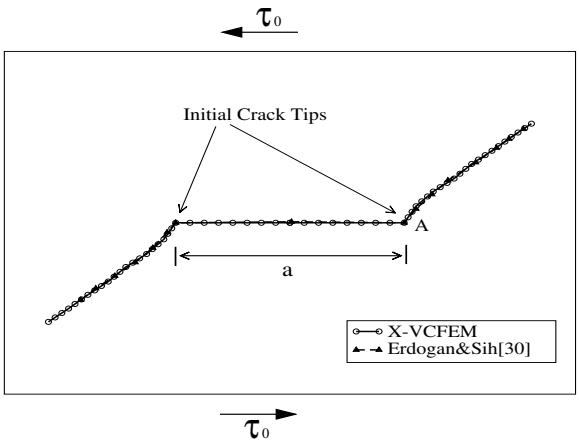

(b)

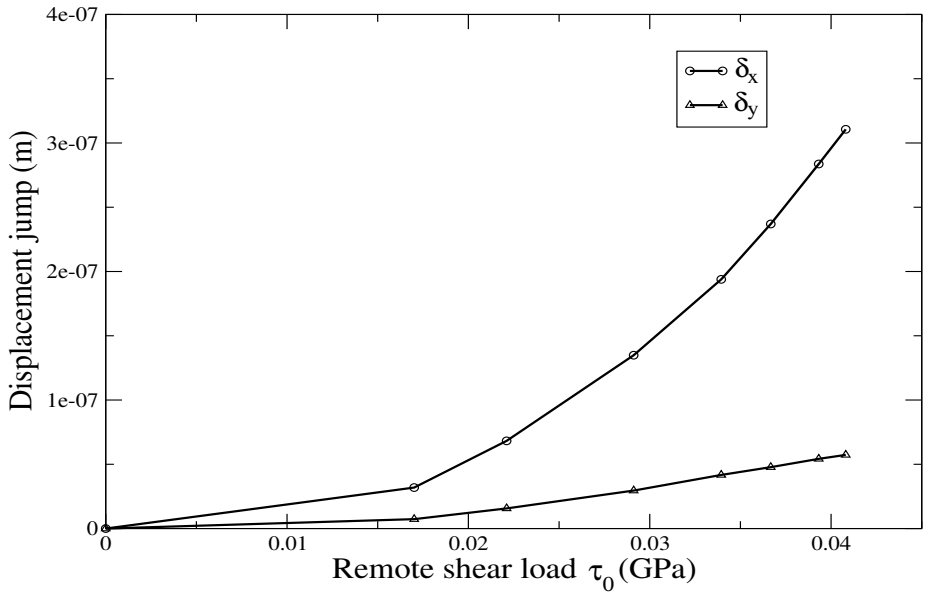

(c)

Figure 4.16: (a) Optical micrograph showing the path of cracking in a plate with a central crack subjected to far-field shear [28], (b) corresponding crack crack path generated by X-VCFEM, (c) crack opening displacement at the tip A.

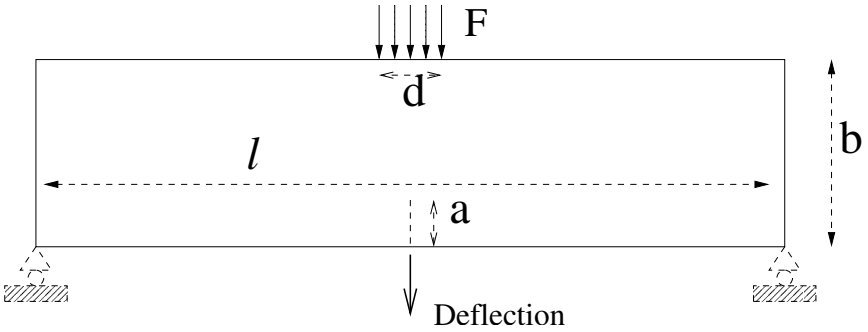

Figure 4.17: A three-point symmetric bending specimen.

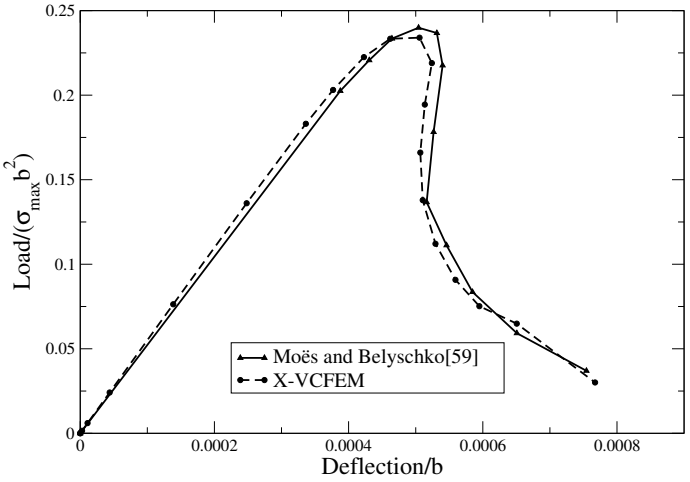

(a)

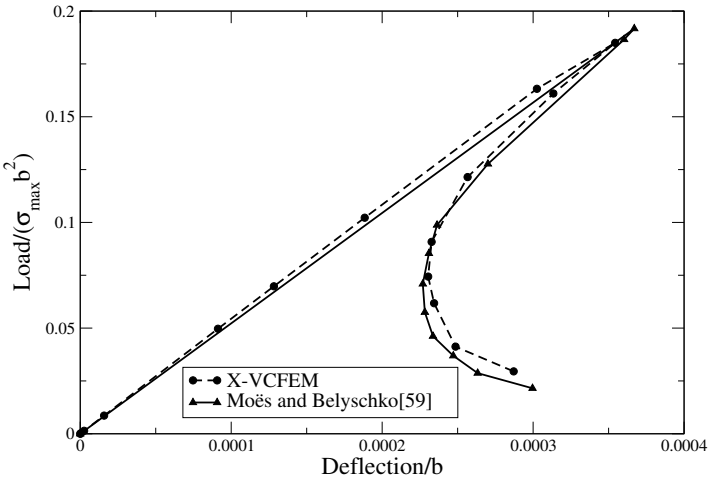

(b)

Figure 4.18: Comparison of normalized load-deflection curves for the three-point bending beam: (a) $\delta_e = 3.134796 \times 10^{-5}\ m$ and (b) $\delta_e = 6.26959 \times 10^{-6}\ m$.

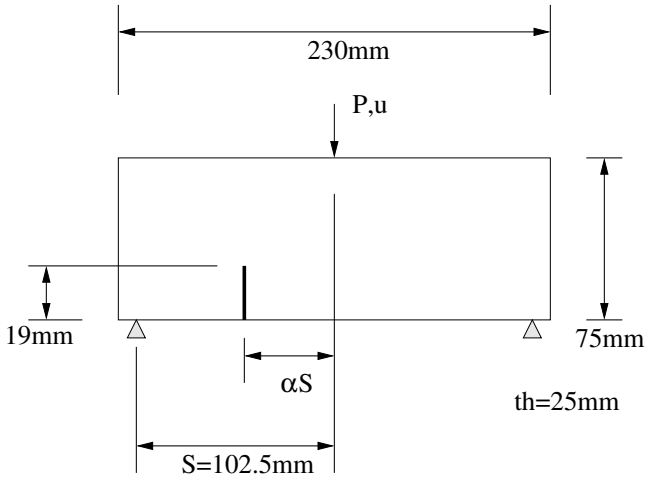

(a)

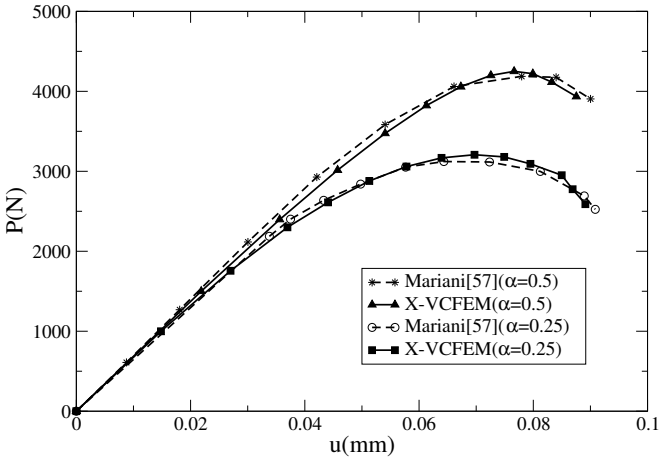

(b)

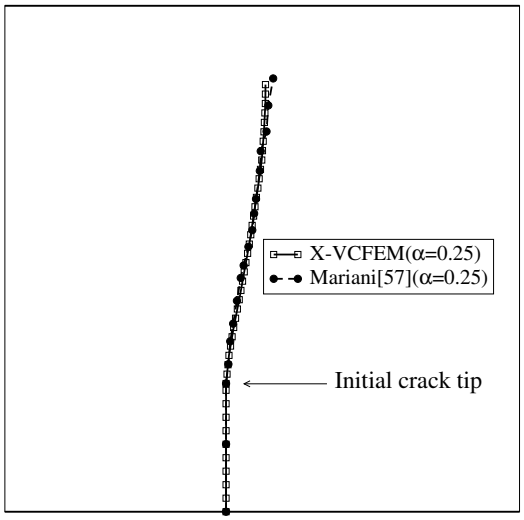

(c)

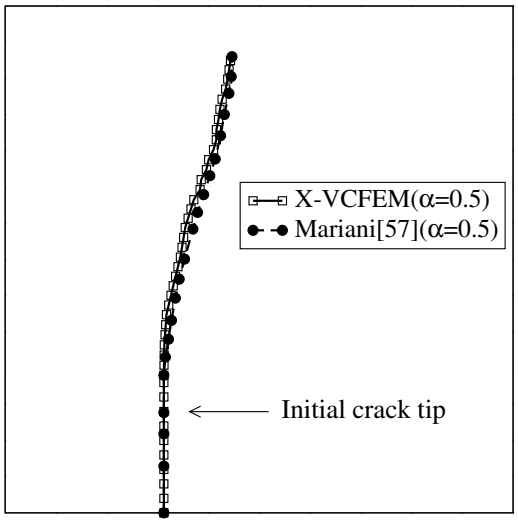

(d)

Figure 4.19: (a) A three-point bending specimen with an unsymmetric initial crack, (b) comparison of load-deflection curves from X-VCFEM and literature [56] , (c) and (d) comparison of the crack paths by X-VCFEM with that in [56] for $\alpha = 0.25$ and $\alpha = 0.5$, respectively.

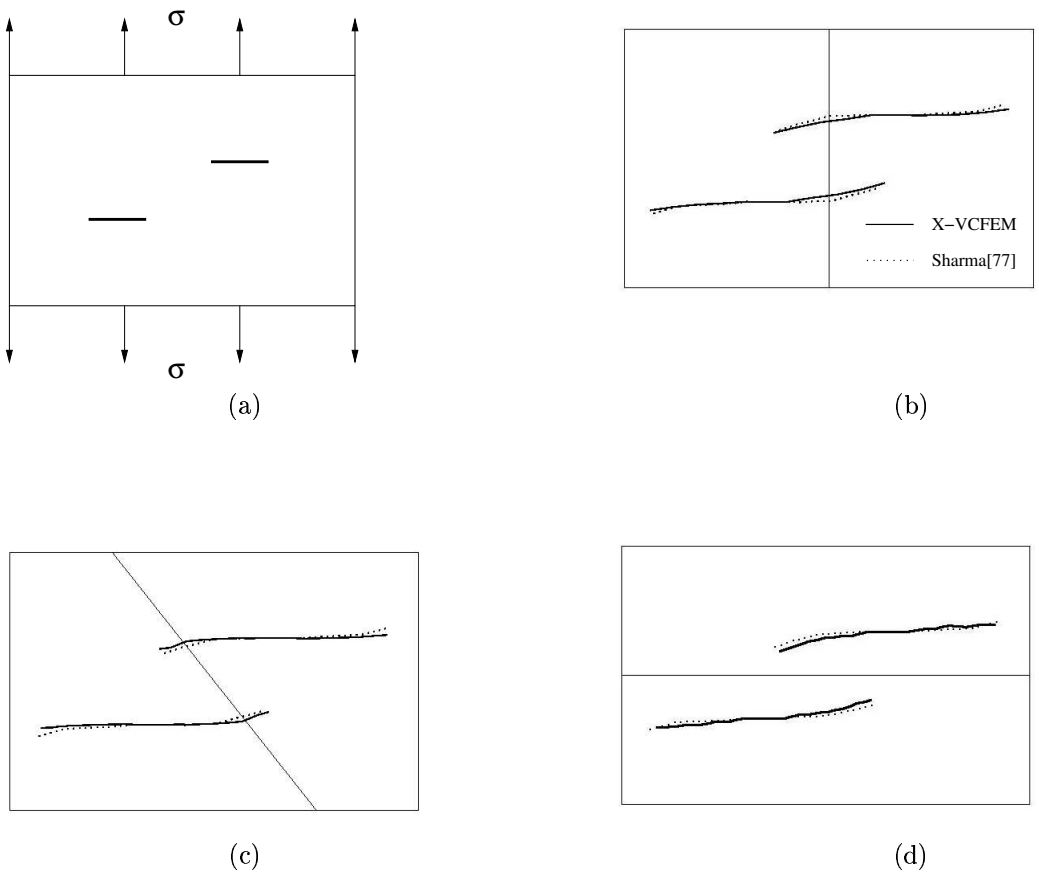

Figure 4.20: A plate with two cracks in arbitrary locations modeled by X-VCFEM using elements of different topologies located cracks, (b,c and d) show crack path at the end of the loading for the different elements and also a comparison with [87].

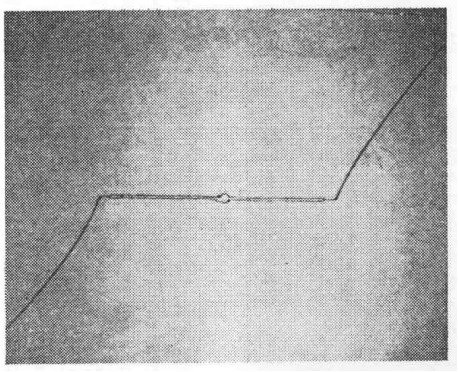

(a)

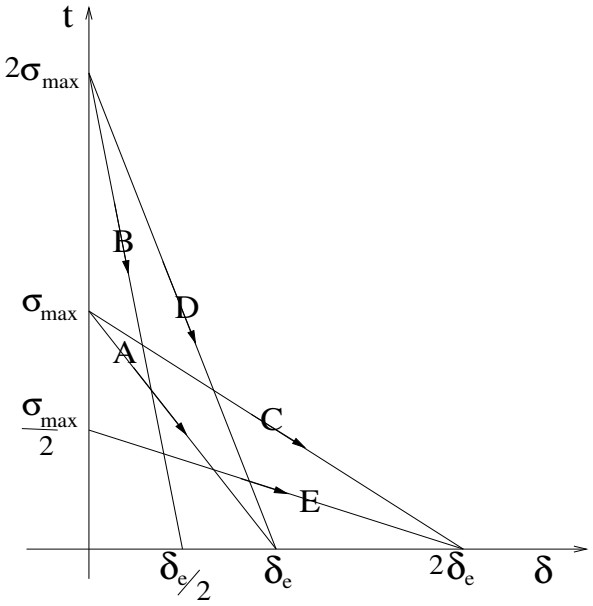

(b)

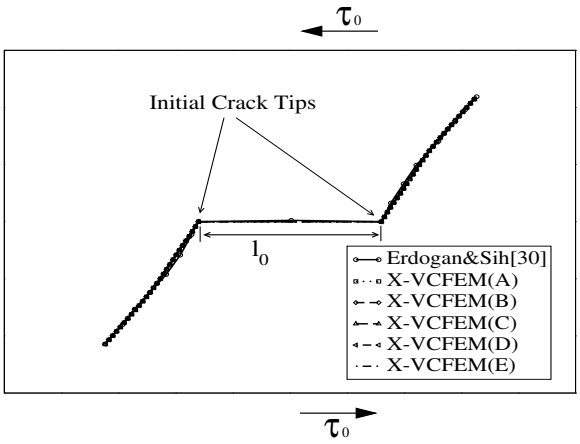

(c)

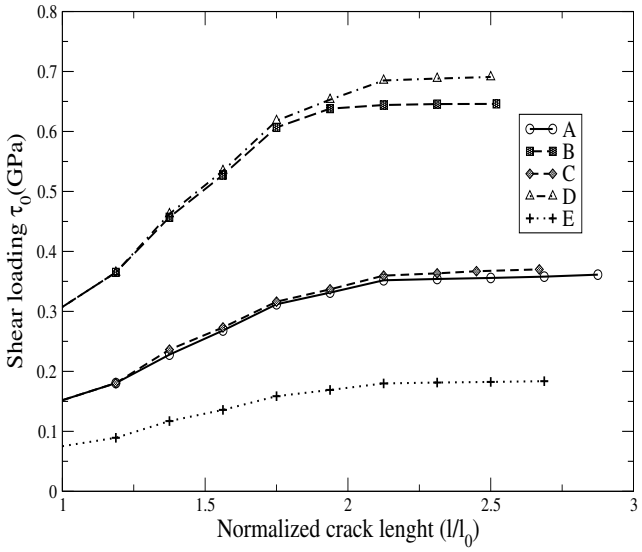

(d)

Figure 4.21: (a) Optical micrograph showing the path of cracking in a plate with a central crack subjected to far-field shear [28], (b) 5 different sets of cohesive parameters for X-VCFEM simulations, (c) corresponding crack path generated by X-VCFEM, (d) comparison of the growth of cracks for different cases.

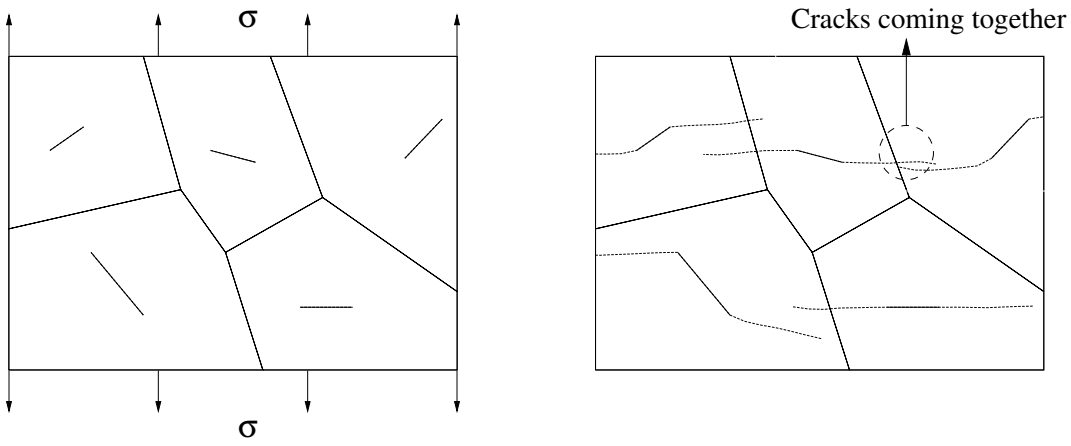

Figure 4.22: (a) X-VCFEM mesh for a plate with five randomly located cracks, (b) crack paths at the end of loading

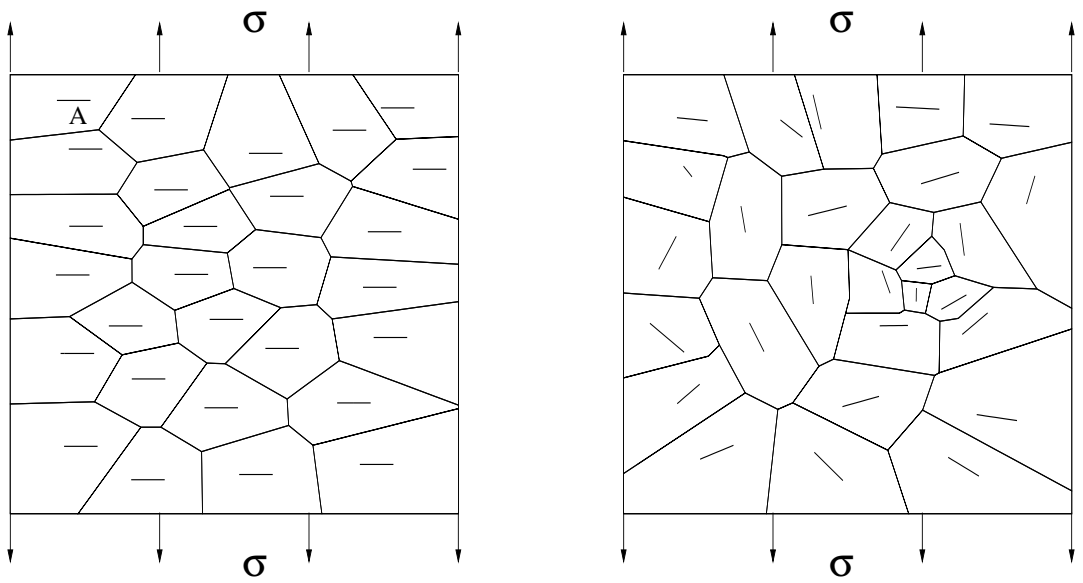

(a) (b)

Figure 4.23: Crack propagation in two square regions containing 28 cracks by X-VCFEM: (a) domain with horizontal cracks of equal length and random distribution, (b) domain with random orientation, length and distribution of cracks but containing a cluster.

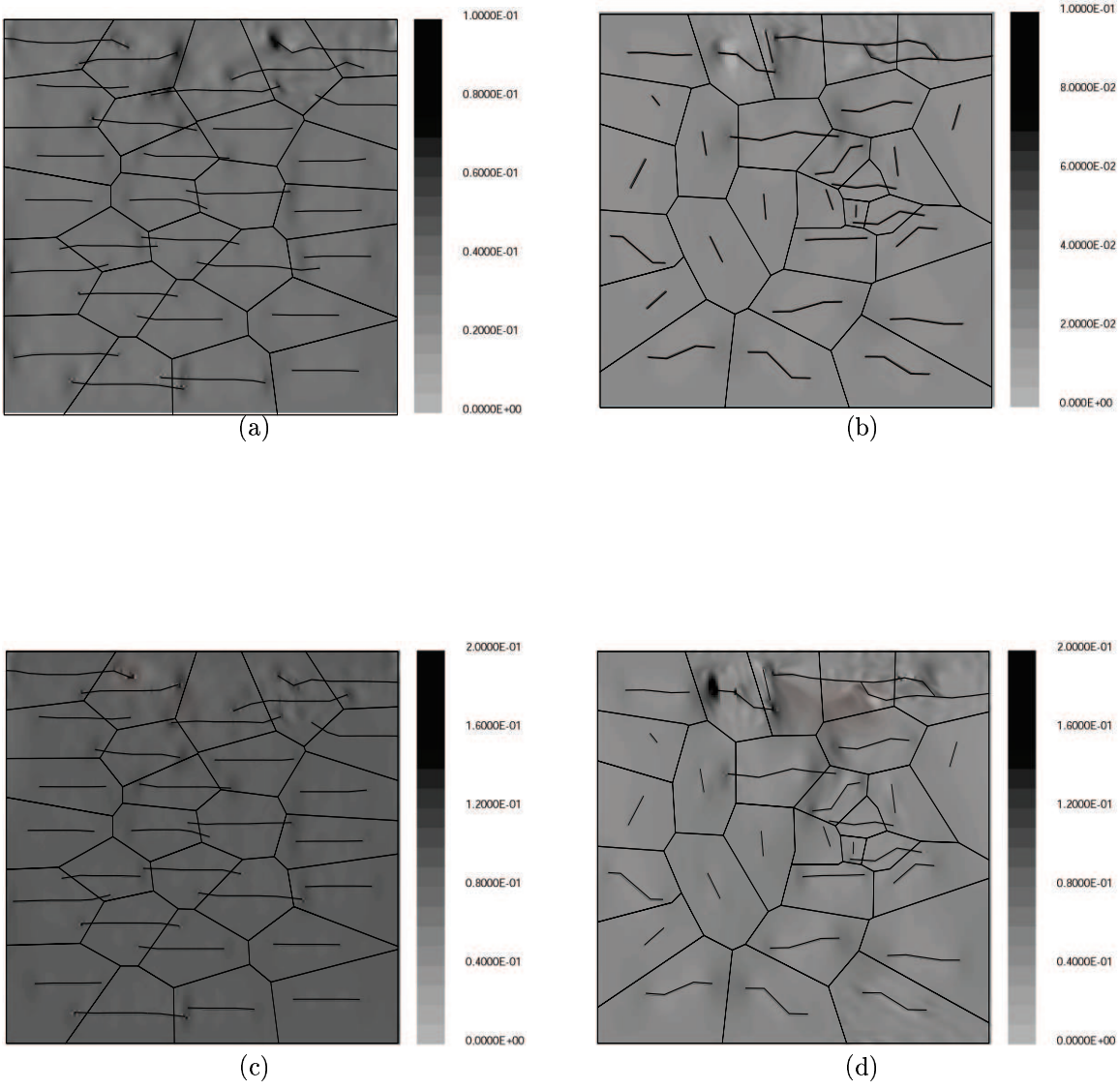

Figure 4.24: Crack propagation in two square regions containing 28 cracks by X-VCFEM: (a,b) contour plots of σ_{yy} (MPa) with cohesive parameters *CP-1* for the domains in figure 23 (a) and (b), (c,d) contour plots of σ_{yy} (MPa) with cohesive parameters *CP-2* for the domains in figure 23 (a) and (b)
.

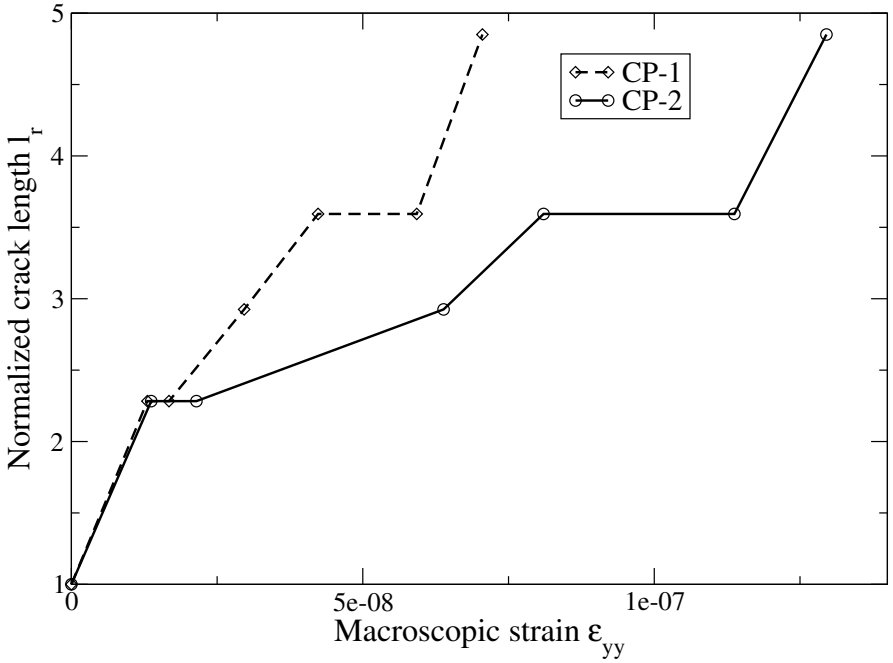

Figure 4.25: Comparison of the growth of crack **A** in *microstructure 1* with different cohesive parameters.

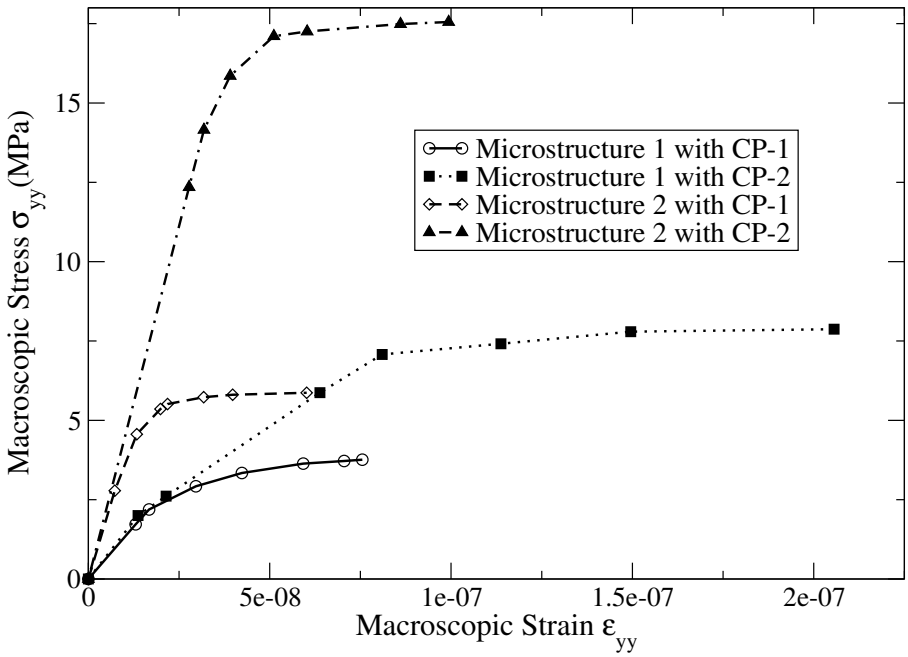

Figure 4.26: Macroscopic stress-strain response for different microstructural morphologies and cohesive parameters.

Chapter 5

Extended Voronoi Cell Finite Element for Modeling Interfacial Debonding with Matrix Cohesive Cracking in Fiber Reinforced Composites

5.1 Introduction

Interfacial debonding and cohesive cracks propagation in brittle matrix are two important damage phenomena in fiber-matrix composites. Experiments show that the two damage phenomena appear in the same material, where the failure often starts from the interface between fiber and matrix, and is subsequently advanced into matrix. Researches regarding a crack meeting a bimaterial interface to either deflect along the interface or penetrate into the next layer were made in [2, 41, 42, 55], where the criterion of deflection versus penetration was established based on the energy release rate and fracture energy. However, the present research is aimed at only elastic cases, which requires that the fracture process zone at the crack tip is small compared to

the size of the crack and the size of the specimen. In chapter 4, cohesive zone models are introduced into VCFEM to study damage of interface and matrix, where the stress field in composites are described by a set of specifical functions accurately. And the effect of cohesive parameters and morphological distributions are studied as important factors to the damage process. All work in the two chapters are theoretical and computational preparation for solving interfacial debonding problems coupled with matrix cracking.

In this chapter, a criterion based on cohesive zone models is proposed for assessing the direction of damage development. The improved X-VCFEM is developed for modeling both the growth of interfacial debonding and the propagation of multiple cohesive cracks in the brittle matrix of fiber-reinforced composites. The mechanics theories and numerical algorithm in previous chapters are organized as an organic whole, not just a simple superposition. It begins with the X-VCFEM formulation and numerical implementation, followed by the numerical example showing the effectiveness of this model and the interaction of interface and crack propagation.

5.2 Extended Voronoi cell FEM formulation for composites with interfacial debonding and matrix cracking

The Voronoi cell finite element mesh for a microstructure with both debonded interfaces and cohesive cracks is shown in figure 5.1(a), where the region is divided into an unstructured finite element mesh of arbitrary Voronoi cells. A typical Voronoi cell element Ω_e is shown in figure 5.1 (b). Each VC element is composed of the matrix phase (Ω_m), the inclusion phase(Ω_c), the interface (Ω_{in}), and cracks (Ω_{cr}), such that $\Omega_e = \Omega_m \bigcup \Omega_c \bigcup \Omega_{in} \bigcup \Omega_{cr}$, where interface and cracks are consider as zero thickness regions. The element outer boundary consists of the prescribed displacement boundary (Γ_{um}), prescribed traction boundary (Γ_{tm}) and the inter-element boundary (Γ_m), so i.e. $\partial\Omega_e = \Gamma_{um} \bigcup \Gamma_{tm} \bigcup \Gamma_m$. Compatible displacement conditions apply on $\partial\Omega_e$. $\partial\Omega_c^c$ has an outward normal $\mathbf{n}^c$ ($=\mathbf{n}^m$), while $\mathbf{n}^e$ is the outward normal to $\partial\Omega_e$. In order to describe debonding with progressing deformation through decohesion, the interface is lined with a set of node-pairs with nodes belonging to the matrix interface ($\partial\Omega_c^m$) and inclusion interface ($\partial\Omega_c^c$) respectively. The traction $\mathbf{t}^{coh}$ between node-pairs on the crack surface are modeled by the cohesive zone traction-separation law. The

behaviors of cohesive cracks in the brittle matrix are described by a similar method, where nodes in node-pairs are arranged at different sides of a crack ($\overset{1}{\Gamma}_{cr}$ and $\overset{2}{\Gamma}_{cr}$). In the incremental assumed stress hybrid X-VCFEM formulation, the complementary energy functional for each element is expressed in terms of increments of stress and displacement fields as:

$$
\begin{aligned}
\Pi_e(\boldsymbol{\sigma}, \Delta\boldsymbol{\sigma}, \mathbf{u}, \Delta\mathbf{u}) \;=\; & -\int_{\Omega_m} \Delta B(\boldsymbol{\sigma}^m, \Delta\boldsymbol{\sigma}^m) d\Omega - \int_{\Omega_c} \Delta B(\sigma^c, \Delta\sigma^c) d\Omega \\
& - \int_{\Omega_m} \boldsymbol{\epsilon}^m : \Delta\boldsymbol{\sigma}^m d\Omega - \int_{\Omega_c} \boldsymbol{\epsilon}^c : \Delta\boldsymbol{\sigma}^c d\Omega \\
& + \int_{\partial\Omega_e} (\boldsymbol{\sigma}^m + \Delta\boldsymbol{\sigma}^m) \cdot \mathbf{n}^e \cdot (\mathbf{u}^e + \Delta\mathbf{u}^e) d\partial\Omega \\
& - \int_{\Gamma_{tm}} (\bar{\mathbf{t}} + \Delta\bar{\mathbf{t}}) \cdot (\mathbf{u}^m + \Delta\mathbf{u}^m) d\Gamma \\
& - \int_{\partial\Omega_c^m} (\boldsymbol{\sigma}^m + \Delta\boldsymbol{\sigma}^m) \cdot \mathbf{n}^c \cdot (\mathbf{u}^m + \Delta\mathbf{u}^m) d\partial\Omega \\
& + \int_{\partial\Omega_c^c} (\boldsymbol{\sigma}^c + \Delta\boldsymbol{\sigma}^c) \cdot \mathbf{n}^c \cdot (\mathbf{u}^c + \Delta\mathbf{u}^c) d\partial\Omega \\
& + \int_{\overset{1}{\Gamma}_{cr}} (\boldsymbol{\sigma}^m + \Delta\boldsymbol{\sigma}^m) \cdot \mathbf{n}^{cr} \cdot (\overset{1}{\mathbf{u}}^{cr} + \Delta\overset{1}{\mathbf{u}}^{cr}) d\Gamma_{cr} \\
& - \int_{\overset{2}{\Gamma}_{cr}} (\boldsymbol{\sigma}^m + \Delta\boldsymbol{\sigma}^m) \cdot \mathbf{n}^{cr} \cdot (\overset{2}{\mathbf{u}}^{cr} + \Delta\overset{2}{\mathbf{u}}^{cr}) d\Gamma_{cr} \\
& - \boxed{\int_{\partial\Omega_c^m / \partial\Omega_c^c} \int_{(\mathbf{u}^m - \mathbf{u}^c)}^{(\mathbf{u}^m + \Delta\mathbf{u}^m - \mathbf{u}^c - \Delta\mathbf{u}^c)} \mathbf{T}^m \cdot d(\mathbf{u}^m - \mathbf{u}^c) d\partial\Omega} \\
& - \int_{\Gamma_{cr}} \int_{\overset{1}{\mathbf{u}}^{cr} - \overset{2}{\mathbf{u}}^{cr}}^{\overset{1}{\mathbf{u}}^{cr} + \Delta\overset{1}{\mathbf{u}}^{cr} - \overset{2}{\mathbf{u}}^{cr} - \Delta\overset{2}{\mathbf{u}}^{cr}} \mathbf{T}^{cr} \cdot d(\overset{1}{\mathbf{u}}^{cr} - \overset{2}{\mathbf{u}}^{cr}) d\Gamma_{cr}
\end{aligned}
\tag{5.1}
$$

Here B is the complementary energy density and the superscripts m and c correspond to variables associated with the matrix and inclusion phases. $\boldsymbol{\sigma}^m$ and $\boldsymbol{\sigma}^c$ are the equilibrated stress fields, $\boldsymbol{\epsilon}^m$ and $\boldsymbol{\epsilon}^c$ the corresponding strain fields in different phases of each Voronoi element. Also, $\mathbf{u}^e$, $\mathbf{u}^m$, $\mathbf{u}^c$, $\overset{1}{\mathbf{u}}^{cr}$ and $\overset{2}{\mathbf{u}}^{cr}$ are the kinematically admissible displacement fields on $\partial\Omega_e$, $\partial\Omega_c^m$, $\partial\Omega_c^c$, $\overset{1}{\Gamma}_{cr}$ and $\overset{2}{\Gamma}_{cr}$ respectively. The prefix Δ corresponds to increments. The term in the box in equation (5.1) provide the work done by the interfacial tractions $\mathbf{T}^m = T_n^m \mathbf{n}^m + T_t^m \mathbf{t}^m$ due to interfacial separation $(\mathbf{u}^m - \mathbf{u}^c)$, where T_n^m and T_t^m are the normal and tangential components that are described by cohesive laws at the interface. Similarly, the last term provide the work done by the cohesive tractions $\mathbf{T}^{cr} = T_n^{cr} \mathbf{n}^{cr} + T_t^{cr} \mathbf{t}^{cr}$ due to displacement separation $(\overset{1}{\mathbf{u}}^{cr} - \overset{2}{\mathbf{u}}^{cr})$ along the crack, where T_n^{cr} and T_t^{cr} are the normal and tangential components of the cohesive

force. The total energy for the entire composite domain is obtained by adding the energy functionals for N elements as

$$\Pi = \sum_{e=1}^{N} \Pi_e \tag{5.2}$$

5.2.1 General element assumptions and weak form

In the absence of body forces, two dimensional stress fields satisfying equilibrium relations can be generated from the Airy's stress function $\Phi(x,y)$. In the incremental formulation, stress increments in matrix and inclusion are obtained from derivatives of the stress functions $\Delta\Phi^m(x,y)$ and $\Delta\Phi^c(x,y)$ as:

$$\begin{aligned}
\begin{pmatrix} \Delta\sigma^m_{xx} \\ \Delta\sigma^m_{yy} \\ \Delta\sigma^m_{xy} \end{pmatrix} &= \begin{pmatrix} \frac{\partial^2 \Delta\Phi^m}{\partial y^2} \\ \frac{\partial^2 \Delta\Phi^m}{\partial x^2} \\ -\frac{\partial^2 \Delta\Phi^m}{\partial x \partial y} \end{pmatrix} = [\mathbf{P}^m(x,y)]\{\Delta\beta^m\}, \\
\begin{pmatrix} \Delta\sigma^c_{xx} \\ \Delta\sigma^c_{yy} \\ \Delta\sigma^c_{xy} \end{pmatrix} &= \begin{pmatrix} \frac{\partial^2 \Delta\Phi^c}{\partial y^2} \\ \frac{\partial^2 \Delta\Phi^c}{\partial x^2} \\ -\frac{\partial^2 \Delta\Phi^c}{\partial x \partial y} \end{pmatrix} = [\mathbf{P}^c(x,y)]\{\Delta\beta^c\}
\end{aligned} \tag{5.3}$$

where $\{\Delta\beta^m\}$ and $\{\Delta\beta^c\}$ are the column of unknown stress increment coefficients. Convergence properties and efficiency of X-VCFEM depend on the choice of Φ^m. These functions should adequately account for the geometry and location of the heterogeneity in the element, so stress functions for matrix are decomposed into (a) a purely polynomial function $\mathbf{\Phi}^m_{poly}$, (b) a reciprocal function $\mathbf{\Phi}^m_{rec}$, (c) a branch function $\mathbf{\Phi}^m_{branch}$ and (d) wavelet functions $\mathbf{\Phi}^m_{wvlt}$ ($\mathbf{\Phi}^m = \mathbf{\Phi}^m_{poly} + \mathbf{\Phi}^m_{rec} + \mathbf{\Phi}^m_{branch} + \mathbf{\Phi}^m_{wvlt}$). The selection of stress functions are discussed in chapter 4 detailed. Inclusion stress functions are admitted as polynomial function $\mathbf{\Phi}^c_{poly}$ ($\mathbf{\Phi}^c = \mathbf{\Phi}^c_{poly}$). Compatible displacement fields satisfying inter-element continuity on the element boundary $\partial\Omega^E_e$ and intra-element continuity on both the interface $\partial\Omega^m_c/\partial\Omega^c_c$ and the crack face Γ_{cr} are generated by

interpolation of nodal displacements as:

$$
\begin{aligned}
&\{\triangle \mathbf{u}^e\} = [\mathbf{L}^e]\{\triangle \mathbf{q}^e\} \ \text{ on } \partial\Omega_e \\
&\{\triangle \mathbf{u}^m\} = [\mathbf{L}^m]\{\triangle \mathbf{q}^m\} \ \text{ on } \partial\Omega_c^m \\
&\{\triangle \mathbf{u}^c\} = [\mathbf{L}^c]\{\triangle \mathbf{q}^c\} \ \text{ on } \partial\Omega_c^c \\
&\{\triangle \overset{1}{\mathbf{u}}{}^{cr}\} = [\overset{1}{\mathbf{L}}{}^{cr}]\{\triangle \overset{1}{\mathbf{q}}{}^{cr}\} \ \text{ on } \ \overset{1}{\Gamma}_{cr}, \\
&\{\triangle \overset{2}{\mathbf{u}}{}^{cr}\} = [\overset{2}{\mathbf{L}}{}^{cr}]\{\triangle \overset{2}{\mathbf{q}}{}^{cr}\} \ \text{ on } \ \overset{2}{\Gamma}_{cr}
\end{aligned}
\tag{5.4}
$$

The interpolation matrices $[\mathbf{L}^e], [\mathbf{L}^m], [\mathbf{L}^c], [\overset{1}{\mathbf{L}}{}^{cr}], [\overset{2}{\mathbf{L}}{}^{cr}]$ for the nodal displacements on the respective boundaries are constructed using standard linear or hierarchical shape functions. Since nodes on the interface and crack surfaces are always belonging to some node-pair, the interpolation matrices are chosen as $[\mathbf{L}^m] = [\mathbf{L}^c]$ and $[\overset{1}{\mathbf{L}}{}^{cr}] = [\overset{2}{\mathbf{L}}{}^{cr}]$.

Substituting the interpolations of stress and displacement fields from equations (5.3) and (5.4) into equation (5.1) results in the matrix form of the element complimentary energy

$$
\begin{aligned}
\Pi_e \;=\; & -\frac{1}{2}\{\boldsymbol{\beta^m} + \Delta\boldsymbol{\beta^m}\}^T[\mathbf{H}^m]\{\boldsymbol{\beta^m} + \Delta\boldsymbol{\beta^m}\} - \frac{1}{2}\{\boldsymbol{\beta^c} + \Delta\boldsymbol{\beta^c}\}^T[\mathbf{H}^c]\{\boldsymbol{\beta^c} + \Delta\boldsymbol{\beta^c}\} \\
+ \; & \{\boldsymbol{\beta^m} + \Delta\boldsymbol{\beta^m}\}^T[\mathbf{G}]^e\{\mathbf{q}^e + \Delta\mathbf{q}^e\} - \{\boldsymbol{\beta^m} + \Delta\boldsymbol{\beta^m}\}^T[\mathbf{G}]^m\{\mathbf{q}^m + \Delta\mathbf{q}^m\} \\
+ \; & \{\boldsymbol{\beta^c} + \Delta\boldsymbol{\beta^c}\}^T[\mathbf{G}]^c\{\mathbf{q}^c + \Delta\mathbf{q}^c\} + \{\boldsymbol{\beta^m} + \Delta\boldsymbol{\beta^m}\}^T[\overset{1}{\mathbf{G}}{}^{cr}]\{\overset{1}{\mathbf{q}}{}^{cr} + \Delta\overset{1}{\mathbf{q}}{}^{cr}\} \\
- \; & \{\boldsymbol{\beta^m} + \Delta\boldsymbol{\beta^m}\}^T[\overset{2}{\mathbf{G}}{}^{cr}]\{\overset{2}{\mathbf{q}}{}^{cr} + \Delta\overset{2}{\mathbf{q}}{}^{cr}\} - \{\hat{\mathbf{t}}\}^T\{\mathbf{q}^e + \Delta\mathbf{q}^e\} \\
- \; & \int_{\partial\Omega_c^m/\partial\Omega_c^c} \int_{(\mathbf{u}^m - \mathbf{u}^c)}^{(\mathbf{u}^m + \Delta\mathbf{u}^m - \mathbf{u}^c - \Delta\mathbf{u}^c)} \mathbf{T}^m \cdot d(\mathbf{u}^m - \mathbf{u}^c) d\partial\Omega \\
- \; & \int_{\Gamma_{cr}} \int_{\overset{1}{\mathbf{u}}{}^{cr} - \overset{2}{\mathbf{u}}{}^{cr}}^{\overset{1}{\mathbf{u}}{}^{cr} + \Delta\overset{1}{\mathbf{u}}{}^{cr} - \overset{2}{\mathbf{u}}{}^{cr} - \Delta\overset{2}{\mathbf{u}}{}^{cr}} \mathbf{T}^{cr} \cdot d(\overset{1}{\mathbf{u}}{}^{cr} - \overset{2}{\mathbf{u}}{}^{cr}) d\Gamma_{cr}
\end{aligned}
\tag{5.5}
$$

where

$$
\begin{aligned}
[\mathbf{H}^m] &= \int_{\Omega_e} [\mathbf{P}^m]^T [\mathbf{S}^m][\mathbf{P}^m] d\Omega_m \quad [\mathbf{H}^c] = \int_{\Omega_e} [\mathbf{P}^c]^T [\mathbf{S}^c][\mathbf{P}^c] d\Omega_c \\
[\mathbf{G}^e] &= \int_{\partial\Omega_e} [\mathbf{P}^m]^T [\mathbf{n}^e][\mathbf{L}^e] d\partial\Omega_m \quad [\mathbf{G}^m] = \int_{\partial\Omega_e} [\mathbf{P}^m]^T [\mathbf{n}^m][\mathbf{L}^m] d\partial\Omega_m \\
[\mathbf{G}^c] &= \int_{\partial\Omega_e} [\mathbf{P}^c]^T [\mathbf{n}^c][\mathbf{L}^c] d\partial\Omega_c \quad [\overset{1}{\mathbf{G}}{}^{cr}] = \int_{\overset{1}{\Gamma}_{cr}} [\mathbf{P}]^T [\mathbf{n}^{cr}][\overset{1}{\mathbf{L}}_{cr}] d\Gamma_{cr} \\
[\overset{2}{\mathbf{G}}{}^{cr}] &= \int_{\overset{2}{\Gamma}_{cr}} [\mathbf{P}]^T [\mathbf{n}^{cr}][\overset{2}{\mathbf{L}}_{cr}] d\Gamma_{cr} \; \{\hat{\mathbf{t}}\} = \int_{\Gamma_{tm}} [\mathbf{L}_e]^T \{\bar{\mathbf{t}} + \Delta\bar{\mathbf{t}}\} d\Gamma_{tm}
\end{aligned}
\tag{5.6}
$$

Construction of appropriate stress functions with optimally high resolution is necessary for accurately depicting high stress gradients near the crack tip.

5.2.2 Solution Method

Crack growth in multiply cracked materials is solved using an incremental approach, where a set of elemental and global equations are solved in each increment for stresses and displacements.

1. Local equations for each element are obtained by setting the variation of equation (5.5) with respect to the stress coefficients $\Delta\boldsymbol{\beta^m}$ and $\Delta\boldsymbol{\beta^c}$ to zero. This results in the weak form of the element kinematic relations

$$
\begin{bmatrix} [\mathbf{H}^m] & [\mathbf{0}] \\ [\mathbf{0}] & [\mathbf{H}^c] \end{bmatrix} \begin{Bmatrix} \boldsymbol{\beta}^m + \triangle\boldsymbol{\beta}^m \\ \boldsymbol{\beta}^c + \triangle\boldsymbol{\beta}^c \end{Bmatrix} =
$$

$$
\begin{bmatrix} [\mathbf{G}^e] & -[\mathbf{G}^m] & [\mathbf{0}] & [\overset{1}{\mathbf{G}}{}^{cr}] & -[\overset{2}{\mathbf{G}}{}^{cr}] \\ [\mathbf{0}] & [\mathbf{0}] & [\mathbf{G}^c] & [\mathbf{0}] & [\mathbf{0}] \end{bmatrix} \begin{Bmatrix} \mathbf{q}^e + \triangle\mathbf{q}^e \\ \mathbf{q}^m + \triangle\mathbf{q}^m \\ \mathbf{q}^c + \triangle\mathbf{q}^c \\ \overset{1}{\mathbf{q}}{}^{cr} + \Delta\overset{1}{\mathbf{q}}{}^{cr} \\ \overset{2}{\mathbf{q}}{}^{cr} + \Delta\overset{2}{\mathbf{q}}{}^{cr} \end{Bmatrix}
\tag{5.7}
$$

or in a condensed form

$$
[\mathbf{H}]_e \{\boldsymbol{\beta} + \Delta\boldsymbol{\beta}\}_e = [\mathbf{G}]_e \{\mathbf{q} + \Delta\mathbf{q}\}_e \tag{5.8}
$$

Since equation (5.8) is linear, the stress coefficients can be directly expressed in terms of the nodal displacements, provided the element $[\mathbf{H}]_e$ matrix is invertible.

2. Subsequently, the weak forms of the global traction continuity conditions are solved by setting the variation of the total domain energy functional with respect to the generalized displacement components to zero. This results in the weak form of the traction reciprocity conditions

$$\sum_{e=1}^{N} \begin{bmatrix} [\mathbf{G}^e] & -[\mathbf{G}^m] & [\mathbf{0}] & [\overset{1}{\mathbf{G}}{}^{cr}] & -[\overset{2}{\mathbf{G}}{}^{cr}] \\ [\mathbf{0}] & [\mathbf{0}] & [\mathbf{G}^c] & [\mathbf{0}] & [\mathbf{0}] \end{bmatrix}_e^T \begin{Bmatrix} \boldsymbol{\beta^m} + \Delta\boldsymbol{\beta^m} \\ \boldsymbol{\beta^c} + \Delta\boldsymbol{\beta^c} \end{Bmatrix}_e = \sum_{e=1}^{N} \begin{Bmatrix} \hat{\mathbf{t}} \\ \bar{\mathbf{f}}_{coh}^{in} \\ -\bar{\mathbf{f}}_{coh}^{in} \\ \bar{\mathbf{f}}_{coh}^{cr} \\ -\bar{\mathbf{f}}_{coh}^{cr} \end{Bmatrix}_e \tag{5.9}$$

or in a condensed form:

$$\sum_{e=1}^{N} [\mathbf{G}]_e^T \{\beta + \Delta\beta\}_e = \sum_{e=1}^{N} \{\bar{\mathbf{T}}_{ext}\}_e \tag{5.10}$$

The forces at the interface and crack surface are expressed in terms based on the cohesive energy as

$$\begin{aligned} \bar{\mathbf{f}}_{coh}^{m} &= \int_{\partial\Omega_e^m / \partial\Omega_e^c} \frac{\partial}{\partial \Delta \mathbf{q}^m} \left[\int_{(\mathbf{u}^m - \mathbf{u}^c)}^{(\mathbf{u}^m + \Delta\mathbf{u}^m - \mathbf{u}^c - \Delta\mathbf{u}^c)} \mathbf{T}^m \cdot d(\mathbf{u}^m - \mathbf{u}^c) \right] d\partial\Omega \\ &= \int_{\partial\Omega_e^m / \partial\Omega_e^c} [\mathbf{L}^m]^T \{\mathbf{T}^m(\mathbf{u}^m + \Delta\mathbf{u}^m - \mathbf{u}^c - \Delta\mathbf{u}^c)\} d\partial\Omega \end{aligned} \tag{5.11}$$

$$\begin{aligned} \bar{\mathbf{f}}_{coh}^{cr} &= \int_{\Gamma_{cr}} \frac{\partial}{\partial \Delta \overset{1}{\mathbf{q}}{}^{cr}} \left[\int_{\overset{1}{\mathbf{u}}{}^{cr} - \overset{2}{\mathbf{u}}{}^{cr}}^{\overset{1}{\mathbf{u}}{}^{cr} + \Delta\overset{1}{\mathbf{u}}{}^{cr} - \overset{2}{\mathbf{u}}{}^{cr} - \Delta\overset{2}{\mathbf{u}}{}^{cr}} \mathbf{T}^{cr} \cdot d(\overset{1}{\mathbf{u}}{}^{cr} - \overset{2}{\mathbf{u}}{}^{cr}) \right] d\Gamma_{cr} \\ &= = \int_{\Gamma_{cr}} [\overset{1}{\mathbf{L}}{}^{cr}]^T \{\mathbf{T}^{cr}(\overset{1}{\mathbf{u}}{}^{cr} + \Delta\overset{1}{\mathbf{u}}{}^{cr} - \overset{2}{\mathbf{u}}{}^{cr} - \Delta\overset{2}{\mathbf{u}}{}^{cr})\} d\Gamma_{cr} \end{aligned} \tag{5.12}$$

Combining equations (5.8) and (5.10) and eliminating the stress coefficients $\{\beta+\Delta\beta\}_e$, results in the equation for solving the generalized displacements

$$\sum_{e=1}^{N}\{[\mathbf{G}]_e^T[\mathbf{H}]_e^{-1}[\mathbf{G}]_e\}\{\mathbf{q}+\Delta\mathbf{q}\}=\sum_{e=1}^{N}\{\bar{\mathbf{T}}_{ext}\}_e \tag{5.13}$$

Equation (5.13) is a nonlinear matrix equation system due to the cohesive laws. Consequently, a Newton-Raphson iterative solver is invoked to solve for the increments of nodal displacements. The linearized form of equation (5.13) for the j-th iteration is

$$\begin{aligned}&\left\{\sum_{e=1}^{N}\frac{\partial\{\bar{\mathbf{T}}_{ext}\}_e}{\partial\{\mathbf{q}\}}-\sum_{e=1}^{N}\{[\mathbf{G}]^T[\mathbf{H}]^{-1}[\mathbf{G}]\}_e\right\}^j\{d\mathbf{q}\}^j=\\&\left\{\sum_{e=1}^{N}\{\bar{\mathbf{T}}_{ext}\}_e-\sum_{e=1}^{N}\{[\mathbf{G}]^T[\mathbf{H}]^{-1}[\mathbf{G}]\}_e\{\mathbf{q}+\Delta\mathbf{q}\}\right\}^j\end{aligned} \tag{5.14}$$

which, in a condensed form is

$$[\mathbf{K}^g]^j d\mathbf{q}^j=\{\mathbf{R}_{ext}^g\}-\{\mathbf{R}_{int}^g\}^j \tag{5.15}$$

Many numerical examples in Chapter 4 prove that only a Newton-Raphson iterative solver cannot obtain the entire failure solution for the problems with damage, especially when a snap-back appears in the load-deformation curve.

According to the arc-length method proposed in [19, 20, 84], an unknown loading parameter $(\lambda+d\lambda)$ is introduced to govern the load increments. Equation (5.15) is modified with this loading parameter as

$$[\mathbf{K}^g]^j d\mathbf{q}^j=(\lambda^j+d\lambda^j)\{\mathbf{R}_{ext}^g\}-\{\mathbf{R}_{int}^g\}^j \tag{5.16}$$

where both $d\lambda^j$ and $d\mathbf{q}^j$ are unknowns, and $d\lambda^j$ can be either positive or negative. The orthogonality condition is chosen to be the constraint equation required by the additional unknown $d\lambda^j$.

5.2.3 Stability conditions

Following the stability conditions derived for displacement-based and stress-based finite element approximations in [4, 12, 104], the stability conditions of the stress-displacement field variational problem in X-VCFEM are stated in section 4.2.3. They are positive definite $[\mathbf{H}^m]$ and $[\mathbf{H}^c]$, unique stress interpolation functions, and non-zero stress parameters for all non-rigid body displacement fields. The two conditions can be satisfied by implementing numerical methods in section 4.5. And the third one is accomplished by choosing $n_{\beta^m} > n_q^e + n_q^m + n_q^{cr} * 2 - 3$ and $n_{\beta^c} > n_q^c - 3$.

5.3 Aspects of Numerical Implementation

5.3.1 Adaptive criteria for cohesive crack growth

A. The criterion for the incremental cohesive crack advance into matrix:

The static deflection/penetration behavior at an interface has been the subject of numerical research efforts in the past years and many significant results for various kinds of materials have been obtained([2, 41, 42, 55]). The fracture toughness ratio of the interface and the matrix material has been identified as the most important parameter governing the crack deflection/penetration phenomenon. Predicting crack growth requires to calculate the energy release rate, G, and a knowledge of the surface fracture energy, G_c. In this chapter, we denote by G^i and G_c^i the energy release rate and the critical energy release rate for the case of growth along interfaces, and by G^m and G_c^m the corresponding quantities for penetration into matrix.

As seen in previous results, stress concentration always appears in the matrices around fibers, which results in cohesive interfaces between fiber and matrix becoming weak and even debonded. Simultaneously, damage at the interface results in larger concentrated stress fields in matrix. Once the stress in matrix reaches some critical value, the material at this matrix point might become softening and damage propagates into matrix from the interface. All points with critical stresses are regarded as the candidate damage position, where the criterion is necessary for selecting the crack growth direction, along the interface or branching into matrix. The candidate positions are usually chosen from the Gaussian integration points on the interface. In the program, 18 Gaussian integration points are distributed between any two consecutive nodes at the interface.

At the candidate points, the criterion for assessing the crack penetrating into matrix is defined as

$$G^m/G^i > G_c^m/G_c^i \tag{5.17}$$

In this thesis, the energy release rate is calculated based on cohesive zone models, which are shown in figure 5.2. The bilinear model in figure 5.2 (a) is for describing the damage at interface, and the linear model in figure 5.2 (b) is for the matrix cracking. The areas of the shadow regions express the current energy release rates G^i and G^m. According to the relation between the cohesive energy ϕ for complete decohesion and the critical energy release rate G_c in equation (4.55), the critical release rates for interface and matrix are

$$G_c^i = \frac{1}{2}\sigma_{max}^i \delta_e^i \quad \text{and} \quad G_c^m = \frac{1}{2}\sigma_{max}^m \delta_e^m \tag{5.18}$$

In order to obtain the energy release rate G^m, the effective cohesive traction t is calculated according to stresses (σ_{xx}, σ_{yy} and σ_{xy}) at every candidate point. Recalling equations (4.58–4.62) in Chapter 4, effective cohesive traction $t(\alpha_c)$, the cohesive energy $\phi(\alpha_c)$ and the energy release rate G^m are obtained

$$t(\alpha) = \sqrt{(\sigma_{xx}\sin^2\alpha - \sigma_{xy}\sin 2\alpha + \sigma_{yy}\cos^2\alpha)^2 + \beta^{-2}(-\frac{1}{2}\sigma_{xx}\sin 2\alpha + \sigma_{xy}\cos 2\alpha + \frac{1}{2}\sigma_{yy}\sin 2\alpha)^2} \tag{5.19}$$

$$G^m = \phi(\alpha_c) \quad = \quad \frac{\delta_e^m}{2\sigma_{max}^m}({\sigma_{max}^m}^2 - t(\alpha_c)^2) \tag{5.20}$$

where α_c is the angle maximizing the cohesive energy.

The current energy release rates for interface, G^i, is obtained

$$G^i = \begin{cases} \sigma_{max}^i \delta^i/\delta_c & \delta < \delta_c \\ \frac{\sigma_{max}^i}{2}(\delta_e^i - \frac{(\delta_e^i - \delta)^2}{\delta_e^i - \delta_c}) & \delta \geq \delta_c \end{cases} \tag{5.21}$$

According to equations (5.18, 5.20, 5.21) and inequality (5.17), the damage propagation directions are determined at the candidate points.

B. Direction and length of the incremental cohesive crack advance:

Recalling results in chapter 4, the direction of matrix cracking α_c is obtained at the damage onset points as

$$\alpha_c = \begin{cases} \arctan\left(\frac{-\sigma_{xx}+\sigma_{yy}\pm\sqrt{(\sigma_{xx}-\sigma_{yy})^2+4\sigma_{xy}^2}}{2\sigma_{xy}}\right) \\ \arctan\left(\frac{2(\beta^{m\,2}-1)\sigma_{xy}\pm\sqrt{(4\beta^{m\,4}-8\beta^{m\,2}+4)\sigma_{xy}^2-(4\beta^{m\,4}-4\beta^{m\,2}+2)\sigma_{xx}\sigma_{yy}-(2\beta^{m\,2}-1)(\sigma_{xx}^2+\sigma_{yy}^2)}}{2\beta^{m\,2}\sigma_{xx}-\sigma_{xx}+\sigma_{yy}}\right) \end{cases} \tag{5.22}$$

The sign in equation (5.22) is chosen as the one that maximizes the cohesive energy ϕ_c by satisfying the condition in equation (4.61) c.

Upon establishing the direction of incremental cohesive crack growth α_c, the length of cohesive zone advance ($\Delta\bar{l}$) should be estimated in the crack evolution scheme according to the same algorithm shown in chapter 4 as:

$$\Delta\bar{l} = \frac{\phi_A}{\phi_A - \phi_B}|AB|, \tag{5.23}$$

where **B** is a point close to **A** in the direction of crack propagation.

5.3.2 Generation of $[\mathbf{G}^c]$

Once damage is driven from interface into matrix, two node-pairs (m_1, n_1) and (m_2, n_2), shown in figure 5.3, are added at the interface, where nodes m_1 and m_2 are at the matrix side and nodes n_1 and n_2 are at the inclusion side. The separation between m_1 and m_2 describes the displacement discontinuity at the crack surface. Since crack doesn't propagates into the inclusion, the node-pair (n_1, n_2) merges by sharing the same displacement. This can be implemented at assembling matrix $[\mathbf{G}^c]$. In matrix $[\mathbf{G}^c]$, the elements in column DOF_{n2} are added to the corresponding elements in column DOF_{n1}, and the entire column DOF_{n2}

is assigned zero. The process is shown in equation (5.24) as

$$
\begin{array}{c}
\begin{array}{ccccc} & DOF_{n1} & & DOF_{n2} & \end{array} \\
\begin{pmatrix} \cdots & * & \cdots & \# & \cdots \\ \cdots & * & \cdots & \# & \cdots \\ \cdots & * & \cdots & \# & \cdots \end{pmatrix}_{n_{\beta^c} \times n_{q^c}}
\end{array}
\Rightarrow
$$

$$
\begin{array}{c}
\begin{array}{ccccc} & DOF_{n1} & & DOF_{n2} & \end{array} \\
\begin{pmatrix} \cdots & *+\# & \cdots & 0 & \cdots \\ \cdots & *+\# & \cdots & 0 & \cdots \\ \cdots & *+\# & \cdots & 0 & \cdots \end{pmatrix}_{n_{\beta^c} \times n_{q^c}}
\end{array}
\tag{5.24}
$$

5.4 Numerical Example

An example with a square microstructure containing a single circular fiber with a debonding interface is considered to check the effectiveness of X-VCFEM and study the interaction between the interface and matrix cohesive cracking. The geometrical dimensions for the specimen in figure 5.4(a) are **a**= 20 mm, **r**= 5 mm. The material parameters for matrix and fiber are: Young's modulus $E_m = 72\ GPa$, $E_f = 450\ GPa$, and Poisson ratio $\nu_m = 0.32$, $\nu_f = 0.17$, where subscript $(\cdot)_m$ and $(\cdot)_f$ denote matrix and fiber respectively. The interface uses the bilinear cohesive zone model with the properties $\sigma^i_{max} = 0.04\ GPa$, $\delta_c = 0.001mm$, $\delta^i_e = 0.02mm$, $\beta^i = 0.707$. The linear cohesive zone model is used to describe matrix cracking with parameters: $\sigma^m_{max} = 0.05\ GPa$, $\delta^m_e = 0.002mm$, and $\beta^m = 1$. The cohesive parameters are chosen to make $\sigma^m_{max} > \sigma^i_{max}$, so that the damage starts from interface instead of matrix. Under plane strain conditions, the displacement boundary conditions are shown in figure 5.4(a). The whole microstructure is modeled with one X-VCFEM element, consisting of 16 nodes on the cell boundary and 20 node pairs on the interface for displacement interpolation. Before damage propagates into matrix, the stress functions in this example consist of 102 terms of polynomial functions and 45 terms of reciprocal functions. After the cracks advance into matrix, one branch function and 16 wavelet functions are added into the stress interpolation for

each crack. Figures 5.4(b) shows the contour plots of the microstructural stress σ_{yy} together with evolved position of the cracks at the final stage of loading. The growth pattern of each crack can be observed by comparing with its initial configuration in figures 5.4(a), where there is no matrix cracks.

The relation of the propagation of multiple cracks to the interface debonding is in general complicated. However, several observations can be made based on the results of the simulation by this model.

- As shown in figures 5.4(b), the lower stress at point **A** implies that interface there becomes weak even debonded, which results in the load can not be transfered into the fiber at this position effectively. The positions with concentrated stress bifurcate from point **A** and move to left and right sides respectively along the interface, which might drive the damage into matrix from the interface. The same thing happens at the bottom point of the circular fiber.

- Due to symmetry, four cracks propagate into matrix from the interface. Largest stresses appear at tips of cracks and the stress in fiber is released. In this example, since cracks result in larger concentrated stress than interfaces, cracks propagation in matrix becomes the key damage phenomenon in following failure process.

- The evolved crack path tends to align in a direction perpendicular to the applied load direction, which agrees with the observation in chapter 4.

5.5 Concluding Remarks

The extended Voronoi cell finite element model is improved in this chapter to predict the damage advancing into matrix and study the interaction between interfacial debonding and matrix cracking. Polynomial functions, reciprocal functions, branch functions and wavelet functions are made to the element stress interpolations to accurately depict the stress discontinuities and concentrations at interfaces and cracks. The damage in interface and matrix are modeled by cohesive models. A criterion for assessing the crack penetrating into matrix is proposed, which is based on the energy release rate and cohesive energy. A square specimen containing a single circular fiber with a debonding interface is considered to check the effectiveness of X-VCFEM and the criterion.

The damage analysis in fiber-reinforced composites is in general complicated. X-VCFEM is easy to be extended to study effects of material properties and geometric characterization, such as clustering, alignment, fiber shape, relative sizes etc., which are critical to the failure process in the microstructure. This will be explored in the future work.

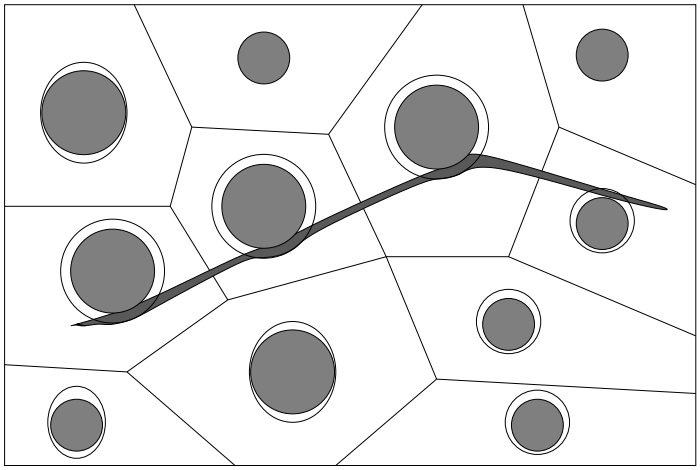

(a)

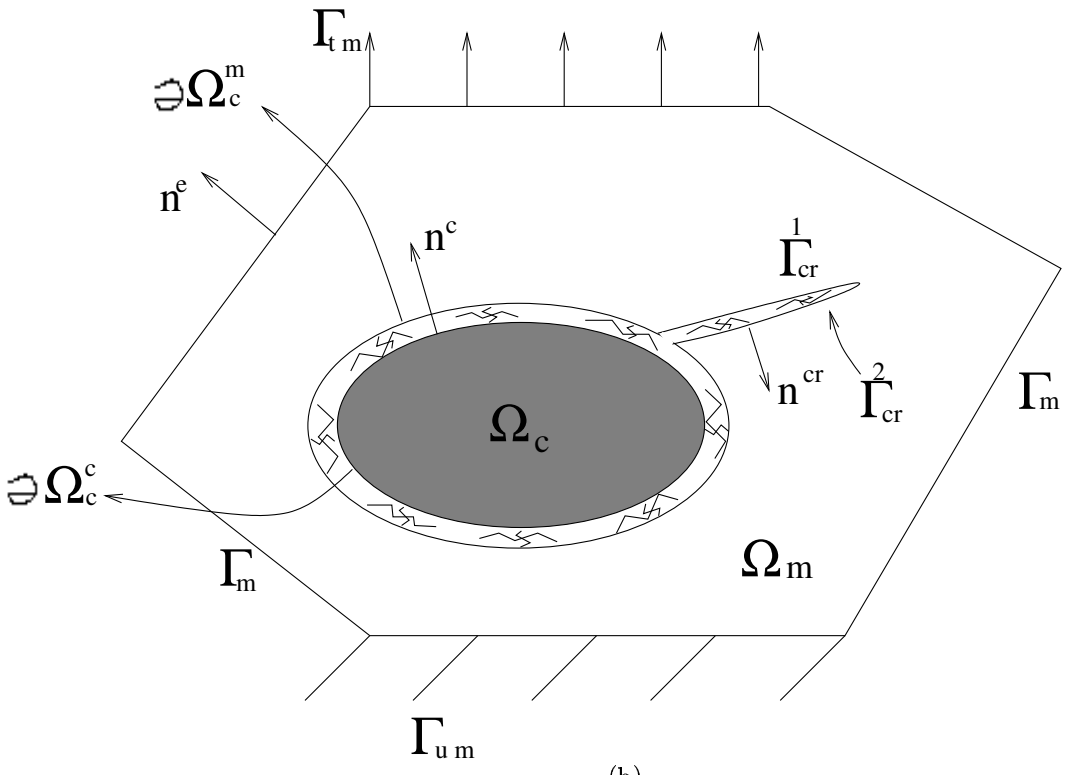

(b)

Figure 5.1: (a) Voronoi mesh for composite microstructure with interface debonding and matrix cracking, (b) a typical Voronoi cell element with interface and crack.

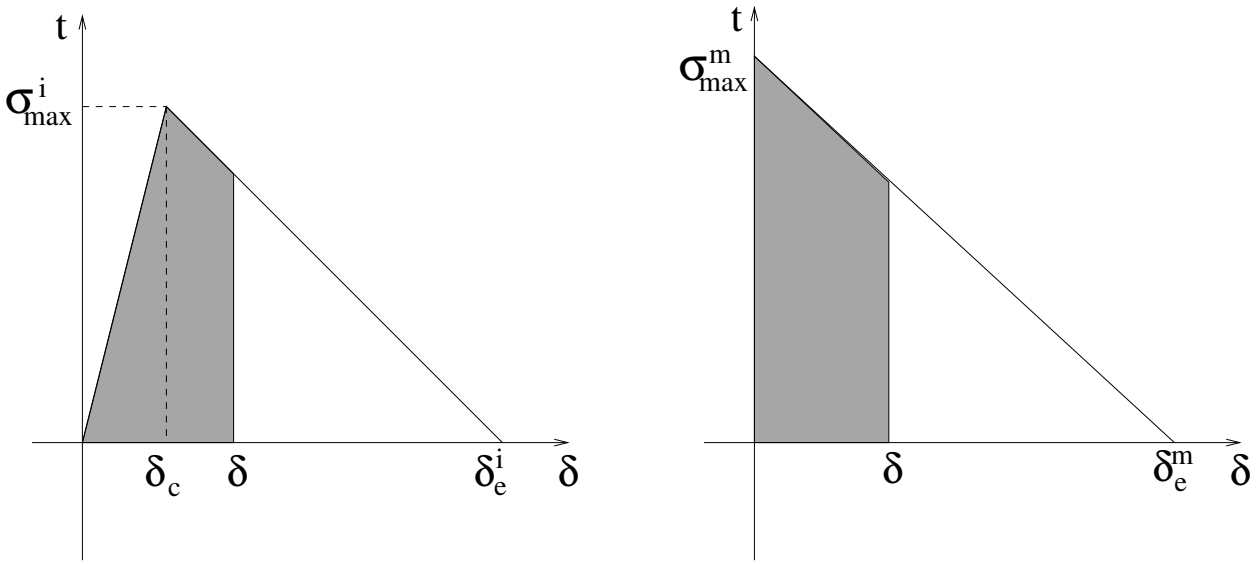

(a) (b)

Figure 5.2: Cohesive zone models for calculating energy release rates: (a) the bilinear law for interface debonding and (b) the linear law for matrix cracking.

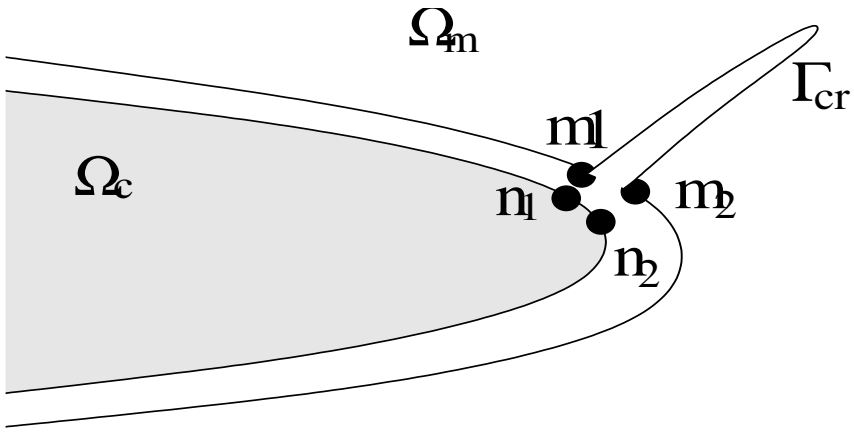

Figure 5.3: Node pairs (n_1, m_1) and (n_2, m_2) for describing damage advancing into matrix.

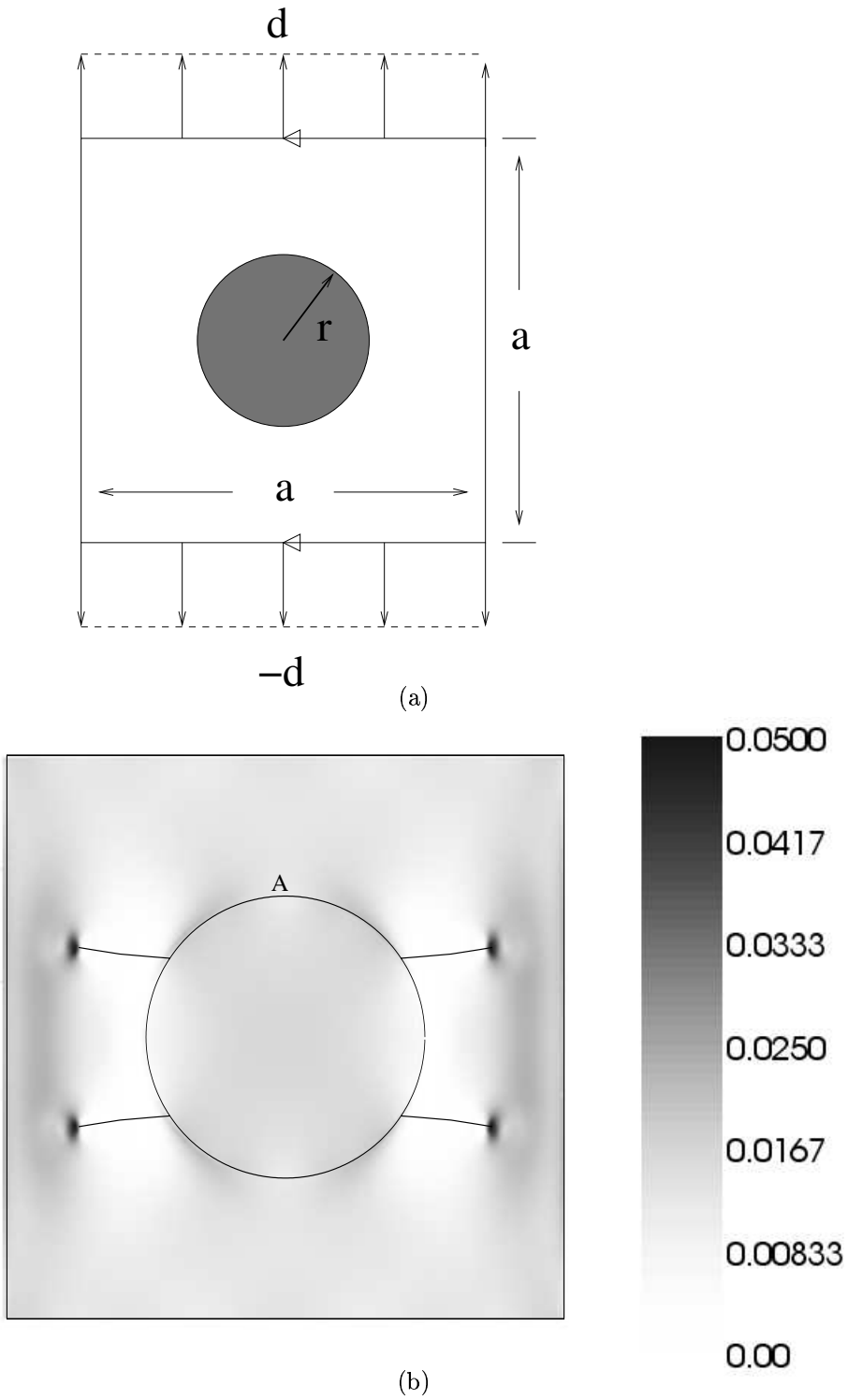

Figure 5.4: (a) A square microstructure containing a single circular fiber, (b) contour plot for σ_{yy} (GPa) with four cohesive cracks propagated from the interface.

Chapter 6

Concurrent Multi-level Model for Damage Evolution in Microstructurally Debonding Composites

6.1 Introduction

Analysis of composite materials with microstructural heterogeneities is conventionally done with macroscopic properties obtained by homogenizing response functions in the representative volume element (RVE) from microscopic analyses at smaller length scales. While these "bottom-up" homogenization models are efficient and can reasonably predict macroscopic or averaged behavior, such as stiffness or strength, they have limited predictive capabilities with problems involving localization, failure or instability. Assumptions of macroscopic uniformity and RVE periodicity, the two basic requirements of homogenization, break down under these circumstances. The uniformity assumption ceases to hold in critical regions of high local solution gradients,

such as near free edges, interfaces, material discontinuities or evolving damage. RVE periodicity, on the other hand, is unrealistic for non-uniform microstructures, e.g. in the presence of clustering of heterogeneities or microscopic damage. Even with a uniform phase distribution in the microstructure, the evolution of localized stresses, strains or damage path can violate the periodicity conditions. Problems like this have been effectively tackled by multi-scale modeling methods e.g. in [72, 29, 44, 67, 66, 81, 74, 73, 94, 108, 92]. Multi-scale analyses methods can be broadly classified into two classes. The first is known as "hierarchical models" [29, 44, 94, 92] in which information is passed from lower to higher scales, usually in the form of material properties. The hierarchical homogenization models assume periodic representative volume elements (RVE) in the microstructure and uniformity of macroscopic field variables. The second class, known as "concurrent methods" [67, 66, 82, 74, 73, 108], implement sub-structuring and simultaneously solve different models at regions with different resolutions or scales.

The two-way coupling of scales enabled in the concurrent methods is suitable for problems involving localization, damage and failure. Macroscopic analysis, using bottom-up homogenization in regions of relatively benign deformation, enhances the efficiency of the computational analysis. As a matter of fact, it would be impossible to analyze large structural regions without the advantage of a continuum model based macroscopic analysis. On the other hand, the top-down localization process cascading down to the microstructure in critical regions of localized damage or instability for pure microscopic analysis, is necessary for accurately predicting the damage path. These microscopic computations, depicting the real microstructure are often complex and computationally prohibitive. Hence, a concurrent setting makes such analyses feasible, provided the "zoom-in" regions are kept to a minimum. The adaptive multi-level models, promoted in [67, 66, 82, 74, 73, 108], are attempts to achieve this objective, with the adaptivity motivated from physical and mathematical perspectives. However, there is a paucity of such studies in the literature involving material nonlinearity and evolving microstructural damage. In their previous studies, Ghosh and coworkers have proposed adaptive multi-level analysis using the microstructural Voronoi cell FEM model for modeling elastic-plastic composites with particle cracking and porosities in [81], and for elastic composites with free edges and stress singularities in [74, 73].

In a preceding paper [75], the authors have derived and computationally modeled an anisotropic con-

tinuum damage mechanics (CDM) model for unidirectional fiber-reinforced composites undergoing interfacial debonding from by using homogenization theory. The CDM model homogenizes the damage incurred through initiation and growth of interfacial debonding in a microstructural RVE with nonuniform distribution of fibers. Additionally, arbitrary loading conditions are also effectively handled by this model. The present paper uses this CDM model of [75] in an adaptive concurrent multi-level computational model to analyze multi-scale evolution of damage. Damage by fiber-matrix interface debonding, is explicitly modeled over extended microstructural regions at critical locations [35, 53]. The adaptive model addresses issues of efficiency and accuracy through considerations of physically-based modeling errors.

The adaptive multi-level model consists of three levels of hierarchy viz. *level-0*, *level-1* and *level-2*), which evolve in sequence. The continuum damage model developed in [75] is used for *level-0* computations. The *level-1* domain is used as a 'swing region' to establish criteria for switching from macroscopic to microscopic calculations. Physical criteria involving variables at the macroscopic and microstructural RVE levels, trigger switching from pure macroscopic to pure microscopic calculations, i.e. the $level-0 \rightarrow level-1 \rightarrow level-2$. A transition layer is placed between the $level-1$ and microscopic $level-2$ domains for smooth transition from one scale to the next. All computations in the composite microstructure with explicit representations of the fiber and matrix phases are done with the Voronoi cell finite element model or VCFEM [35, 53]. In VCFEM, debonding at the fiber-matrix interface is achieved by a layer of cohesive springs [68]. Two numerical examples are solved in this paper to examine the effectiveness of the multi-level computational model in multi-scale damage analysis. The first example considers a small region of a fiber matrix composite microstructure for comparison with an explicit micromechanics model. The second set of problems models a double lap bonded composite joint for demonstrating its capability in handling large structural problems.

6.2 Levels in the Multi-scale Computational Model

The multi-phase composite computational domain Ω_{het} is adaptively decomposed into a set of non-intersecting open subdomains, belonging to *levels-0, -1* and *-2* with different algorithmic treatments, i.e. $\Omega_{het} = \Omega_{l0} \bigcup \Omega_{l1} \bigcup \Omega_{l2} \bigcup \Omega_{tr}$. The different levels of computational hierarchy, in the order of sequence of emer-

gence, are depicted in figure (6.1) and discussed briefly here.

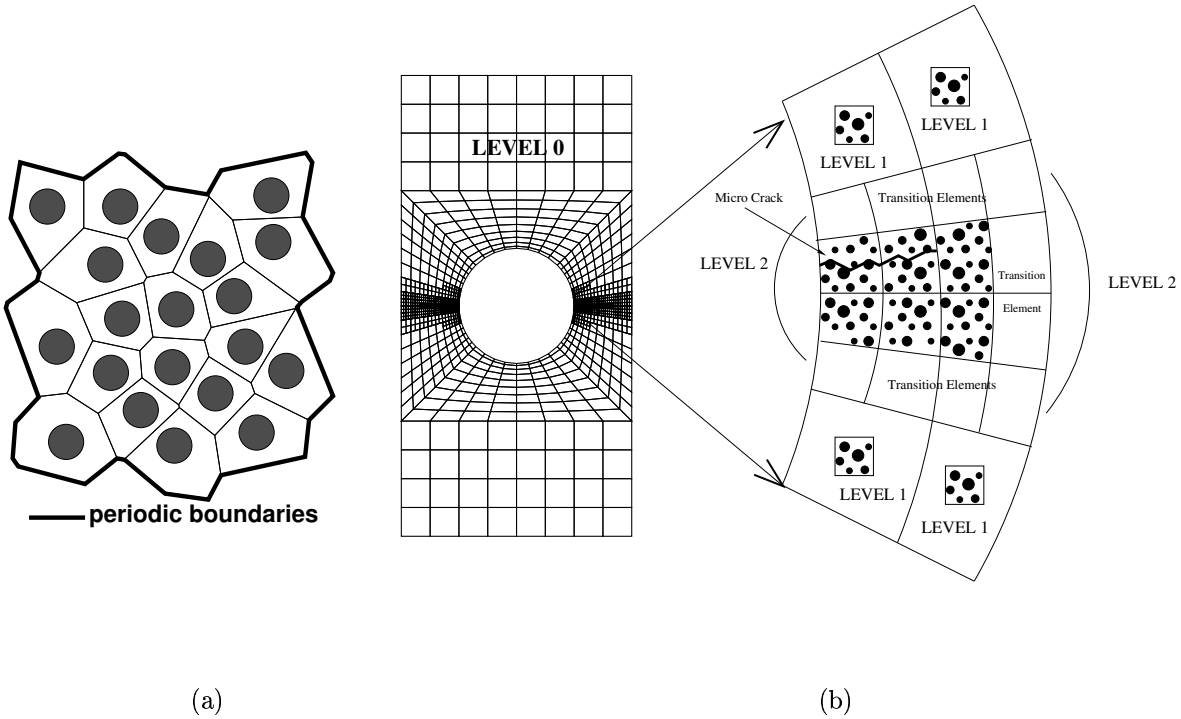

(a) (b)

Figure 6.1: Schematic of the two-way coupled concurrent multi-level model: (a) a representative volume element (RVE) for a non-uniformly distributed composite microstructure generated by tessellating the local microstructure, (b) the top-down multi-level model showing components of concurrent coupling, viz. continuum *level-0*, *level-1* of asymptotic homogenization and *level-2* of micromechanical analysis.

6.2.1 Computational Subdomain Level-0 (Ω_{l0})

This level corresponds to regions where continuum constitutive laws can be used in macroscopic analysis. Macroscopic field variables like stresses and strains in Ω_{l0} are relatively uniform and there is no strong non-periodicity in the microstructure. Hence, microscopic 'statistical' periodicity in the RVE is assumed to be valid in this level. Scale effects are negligible and it is possible to derive effective constitutive relations by volume averaging the RVE response with imposed periodicity conditions, in the limit that the RVE tends to zero volume. This is generally the starting level in the multi-scale analysis model, as long as RVE's can be identified for the computational domain. Macroscopic analysis with the continuum constitutive models in *level-0*, reduce the computing effort by several orders of magnitude in comparison with models that require

complete microscopic analysis .

For undamaged microstructures with linear elastic or elastic-plastic phases, homogenized anisotropic constitutive laws have been developed by the authors in [82, 34]. In the case of microstructures with randomly evolving microcracks causing diffused damage, the homogenized material behavior is best represented by a continuum damage mechanics (CDM) law. An anisotropic CDM model with a fourth order damage tensor has been developed from rigorous micromechanical analyses in [75]. The general form of CDM models [49] introduce a fictitious effective stress $\tilde{\Sigma}_{ij}$ acting on an effective resisting area ($\tilde{A}$), which is caused by reduction of the original resisting area A due to material degradation from the presence of microcracks and stress concentration in the vicinity of cracks. In [75], the effective stress $\tilde{\Sigma}_{ij}$ is related to the actual Cauchy stress Σ_{ij} through the fourth order damage effect tensor M_{ijkl} as

$$\tilde{\Sigma}_{ij} = M_{ijkl}(\mathbf{D})\Sigma_{kl} \tag{6.1}$$

where M_{ijkl} is a function of the fourth order damage tensor $\mathbf{D}(= D_{ijkl}\mathbf{e_i} \otimes \mathbf{e_j} \otimes \mathbf{e_k} \otimes \mathbf{e_l})$. The hypothesis of equivalent elastic energy is used to evaluate M_{ijkl} and hence establish a relation between the damaged and undamaged stiffnesses [18, 15, 106]. Equivalence is established by equating the elastic energy in the damaged state to that in a hypothetical undamaged state as

$$W(\mathbf{\Sigma}, \mathbf{D}) = \frac{1}{2}\Sigma_{ij}(E_{ijkl}(\mathbf{D}))^{-1}\Sigma_{kl} \;=\; W(\tilde{\mathbf{\Sigma}}, \mathbf{0}) = \frac{1}{2}\tilde{\Sigma}_{ij}(E^o_{ijkl})^{-1}\tilde{\Sigma}_{kl} \tag{6.2}$$

where $\mathbf{\Sigma} = \Sigma_{ij}\mathbf{e_i} \otimes \mathbf{e_j}$, E^o_{ijkl} is the elastic stiffness tensor in the undamaged state and $E_{ijkl}(\mathbf{D})$ is the stiffness in a damaged state. From equations 6.1 and 6.2, the relation between the damaged and undamaged stiffnesses is established as

$$E_{ijkl} = (M_{pqij})^{-1}E^o_{pqrs}(M_{rskl})^{-1} \tag{6.3}$$

With an appropriate assumption of a function for M_{ijkl}, equation (6.3) can be used to formulate a damage evolution model using micromechanics and homogenization. In [75], a damage evolution surface is introduced

to delineate the interface between damaged and undamaged domains in the strain **e**-space as

$$F = \frac{1}{2} e_{ij} P_{ijkl} e_{kl} - \kappa(\alpha W_d) = 0 \tag{6.4}$$

Here W_d corresponds to the dissipation of the strain energy density due to stiffness degradation for constant strain without an external work supply. Also called the degrading dissipation energy (see [43]), it is an internal variable denoting the current state of damage, and is expressed as:

$$W_d = \int \frac{1}{2} e_{ij} e_{kl} dE_{ijkl} \tag{6.5}$$

P_{ijkl} is a symmetric negative-definite fourth order tensor that will be expressed as a function of the strain tensor e_{ij}, α is a scaling parameter and κ is a function of W_d. Assuming associativity rule in the stiffness space, the evolution of the fourth order secant stiffness is obtained as

$$\dot{E}_{ijkl} = \dot{\lambda} \frac{\partial F}{\partial(\frac{1}{2} e_{ij} e_{kl})} = \dot{\lambda} P_{ijkl} \tag{6.6}$$

$P_{ijkl}(\mathbf{e})$ corresponds to the direction of the rate of stiffness degradation tensor $\dot{E}_{ijkl}$. For a composite material with interfacial debonding, the direction of rate of stiffness degradation varies with increasing damage and hence $P_{ijkl}(\mathbf{e})$ does not remain a constant throughout the loading process. The model requires the evaluation of κ, α and P_{ijkl} in equation (6.4). These are determined from the results of micromechanical simulations of a RVE with periodic boundary conditions. The function $\kappa(W_d)$ is evaluated for a reference loading path and all other strain paths are scaled with respect to this reference. Upon determination of the maximum value W_d for a reference loading condition, the value of α for any strain path can be obtained by simple scaling. To account for the variation of $P_{ijkl}(\mathbf{e})$, any macroscopic strain evolution path is discretized into a finite set of points. The values of P_{ijkl} are explicitly evaluated at these points from RVE based simulations. Values of P_{ijkl} for any arbitrary macroscopic strain value can then be determined by interpolating between nodal values using shape functions of a 3D linear hexahedral element. The details of the parameter evaluation process in the macroscopic CDM model are discussed in [75].

6.2.2 Computational Subdomain Level-1 (Ω_{l1})

Level-1 is an intermediate computational subdomain, introduced as a swing region for establishing criteria for switching from macroscopic *level-0* regions to *level-2* regions of pure microscopic computations. The switching criteria are based on analyses of the macroscopic problem, as well as of the microstructural RVE problem. The asymptotic homogenization theory is used for this level to decouple the set of governing equations into a set of *(i)* homogenized equations representing the macroscopic problem corresponding to a length scale $\mathbf{x}$, and *(ii)* microscopic equations for the RVE $Y(\mathbf{x})$, represented by a length scale $\mathbf{y}$. Details of the decoupled macro- and micro-equations are given in the appendix section 6.7.1.

Gradients of important field variables are evaluated from macroscopic analysis to assess the deviation of macroscopic uniformity. Such gradients may be the effect of strong microscopic non-homogeneity in the form of highly localized stresses and strains or damage. The RVE-based microscopic analysis, on the other hand, provides effective criteria to estimate departure from periodicity conditions, especially in the event of evolving microstructural damage. The adaptation criteria for level transitions are discussed in section 6.4. Two sets of finite element problems are solved for the *level-1* subdomain in sequence, viz.,

1. Macroscopic analysis: Incremental macroscopic analysis of the computational domain is performed using the CDM model to evaluate macroscopic variables e.g. stresses and strains due to the increments in applied loads.

2. Microstructural RVE analysis: This is a post-processing operation in which microstructural analysis of the RVE is conducted for each integration point of the macroscopic elements. The strain field e_{ij}, obtained from macroscopic analysis with the CDM model, is imposed on the RVE as an external driver, together with periodic boundary conditions on the boundary of the RVE as shown in figure (6.1)a. Microscopic stresses σ_{ij}, strains ε_{ij} and other variables are computed in this post-processing stage for each RVE.

Remark 1: The macroscopic computations of *level-0* and *level-1* elements are performed with the conventional displacement-based finite element method, while all microscopic calculations in the RVE of *level-1* elements

are performed using the Voronoi cell FEM [80, 35, 53].

Remark 2: Computational models in the macroscopic *level-0* and *level-1* subdomains are refined adaptively by selective h- or h-p strategies. 'Error' and convergence criteria for this refinement have been discussed in [74]. Local enrichment through successive mesh refinement or enhancement, serves a dual purpose in the multi-level computational strategy. The first goal is to identify regions of high discretization 'error' and improve convergence through mesh enhancement. The second is to identify regions of high modeling error and zoom in on these regions to create higher resolution. These regions are generally characterized by large gradients and localization of macroscopic variables. Element refinement in these regions is helpful for reducing the length-scale difference between macroscopic elements in the homogenized domain and microscopic regions with explicit representation of heterogeneities.

6.2.3 Computational Subdomain Level-2 (Ω_{l2})

The *level-2* subdomain of pure microscopic analysis emerges from *level-1* elements in regions characterized by (a) departure from macroscopic uniformity, e.g. regions of localization or fracture, and (b) significant microstructural non-uniformities manifested by e.g. growth of localized damage. Prior to transition to *level-2* elements, a high spatial resolution is reached in the macroscopic mesh, resulting in small elements, by h- or hp- refinement. The successive refinement process stops when a certain element size is achieved and subsequently the model changes from macroscopic to pure microscopic. A scale ratio SR is chosen a-priori to ascertain this element size. Depending on the choice of $SR = \frac{Size\ of\ level-2\ element}{Size\ of\ local\ RVE}$, the microscopic model in any given *level-2* element can encompass large portions of the microstructure with many discrete heterogeneities. The *level-2* elements are constructed by filling with the exact microstructure at that location, as outlined in the following steps and shown in figure 6.2.

- Use appropriate adaptation criteria to determine if a *level-1* element needs to switch to *level-2* element.
- Identify a region in the microstructure Ω_{micro} that is located in the same region as the *level-2* element. Ω_{micro} should extend beyond the element boundary by approximately two fiber lengths.
- Tessellate the local microstructure to generate a mesh of Voronoi cell elements as shown in figure (6.3).

- Carve out the microstructural region of the *level-2* element from the local microstructure Ω_{micro}. This procedure will result in dissecting some of the fibers on the boundary. When this happens, additional nodes are generated on the Voronoi cell boundary at locations where the fiber surface and Voronoi cell edges intersect the boundary of the *level-2* element. The dissected conjugate pieces of a fiber belonging to two contiguous *level-2* elements are joined together when the two contiguous elements share a common edge.

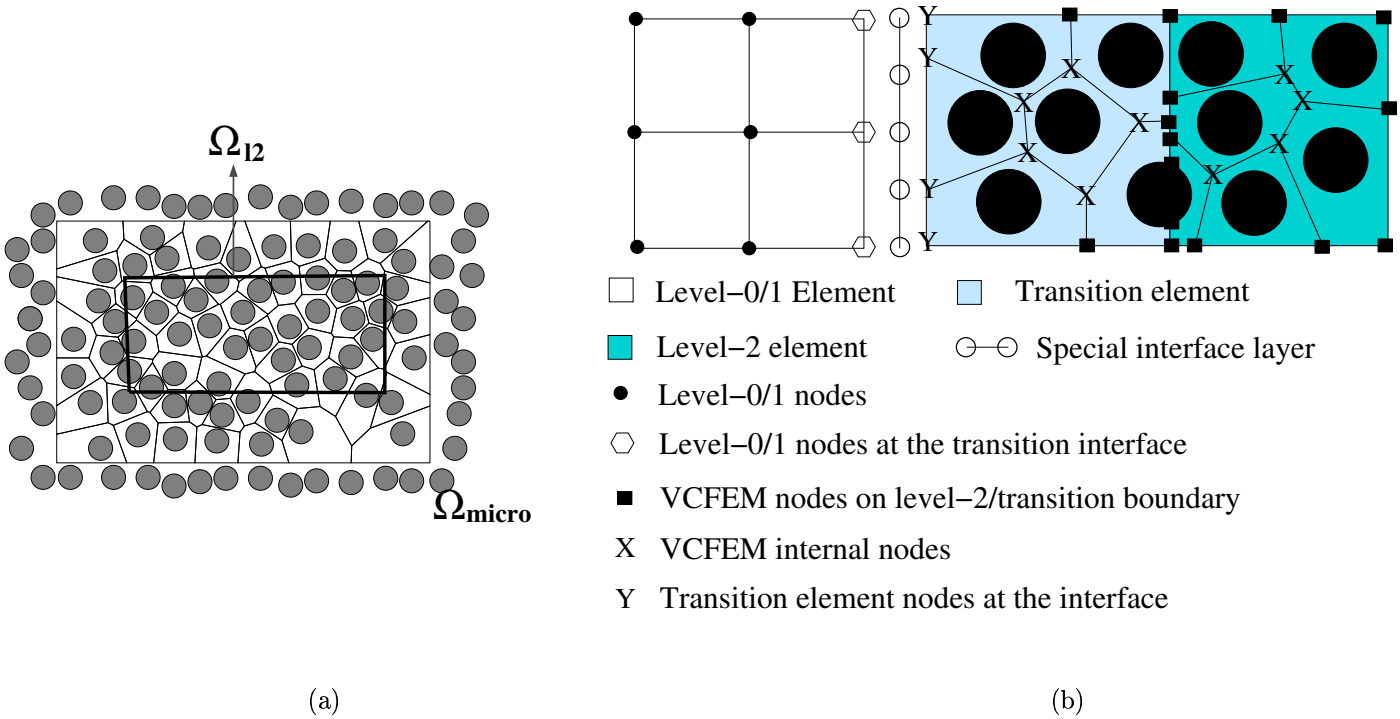

Figure 6.2: (a) Process of carving out *level-2* element microstructure (b) Interface constraints between *level-0/level-1* and *tr* elements

Requirement of high-resolution micromechanical models in these elements entails prohibitively large computations using conventional finite element methods. The microstructure-based Voronoi cell FEM [35, 53, 80] is particularly effective for modeling *level-2* elements because of its efficiency in modeling large heterogeneous regions [35, 53, 80, 81, 74]. Each Voronoi cell with embedded heterogeneities (particle, fiber, void, crack etc.)

represents the region of contiguity for the heterogeneity, and is treated as an element in VCFEM. VCFEM elements can be considerably larger than conventional FEM elements and incorporate a special hybrid FEM formulation. Incorporation of known functional forms from analytical micromechanics substantially enhances its convergence. A schematic diagram of Voronoi cell elements is shown in figure (6.3). A high level of accuracy has been achieved with VCFEM for modeling problems with microstructural damage by particle cracking [36] and fiber-matrix interfacial debonding [35, 53]. For debonding simulation, imperfect interfaces are represented by the cohesive zone model [68]. Displacement degrees of freedom on the fiber-matrix interface are constrained by the cohesive zone models as discussed in section 6.3. VCFEM has been shown to be significantly more efficient than commercial displacement based FE packages for modeling complex microstructures with evolving damage.

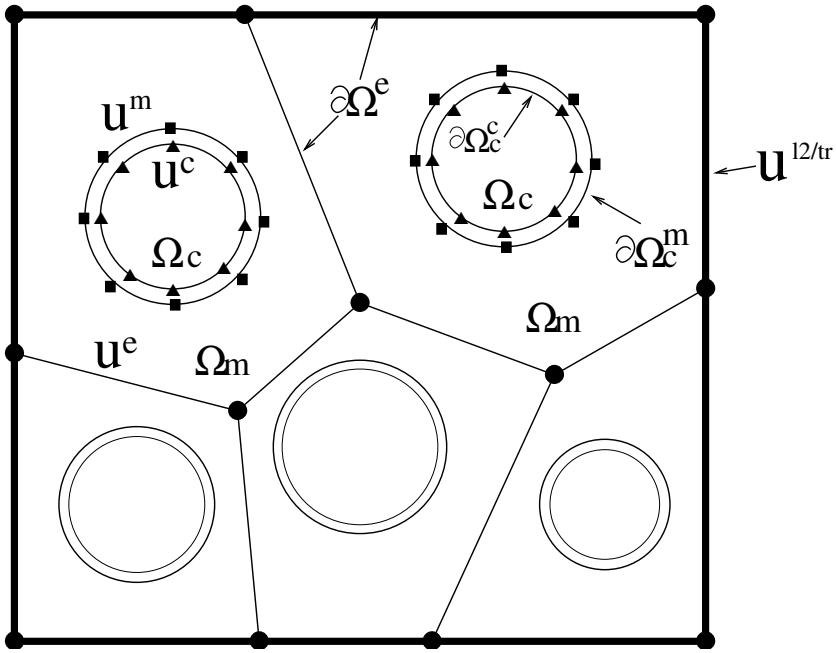

Figure 6.3: A typical *level-2* element containing an aggregate of microstructural Voronoi cell elements with relevant notations.

6.2.4 Scale Transition Subdomain (Ω_{tr})

The interface between the *level-0* or *level-1* elements and the *level-2* elements with explicit representation of the heterogeneous microscopic domain, needs a special treatment to facilitate smooth transition of scales across the element boundaries. A layer of transition elements ($E_{tr} \in \Omega_{tr}$) is sandwiched between these elements, where (Ω_{tr}) is the transition subdomain as shown in figure (6.2)b. The E_{tr} elements are essentially *level-2* elements with compatibility and traction continuity constraints imposed at the interface with *level-0/level-1* elements. It is assumed that layers of E_{tr} elements are located beyond the critical hot-spots, at which homogenization fails. Hence, the homogenized laws are sufficient at their interfaces with *level-1/level-0* elements. A weak form of the interface displacement continuity is incorporated through the use of Lagrange multipliers on this interface [74, 73]. This results in a weak satisfaction of the interface displacement compatibility and avoids the occurrence of spurious forces that arise if the displacements are strongly coupled.

6.3 Coupling Different Levels in the Concurrent Multi-Scale Algorithm

The concurrent multi-scale analysis requires that all levels be coupled for simultaneously solving for variables in the different computational subdomains. Consequently, the global stiffness matrix and load vectors are derived for the entire computational domain ($\Omega_{het} = \{\Omega_{l0} \cup \Omega_{l1} \cup \Omega_{l2} \cup \Omega_{tr}\}$). The corresponding domain boundary is delineated as $\Gamma_{het} = \{\Gamma_{l0} \cup \Gamma_{l1} \cup \Gamma_{l2}\}$ where $\Gamma_{l0} = \partial\Omega_{l0} \cap \Gamma_{het}$; $\Gamma_{l1} = \partial\Omega_{l1} \cap \Gamma_{het}$; $\Gamma_{l2} = \partial\Omega_{l2} \cap \Gamma_{het}$. Let $\Gamma_{int} = \partial\Omega_{l1} \cap \partial\Omega_{tr}$ delineate the boundary between the *level-1* and transition elements, where the displacement continuity is satisfied using Lagrange multipliers. The incremental form of the equation of principle of virtual work equation for Ω_{het} at the end of an increment, can be written as the sum

of contributions from each individual domain, as

$$
\begin{aligned}
&\int_{\Omega_{l0}} (\Sigma_{ij} + \Delta\Sigma_{ij}) \frac{\partial \delta u_i^{l0}}{\partial x_j}\, d\Omega - \int_{\Gamma_{l0}} (t_i + \Delta t_i)\delta u_i^{l0}\, d\Gamma \\
&+ \int_{\Omega_{l1}} (\Sigma_{ij} + \Delta\Sigma_{ij}) \frac{\partial \delta u_i^{l1}}{\partial x_j}\, d\Omega - \int_{\Gamma_{l1}} (t_i + \Delta t_i)\delta u_i^{l1}\, d\Gamma \\
&\boxed{+ \int_{\Omega_{tr}} (\sigma_{ij} + \Delta\sigma_{ij}) \frac{\partial \delta u_i^{tr}}{\partial x_j}\, d\Omega - \int_{\Gamma_{tr}} (t_i + \Delta t_i)\delta u_i^{tr}\, d\Gamma} \\
&\boxed{+ \int_{\Omega_{l2}} (\sigma_{ij} + \Delta\sigma_{ij}) \frac{\partial \delta u_i^{l2}}{\partial x_j}\, d\Omega - \int_{\Gamma_{l2}} (t_i + \Delta t_i)\delta u_i^{l2}\, d\Gamma} \\
&+\delta \int_{\Gamma_{int}} (\lambda_i^{l0/l1} + \Delta\lambda_i^{l0/l1})(v_i + \Delta v_i - u_i^{l0/l1} - \Delta u_i^{l0/l1}) d\Gamma \\
&+\delta \int_{\Gamma_{int}} (\lambda_i^{tr} + \Delta\lambda_i^{tr})(v_i + \Delta v_i - u_i^{tr} - \Delta u_i^{tr}) d\Gamma = 0
\end{aligned}
\tag{6.7}
$$

The prefix Δ symbolizes increments of the respective variables in the incremental solution process. The superscripts $l0$, $l1$, $l2$, tr correspond to association with the respective level, while the (/) sign refers to variables that could belong to either level. Σ_{ij} are the components homogenized macroscopic stresses obtained from the CDM constitutive model for Ω_{l0} and Ω_{l1}. The applied tractions t_i are at traction boundaries of the respective domains. The boxed parts in equation (6.7) correspond to contributions from *level-2* and transition computational subdomains that are generated from VCFEM solutions of the microstructural regions. Displacement components u_i^{l0}, u_i^{l1}, u_i^{tr} and u_i^{l2} are on the boundaries of elements coinciding with the boundaries of the Ω_{l0}, Ω_{l1}, Ω_{tr} and Ω_{l2} subdomains. An intermediate segment Γ_{int} is added at the interface between the *level-1* and *tr* elements, as shown in figure 6.2. On these segments, displacement components v_i are interpolated with any order polynomial functions, independent of the interpolations on $\partial\Omega^{l0/l1}$ or $\partial\Omega^{tr}$. Even for highly nonhomogeneous displacements, high order interpolations on the intermediate segment are able to smoothen the transition between levels. This has been demonstrated for problems without damage through numerical examples in [74]. The last two terms in equation (6.7) use Lagrange multipliers to facilitate incorporation of a weak form of the interfacial displacement continuity on Γ_{int}. $\lambda^{l0/l1}$ and λ^{tr} are vector columns of Lagrange multipliers belonging to domains $\Omega_{l0/l1}$ and Ω_{tr} respectively at Γ_{int}. The Euler's equations, obtained from setting the coefficients of δv_i, $\delta\lambda_i^{l0/l1}$ and $\delta\lambda_i^{tr}$ to zero respectively in the principle

of virtual work (6.7), are

$$\lambda_i^{l0/l1} + \Delta\lambda_i^{l0/l1} = (\sigma_{ij} + \Delta\sigma_{ij})^{l0/l1} n_j = -(\lambda_i^{tr} + \Delta\lambda_i^{tr}) = -(\sigma_{ij} + \Delta\sigma_{ij})^{tr} n_j$$

$$(u_i + \Delta u_i)^{l0/l1} = (u_i + \Delta u_i)^{tr} = (v_i + \Delta v_i) \tag{6.8}$$

where n_i is the unit normal vector and $\lambda_i^{l0/l1}$ and λ_i^{tr} correspond to the interfacial traction components on $\partial\Omega_{l0/l1}$ and $\partial\Omega_{tr}$ respectively. The displacements v_i and the Lagrange multipliers $\lambda_i^{l0/l1}$ and $\lambda_i^{l2/tr}$ on the intermediate boundary segment are interpolated from nodal values using suitably assumed shape functions as:

$$\{\mathbf{v}\} = [L_{int}]\{\mathbf{q}_{int}\} \quad , \quad \{\boldsymbol{\lambda}^{l0/l1}\} = [L_{\lambda^{l0/l1}}]\{\boldsymbol{\Lambda}_{l0/l1}\} \quad , \quad \{\boldsymbol{\lambda}^{tr}\} = [L_{\lambda^{tr}}]\{\boldsymbol{\Lambda}_{tr}\} \tag{6.9}$$

The displacements u_i^{l0} and u_i^{l1} in each *level-0* and *level-1* elements are interpolated by the standard or hierarchical Legendre polynomials based shape functions as:

$$\begin{aligned} \{\mathbf{u}\}^{l0} &= [\mathbf{N}_{l0}]\{\mathbf{q}_{l0}\} = [\mathbf{N}_{l0}^I \ \mathbf{N}_{l0}^O] \left\{ \begin{array}{c} \mathbf{q}_{l0}^I \\ \mathbf{q}_{l0}^O \end{array} \right\} \\ \{\mathbf{u}\}^{l1} &= [\mathbf{N}_{l1}]\{\mathbf{q}_{l1}\} = [\mathbf{N}_{l1}^I \ \mathbf{N}_{l1}^O] \left\{ \begin{array}{c} \mathbf{q}_{l1}^I \\ \mathbf{q}_{l1}^O \end{array} \right\} \end{aligned} \tag{6.10}$$

As shown in figure 6.2, the generalized displacements in the *level-0* and *level-1* elements are subdivided into two classes: (i) those at nodal points, which interface with transition elements, and (ii) those at all other nodes. Generally, only *level-1* elements will interface with transition elements because of the sequence of introduction of computational levels. The generalized displacements $\mathbf{q}_{l0/l1}^I$ corresponds to the nodal degrees of freedom in level-0/level-1 elements at the interface with transition elements, while $\mathbf{q}_{l0/l1}^O$ correspond to the remaining degrees of freedom in these elements. The solution of the algebraic form of equation (6.7) is obtained using the Newton Raphson iterative solver. Setting up the tangent stiffness matrix requires consistent linearization by taking directional derivative of equation (6.7) along incremental displacement vectors

$\Delta\mathbf{u}$ and $\Delta\mathbf{v}$, and the Lagrange multipliers $\Delta\lambda$. For the $i-$th iteration in the solution of the incremental variables, assembled matrix equations derived from equation (6.7) has the following structure.

$$\begin{bmatrix} \mathbf{K}^{\mathrm{I,I}}_{l0/l1} & \mathbf{K}^{I,O}_{l0/l1} & 0 & 0 & 0 & \mathbf{P}_{l0/l1} & 0 \\ \mathbf{K}^{\mathrm{O,I}}_{l0/l1} & \mathbf{K}^{O,O}_{l0/l1} & 0 & 0 & 0 & 0 & 0 \\ 0 & 0 & \mathbf{K}^{\mathrm{I,I}}_{tr} & \mathbf{K}^{\mathrm{I,O}}_{tr} & 0 & 0 & \mathbf{P}_{tr} \\ 0 & 0 & \mathbf{K}^{\mathrm{O,I}}_{tr} & \mathbf{K}^{\mathrm{O,O}}_{l2/tr} & 0 & 0 & 0 \\ 0 & 0 & 0 & 0 & 0 & \mathbf{Q}_{l0/l1} & \mathbf{Q}_{tr} \\ \mathbf{P}^T_{l0/l1} & 0 & 0 & 0 & \mathbf{Q}^T_{l0/l1} & 0 & 0 \\ 0 & 0 & \mathbf{P}^T_{tr} & 0 & \mathbf{Q}^T_{tr} & 0 & 0 \end{bmatrix}^i \begin{Bmatrix} \Delta\mathbf{q}^{\mathrm{I}}_{\mathrm{l0/l1}} \\ \Delta\mathbf{q}^{\mathrm{O}}_{\mathrm{l0/l1}} \\ \Delta\mathbf{q}^{\mathrm{I}}_{\mathrm{tr}} \\ \Delta\mathbf{q}^{\mathrm{O}}_{\mathrm{l2/tr}} \\ \Delta\mathbf{q}_{int} \\ \Delta\mathbf{\Lambda}_{\mathrm{l0/l1}} \\ \Delta\mathbf{\Lambda}_{\mathrm{tr}} \end{Bmatrix}^i = \begin{Bmatrix} \Delta\mathbf{F}^{\mathrm{I}}_{\mathrm{l0/l1}} \\ \Delta\mathbf{F}^{\mathrm{O}}_{\mathrm{l0/l1}} \\ \Delta\mathbf{F}^{\mathrm{I}}_{\mathrm{tr}} \\ \Delta\mathbf{F}^{\mathrm{O}}_{\mathrm{l2/tr}} \\ \Delta\mathbf{F}_{int} \\ \Delta\mathbf{F}_{\lambda l0/l1} \\ \Delta\mathbf{F}_{\lambda 12/tr} \end{Bmatrix}^i \tag{6.11}$$

As explained before, the superscript I represents quantities associated with nodal points at the interface with transition elements while superscript O indicate association with nodes at other regions. The two notations in the superscript separated by comma, represents the node coupling effect. For example, the superscript I, O corresponds to the coupling between the non-interface and interface nodes. The stiffness submatrices $[\mathbf{K}_{l0/l1}]$ and sub-vector $\{\mathbf{F}_{l0/l1}\}$ correspond to those for the *level-0* and *level-1* elements and are expressed as

$$\begin{aligned} (K_{l0/l1})_{m\alpha n\beta} &= \int_{\Omega_{l0}\cup\Omega_{l1}} \frac{\partial N_\alpha}{\partial x_k}\frac{\partial \Sigma_{mn}}{\partial e_{kl}}\frac{\partial N_\beta}{\partial x_l}d\Omega \\ (\Delta\mathbf{F}_{l0/l1})_{m\alpha} &= \int_{\Gamma_t}(t_m+\Delta t_m)N_\alpha d\Gamma + \int_{\Gamma_{int}}(\lambda_i+\Delta\lambda_i)N_\alpha d\Gamma \\ &\quad - \int_{\Omega_{l0}\cup\Omega_{l1}}(\Sigma_{ij}+\Delta\Sigma_{mn})\frac{\partial N_\alpha}{\partial x_n}d\Omega \end{aligned} \tag{6.12}$$

The subscripts (m, n) correspond to the degrees of freedom while (α, β) correspond to the node numbers in the element. These matrices and vectors are further divided based on the classification of the I and O nodes. The coupling between the *level-0/level-1* and *tr* elements is achieved through the $[\mathbf{P}]$ and $[\mathbf{Q}]$ matrices, which

may be expressed as

$$
\begin{aligned}
(P_{l0/l1})_{m\alpha n\beta} &= -\int_{\Gamma_{int}} \mathbf{N}^T_{m\alpha}(\mathbf{L}_{\lambda^{l0/l1}})_{n\beta} d\Gamma \\
(P_{tr})_{m\alpha n\beta} &= -\int_{\Gamma_{int}} \mathbf{N}^T_{m\alpha}(\mathbf{L}_{\lambda^{l2/tr}})_{n\beta} d\Gamma \\
(Q_{l0/l1})_{m\alpha n\beta} &= \int_{\Gamma_{int}} (\mathbf{L}^T_{int})_{m\alpha}(\mathbf{L}_{\lambda^{l0/l1}})_{n\beta} d\Gamma \\
(Q_{tr})_{m\alpha n\beta} &= \int_{\Gamma_{int}} (\mathbf{L}^T_{int})_{m\alpha}(\mathbf{L}_{\lambda^{tr}})_{n\beta} d\Gamma
\end{aligned}
\tag{6.13}
$$

Contributions to the load vector $\{\mathbf{F}\}$ due to coupling between *level-0/level-1* and *tr* elements are given as

$$
\begin{aligned}
(\Delta F_{int})_{m\alpha} &= -\int_{\Gamma_{int}} (L^T_{int})_\alpha (\lambda^{l0/l1} + \Delta\lambda^{l0/l1})_m d\Gamma - \int_{\Gamma_{int}} (L^T_{int})_\alpha (\lambda^{l2/tr} + \Delta\lambda^{l2/tr})_m d\Gamma \\
(\Delta F_{\lambda l0/l1})_{m\alpha} &= -\int_{\Gamma_{int}} (L^T_{\lambda^{l0/l1}})_\alpha \{v_m + \Delta v_m - (u_{l0/l1})_m - \Delta(u_{l0/l1})_m\} d\Gamma \\
(\Delta F_{\lambda l2/tr})_{m\alpha} &= -\int_{\Gamma_{int}} (L^T_{\lambda^{tr}})_\alpha \{v_m + \Delta v_m - (u_{l2/tr})_m - \Delta(u_{l2/tr})_m\} d\Gamma
\end{aligned}
\tag{6.14}
$$

Finally, the stiffness $[\mathbf{K_{l2/tr}}]$ and the load vector $\{\mathbf{F_{l2/tr}}\}$ for *level-2* and *tr* elements are obtained by VCFEM calculations followed by static condensation to represent the virtual work in terms of the boundary terms only.

6.3.1 Modified Voronoi Cell FEM Formulation for a RVE in Level-1 Elements

Details of the Voronoi Cell FEM are provided in [80, 35, 53] and have been summarized in the appendix section 6.7.2. As discussed in section 6.2.2, the post-processing phase for *level-1* elements require the evaluation of different variables in the RVE from known values of macroscopic strains. A small variant of the formulation in equation (6.40) enables this execution. The energy functional for a RVE (Y) with Y-periodic displacements and Y-anti-periodic tractions on the boundary, and imposed macroscopic strain ($e_{ij} + \Delta e_{ij}$), may be written

as

$$\Pi_e^{RVE} = -\int_{Y_m} \frac{1}{2} S^m_{ijkl} \Delta\sigma^m_{ij} \Delta\sigma^m_{kl}\ dY - \int_{Y_m} S^m_{ijkl}\sigma^m_{kl}\Delta\sigma^m_{ij}\ dY \tag{6.15}$$

$$-\int_{Y_c} \frac{1}{2} S^c_{ijkl} \Delta\sigma^c_{ij} \Delta\sigma^c_{kl}\ dY - \int_{Y_c} S^c_{ijkl}\sigma^c_{kl}\Delta\sigma^c_{ij}\ dY$$
$$+\int_{\partial Y_e} (\sigma^m_{ij} + \Delta\sigma^m_{ij}) n^e_j (u^e_i + \Delta u^e_i) d\partial Y - \int_{\partial Y^m_c} (\sigma^m_{ij} + \Delta\sigma^m_{ij}) n^c_j (u^m_i + \Delta u^m_i) d\partial Y$$
$$+\int_{\partial Y^c_c} (\sigma^c_{ij} + \Delta\sigma^c_{ij}) n^c_j (u^c_i + \Delta u^c_i) d\partial Y - \int_{\partial Y_c} \int_{u^m_n - u^c_n}^{u^m_n + \Delta u^m_n - u^c_n - \Delta u^c_n} T^m_n d(u^m_n - u^c_n) d\partial Y$$
$$-\int_{\partial Y_c} \int_{u^m_t - u^c_t}^{u^m_t + \Delta u^m_t - u^c_t - \Delta u^c_t} T^m_t d(u^m_t - u^c_t) d\partial Y$$
$$+\boxed{\int_{Y_m} (e_{ij} + \Delta e_{ij}) \Delta\sigma^m_{ij} dY + \int_{Y_c} (e_{ij} + \Delta e_{ij}) \Delta\sigma^c_{ij} dY} \tag{6.16}$$

The boxed term corresponds to the additional energy due to the imposed macroscopic strain field on the RVE region Y. The Euler-Lagrange equations corresponding to this energy functional are:

$$\varepsilon_{ij}(\mathbf{x},\mathbf{y}) + \Delta\varepsilon_{ij}(\mathbf{x},\mathbf{y}) = S_{ijkl}(\sigma_{ij} + \Delta\sigma_{ij}) = (e_{ij}(\mathbf{x}) + \Delta e_{ij}(\mathbf{x}))$$
$$+\frac{1}{2}[\frac{\partial(u_i(\mathbf{y}) + \Delta u_i(\mathbf{y}))}{\partial y_j} + \frac{\partial(u_j(\mathbf{y}) + \Delta u_j(\mathbf{y}))}{\partial y_i}] \quad \forall\ \mathbf{y} \in Y_m,\ Y_c \tag{6.17}$$

$$u_i \text{ is } Y\text{-periodic and } \sigma^m_{ij} n^e_j \text{ is } Y\text{-anti-periodic on } \partial Y_e \tag{6.18}$$

The corresponding weak form of the element kinematic relation is written in a matrix equation form as

$$\begin{bmatrix} \int_{\Omega_m} [\mathbf{P}^m]^T [\mathbf{S}^m] [\mathbf{P}^m] d\Omega & [\mathbf{0}] \\ [\mathbf{0}] & \int_{\Omega_c} [\mathbf{P}^c]^T [\mathbf{S}^c] [\mathbf{P}^c] d\Omega \end{bmatrix} \begin{Bmatrix} \boldsymbol{\beta}^m + \triangle\boldsymbol{\beta}^m \\ \boldsymbol{\beta}^c + \triangle\boldsymbol{\beta}^c \end{Bmatrix} =$$
$$\begin{bmatrix} \int_{\partial\Omega_e} [\mathbf{P}^m]^T [\mathbf{n}^e] [\mathbf{L}^e] d\partial\Omega & -\int_{\partial\Omega_c} [\mathbf{P}^m]^T [\mathbf{n}^c] [\mathbf{L}^c] d\partial\Omega & [\mathbf{0}] \\ [\mathbf{0}] & [\mathbf{0}] & \int_{\partial\Omega_c} [\mathbf{P}^c]^T [\mathbf{n}^c] [\mathbf{L}^c] d\partial\Omega \end{bmatrix} \begin{Bmatrix} \mathbf{q}^e + \triangle\mathbf{q}^e \\ \mathbf{q}^m + \triangle\mathbf{q}^m \\ \mathbf{q}^c + \triangle\mathbf{q}^c \end{Bmatrix}$$
$$- \begin{Bmatrix} \int_{\Omega_m} [\mathbf{P}^m]^T \{\mathbf{e} + \Delta\mathbf{e}\} d\Omega \\ \int_{\Omega_c} [\mathbf{P}^c]^T \{\mathbf{e} + \Delta\mathbf{e}\} d\Omega \end{Bmatrix} \tag{6.19}$$

or in a condensed form

$$[\mathbf{H}^e]\{\beta + \triangle\beta\} = [\mathbf{G}^e]\{\mathbf{q} + \triangle\mathbf{q}\} - \{\mathbf{R}_1^e\} \tag{6.20}$$

This relation is then substituted in equation (6.44) for obtaining the RVE based solutions. It should be noted that displacement periodicity is imposed on the RVE boundary for solving this problem.

6.4 Criteria for Adaptive Mesh Refinement and Level Transitions

In the application of the multi-level model, the following criteria are used for mesh-refinement and level transitions due to discretization and modeling error respectively. Many of these adaptation criteria are based on the physics of the problem in consideration, since rigorous mathematical error bounds are scarce (or even non-existent) for these nonlinear problems. Consequently they are nonunique and other indicators may be used if appropriate.

6.4.1 Refinement of Level-0 and Level-1 Meshes by h-Adaptation

The computational models in *level-0* and *level-1* subdomains are enriched by *h-adaptation* based mesh refinement to reduce discretization 'error'. The $h-$adaptation procedure subdivides candidate macroscopic elements into smaller elements to reduce a suitably chosen error. It is necessary to impose boundary displacement compatibility constraint conditions between contiguous divided and undivided elements in this method [82]. This local mesh enrichment is intended to reduce discretization error and to identify regions of modeling error by zooming in on localization regions with evolving gradients. For CDM based evolving problems, an adaptation criterion is formulated in this paper in terms of the jump in traction across adjacent

element boundaries that signifies local stress gradients. The condition is stated as:

Refine element 'e', if the traction jump error across the element

satisfies the condition: $E_e^{tj} \geq C_1 * E_{avg}^{tj}$,

where

$$E_{avg}^{tj} = (\frac{\sum_{i=1}^{NE}(E_e^{tj})^2}{NE})^{1/2} \quad \text{and} \quad (E^{tj})_e^2 = \frac{\int_{\partial\Omega_e}\left([[T_x]]^2 + [[T_y]]^2\right) d\partial\Omega}{\int_{\partial\Omega_e} d\partial\Omega} \tag{6.21}$$

Here NE is the total number of *level-0* and *level-1* elements in the entire computational domain, T_x, T_y are the components of element boundary tractions in the x and y directions and [[.]] is the jump operator across element boundary $\partial\Omega_e$. A factor C_1 (< 1) has been chosen from numerical experiments.

6.4.2 Criteria for Switching from Level-0 to Level-1 Elements

Level-0 to *level-1* element transition takes place according to criteria signaling departure from conditions of the homogenizability that are based on macroscopic variables in the continuum model of *level-0* elements. The degrading dissipation energy W_d in the CDM model is a strong indicator of localized damage evolution. Consequently, a criterion is formulated as:

Switch element 'e' from *level-0* to *level-1* if :

$$E_e^{gde} * (W_d)_e > C_2 * E_{max}^{gde} * (W_d)_{max} \tag{6.22}$$

where E_i^{gde} is the norm of the local gradient of the degrading dissipation energy $(W_d)_e$, expressed as:

$$E_e^{gde} = \sqrt{(\frac{\partial(W_d)_e}{\partial x_1})^2 + (\frac{\partial(W_d)_e}{\partial x_2})^2} \tag{6.23}$$

E_{max}^{gde} is the maximum value of E_e^{gde} for all elements and C_2 (< 1) is a prescribed factor. The criterion (6.22) is helpful for seeking out regions with high gradients of W_d in regions of high W_d itself. In a previous paper by the authors [74], the gradient E_e^{gde} was expressed in terms of the maximum difference in the damage for

neighboring elements as $E_e^{gde} = \text{Max}|(W_d)_e - (W_d)_{\text{adjacent}}|$. A more accurate definition of the local gradient is adopted in the present work, using the Zienkiewicz-Zhu (ZZ) gradient patch recovery method [107]. In this method, interpolation of W_d is assumed in the form of a polynomial over a patch of elements adjoining a nodal point in a *level-0* element. The least square minimization process leads to the local matrix equation

$$\sum_{e=1}^{ne}[\hat{\mathbf{N}}_e(x_1,x_2)]^T[\hat{\mathbf{N}}_e(x_1,x_2)]\{\mathbf{a}\} = \sum_{e=1}^{ne}[\hat{\mathbf{N}}_e(x_1,x_2)]^T(W_d)_e(x_1,x_2) \tag{6.24}$$

where $[\hat{\mathbf{N}}_e(x_1,x_2)]$ is a matrix containing polynomial interpolation terms and ne is the number of elements in the patch. The equation (6.24) is solved for the coefficients $\{\mathbf{a}\}$. The gradients of W_d in each element are calculated from the nodal values using element shape functions as

$$\frac{\partial W_d}{\partial x_1} = \sum_{\alpha=1}^{4}\frac{\partial N_\alpha}{\partial x_1}(W_d)_\alpha, \quad \frac{\partial W_d}{\partial x_2} = \sum_{\alpha=1}^{4}\frac{\partial N_\alpha}{\partial x_2}(W_d)_\alpha \tag{6.25}$$

6.4.3 Criteria for Switching from Level-1 to Level-2 Elements

For elements in which macroscopic nonuniformity has been established according to equation (6.22), departure from RVE periodicity is taken as an indicator for activating a switch from *level-1* to *level-2*. The switching criterion is developed in terms of evolving variables, e.g. the averaged strain at the fiber-matrix interface in the local microstructural RVE. The averaged strain is stated as:

$$D_{ij} = \frac{1}{\int_{\cup\partial\Omega_c} d\partial\Omega}\int_{\cup\partial\Omega_c}\epsilon_{ij}d\partial\Omega = \frac{1}{2\Omega_c\int_{\cup\partial\Omega_c} d\partial\Omega}\int_{\cup\partial\Omega_c}([u_i]n_j + [u_j]n_i)d\partial\Omega \tag{6.26}$$

where the integral is evaluated over all the fiber-matrix interfaces in the RVE. The jump in displacement across the fiber-matrix interface with a normal n_i is denoted by $[u_i]$. For perfect interfaces $[u_i]$ will be zero. Thus, D_{ij} corresponds to the contributions to macroscopic strain due to damage only, and $D_{ij} = 0$ in the absence of damage. Departure from periodicity will result in a significantly different averaged strain D_{ij} in response to different conditions on the boundary of the microstructural region. For example, let $D_{ij}^{e,l2}$ correspond to the solution of a boundary value problem of the local microstructure included in a *level-2*

element (see figure 6.2) subject to boundary displacements that have been obtained from the macroscopic *level-0/1* analysis. The scale of the microstructure is relevant in this analysis since periodicity is not imposed on the boundary. On the other hand, let $D_{ij}^{e,RVE}$ be from the solution of a boundary value problem of the local RVE with imposed macroscopic strains and subjected to periodic boundary displacements constraints. The difference in these two strains for a *level-1* element e may be quantified as

$$E_e^{dper} = \max(|D_{11}^{e,l2} - D_{11}^{e,RVE}|, |D_{22}^{e,l2} - D_{22}^{e,RVE}|, |D_{12}^{e,l2} - D_{12}^{e,RVE}|) \tag{6.27}$$

For evaluating $D_{ij}^{e,l2}$ in a given step of the incremental solution, only the increments in the present step are calculated by the *level-1* macroscopic displacement boundary conditions. It is assumed that the RVE-based solution is valid all the way upto (but excluding) the present step. The departure from periodicity is measured in terms of the difference in averaged strains E_e^{dper}, and hence the criterion,

Switch element 'e' from *level-1* to *level-2* if :

$$E_e^{dper} > C_3 D_{max}^{RVE} \tag{6.28}$$

where D_{max}^{RVE} is the maximum value of $|D_{ij}^{e,RVE}|$ for all the *level-1* elements in the computational domain.

Remark: Once the regions of *level-2* and *transition* elements have been identified, it is important to update the local micromechanical states of stress, strain and damage to the current state. This step should precede the coupled concurrent analysis. For this analysis, the history of the macroscopic displacement solution on the *level-0/level-1* element boundary prior to the switch is utilized. The local micromechanical (VCFEM) boundary value problem for the *level-2* element is incrementally solved from the beginning to obtain the history of stresses, strains and damage in the microstructure from the macroscopic boundary displacement history.

6.5 Numerical Examples with the Adaptive Multilevel Model

Two sets of numerical examples are solved to study the effectiveness of the multi-level computational model for composite materials.

6.5.1 Multi-level Model vs. Micromechanical Analysis

This example is aimed at understanding the effectiveness of the multi-level model in analyzing a nonuniform composite microstructure by comparing its predictions with those by pure micromechanical analysis. It is computationally intensive to conduct pure micromechanical analysis with evolving damage for very large microstructural regions. Consequently a computational domain with a small population of fibers, as shown in the optical micrograph of figure 6.4(a), is considered. The micrograph is for a polymer matrix composite with a random dispersion of uniaxial fibers. The dimensions of the micrograph analyzed are $100\mu m \times 70.09\mu m$, containing 264 circular fibers of diameter $1.645\mu m$ each, corresponding to a volume fraction of 32%. Though the domain may not be adequate for a clear separation between continuum and micromechanical regions (since relatively large regions are needed to materialize the RVE), the results of this example are enough to show the effectiveness of the overall framework.

The optical micrograph is mapped onto a simulated microstructure with circular fibers that is tessellated into a mesh of 264 Voronoi cell elements, as shown in figure 6.4(b). The constituent materials in the composite system are an epoxy resin matrix, stainless steel reinforcing fibers and a very thin film of freekote ($< 0.1\mu m$) at the fiber-matrix interface. The freekote imparts a weak strength to the steel-epoxy interface, which allows a stable growth of the debond crack for experimental observation. The experimental methods of material and interface characterization have been discussed in [35]. Both the matrix and fiber materials are characterized by isotropic elasticity properties. The matrix material has a Young's modulus, $E_{epoxy} = 4.6\ GPa$ and Poisson's ratio, $\nu_{epoxy} = 0.4$, while the fiber material has a Young's modulus, $E_{steel} = 210\ GPa$ and Poisson's ratio, $\nu_{steel} = 0.3$. A bilinear cohesive law described in [53, 68] is used in this analysis for modeling

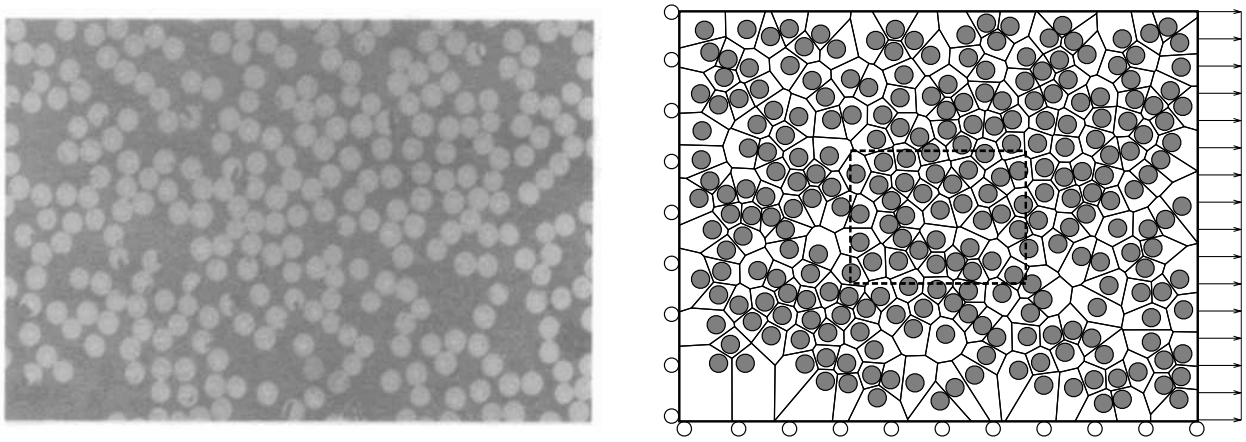

(a) (b)

Figure 6.4: (a) Optical micrograph of a steel fiber-epoxy matrix composite with 264 fibers (b) the simulated computational model with a Voronoi cell mesh

the fiber-matrix interface. In this model, the normal and tangential tractions are given as

$$T_n = \frac{\partial \phi}{\partial \delta_n} = \frac{\partial \phi}{\partial \delta}\frac{\partial \delta}{\partial \delta_n} = \begin{cases} t\delta_n & \text{if} \quad \delta \leq \delta_c \\ t\delta_n & \text{if} \quad \delta_c < \delta \leq \delta_e \\ 0 & \text{if} \quad \delta > \delta_e \end{cases}$$

$$T_t = \frac{\partial \phi}{\partial \delta_t} = \frac{\partial \phi}{\partial \delta}\frac{\partial \delta}{\partial \delta_t} = \begin{cases} t\beta^2\delta_t & \text{if} \quad \delta < \delta_c \\ t\beta^2\delta_t & \text{if} \quad \delta_c < \delta \leq \delta_e \\ 0 & \text{if} \quad \delta > \delta_e \end{cases} \tag{6.29}$$

where t is a bilinear function of the interfacial separation as

$$t = \begin{cases} \frac{\sigma_{max}}{\delta_c}\delta & \forall \delta < \delta_c \\ \frac{\delta - \delta_e}{\delta_c - \delta_e}\sigma_{max} & \forall \delta \geq \delta_c \end{cases} \tag{6.30}$$

The unloading behavior in the hardening region is linear following the loading path. In the softening region,

the unloading proceeds along a different linear path from the current position to the origin with a reduced stiffness, for which the $t - \delta$ relation is

$$t = \frac{\sigma_{max}}{\delta_{max}} \frac{\delta_{max} - \delta_e}{\delta_c - \delta_e} \delta \qquad \delta_c < \delta_{max} < \delta_e \text{ and } \delta < \delta_{max} \tag{6.31}$$

It is expected that the degrading dissipation energy W_d in the macroscopic CDM model depends on the cohesive parameters in the microstructural debonding model. A square RVE with a single circular fiber is simulated for interfacial debonding with three different sets of cohesive parameters, as shown in the inset of figure 6.5. The cohesive energies are the same for all cases. However in one case, the critical separation length δ_e is increased while in the other, the corresponding peak stress σ_{max} is reduced. The figure 6.5 infers that while δ_e has a small influence on W_d, the effect of σ_{max} is certainly significant, at least in the early stages of straining.

The cohesive parameters used in this paper are: $\sigma_{max} = 0.005$ GPa, $\delta_c = 5.1 \times 10^{-5}\ m$ and $\delta_e = 3.1 \times 10^{-4}\ m$. The microstructure is loaded in tension in the horizontal direction with a displacement of $0.1 \mu m$ that is uniformly increased in 20 equal increments, corresponding to a total strain of $\epsilon_{11} = 0.1\%$. The displacement boundary condition is imposed along the right edge, as shown in figure 6.4(b).

Micromechanical analysis by VCFEM

The pure micromechanical VCFEM solution using the mesh of figure 6.4(b) has been presented in [53] and are used here as reference solutions for the multi-scale simulation. Figure 6.6(a) shows the contour plot of microscopic stress σ_{xx} at the final step of the micromechanical simulation with a depiction of interfacial debonding. The right side of the microstructure shows significant concentrated damage with this load. The debonding initiates at the top and percolates to the bottom of the microstructure along a narrow band.

Multi-Scale Analysis with the Multi-Level Model

Multi-scale analysis is performed by the concurrent multi-level computational model and the results are compared with those from the micromechanical VCFEM analysis. For the multi-level model, the entire com-

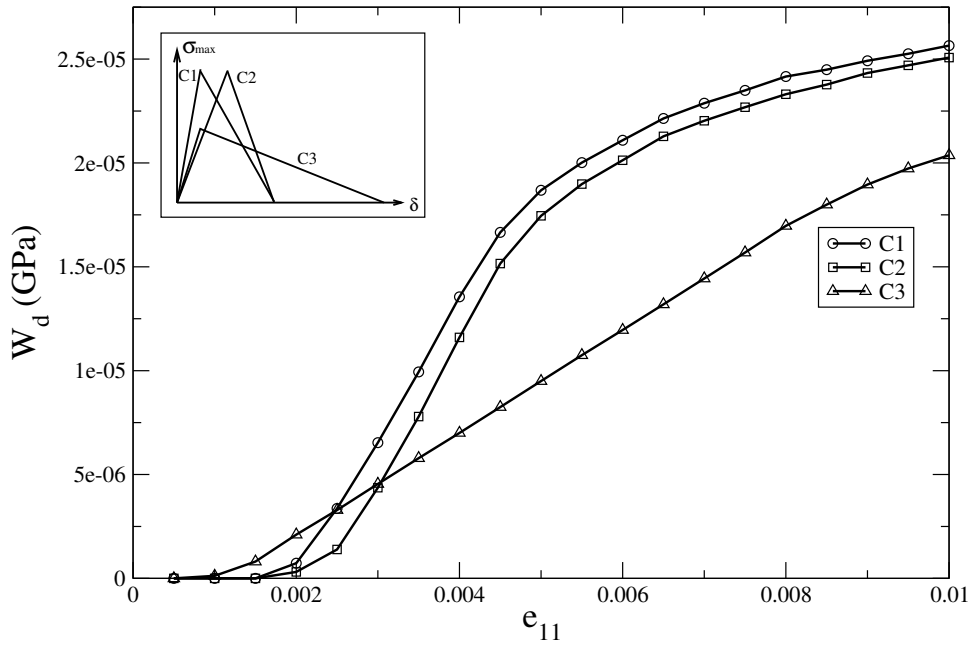

Figure 6.5: The degrading dissipation energy W_d as a function of strain, evaluated for different cohesive zone parameters in the bilinear cohesive law

putational region of 264 fibers is first divided into 9 macroscopic finite elements as shown in figure 6.7(a). For evaluating the homogenized constitutive properties for each of element, statistically equivalent representative volume element or *SERVE* for the microstructure underlying each macroscopic element is first identified. Various statistical methods have been used to determine the size scale of the RVE and the number of inclusions contained in it [70, 37, 86, 98]. Rigorous methods of evaluating statistically equivalent representative volume elements by a combination of statistical methods and micromechanical analyses have been conducted by the first author in [83, 90]. However, since the number of fibers in the micrograph is limited in this exercise, a simpler assumption is made. The SERVE for each element is assumed to consist of all the fibers belonging to that element. For example, to generate the SERVE for an element window in the micrograph of figure 6.4(b), all fibers whose centers are located within this window are first identified as constituents of the RVE. This is shown by the aggregate of black fibers in figure 6.8(a). The homogenization method, discussed in sections 6.2.2 and 6.3, requires a periodic distribution of the RVE and this is achieved by locally

repeating the arrangement of fibers in both the x_1 and x_2 directions for a period length in figure 6.8(a). This means that for each fiber identified in the element, at (x_1, x_2), four identical fibers are placed at the locations $(x_1 \pm X_1, x_2), (x_1, x_2 \pm X_2)$ where (X_1, X_2) are periods in the two directions. The period lengths X_1, X_2 are selected such that the volume fraction of RVE matches that of the local microstructure. Finally, the domain is tessellated into a network of Voronoi cells as shown in figure 6.8(b) Tessellation provides a natural way of creating periodic SERVE boundary. For non-uniform fiber arrangements, the SERVE boundary consists of non-straight line edges. The nodes on this SERVE boundary are periodic, i.e. for every boundary node a periodic pair can be identified on the boundary at a distance of one period along each of the coordinate directions. In figure 6.8(b), the node pairs are identified as AA, BB etc. The number of fibers and their distribution in the SERVE of each macroscopic element is shown in figure 6.7(a).

Since the number of elements in this exercise is very small (only 9), *level-0* simulations with the CDM model is bypassed in the multi-level analysis. All elements are *level-1* at the start of the multi-level simulation. Switch to *level-2* elements is made in accordance with equations (6.27) and (6.28) with $C_2 = 0.2$. However the $D_{ij}^{e,l2} - D_{ij}^{e,RVE}$ terms for each element in equation (6.27) are replaced by the difference in RVE based averaged strains between adjacent elements $D_{ij}^{e1,RVE} - D_{ij}^{e2,RVE}$. Also, as opposed to an entire macroscopic element, a single layer of transition Voronoi cell elements is included between the *level-1* and *level-2* elements. In figure 6.7(b) the Voronoi elements containing the grey fibers constitute the *transition* layer, while those containing the black fibers belong to *level-2*. An interface segment Γ_{int} is inserted between the *transition* and *level-1* elements at a distance $L_{tr/l2}$ from the right edge. Convergence properties of the multi-level model are studied by considering two cases with $\frac{L_{tr/l2}}{L} = 0.35$ and $\frac{L_{tr/l2}}{L} = 0.45$. This is achieved by changing the size of the initial level-1 elements.

As depicted in figure 6.7(b), only three elements (3, 6 and 9) at the right side of the initial mesh switch from *level-1* to *level-2*. A comparison of results by (a) VCFEM based micromechanical analyses (all *level-2* elements) , (b) homogenization based macroscopic analysis (all *level-1* elements), and (c) concurrent multi-level analysis (*level-1* and *level-2* elements) for $\frac{L_{tr/l2}}{L} = 0.35$ and 0.45 is made. Contour plots of σ_{11} (GPa) showing interfacial debonding at the end of the simulation are shown for the concurrent multi-scale analysis

in figure 6.6(b,c). The discrepancy in the damage path predicted by the micromechanical analysis and the multi-level analysis reduces sharply with increasing $\frac{L_{tr/l2}}{L}$ value. This can be attributed to the fact, that the damage path is very sensitive to the macro-micro interface conditions. Since the sample size is small and there is no real periodicity in the microstructure, the proximity of the *level-1* boundary to the damage localization zone alters the local boundary conditions. However as this distance is increased, the microscopic stress distribution, debonding pattern and damage zone replicates the real event observed in micromechanical analysis. The distribution of the micromechanical stresses σ_{11}, generated by pure micromechanical and multi-level analyses, are plotted along a line through the middle of micrograph in figure 6.9. The micromechanical stresses show only minor oscillations about an averaged value of the 0.005 GPa in the region to the left of the *level-1-level-2* interface. In the region to the right, where damage is predominant, there is clearly a convergence of the stresses with increasing $\frac{L_{tr/l2}}{L}$ value.

The macroscopic or averaged stress-strain response for element 1 (always *level-1*) and element 9 (changes levels) are plotted in figures 6.10. For the micromechanical problems with debonding, the volume averaged stresses and strains are evaluated by averaging the local fields over the microscopic domain as:

$$\Sigma_{ij} = \frac{1}{\Omega}\int_{\Omega} \sigma_{ij}(x_1, x_2)d\Omega \qquad \text{and} \qquad e_{ij} = \frac{1}{\Omega}\int_{\Omega} \epsilon_{ij}(x_1, x_2)d\Omega - D_{ij} \tag{6.32}$$

where D_{ij} is the strain jump defined in equation (6.26). The results for all the models are in good agreement for the element 1, where there is no significant microstructural damage. The small difference is due to the periodicity constraints imposed on the microstructure. Also there is a difference between the results of case 1: $\frac{L_{tr/l2}}{L} = 0.35$ and case 2: $\frac{L_{tr/l2}}{L} = 0.45$, due to the interface conditions at Γ_{int}. However, as is expected the results are quite different for element 9, where significant damage is observed in figure 6.6. The *level-1* analysis shows significant deviation from the micromechanical analysis due to imposed periodicity in the damage zone. Once again, the results improve significantly with increasing $\frac{L_{tr/l2}}{L}$ ratio.

6.5.2 A Composite Double Lap Joint with Microstructural Debonding

Adhesive bonded joints are considered as preferred alternatives to fasteners for joining structural components due to their light weight. However, adhesively bonded structures consisting of different materials, can induce high stresses near the interface leading to failure initiation by interfacial debonding. A double-lap bonded joint with boron-epoxy composites as adherents, is analyzed in this example. An adhesive shown as ABCD in figure 6.11(a) is used to bond the two composite materials. Only a quarter of the joint is modeled from considerations of symmetry in boundary and loading conditions. For boundary conditions, the displacement component u_1 is set to zero along the face $x_2 = 0$ implying symmetry about the x_1 axis. The displacement components u_1 and u_2 along the face $x_1 = 8h$ are set to zero corresponding to a fixed edge. A tensile displacement u_1 is applied on the face of the lower ply at $x_1 = 0$. Both plies above and below the adhesive are made of unidirectional boron fiber- epoxy matrix composite materials. The fibers are uniformly arranged in a square array in the microstructure, implying a square unit cell with a single circular fiber. The epoxy matrix has a Youngs modulus $E = 4.6$ GPa and Poisson's ratio $\nu = 0.4$, while boron fibers have a Youngs modulus $E = 210$ GPa and Poisson's ratio $\nu = 0.3$. The material properties of the isotropic adhesive are: Young's modulus $E = 3.45$ GPa and Poisson's ratio $\nu = 0.34$. The bilinear cohesive law parameters for the matrix-fiber interface are: $\sigma_{max} = 0.02$ GPa, $\delta_c = 5.0 \times 10^{-5}$ m and $\delta_e = 20.0 \times 10^{-4}$ m.

Multi-level analysis for model with 450 fibers

In this model, the top ply above the adhesive consists of 10 rows of fiber, while the bottom row consists of 5 rows resulting in a total of 450 fibers. The microstructural volume fraction of fibers is $V_f = 20\%$. The applied displacement on the face at $x_1 = 0$, is uniformly increased from zero to $u_1 = 1.2 \times 10^{-3}h$ in 15 uniform increments. The number of fibers is kept low in this example, such that a micromechanical analysis can be easily done for this example with a mesh of 450 Voronoi elements, each of which is a square unit cell. The micromechanics solutions are used as a reference to determine the accuracy of multi-scale simulations. Three different approaches are used to solve this problem. They are: (a) a macroscopic model using the continuum damage model for constitutive behavior, (b) a detailed micromechanical VCFEM analysis, and (c) a multi-level model for multi-scale analysis. The starting mesh in the multi-level model of the bonded

joint consists of a uniform grid of 470 QUAD4 elements for macroscopic analysis as shown in figure 6.11. The constitutive relation for each element is a fourth order anisotropic CDM model that has been developed for this unit cell with interfacial cohesive zone in [75]. Figure 6.12(a) shows the contour of degrading dissipation energy W_d, at the final stage of loading by a pure CDM based macroscopic analysis. Damage initiates near the bottom left corner A of the adhesive joint and propagates downwards to span the entire region on the left of point A. *Level-0* $\rightarrow$ *level-1* transition in the multi-level analysis is performed using equation (6.22) and *level-1* $\rightarrow$ *level-2* transition uses equation (6.28) with factors $C_2 = 0.5$ and $C_3 = 0.1$. The gradient of the energy $\sqrt{(\frac{\partial W_d}{\partial x_1})^2 + (\frac{\partial W_d}{\partial x_2})^2}$ at the final loading stage, used in equation (6.22), is shown in figure 6.12(b). The corresponding evolution of various levels in the multi-scale model is depicted in figure 6.13 at two different loading stages. There are 7 *level-1* elements at 87% of the final loading. At the final load increment, the multi-level mesh consists of 446 *level-0* elements, 0 *level-1* elements, 14 *level-2* elements and 10 *transition* elements. All *level-2* elements emerge in critical the regions where both the gradient and intensity of W_d are high in the macroscopic analysis. Figure 6.14(a,b) depict the contours of microscopic stress σ_{11} and the regions of debonding obtained by pure micromechanical and the multi-level models. The results of the multi-level model are in excellent agreement with the micromechanical analysis, both with respect to debonding regions and evolving variables. The maximum error in σ_{11} is around 1%. The excellent agreement is further corroborated in the plot of σ_{11} along the vertical line through the microstructure in figure 6.9. Figure 6.10(a,b) plot the macroscopic (averaged) $\Sigma_{11} - e_{11}$ curve obtained from (a) macroscopic CDM-based analysis, (b) micromechanical analysis and (c) multi-scale analysis with the multi-level model at two different locations, P1 and P2 shown in figure 6.11(b). At P2, where the damage and its gradient are low, solutions by the CDM model and micromechanics are in relatively good agreement. At this point, the multi-scale model uses the CDM constitutive law. However, the CDM results are quite different from the other two at P1, a hotspot where the damage and its gradient are high. It is assuring to note that the multi-level model matches the micromechanics results quite well at this point.

The computational efficiency of the multi-level model is examined by a comparison of the CPU time on a IA32 computer cluster for the different models. The computations are carried out in a serial manner

using a single processor. The results are tabulated in table 6.1. Although the macroscopic CDM analysis is faster, it can lead to significant errors. The complete *level-1* solution is even slower than the micromechanics solution, since it solves the RVE problem in every element. Accurate analysis with the multi-level model is at least 7 times faster than the complete micromechanics and *level-1* solutions for this problem. The efficiency increases rapidly with increasing number of fibers in the analysis.

Model	Level-0	Level-1	Micromechanics (Level-2)	Multi-scale
Time in seconds	71	300330	300310	42260

Table 6.1: CPU time on a IA32 cluster to solve the double lap joint model by various methods.

Multi-level analysis for model with 192000 fibers

This is a more realistic model of the composite joint with a large number of fibers, to realize the potential of the multi-level model. The top ply consists of 160 rows of fiber, while the bottom row consists of 80 rows resulting in a total of 192000 fibers. The geometric and material parameters are the same as in the previous example, except for the special cases mentioned. A pure micromechanical analysis is not conducted due to the large number of fibers. The problem is analyzed by (a) a macroscopic model by CDM and (b) the multi-level model. The multi-level analysis activates all three types of adaptation:

- Refinement of *level-0* elements by h-adaptation in accordance with equation (6.21), for $C_1 = 0.7$.
- Transition from *level-0* to *level-1* elements in accordance with equation (6.22), with $C_2 = 0.5$.
- Transition from *level-1* to *level-2* elements in accordance with equation (6.28), with $C_3 = 0.1$.

The effects of variation of cohesive zone parameters and the effect of volume fraction are studied. The unit cells considered in this example have 2 volume fractions: (i) $V_f = 20\%$. and (ii) $V_f = 40\%$. Three different cases with different parameters in the bilinear cohesive law are considered.

- *C1*: Same cohesive parameters as in section 6.5.2.
- *C2*: σ_{max} and δ_e are the same as in section 6.5.2. However, δ_c is 4 times that in case *C1*. This reflects the same cohesive energy with a smaller ascending slope.

- *C3*: σ_{max} is reduced by half and δ_e is doubled. Hence the cohesive energy is the same as *C1* with a smaller peak stress. Also δ_c is the same as that in *C1*.

The starting mesh has 470 *level-0* elements. For $V_f = 40\%$ and case *C1*, the final mesh has 1688 *level-0* elements, 24 *level-2* elements and 33 *transition* elements as shown in figure 6.15(a). Figure 6.15(b) illustrates the corresponding microscopic stress distribution and debonding in the *level-2* regions near the hotspot at A. The macroscopic (averaged) stress-strain plots are shown for two points in the composite joint: (a) near the critical point A and (b) at a non critical point B are shown in figure 6.16. The predictions of the CDM model agree with the multi-level model at the point B. However, the stress predictions by the CDM model are considerably higher than those by the multi-level model at A, where damage is very localized and the periodicity condition imposed by the CDM model is unrealistic.

The effect of V_f on the damage evolution near the corner P1 is seen in figure 6.17 for the case *C1*. A significantly higher W_d is observed for the higher volume fraction, which increases with evolving strain. Figure 6.18 shows the distribution of W_d at the end of the analysis for the different cohesive parameters. Intense damage localization takes place near the junction A in the bond (see figure 6.11(b). Damage starts from this location and propagates down and left towards the edge of the applied loading. Damage localization is the strongest for the case *C1*, and propagates almost vertically down in a narrow zone. It is in these regions, that scale transition to *level-2* occurs. The damage distribution in the remaining parts of the composite joint is rather low and uniform. Moving the peak stress in case *C2* with a lower traction-displacement slope results in a more diffused damage region and the damage seem to spread more in the region to the left of point A. The damage localization reduces for the case *C3* with lower peak stress and the damage is more evenly distributed. For $V_f = 20\%$, the damaged regions are less localized.

6.6 Conclusions

An adaptive concurrent multi-level computational model is developed in this paper for multi-scale analysis and prediction of damage in fiber reinforced composite materials. Microstructural damage is manifested by

fiber-matrix interfacial debonding in this paper. Microstructural damage mechanisms leading to complete failure are more complex than the singular mode of damage considered in this paper. The authors are currently working towards this goal, where interfacial debonds bifurcate into the matrix and eventually coalesce to cause a continuous fracture path. A step forward in this direction can be seen in a recent paper on the growth and coalescence of multiple cohesive cracks [54]. However, the intent of the present paper is to create a framework for the multi-scale coupling so that more complex damage mechanisms may eventually be incorporated. Hence interfacial debonding is deemed sufficient for this purpose.

The multi-level model invokes two-way coupling of scales, viz. a bottom-up coupling with homogenization at lower scales to introduce reduced order continuum models and a top-down coupling at critical hotspots to transcend scales for following the microstructural damage evolution. The bottom-up coupling results in a continuum damage mechanics (CDM) model developed in a preceding paper [75]. Three levels of hierarchy, with different resolutions, evolve in this model with adaptation. Adaptive capabilities enable effective domain decomposition in the evolving problem with damage, keeping a balance between computational efficiency and accuracy. Macroscopic analysis is done with the CDM model of [75] for high efficiency. Pure micromechanical analysis is computationally exhaustive and the adaptive methodology optimally reduces this region to a minimum. The Voronoi cell finite element model [35, 53] is effectively utilized for efficient micromechanical analysis of extended microstructural regions. The numerical examples establish the accuracy and efficiency aspects of the model, as well as demonstrate its capability in handling problems involving damage in large composite domains. Overall this work lays an effective foundation for solving multi-scale problems involving localization, damage and crack evolution that may be impossible to achieve using any single scale model.

6.7 APPENDIX

6.7.1 Microscopic and Macroscopic Equations in Computational Subdomain Level-1 (Ω_{l1})

Any function f in the RVE is assumed to be Y-periodic, i.e. $f(\mathbf{x}, \mathbf{y}) = f(\mathbf{x}, \mathbf{y} + \mathbf{kY})\ \forall k = 1, 2, \cdots$. Periodicity conditions are used on the RVE boundary to decouple the set of equations at different levels as:

Microscopic equations

$$\begin{aligned}
\epsilon_{ij}(\mathbf{x},\mathbf{y}) &= e_{ij}(\mathbf{x}) + \frac{1}{2}(\frac{\partial u_i(\mathbf{y})}{\partial y_j} + \frac{\partial u_j(\mathbf{y})}{\partial y_i}) \\
&= e_{kl}(\mathbf{x})[\delta_{ki}\delta_{lj} + e^{-1}_{ki}(\mathbf{x})\frac{\partial u_l(\mathbf{y})}{\partial y_j}] \qquad \text{(Kinematics)} \\
\sigma_{ij}(\mathbf{x},\mathbf{y}) &= E_{ijkl}\delta_{mk}\delta_{nl} + e^{-1}_{mk}(\mathbf{x})\frac{\partial u_n(\mathbf{y})}{\partial y_l}e_{mn}(\mathbf{x}) \qquad \text{(Constitutive)} \\
\frac{\partial \sigma_{ij}(\mathbf{x},\mathbf{y})}{\partial y_j} &= 0 \qquad \text{(Equilibrium)}
\end{aligned} \tag{6.33}$$

Macroscopic equations

$$\begin{aligned}
&\Sigma_{ij}(\mathbf{x}) = \frac{1}{|Y|}\int_Y E_{ijkl}(\delta_{km}\delta_{ln} + e^{-1}_{km}\frac{\partial u_n}{\partial y_l})\, dY e_{mn} = E^H_{ijmn}e_{mn}(\mathbf{x}) \qquad \text{(Constitutive)} \\
&\frac{\partial \Sigma_{ij}(\mathbf{x})}{\partial x_j} + f_i = 0 \qquad \text{(Equilibrium)}
\end{aligned} \tag{6.34}$$

In the above equations u_i is a Y-periodic displacement function and $\sigma_{ij}(\mathbf{x},\mathbf{y})$ is the stress field in the RVE respectively, while $\Sigma_{ij}(\mathbf{x})$ and e_{ij} are the homogenized stress and strain tensors. E_{ijkl} and E^H_{ijkl} correspond to microscopic and homogenized anisotropic elasticity tensor respectively. The details of the derivation of equations (6.33) and (6.34)are discussed in [81, 74].

6.7.2 The Voronoi Cell Finite Element Model

A typical *level-2/ transition* element consisting of microstructural Voronoi cell elements is shown in figure 6.3. The following assumptions are made in the formulation of each VCFEM element.

- Stress fields σ^m_{ij} in the matrix phase Ω_m and σ^c_{ij} in the inclusion phase Ω_c of each Voronoi cell element Ω_e are independent and equilibrated. The stress interpolations in each phase are expressed as :

$$\{\boldsymbol{\sigma}^{\,m}\} = [\mathbf{P}^m]\{\boldsymbol{\beta}^m\} \text{ in } \Omega_m \quad \text{and} \quad \{\boldsymbol{\sigma}^{\,c}\} = [\mathbf{P}^c]\{\boldsymbol{\beta}^c\} \text{ in } \Omega_c \tag{6.35}$$

  where the matrices $[\mathbf{P}^{m/c}]$ are obtained from assumed stress functions like the Airy's stress function

and $\{\beta^{m/c}\}$ are unknown coefficients to be solved.

- Compatible displacement field u_i^e are assumed on each Voronoi cell element boundary $\partial\Omega_e$ and interpolated as:

$$\{\mathbf{u^e}\} = [\mathbf{L^e}]\{\mathbf{q^e}\} \tag{6.36}$$

- Compatible displacement fields u_i^m and u_i^c are assumed on the matrix and inclusion sides of the matrix-inclusion interface $\partial\Omega_c$ respectively, and are interpolated as :

$$\{\mathbf{u}^m\} = [\mathbf{L}^c]\{\mathbf{q}^m\} \text{ on } \partial\Omega_c^m \quad \text{and} \quad \{\mathbf{u}^c\} = [\mathbf{L}^c]\{\mathbf{q}^c\} \text{ on } \partial\Omega_c^c \tag{6.37}$$

In an incremental formulation, the potential energy functional for each element is expressed in terms of the incremented stresses and displacements as:

$$\begin{aligned}
&\Pi_e(\sigma_{ij}^m, \Delta\sigma_{ij}^m, \sigma_{ij}^c, \Delta\sigma_{ij}^c, u_i^e, \Delta u_i^e, u_i^m, \Delta u_i^m, u_i^c, \Delta u_i^c) = -\int_{\Omega_m} \Delta B^m(\sigma_{ij}^m, \Delta\sigma_{ij}^m)d\Omega \\
&- \int_{\Omega_c} \Delta B^c(\sigma_{ij}^c, \Delta\sigma_{ij}^c)d\Omega + \int_{\Omega_m} (\sigma_{ij}^m + \Delta\sigma_{ij}^m)(\epsilon_{ij}^m + \Delta\epsilon_{ij}^m)d\Omega \\
&+ \int_{\Omega_c} (\sigma_{ij}^c + \Delta\sigma_{ij}^c)(\epsilon_{ij}^c + \Delta\epsilon_{ij}^c)d\Omega - \int_{\partial\Omega_c} \int_{u_n^m - u_n^c}^{u_n^m + \Delta u_n^m - u_n^c - \Delta u_n^c} T_n^m d(u_n^m - u_n^c)d\partial\Omega \\
&- \int_{\partial\Omega_c} \int_{u_t^m - u_t^c}^{u_t^m + \Delta u_t^m - u_t^c - \Delta u_t^c} T_t^m d(u_t^m - u_t^c)d\partial\Omega - \int_{\Gamma_{tm}} (t_i + \Delta t_i)(u_i^e + \Delta u_i^e)d\Gamma
\end{aligned} \tag{6.38}$$

Here $B = \frac{1}{2}S_{ijkl}\sigma_{ij}\sigma_{kl}$ is the complementary energy density and $\Delta B = \frac{1}{2}S_{ijkl}\Delta\sigma_{ij}\Delta\sigma_{kl} + S_{ijkl}\Delta\sigma_{ij}\sigma_{kl}$. The strain fields ϵ_{ij}^m and ϵ_{ij}^c are in the matrix and inclusion phases respectively of each Voronoi element. $\mathbf{t}$ is the prescribed traction on the boundary Γ_{tm}. The prefix Δ corresponds to increments and subscripts n and t correspond to the normal and tangential directions at the matrix-inclusion interface. The two terms on the matrix-inclusion interface $\partial\Omega^m/\partial\Omega^c$ provide the work done by the interfacial tractions $\mathbf{T}^m = T_n^m\mathbf{n}^m + T_t^m\mathbf{t}^m$ due to interfacial separation $(\mathbf{u}^m - \mathbf{u}^c)$. T_n^m and T_t^m are the normal and tangential components that are

described by cohesive laws in [35, 53]. Using divergence theorem, the potential energy can be written as:

$$\Pi_e = -\int_{\Omega_m} \frac{1}{2} S^m_{ijkl} \Delta\sigma^m_{ij} \Delta\sigma^m_{kl} \; d\Omega - \int_{\Omega_m} S^m_{ijkl} \sigma^m_{kl} \Delta\sigma^m_{ij} \; d\Omega \tag{6.39}$$

$$\begin{aligned}
&- \int_{\Omega_c} \frac{1}{2} S^c_{ijkl} \Delta\sigma^c_{ij} \Delta\sigma^c_{kl} \; d\Omega - \int_{\Omega_c} S^c_{ijkl} \sigma^c_{kl} \Delta\sigma^c_{ij} \; d\Omega \\
&+ \int_{\partial\Omega_e} (\sigma^m_{ij} + \Delta\sigma^m_{ij}) n^e_j (u^e_i + \Delta u^e_i) d\partial\Omega - \int_{\partial\Omega^m_c} (\sigma^m_{ij} + \Delta\sigma^m_{ij}) n^c_j (u^m_i + \Delta u^m_i) d\partial\Omega \\
&+ \int_{\partial\Omega^c_c} (\sigma^c_{ij} + \Delta\sigma^c_{ij}) n^c_j (u^c_i + \Delta u^c_i) d\partial\Omega - \int_{\partial\Omega_c} \int_{u^m_n - u^c_n}^{u^m_n + \Delta u^m_n - u^c_n - \Delta u^c_n} T^m_n d(u^m_n - u^c_n) d\partial\Omega \\
&- \int_{\partial\Omega_c} \int_{u^m_t - u^c_t}^{u^m_t + \Delta u^m_t - u^c_t - \Delta u^c_t} T^m_t d(u^m_t - u^c_t) d\partial\Omega \\
&- \int_{\Gamma_{tm}} (t_i + \Delta t_i)(u^e_i + \Delta u^e_i) d\Gamma
\end{aligned} \tag{6.40}$$

Here $\mathbf{n}^e$ and $\mathbf{n}^c$ are the outward normal on $\partial\Omega_e$ and $\partial\Omega_c$ respectively. The integration over the incremental displacements at the interface $\partial\Omega_c$ is conducted by the backward Euler method. The total potential energy functional for each *level-2* or *tr* element containing N_{vc} Voronoi cell elements as shown in figure 6.3 is

$$\Pi^{l2/tr} = \sum_{e=1}^{N_{vc}} \Pi_e \tag{6.41}$$

Substituting stress interpolations (6.35) and displacement interpolations (6.36,6.37) in equation (6.40) and setting variations with respect to the stress coefficients $\Delta\beta^{\mathbf{m}}$, $\Delta\beta^{\mathbf{c}}$ respectively to zero results in the weak form of the element kinematic relation.

$$\begin{bmatrix} \int_{\Omega_m} [\mathbf{P}^m]^T [\mathbf{S}^m] [\mathbf{P}^m] d\Omega & [\mathbf{0}] \\ [\mathbf{0}] & \int_{\Omega_c} [\mathbf{P}^c]^T [\mathbf{S}^c] [\mathbf{P}^c] d\Omega \end{bmatrix} \begin{Bmatrix} \boldsymbol{\beta}^m + \triangle\boldsymbol{\beta}^m \\ \boldsymbol{\beta}^c + \triangle\boldsymbol{\beta}^c \end{Bmatrix} =$$

$$\begin{bmatrix} \int_{\partial\Omega_e} [\mathbf{P}^m]^T [\mathbf{n}^e] [\mathbf{L}^e] d\partial\Omega & -\int_{\partial\Omega_c} [\mathbf{P}^m]^T [\mathbf{n}^c] [\mathbf{L}^c] d\partial\Omega & [\mathbf{0}] \\ [\mathbf{0}] & [\mathbf{0}] & \int_{\partial\Omega_c} [\mathbf{P}^c]^T [\mathbf{n}^c] [\mathbf{L}^c] d\partial\Omega \end{bmatrix} \begin{Bmatrix} \mathbf{q}^e + \triangle\mathbf{q}^e \\ \mathbf{q}^m + \triangle\mathbf{q}^m \\ \mathbf{q}^c + \triangle\mathbf{q}^c \end{Bmatrix}$$

or in a condensed form

$$[\mathbf{H}^e]\{\boldsymbol{\beta} + \triangle\boldsymbol{\beta}\} = [\mathbf{G}^e]\{\mathbf{q} + \triangle\mathbf{q}\} \tag{6.42}$$

The weak forms of the global traction continuity conditions are subsequently solved by setting the variation of the total energy function in equation (6.41) with respect to $\Delta\mathbf{q}$, $\Delta\mathbf{q^m}$ and $\Delta\mathbf{q^c}$ to zero. This results in the weak form of the traction reciprocity conditions as:

$$\sum_{e=1}^{N_{vc}} \begin{bmatrix} \int_{\partial\Omega_e}[\mathbf{L}^e]^T[\mathbf{n}^e]^T[\mathbf{P}^m]d\partial\Omega & [\mathbf{0}] \\ -\int_{\partial\Omega_m^c}[\mathbf{L}^c]^T[\mathbf{n}^c]^T[\mathbf{P}^m]d\partial\Omega & [\mathbf{0}] \\ [\mathbf{0}] & \int_{\partial\Omega_c^c}[\mathbf{L}^c]^T[\mathbf{n}^c]^T[\mathbf{P}^c]d\Omega \end{bmatrix} \begin{Bmatrix} \boldsymbol{\beta}^{\,m} + \triangle\boldsymbol{\beta}^{\,m} \\ \boldsymbol{\beta}^{\,c} + \triangle\boldsymbol{\beta}^{\,c} \end{Bmatrix} =$$

$$\sum_{e=1}^{N_{vc}} \begin{Bmatrix} \int_{\Gamma_{tm}}[\mathbf{L}^e]^T\{\bar{\mathbf{t}} + \triangle\bar{\mathbf{t}}\}d\Omega \\ -\int_{\partial\Omega_m^c}[\mathbf{L}^c]^T\left(\{\mathbf{n}^c\}T_n^m(u_n+\triangle u_n, u_t+\triangle u_t) + \{\mathbf{t}^c\}T_t^m(u_n+\triangle u_n, u_t+\triangle u_t)\right)d\partial\Omega \\ -\int_{\partial\Omega_c^c}[\mathbf{L}^c]^T\left(\{\mathbf{n}^c\}T_n^m(u_n+\triangle u_n, u_t+\triangle u_t) + \{\mathbf{t}^c\}T_t^m(u_n+\triangle u_n, u_t+\triangle u_t)\right)d\partial\Omega \end{Bmatrix} \tag{6.43}$$

or in a condensed form

$$\sum_{e=1}^{N_{vc}}[\mathbf{G}^e]^T\{\boldsymbol{\beta} + \triangle\boldsymbol{\beta}\} = \sum_{e=1}^{N_{vc}}\{\mathbf{R^e}\} \tag{6.44}$$

Substituting (6.42) in (6.44) yields:

$$\sum_{e=1}^{N_{vc}}[\mathbf{G}^e]^T[\mathbf{H}^e]^{-1}[\mathbf{G}^e]\{\mathbf{q} + \triangle\mathbf{q}\} = \sum_{e=1}^{N_{vc}}\{\mathbf{R^e}\} \tag{6.45}$$

In an iterative solution of equation (6.45), its linearized form for the $i-$th iteration is given as:

$$\sum_{e=1}^{N_{vc}}[\mathbf{G}^e]^T[\mathbf{H}^e]^{-1}[\mathbf{G}^e])^i\{\boldsymbol{\Delta}\mathbf{q}\}^i = \sum_{e=1}^{N_{vc}}\{\mathbf{R^e}\}^i - \sum_{e=1}^{N_{vc}}[\mathbf{G}^e]^T[\mathbf{H}^e]^{-1}[\mathbf{G}^e]\{\mathbf{q} + \Delta\mathbf{q}\}^i \tag{6.46}$$

or in a condensed form

$$[\mathbf{K}]^i\{\Delta\mathbf{q}\}^i = \{\Delta\mathbf{F}^{vc}\}^i \tag{6.47}$$

In order to incorporate this relation in the linearized form of the principle of virtual work of equation (6.11), it should be noted that the displacement vector $\mathbf{u}_{l2/tr}$ on the boundary of *level-2* and transition element is

a subset of all the VCFEM displacement fields, i.e. $\mathbf{u}^{vc} = \mathbf{u}^{e} \cup \mathbf{u}^{m} \cup \mathbf{u}^{c}$. Consequently, the displacement field $\mathbf{u}^{vc}$ can be separated into two categories, viz. (i) $\mathbf{u}^{l2/tr}$ on nodal points at the boundary of the *level-2* or transition elements shown is figure 6.3, and (ii) $\mathbf{u}^{int}$ on all the internal nodes. The stiffness matrix and the load vector of the ensemble of all Voronoi cell elements belonging to a *level-2* or transition element can therefore be partitioned as

$$\begin{bmatrix} \mathbf{K}^{\mathrm{l2/tr,l2/tr}} & \mathbf{K}^{\mathrm{l2/tr,int}} \\ \mathbf{K}^{\mathrm{int,l2/tr}} & \mathbf{K}^{\mathrm{int,int}} \end{bmatrix}^{i} \begin{Bmatrix} \Delta\mathbf{q}^{\mathrm{l2/tr}} \\ \Delta\mathbf{q}^{\mathrm{int}} \end{Bmatrix}^{i} = \begin{Bmatrix} \Delta\mathbf{F}^{\mathrm{l2/tr}} \\ \Delta\mathbf{F}^{\mathrm{int}} \end{Bmatrix}^{i} \tag{6.48}$$

Static condensation of the internal degrees of freedom yields

$$\begin{aligned} &\left[\left[\mathbf{K}^{\mathrm{l2/tr,l2/tr}}\right] - \left[\mathbf{K}^{\mathrm{l2/tr,int}}\right]\left[\mathbf{K}^{\mathrm{int,int}}\right]^{-1}\left[\mathbf{K}^{\mathrm{int,l2/tr}}\right]\right]^{i}\left\{\Delta\mathbf{q}^{\mathrm{l2/tr}}\right\}^{i} \\ &\quad = \left\{\Delta\mathbf{F}^{\mathrm{l2/tr}}\right\}^{i} - \left[\mathbf{K}^{\mathrm{l2/tr,int}}\right]\left[\mathbf{K}^{\mathrm{int,int}}\right]^{-1}\left\{\Delta\mathbf{F}^{\mathrm{int}}\right\}^{i} \end{aligned} \tag{6.49}$$

These stiffness matrices and load vectors are then used in global assembly process of equation (6.11).

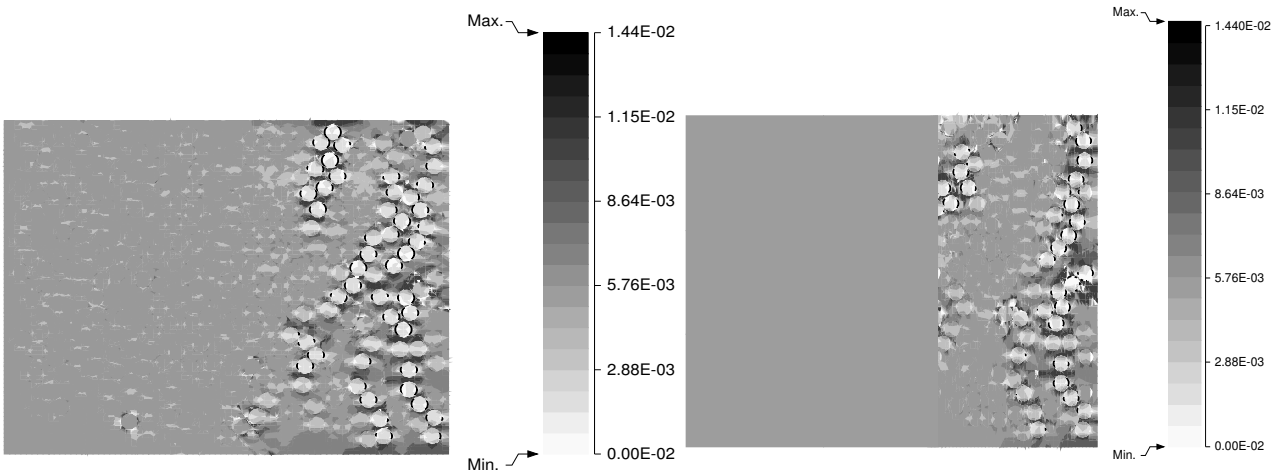

(a) (b)

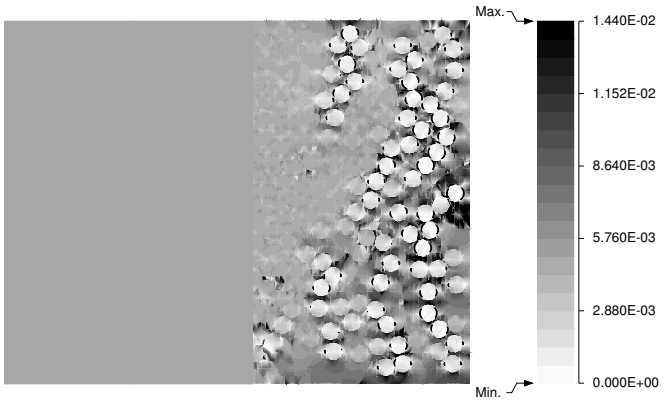

(c)

Figure 6.6: Contour plot of σ_{11} showing interfacial debonding at the end of the simulation, for: (a) pure micromechanical analysis, (b) analysis by multi-scale model with a smaller *level-2* region ($\frac{L_{tr/l2}}{L} = 0.35$), and (c) analysis by multi-scale model with a larger *level-2* region ($\frac{L_{tr/l2}}{L} = 0.45$).

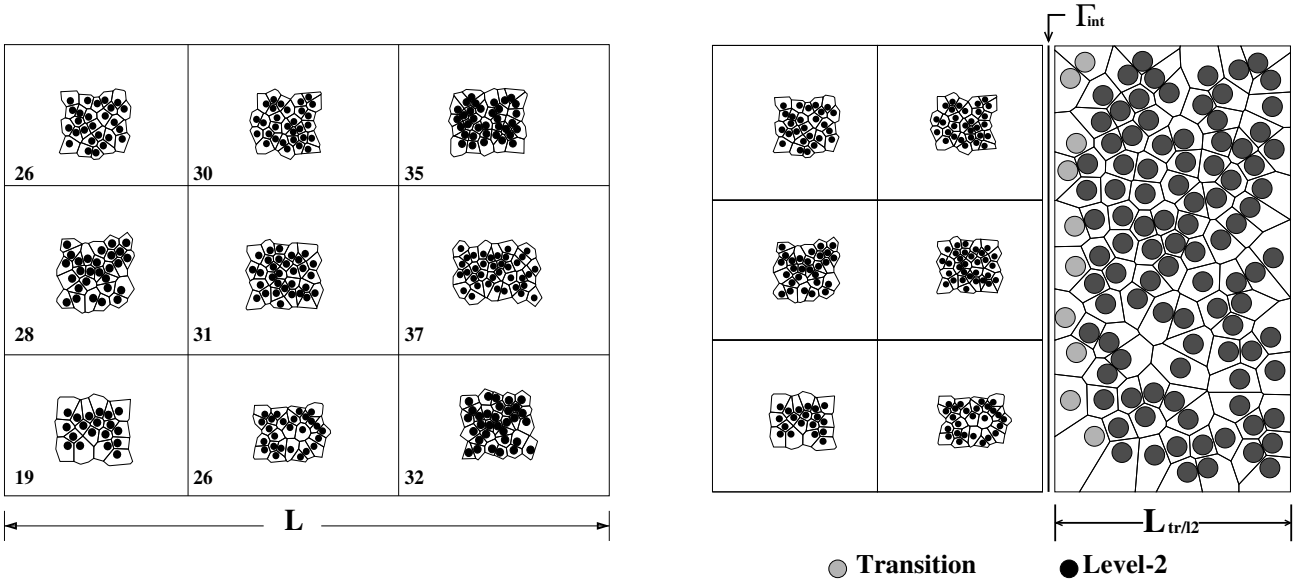

(a) (b)

Figure 6.7: Computational mesh for the computational domain: (a) Macroscopic mesh with different RVE in every element, (b) Multi-level model with the interface between macroscopic and microscopic VCFE elements.

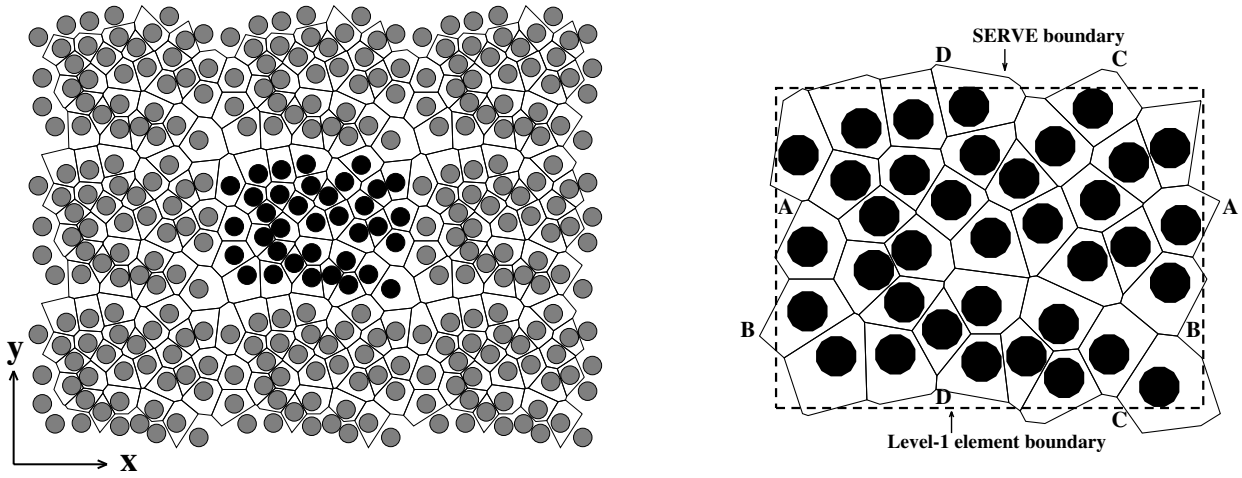

(a) (b)

Figure 6.8: (a) A periodic microstructure containing the tessellated RVE (fibers in black), (b) placement of the RVE in the *level-1* element showing periodic nodes on the boundary.

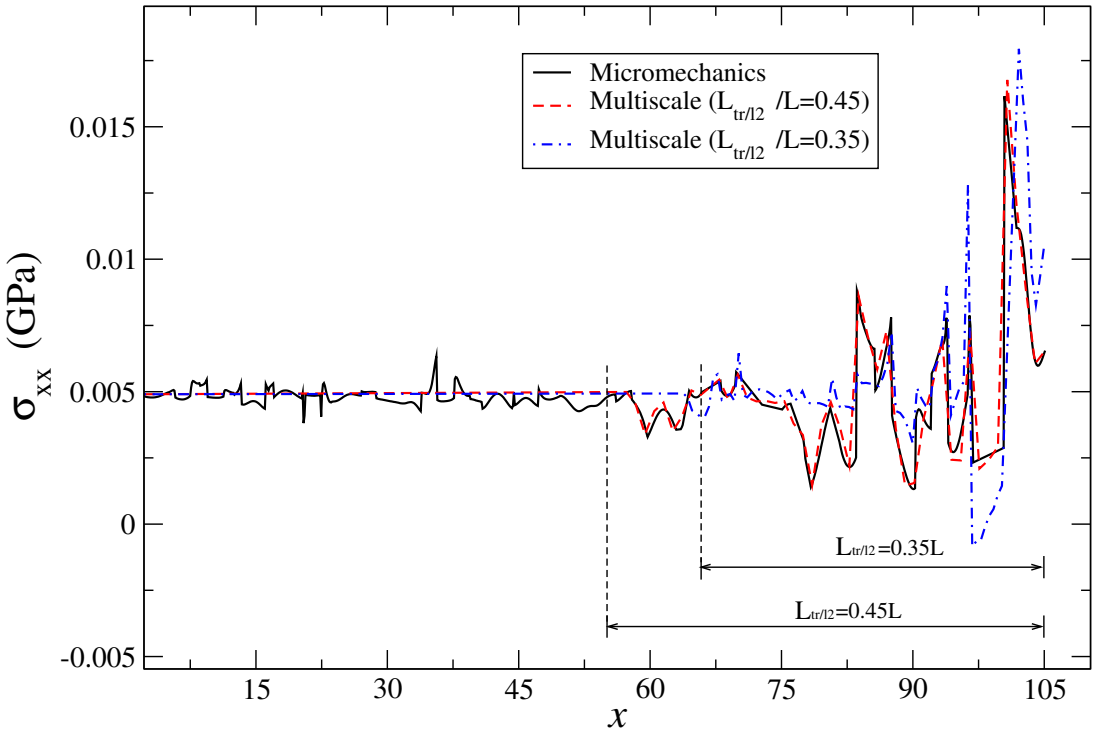

Figure 6.9: Comparison of microscopic stress σ_{11} by different methods, plotted along a line through the middle of microstructure

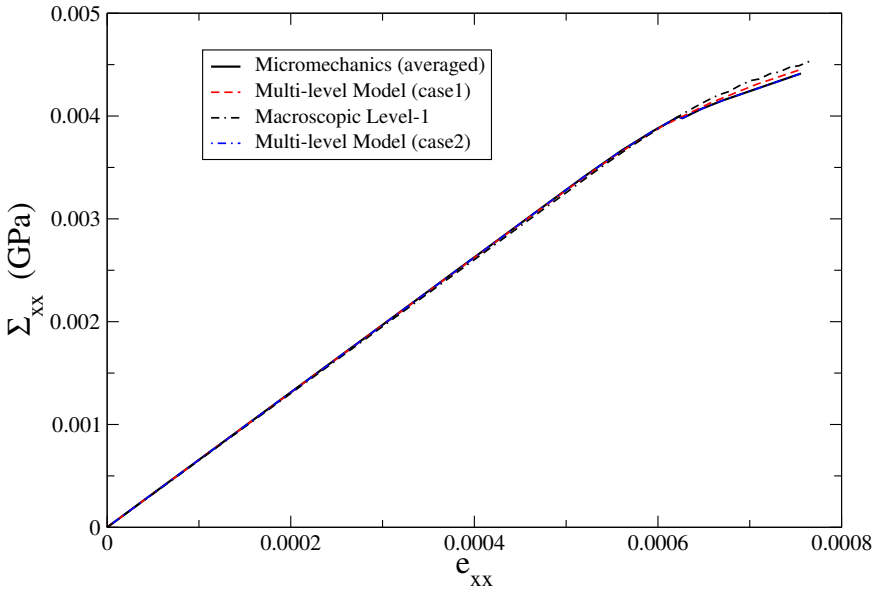

(a)

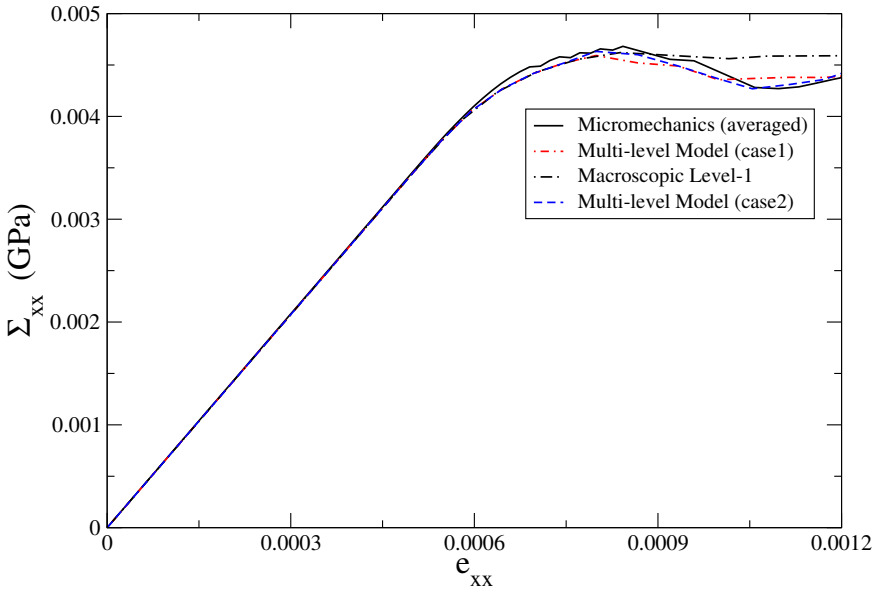

(b)

Figure 6.10: Comparison of macroscopic (volume averaged) $\Sigma_{11} - e_{11}$ curves by different methods of analysis at (a) macroscopic element 1, and (b) macroscopic element 9.

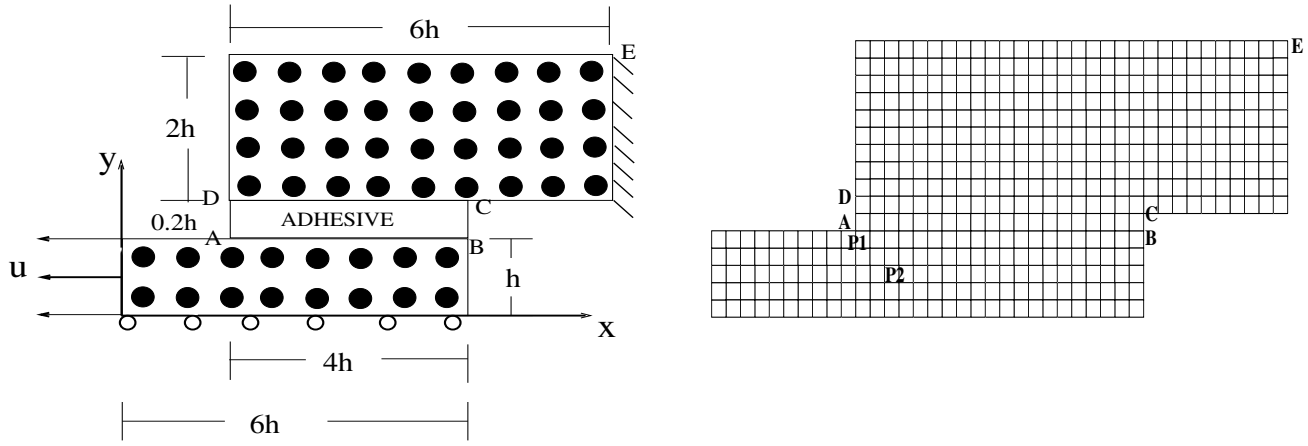

Figure 6.11: (a) Schematic diagram of a composite double lap joint showing dimensions and boundary conditions, (b) the *level-0* computational mesh.

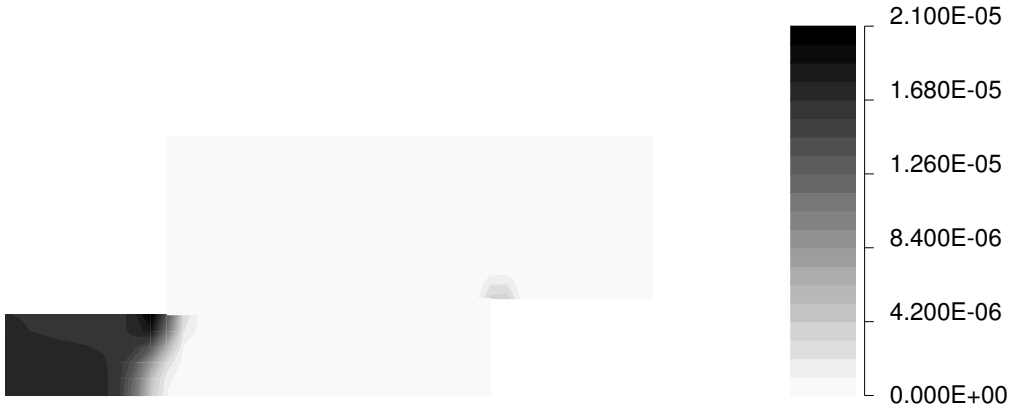

(a)

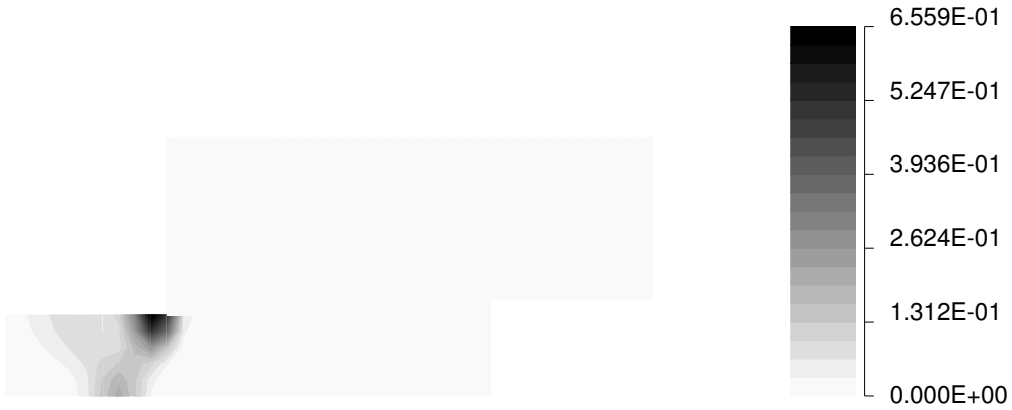

(b)

Figure 6.12: Contour plot of (a) degrading dissipation energy W_d and (b) its gradient $\sqrt{(\frac{\partial W_d}{\partial x_1})^2 + (\frac{\partial W_d}{\partial x_2})^2}$ at the final loading stage.

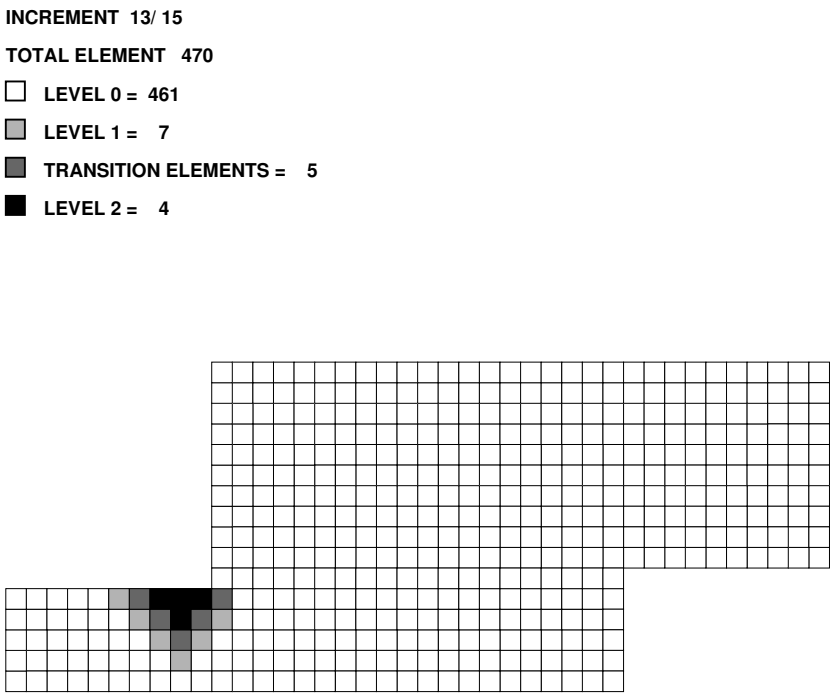

(a)

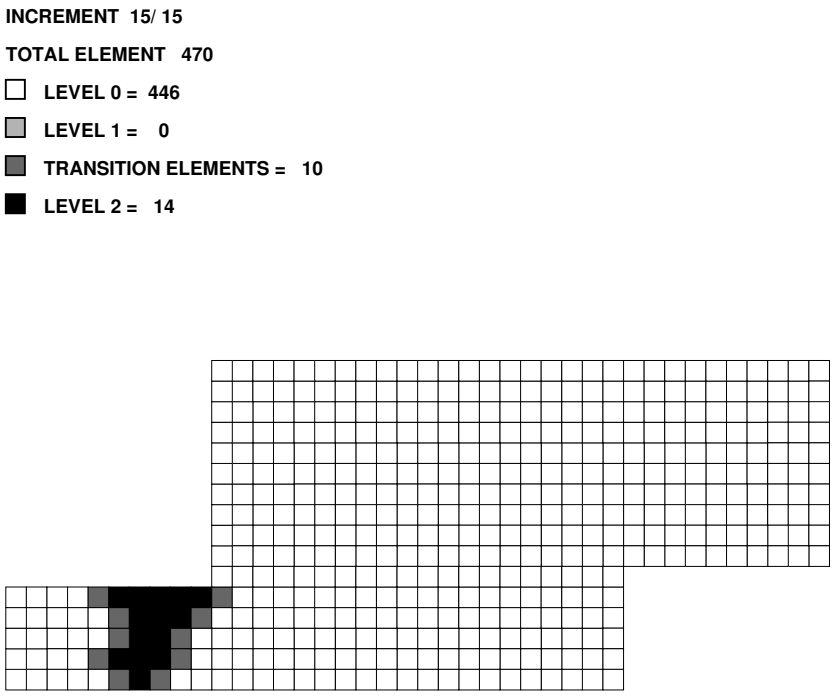

(b)

Figure 6.13: Evolution of the multi-level computational model with level transition (a) at 87 % loading, and (b) at the final loading stage.

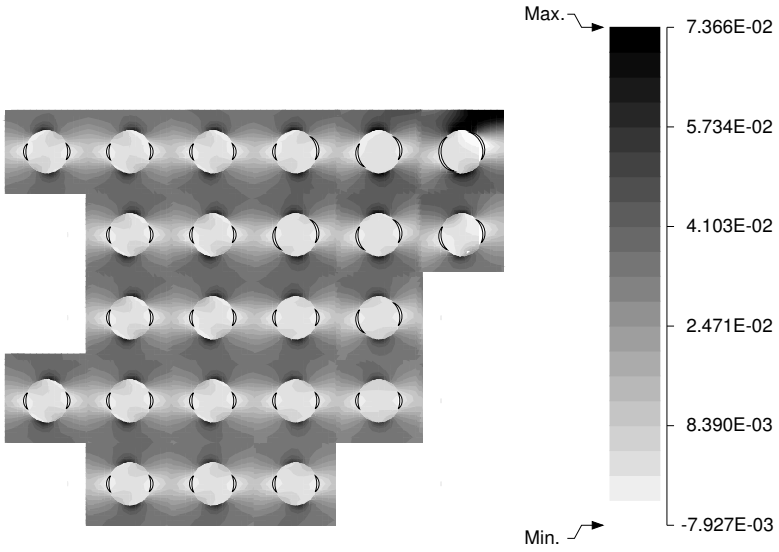

(a)

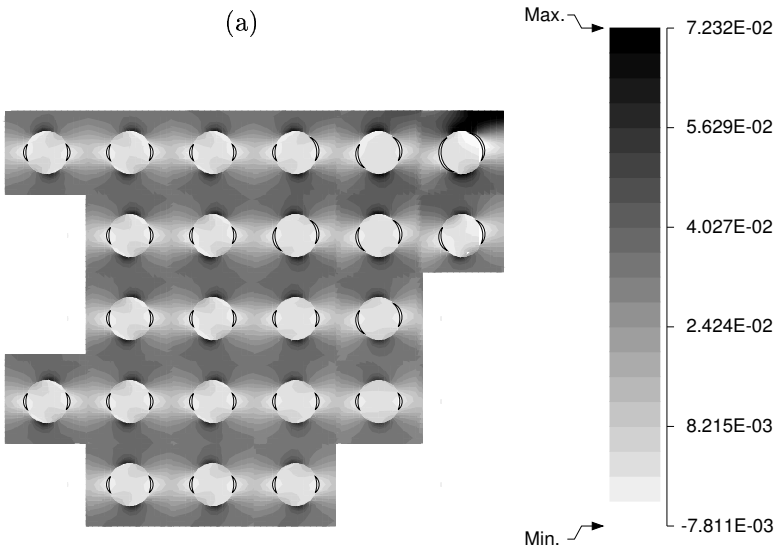

(b)

Figure 6.14: *Level 2* microscopic VCFEM elements near the corner A showing microscopic stress distribution (GPa) and interfacial debonding at the end of the analysis by: (a) pure micromechanical analysis (b) multi-scale analysis.

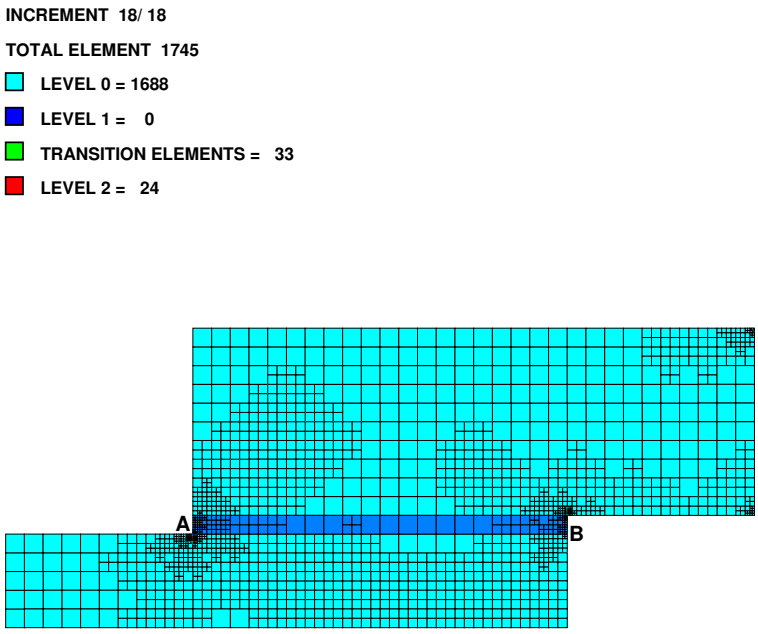

(a)

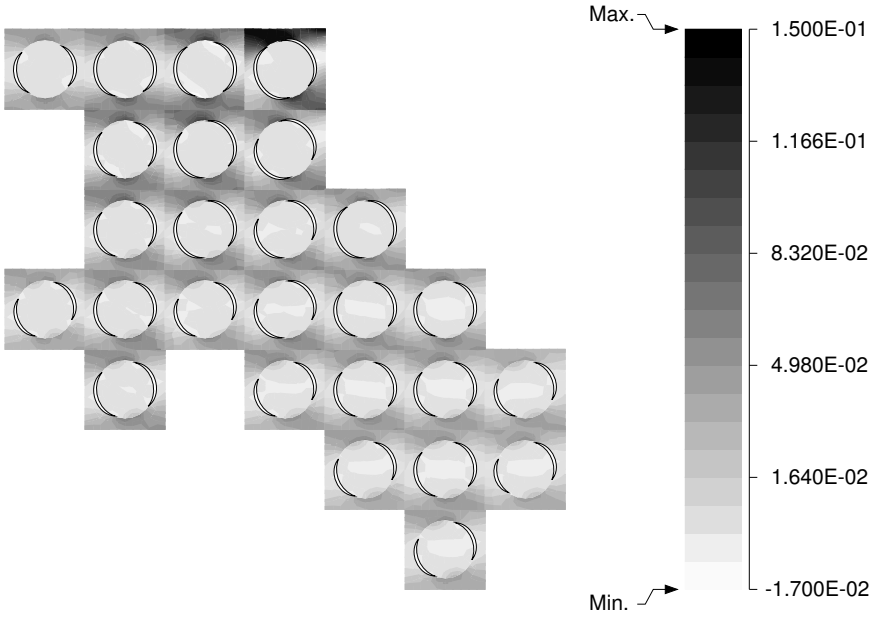

(b)

Figure 6.15: (a) Evolved multi-level model and mesh at the final load step, (b) Microscopic stress distribution and interfacial debonding at the end of analysis for location near corner A, for $V_f = 40\%$ and case *C1*.

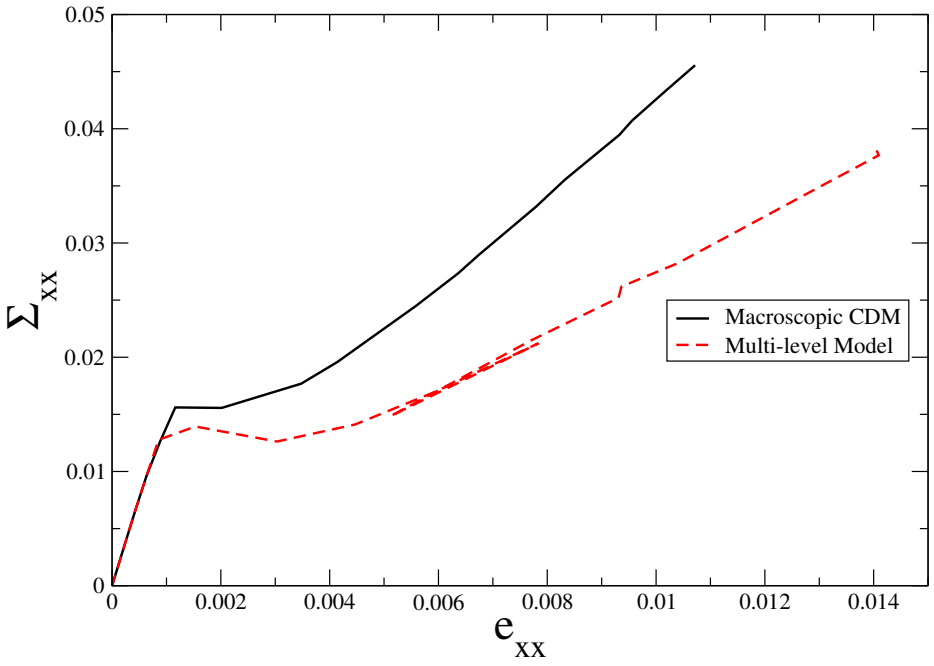

(a)

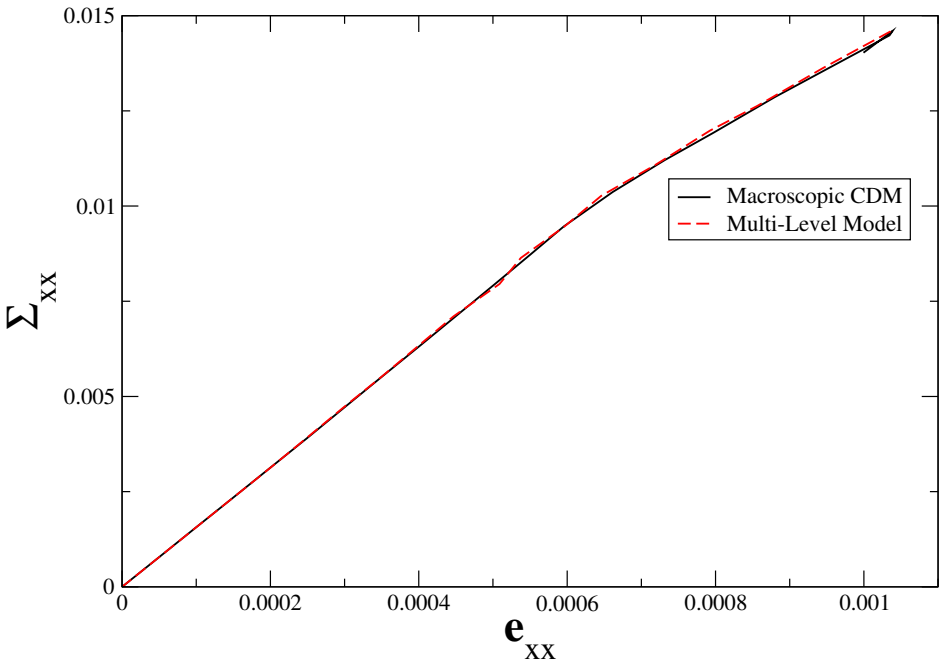

(b)

Figure 6.16: Macroscopic averaged stress-strain ($\Sigma_{11} - e_{11}$) plot at two locations in the double lap joint: (a) critical region A and (b) non-critical region B.

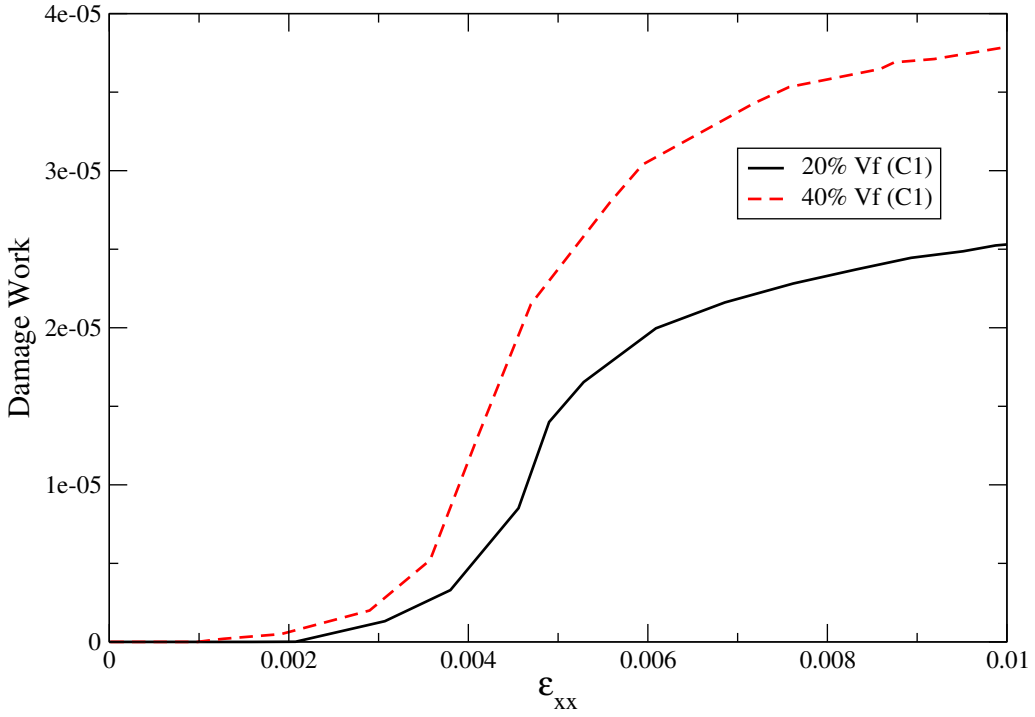

Figure 6.17: Degrading dissipation energy evolution near the corner A of the double lap joint for $V_f = 20\%$ and $V_f = 40\%$, and case *C1*.

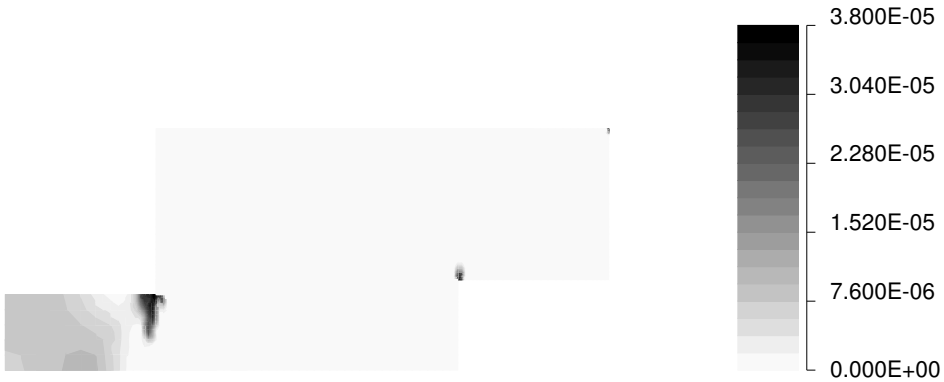

(a)

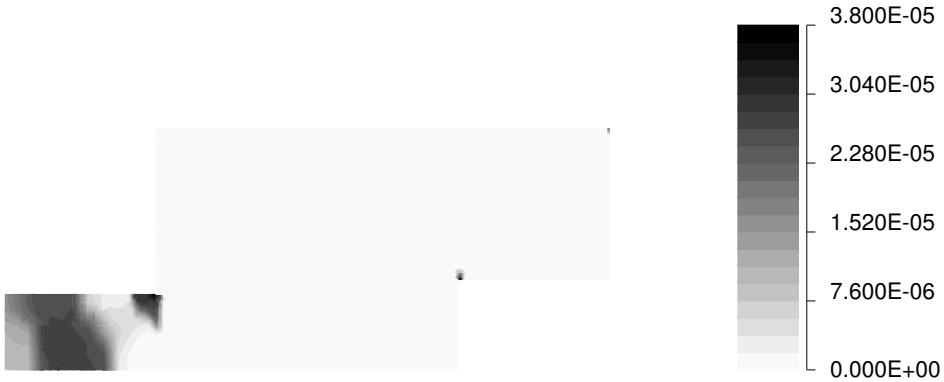

(b)

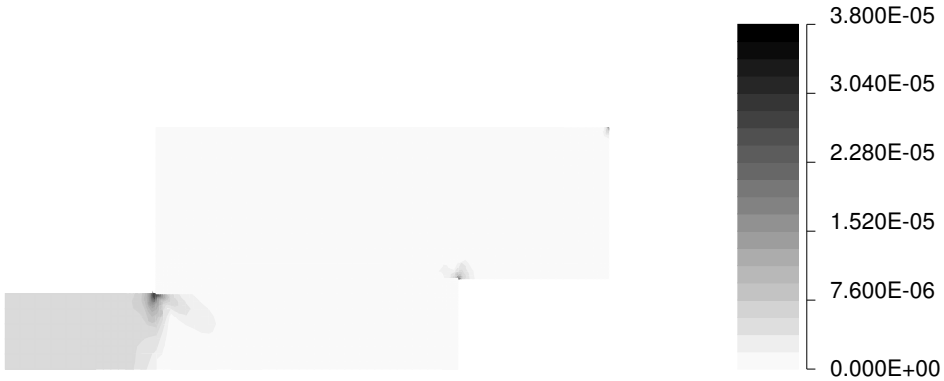

(c)

Figure 6.18: Distribution of W_d with $V_f = 40\%$ and different cohesive parameters: (a) case *C1*, (b) case *C2*, and (c) case *C3*, at the end of loading.

Bibliography

[1] D. Adalsteinsson and JA. Sethian. A fast level set method for propagating interfaces. *Journal of Computational Physics*, 118, 1995.

[2] B.K. Ahn, W.A. Curtin, T.A. Parthasarathy, and R.E. Dutton. Criteria for crack deflection/penetration criteria for fiber-reinforced ceramic matrix composites. *Composites Science and Technology*, 58, 1998.

[3] S. Atluri. An assumed stress hybrid finite element model for linear elastodynamic analysis. *AIAA*, 11(7), 1973.

[4] I. Babuska. The finite element method with lagrange multipliers. *Numer. Math.*, 20, 1973.

[5] GI. Barenblatt. The mathematical theory of equilibrium cracks in brittle fracture. *Adv. Appl. Mech.*, 7, 1962.

[6] K. J. Bathe. *Finite element procedures.* Prentice Hall, 2002.

[7] T. Belytschko and T. Black. Elastic crack growth in finite elements with minimal remeshing. *Int. J. Numer. Meth. Engng.*, 45(5), 1999.

[8] T. Belytschko, Y. Krongauz, D. Organ, M. Fleming, and P. Krysl. Meshless methods: An overview and recent developments. *Comput. Methods Appl. Mech. Engrg.*, 139, 1996.

[9] T. Belytschko, D. Organ, and C. Gerlach. Element-free galerkin methods for dynamic fracture in concrete. *Comp. Meth. Appl. Mech. Engng.*, 187, 2000.

[10] Usui A Belytschko T, Moes N and Parimi C. Arbitrary discontunities in finite element. *Internatinal Journal for Numerical Methods in Engineering*, 50(4), 2001.

[11] JG. Brasseur and Q. Wang. Structural evolution of intermittency and anisotropy at different scales analyzed using three dimensional wavelet transforms. *Phys. fluids*, A4(11), 1992.

[12] F. Brezzi. On the existence, uniqueness and approximation of saddle-point problems arising from lagrange multipliers. *R.A.I.R.O*, 8(R2), 1974.

[13] A. Carpinteri. Finite deformation effects in homogeneous and interfacial fracture. *Engng. Frac. Mech.*, 32, 1989.

[14] A. Carpinteri and G. Colombo. Numerical analysis of catastrophic softening behavior (snap-back instability). *Comput. Struct.*, 31, 1989.

[15] C.L. Chow and J. Wang. An anisotropic theory of elasticity for continuum damage mechanics. *Int. J. Frac.*, 20, 1987.

[16] CK. Chui. *An introduction to wavelets.* Academic Press, 1992.

[17] CK. Chui and JZ. Wang. A general framework of compactly supported splines and wavelets. *J. Appr. Theory*, 71(3), 1992.

[18] J.P. Cordebois and F. Sidoroff. Anisotropic damage in elasticity and plasticity. *Jour. Mech. Theor. Appl.*, 1982.

[19] MA. Crisfield. A fast incremental/iterative solution procedure that handles 'snap-through'. *Comp. Struct.*, 13, 1981.

[20] MA. Crisfield. An arc-length method including line searches and accelerations. *Int. Jour. Numer. Meth. Engng.*, 19, 1983.

[21] I. Daubechies. Orthonormal bases of compactly supported wavelets. *Comm. Pure Appl. Math.*, 41(7), 1988.

[22] I. Daubechies. Ten lectures in wavelets. *Society for Industrial and Applied Mathematics, Philadelphia, Pennsylvania.*, 1992.

[23] I. Daubechies. Orthonormal bases of compactly supported wavelets ii. *SIAM Jour. MAth. Anal.*, 24(2), 1993.

[24] J. Dolbow, N. Moes, and T. Belytschko. Discontinuous enrichent in finite elements with a partition of unity method. *Finite Elements in Analysis and Design*, 36:3-4, 2000.

[25] DS. Dugdale. Yielding in steel sheets containing slits. *J. Mech. Phys. Solids*, 8, 1960.

[26] J. Réthoré, A. Gravouil, and A. Combescure. An energy-conserving scheme for dynamic crack growth using the extended finite element method. *Int. J. Numer. Meth. Engng*, 63, 2005.

[27] R. Everson, L. Sirooich, and KR. Sreenicasan. Wavelet analysis of the tuibulent jet. *Physics Letters A*, 145, 1990.

[28] F. Erdogan F and GC. Sih. On the crack extension in plates under plane loading and transverse shear. *Journal of Basic Engineering*, 1963.

[29] J. Fish and K. Shek. Multiscale analysis of composite materials and structures. *Comp. Sci. Tech.*, 60, 2000.

[30] JW. Foulk, DH. Allen, and KLE. Helms. Formulation of a three-dimensional cohesive zone model for application to a finite element algorithm. *Comput. Meth. Appl. Mech. Engng.*, 183, 2000.

[31] JAT Freitas and Z. M. Wang. Elastodynamic analysis with hybrid stress finite elements. *Computers and Structures*, 79, 2001.

[32] B. A. Gana, T. A. Bogetti, B. K. Fink, C. J. Yu, T. D. Claar, H. H. Eifert, and J. W. Gillespie. Aluminium foam integral armor: a new dimension in armor design. *Composite Structures*, 52, 2001.

[33] PH. Geubelle. Finite deformation effects in homogeneous and interfacial fractur. *Int. J. Solids Struct.*, 32, 1995.

[34] S. Ghosh and K. Lee. A microstructure based numerical method for constitutive modeling of composite and porous materials. *Int. Jour. Solids Struct.*, A272, 1999.

[35] S. Ghosh, Y. Ling, M. Bhaskar, and K. Ran. Interfacial debonding analysis in multiple fiber reinforced composites. *Mech. Mater.*, 32, 2000.

[36] S. Ghosh and S. Moorthy. Particle cracking simulation in non-uniform microstructures of metal-matrix composites. *Acta Metal. Mater.*, 46(3), 1998.

[37] S. Ghosh, Z. Nowak, and K. Lee. Quantitative characterization and modeling of composite microstructures by voronoi cells. *Acta Mater.*, 45, 1997.

[38] R. Glowinski, W. Lawton, M. Ravachol, and E. Tenenbaum. Wavelet solutions of linear and nonlinear elliptic, parabolic and hyperbolic problems in one space dimension. *Computing Methods in Applied Science and Engineering, SIAM, Philadelphia, PA*, 1990.

[39] GT. Camacho GT and M. Ortiz. Computational modeling of impact damage in brittle materials. *Int. Jour. Solids Struct.*, 33, 1996.

[40] A. Haar. Zur theorie der orthogonalen funkktionen-systeme. *Math. Ann.*, 69, 1910.

[41] M.Y. He, C.H. Hsueh, and P.H. Becher. Deflection versus penetration of a wedge-loaded crack: effects of branch-crack length and penetrated-layer width. *Composites, Part B: Engineering*, 31, 2000.

[42] M.Y. He and J.W. Hutchinson. Crack deflection at an interface between dissimilar elastic materials. *Int. J. Solids Struct*, 25(9), 1989.

[43] E. Rizzi I. Carol and K. Willam. A unified theory of elastic degradation and damage based on a loading surface. *Int. J. Solids Struct.*, 31(20), 1995.

[44] Q. Yu J. Fish and K. Shek. Computational damage mechanics for composite materials based on mathematical homogenization. *Int. J. Numer. Meth. Eng.*, 45, 1999.

[45] W. Chen J. Fish and G. Nagai. Non-local dispersive model for wave propagation in heterogeneous media: multi-dimensional dimensional case. *Int. J. Numer. Meth. Engng.*, 54, 2002.

[46] W. Chen J. Fish and G. Nagai. Non-local dispersive model for wave propagation in heterogeneous media: one-dimensional case. *Int. J. Numer. Meth. Engng.*, 54, 2002.

[47] S. Jaffard. Wavelet methods for fast resolution of elliptic problem. *SIAM J. Numer. Anal.*, 29(4), 1992.

[48] M. Jirasek. A comparative study on finite elements with embedded discontinuities. *Comp. Meth. App. Mech. Engng.*, 188(1), 2000.

[49] L.M. Kachanov. Introduction to continuum damage mechanics. *Int. Jour. Solids Struct.*, 1987.

[50] J.K. Kalthoff. Modes of dynamic shear failure in solids. *International Journal of Fracture*, 101, 2000.

[51] J.K. Kalthoff and S. Winkler. Failure mode transition at high rates of loading. *Proceedings of the international conference on impact loading and dynamics behaviour of materials. Chiem C.Y., Kunze H.D. and Meyer L.W. eds.*, 1988.

[52] J. Lewalle. Wavelet analysis of experimental data: some methods and the underlying physics. *AIAA 94-2281, 25th AIM Fluid Dynamics Colorado Springs*, 1994.

[53] S. Li and S. Ghosh. Debonding in composite microstructures with morphologic variations. *International Journal of computational methods*, 1(1), 2004.

[54] S. Li and S. Ghosh. Extended voronoi cell finite element model for multiple cohesive crack propagation in brittle materials. *International Journal for Numerical Methods in Engineering (in press)*, 2005.

[55] A.A. Mammoli, A.L. Graham, I.E. Reimanis, and D.L. Tullock. The effect of flaws on the propagation of cracks at bi-materials interfaces. *Acta Metall. mater.*, 43(3), 1995.

[56] S. Mariani and U. Perego. Extended finite element method for quasi-brittle fracture. *Int. J. Numer. Meth. Engng.*, 58, 2003.

[57] Y. Meyer. *Ondelettes et Fonctions Splines.* Seminaire EDP, Ecole Polytechnique, Paris., 1986.

[58] R. A. W. Mines. A one-dimensional stress wave analysis of a lightweight composite armour. *Composite Structures*, 64, 2004.

[59] N. Moës and T. Belytschko. Extended finite element method for cohesive crack growth. *Engineering Fracture Mechanics*, 69, 2002.

[60] N. Moës, J. Dolbow, and T. Belytschko. A finite element method for crack growth without remeshing. *Engineering Fracture Mechanics*, 46:1, 1999.

[61] S. Moorthy and S. Ghosh. A model for analysis for arbitrary composite and porous microstructures with voronoi cell finite elements. *Int. J. Numer. Meth. Engrg.*, 39, 1996.

[62] RL. Motard and B. Joseph. *Wavelet applications in chemical engineering.* Kluwer Academic Publishers, 1994.

[63] A. Needleman. A continuum model for void nucleation by interfacial debonding. *Jour. Appl. Mech.*, 54, 1987.

[64] A. Needleman. An analysis of decohesion along an imperfect interface. *Int. J. Fracture*, 42, 1990.

[65] A. Needleman. Micromechanical modeling of interfacial decohesion. *Ultramicroscopy*, 40, 1992.

[66] J.T. Oden and K. Vemaganti. Estimation of local modeling error and goal-oriented adaptive modeling of heterogeneous materials, part ii: a computational environment for adaptive modeling of heterogeneous elastic solids. *Comput. Meth. Appl. Mech. Engng.*, 190, 2001.

[67] J.T. Oden and T.I. Zohdi. Analysis and adaptive modeling of highly heterogeneous elastic structures. *Comput. Meth. Appl. Mech. Engng.*, 148, 1997.

[68] M. Ortiz and A. Pandolfi. Finite-deformation irreversible cohesive element for three-dimensional crack-propagation analysis. *Int. Jour. Numer. Meth. Engng.*, 44, 1999.

[69] Y. H. Pao and C. C. Mow. *The diffraction of elastic waves and dynamic stress concentrations.* Crane Russak, 1973.

[70] R. Pyrz. Quantitative description of the microstructure of composites. part i, morphology of unidirectional composite systems. *Comp. Sci. Tech.*, 50, 1994.

[71] S. Qian and J. Weiss. Wavelets and the numerical solution of boundary value problems. *Appl. Math. Lett.*, 6(1), 1993.

[72] W. A. M. Brekelmans R. J. M. Smit and H. E. H. Meijer. Prediction of the mechanical behavior of nonlinear heterogeneous systems by multi-level finite element modeling. *Comp. Meth. Appl. Mech. Engrg.*, 155(1-2), 1998.

[73] P. Raghavan and S. Ghosh. Adaptive multi-scale computational modeling of composite materials. *Comput. Model. Engng. Sci.*, 5(2), 2004.

[74] P. Raghavan and S. Ghosh. Concurrent multi-scale analysis of elastic composites by a multi-level computational model. *Comput. Meth. Appl. Mech. Engng.*, 193(6-8), 2004.

[75] P. Raghavan and S. Ghosh. A continuum damage mechanics model for unidirectional composites undergoing interfacial debonding,. *Mech. Mater.*, 37, 2005.

[76] J. Rethore, A. Gravouil, and A. Combescure. An energy-conserving scheme for dynamic crack growth using the extended finite element method. *International Journal for Numerical Methods in Engineering*, 63, 2005.

[77] A. Romkes and J. T. Oden. Adaptive modeling of wave propagation in heterogeneous elastic solids. *Comput. Methods Appl. Mech. Engrg.*, 193, 2004.

[78] S. Ghosh S and S. Moorthy. Three dimensional voronoi cell finite element model for modeling microstructures with ellipsoidal heterogeneities. *Comput. Mech.*, 34(6), 2004.

[79] S. Ghosh S and S N. Mukhopadhyay. A two dimensional automatic mesh generator for finite element analysis of randomly dispersed composites. *Comput. Struct.*, 41(2), 1991.

[80] S. Moorthy S and S. Ghosh. Adaptivity and convergence in the voronoi cell finite element model for analyzing heterogeneous materials. *Comp. Meth. Appl. Mech. Engin.*, 185, 2000.

[81] K. S. Ghosh, K. Lee and P. Raghavan. A multi-level computational model for multi-scale damage analysis in composite and porous materials. *Int. Jour. Solids Struct.*, 38(14), 2001.

[82] K. Lee S. Ghosh and S. Moorthy. Multiple scale analysis of heterogeneous elastic structures using homogenization theory and voronoi cell finite element method. *Int. Jour. Solids Struct.*, 32(1), 1995.

[83] S. Ghosh S. Swaminathan and N.J. Pagano. Statistically equivalent representative volume elements for composite microstructures, part i: Without damage. *Jour. Comp. Mater.*, 40(7), 2006.

[84] KH. Schweizerhof and Y. Wriggers. Consistent linearization for path following methods in nonlinear f.e. analysis. *Comp. Meth. Appl. Mech. Engng.*, 59, 1986.

[85] JA. Sethian. Evolution, implementation, and application of level set and fast marching methods for advancing fronts. *Jour. Comput. Physics*, 169, 2001.

[86] Z. Shan and A.M. Gokhale. Representative volume element for non-uniform micro-structure. *Comput. Mater. Sci.*, 24, 2002.

[87] K. Sharma, RK. Singh, NN. Kishore, KK. Vase, and AK. Ghosh. Application of efg (element free galerkin) for crack path prediction. *Proceeding of the International Congress on Computational Mechanics and Simulation 04, India*, 2004.

[88] RL. Spilker and SP. Singh. Three-dimensional hybrid-stress isoparametric quadratic displacement elements. *Int. J. Numer. Methods Eng.*, 18, 1982.

[89] K. Sumihara. Hybrid stress finite element formulation based on additional internal displacements-application of microscopic geometric perturbation and extension to linear dynamics. *Finite Elements in Analysis and Design*, 31, 1999.

[90] S. Swaminathann and S. Ghosh. Statistically equivalent representative volume elements for composite microstructures, part ii: With evolving damage. *Jour. Comp. Mater.*, 40(7), 2006.

[91] H. Tada. *The stress analysis of cracks handbook.* Del Research Corporation. Hellertown, PA, 1973.

[92] K.K. Tamma and P.W. Chung. Woven fabric composites: Developments in engineering bounds, homogenization and applications. *Inter. Jour. Numer. Meth. Engng.*, 45, 1999.

[93] H. Tan, C. Liu, Y. Huang, and PH. Geubelle. The cohesive law for the particle/matrix interfaces in high explosives. *Journal of the mechanics and Physics of solids*, 53, 2005.

[94] K. Terada and N. Kikuchi. Simulation of the multi-scale convergence in computational homogenization approaches. *Inter. Jour. Solids and Struc.*, 37, 2000.

[95] P. Tong. A hybrid crack element for rectilinear anisotropic material. *Int. J. Numer. Methods Eng.*, 11, 1977.

[96] P. Tong, THH. Pian, and SJ. Lasry. A hybrid-element approach to crack problems in plane elasticity. *Int. J. Numer. Methods Eng.*, 7, 1973.

[97] V. Tvergaard. Effect of fiber debonding in a whisker-reinforced metal. *Mater. Sci. Engng.*, A125, 1990.

[98] J. Qu V. N. Bulsara, R. Talreja. Damage initiation under transverse loading of unidirectional composites with arbitrarily distributed fibers. *Comp. Sci. Tech.*, 59, 1999.

[99] G. Ventura, E. Budyn, and T. Belytschko. Vector level sets for description of progagating cracks in finite elements. *International Journal for Numerical Methods in Engineering*, 58(10), 2003.

[100] G. Ventura, JX. Xu, and T. Belytschko. A cector level set method and new discontinuity approximations for crack growth by efg. *International Journal for Numerical Methods in Engineering*, 54(6), 2002.

[101] Z. P. Wang and C. T. Sun. Modeling micro-inertia in heterogeneous materials under dynamic loading. *Wave Motion*, 36, 2002.

[102] K. Washizu. *Variational methods in elasticity and plasticity.* Pergamon Press, 1982.

[103] XP. Xu and A. Needleman. Finite deformation effects in homogeneous and interfacial fracture. *J. Mech. Phys. Solids*, 42(9), 1994.

[104] W-M. Xue, LA. Karlovitz, and SN. Atluri. On the existence and stability conditions for mixed-hybrid finite element solutions based on reissner's variational principle. *Int. Jour. Solids. Struc*, 21(1), 1985.

[105] J. Yau, S. Wang, and H. Corten. A mixed-mode crack analysis of isotropic solids using conservation laws of elasticity. *J Appl Mech*, 47, 1980.

[106] Y. Y. Zhu and S. Cescotto. fully coupled elasto-visco-plastic damage theory for anisotropic materials. *Int. J. Frac.*, 32(11), 1995.

[107] O.C. Zienkiewicz and J.Z. Zhu. The superconvergence patch recovery and a posteriori error estimates. part 1: The recovery technique. *Inter. Jour. Numer. Methods Engrg.*, 33, 1992.

[108] T.I. Zohdi and P. Wriggers. A domain decomposition method for bodies with heterogeneous microstructure based on material regularization. *Inter. Jour. Solids and Struc.*, 36, 1999.